Mathematical models of receptor mediated processes in vascular endothelial cells

Maria Nowicka

School of Mathematics

University of Leeds

Submitted in accordance with the requirements for the degree of

Doctor of Philosophy

October, 2017

The candidate confirms that the work submitted is her own and that appropriate credit has been given where reference has been made to the work of others.

Joint Publications

Almost all of the work presented in Chapter 3 and some of the work presented in Chapter 5 has already been refereed and published, as follows:

- López-García M, **Nowicka M**, Fearnley GW, Ponnambalam S, Lythe G, Molina-París C (2016) "Performance measures in stochastic processes and the matrix-analytic approach". In: Munsky B, Hlavacek W, Tsimring L (eds.) Qbio Methods. *In press.*
- **Sawicka M***, Stritesky GL, Reynolds J, Abourashchi N, Lythe G, Molina-París C, Hogquist KA (2014) "From pre-DP, post-DP, SP4, and SP8 thymocyte cell counts to a dynamical model of cortical and medullary selection". *Frontiers in Immunology*, 5: 19.

Also, almost all of the work in Chapter 3 has been submitted and is under review, as follows:

- López-García M^{+}, **Nowicka M**$^{+}$, Bendtsen C, Lythe G, Ponnambalam S, Molina-París C, "Quantifying phosphorylation timescales of receptor-ligand complexes: a Markovian matrix-analytic approach". *Submitted.*

* Change of name, Nowicka M, $^{+}$ equal contribution

Acknowledgements

This research was funded by Engineering and Physical Science Research Council Doctoral Training Grant CASE Studentship, provided jointly by the University of Leeds and Astrazeneca UK Limited.

First and foremost, I thank my supervisors Carmen Molina-París, Grant Lythe and Martin Lopez-García for their constant support during my time spent as a post-graduate at the University of Leeds. This work would not have been possible without your passion for mathematics you shared with me.

I would like to thank Stuart Barber and John Paul Gosling for stimulating conversations and advice, especially on the subject of the Bayesian estimation methods.

I also thank Sreenivasan Ponnambalam for time spent explaining vascular systems, which helped immensely in retaining some resemblance of reality in the mathematical models developed in this thesis.

I thank Gareth Fearnley and Kristin Hogquist for sharing the experimental data used in Chapter 4 and Chapter 5, respectively.

Additionally, I thank all the researchers from Astrazeneca in the field of vascular systems with whom I have discussed my work, particularly Claus Bendtsen.

To my family, most notably my parents, I give my thanks for your support, both during my post-graduate studies, and throughout my life prior to this undertaking.

Lastly, I thank the most important person in my life, Maciek, for being with me these past years. Thank you for believing in me and remembering that *"things are only impossible until they are not"*.

Abstract

I present in this thesis a wide analysis of stochastic and deterministic models of the vascular endothelial growth factor (VEGF) and vascular endothelial growth factor receptor (VEGFR) on human umbilical vein endothelial cells (HUVEC).

Firstly, the analysis addresses the contribution of ligand induced dimerisation, receptor competition between VEGFR1 and VEGFR2 and immediate or delayed dimers phosphorylation in the overall behaviour of the VEGFR/VEGF system. The analysis is based on van Kampen approximation of the solution of the corresponding master equations and matrix-analytic techniques to analyse different signalling hypotheses upon ligand stimulation.

Secondly two mathematical models are provided, with accompanying quantitative experimental data, for binding and trafficking properties of VEGFR on HUVECs, which propose a theoretical dependence of ERK phosphorylation and transport rate of receptors from the Golgi to the cell surface on these properties. The signal for ERK phosphorylation or perturbation of transport rate is generated by intrinsic VEGFR tyrosine kinase activation via VEGF binding at the cell surface, and terminated by receptor/growth factor complex internalisation and degradation. Presented in this thesis models consist of kinetic equations which describe the binding, internalisation, recycling and synthesis of VEGF and VEGFR, along with a simple expression for the dependence of ERK phosphorylation or receptor synthesis on VEGFR/VEGF dynamics.

Contents

List of Figures

LIST OF FIGURES

Chapter 1

Introduction

1.1 Biological introduction

The mammalian vascular network is a system of biological tubes that enables the delivery of diverse array of proteins, lipids, sugars, micelles, vesicles, nucleic acids and cells to different cells, tissues and organs (see de Almodovar *et al.* (2009)). This network is also exploited by blood-borne pathogens (*e.g.* bacteria, viruses) and can also display aberrant regulation that contributes to major disease states such as cancer, heart disease and pre-eclampsia. Many key features of vascular homoeostasis, development and control are dependent on the endothelial cell. This unique cell forms a confluent monolayer that lines all blood vessels, forming a single cell barrier between the blood and the walls of the blood vessels such as arteries, veins and capillaries. The endothelial cell has the unique ability to respond to circulating growth factors, lipid particles and mechanosensory stimuli to integrate the animal response to the environment, diet and other biological cues.

The ability of the endothelial cell to integrate the cellular response to biological cues is dependent on the controlled activation of different signalling networks that impact on cellular homoeostasis and gene expression. One such example is the vascular endothelial growth factor (VEGF) family that is conserved in metazoan species from man to fish (see Smith *et al.* (2015)). The founding member of this family, VEGF-A, exerts complex biological responses from endothelial cells. This is further complicated by the fact that the human VEGF-A gene encodes

multiple protein isoforms such as VEGF-A_{165} and VEGF-A_{121}, which differ within their lengths (see Harper & Bates (2008)). Mounting evidence suggests that the various isoforms are involved in diverse cellular responses (see Olsson *et al.* (2006)). VEGF-A isoforms bind to two different membrane-bound receptors, VEGFR1 and VEGFR2, which are receptor tyrosine kinases (RTK) and potent switches in signal transduction. Each receptor has an extra-cellular domain for binding ligand, a trans-membrane domain, and an intra-cellular or cytoplasmic domain (see Figure 1.1).

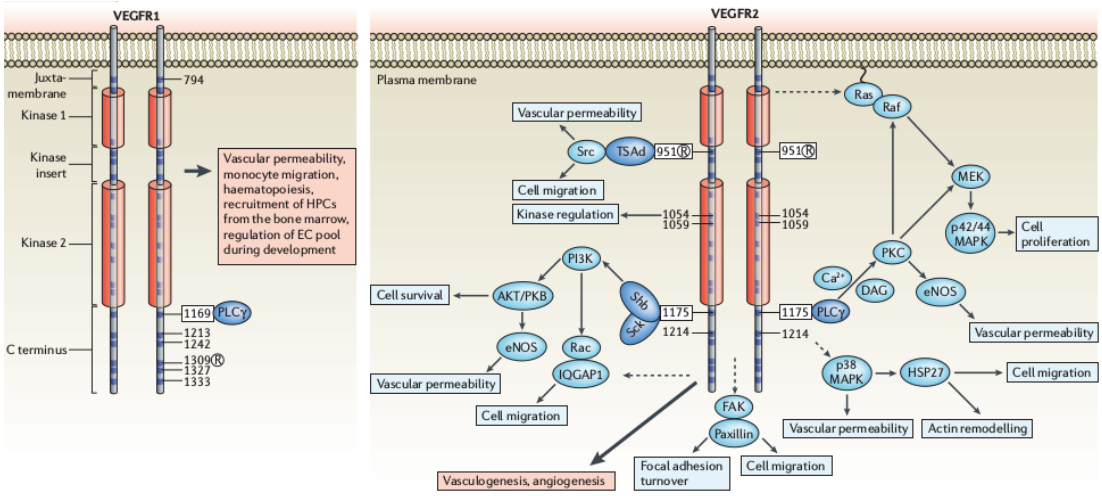

Figure 1.1: VEGFR phosphorylation sites and signal transduction by Olsson *et al.* (2006).

Intracellular domains of dimerised and activated VEGFR1 and VEGFR2 in Figure 1.1 are shown with tyrosine-phosphorylation sites that are indicated by numbers. Circled R indicates that use of the phosphorylation site is regulated dependent on the angiogenic state of the endothelial cell (for VEGFR2) or is regulated by a particular ligand (for VEGFR1) or by hetero-dimerisation. Dark blue squares in the receptor molecules indicate positions of tyrosine residues. Binding of signalling molecules (dark blue ovals) to certain phosphorylation sites (boxed numbers), initiates signalling cascades (light blue ovals), which leads to the establishment of specific biological responses (pale blue boxes). The mode of initiation of certain signalling chains is unclear (dashed arrows). Final biological

outcomes that are coupled to the respective receptors are indicated in pink boxes. The following molecules shown in Figure 1.1 are involved in signalling cascade: DAG, diacylglycerol; EC, endothelial cell; eNOS, endothelial nitric oxide synthase; FAK, focal adhesion kinase; HPC, haematopoietic progenitor cell; HSP27, heat-shock protein-27; MAPK, mitogen-activated protein kinase; MEK, MAPK and ERK kinase; PI3K, phosphatidylinositol 3 kinase; PKC, protein kinase C; PLC, phospholipase C-; Shb, SH2 and -cells; TSAd, T-cell-specific adaptor.

VEGFR1 role is negative regulation of VEGF-A signalling whereas VEGFR2 transduces all known effects of VEGF-A (see Simons (2012), Simons *et al.* (2016)). VEGF-A binding to VEGFR1 or VEGFR2 causes transmission of conformational changes, which induces receptor homo-dimerisation or hetero-dimerisation and results in activation of the tyrosine kinase activity within the VEGFR cytoplasmic domain located on the other side of the lipid bilayer. Phosphotyrosines and surrounding amino acid residues constitute binding sites for adapter molecules, which initiate various intracellular signalling pathways (see Simons *et al.* (2016)). These pathways mediate immediate responses, such as vascular permeability, and longer-term responses that require gene regulation, such as endothelial cell survival, migration and proliferation (see Figure 1.1).

Most of the work in this field has focused on studying the endothelial response to VEGF-A_{165}, the major isoform present in most extracellular fluids, cells and tissues. Nonetheless, work has suggested that differences in the properties of VEGF-A_{165} and VEGF-A_{121} enabled the controlled activation of different signalling pathways (see Whitaker *et al.* (2001), Karihaloo *et al.* (2005), Rennel *et al.* (2009)). Much of the work has focused on VEGFR2, which is thought to be the key molecule that controls the endothelial response to VEGF-A.

In order to model endothelial cell behaviour regulated by VEGFR/VEGF-A signalling, initial cell surface binding events and subsequent intra-cellular trafficking processes must be first quantified. Once this foundation is established, cellular behaviour can more easily be analysed based on the number, state, and location of all molecules and complexes involved. The receptor population is involved in binding to other receptors or membrane associated molecules, internalisation, recycling, degradation and synthesis, broadly termed "trafficking" events. Both VEGFR monomers and VEGFR dimers undergo internalisation by

the same mechanism. The molecules are internalised and transferred to the early endosome, in a process called endocytosis. After entering the early endosome, monomeric and dimeric VEGFRs follow different pathways. The latter are transported to the late endosome and then to the lysosome for degradation, whereas the former are rapidly recycled to the membrane (see Teis & Huber (2003) and Figure 1.2).

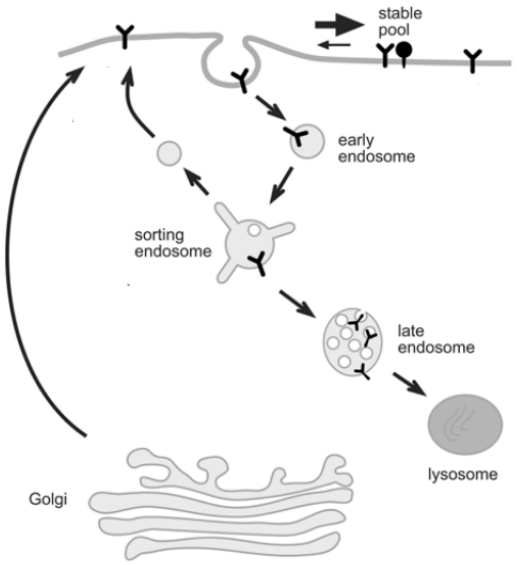

Figure 1.2: Intracellular trafficking adapted from Scott & Mellor (2009). At the surface there are two pools: a stable pool, and a pool that is constantly internalising. Internalised VEGFR is trafficked to the early/sorting endosomal compartment, where it is recycled to the cell surface or sent to late endosome for degradation. New receptors are synthesised from the Golgi apparatus.

VEGF-A-induced signalling cascades can cause diverse cellular responses such as cell motility, division or death (or apoptosis). Thus, a quantitative study of binding and phosphorylation kinetics is crucial to the understanding of processes like angiogenesis and vasculogenesis.

1.2 Short review of previously studied receptor-ligand models

Alarcón & Page (2007) propose a stochastic model which includes binding, dimerisation, endocytosis and early signalling events. The authors carry out an analysis of the master equation of the process, by a generalisation of the Wentzel-Kramers-Brillouin method, to address the contribution of ligand induced receptor dimerisation, activation of src-homology-2 domain-carrying kinases and receptor internalisation in the behaviour of the VEGFR/VEGF-A system, where only one receptor type is considered (VEGFR2).

In order to analyse in detail the dimerisation and phosphorylation kinetics on the cell membrane, it is usual to consider mathematical models which neglect internalisation events, and strictly focus on the biochemical reactions taking place on the cell surface. Mac Gabhann & Popel (2007) introduce a comprehensive set of models with different dimerisation pathways: the first allowing pre-dimerisation without ligand and the second considering only ligand induced receptor dimerisation. In this way, the authors can address the role of pre-formed dimers in the binding process. It is also worth mentioning, that Olsson *et al.* (2006) report that blood flow might activate VEGFRs in a ligand-independent manner (promoting the activation of mechanosensory complexes). The consideration of more than one receptor type by Mac Gabhann & Popel (2007) is also essential, given that the authors note that prostacyclin synthesis has been reported to be under the control of VEGFR heterodimers, which suggests that the signalling of heterodimers is unique and significant for cellular responses. In most papers, VEGFR1 is often neglected, even when it might be essential for the recruitment of haematopoietic precursors and migration of monocytes and macrophages. Furthermore, in many biological responses to VEGF-A, the contribution of both VEGFR1 and VEGFR2 might be required for a balanced signalling (see Olsson *et al.* (2006)). VEGFR signal-transduction models have to provide a context for potential communication between different VEGF receptors at the plasma membrane (through hetero-dimerisation). Therefore, the dynamics of competition for ligand availability between VEGFR1 and VEGFR2 needs still to be analysed in greater depth.

There is a wealth of previous studies that have developed mathematical models of RTKs and their role in cellular responses. For example, Starbuck *et al.* (1990) consider a different receptor tyrosine kinase, the endothelial growth factor receptor (EGFR) to study the role of endothelial growth factor (EGF) on B82 fibroblasts. They argue that the receptor signal is generated at a rate proportional to the number of activated receptors present, so that the amount of phosphorylated dimers is directly related to the initiation of signalling cascades. Tan *et al.* (2013a) consider a mathematical model of pre-formed dimers, with instantaneous phosphorylation of dimers upon ligand binding. However, phosphorylation is in fact a multi-step process, in which the different tyrosine residues of the intracellular tails of the dimeric receptors trans-phosphorylate each other as noted by Olsson *et al.* (2006). Stochastic models of receptor oligomerisation by bivalent ligands are introduced by Alarcón & Page (2006) to study the role of cross-linking in cell activation. A particular feature of this study is that a small number of receptors is considered, making a stochastic approach more appropriate than a deterministic one (see Mac Gabhann *et al.* (2005) for a comparison between deterministic and stochastic approaches in VEGFR models). In order to decipher how the dynamics on the membrane relates to cell activation, the authors define a threshold number, θ, of oligomers that need to be formed in order to trigger a cellular response. Once the process reaches this threshold, they study (by means of Gillespie simulations — see Subsection 2.2.13), the probability of staying above this threshold for a given time, $T = 10\ k_{\text{off}}^{-1}$, which is identified with the time to initiate the signalling pathway as stated by Alarcón & Page (2006).

1.3 Objectives of this thesis

Systems in biology can be analysed, from a mathematical perspective, by deterministic or stochastic approaches. A deterministic approach implies that the outcome of the system is always the same for identical initial conditions, and is generally used in mathematical models that involve large population sizes (large number of particles, molecules, individuals, etc.). The objective when analysing a deterministic system is then to compute the trajectory of the process given initial conditions. On the other hand, a stochastic approach aims to compute

the probability of the different potential outcomes of the system under study, where different outcomes can be obtained under identical initial conditions. A stochastic approach is usually required when dealing with small population sizes, with processes with external stochastic perturbations, or when *extinction* events play a significant role (see Allen (2003)).

When analysing stochastic processes arising in systems biology, the focus is usually on the *transient* behaviour of the process (see Kulkarni (1996)); that is, computing the probability of the process being at each possible state at any given time $t > 0$, which involves the master equation (see Subsection 2.2.5). Solving the master equation in the case of a Markov process, is equivalent to solving the forward Kolmogorov differential equation (see Equation (2.5)) in the theory of continuous-time Markov chains (see Subsection 2.2.1). This is not only an ambitious objective, but the Kolmogorov equations are not explicitly solvable in general. Thus, different alternatives are usually implemented in the literature to find solutions, such as Gillespie stochastic simulations algorithm (see Gillespie (1977) and Subsection 2.2.13) or moment-based approaches (see Van Kampen (1992), Hespanha (2008a) and Section 3.3).

The first part of this thesis (Chapter 3) focuses on finding analytical solutions of mathematical models describing VEGFR/VEGF-A systems. Four different stochastic models for the binding of VEGFR1 and VEGFR2 to VEGF-A ligand, taking place on the membrane of a endothelial cell, are introduced in Section 3.1. Phosphorylation and competition for ligand availability are studied in these models, assuming ligand induced dimerisation. Moment closure methods described in Section 3.3 are used to analyse the transient behaviour of Markov processes describing these four models. The parameters of the models are carefully derived following approach presented by Lauffenburger & Linderman (1993) assuming that the binding process is two-step process (diffusion and intrinsic reaction).

Depending on the objectives pursued, the analysis of the transient behaviour of the stochastic process may not always be the best way to proceed. In particular, it is possible to analyse different probabilistic performance measures that do not require solving the master equation, and allow one to obtain exact information about the stochastic process. In Section 3.4 and Section 3.5 an example of how to obtain the desired information from a stochastic process by analysing a continuous

probabilistic measure, which results in a first-passage time is provided. First-passage times are not the only measures which can be addressed, and in Section 3.5 the analysis of alternative stochastic descriptors, such as time to generate signal upon ligand stimulation, is discussed.

The analysis of these stochastic descriptors can be carried out by means of auxiliary Markov processes, making use of Laplace-Stieltjes transforms (see Subsection 2.1.9) or probability generating functions (see Subsection 2.1.8), or exploiting structural properties of the processes under study. In particular, if these processes have specific structural properties such as quasi-birth-and-death processes (see Latouche & Ramaswami (1999) and Subsection 2.2.12), it is possible to follow the matrix-analytic approach (originally developed by Neuts (1994) in the field of queueing theory), in order to efficiently analyse the stochastic descriptors of interest. This approach is mainly based on the analysis of phase-type distributions (see He (2014)) and the structure of the state space by groups and sub-groups (usually referred as *levels* and *sub-levels*) of states. Thus, transitions between states are seen as transitions between levels and sub-levels, a by-blocks-structure matrix arises in the analysis of the stochastic descriptors, and an algorithmic approach is proposed for the computation of the descriptors of interest.

The second part of this thesis (Chapter 4) focuses on deterministic modelling of experimental data with help of Bayesian methods (see Section 2.4) used for parameterisation of studied models. Understanding VEGFR1 and VEGFR2 kinetics and turnover is important as VEGF-A-stimulated signal transduction and endothelial cell responses depend on activated VEGFR residence at different locations within the cell (see Gourlaouen *et al.* (2013), Jopling *et al.* (2009), Koch *et al.* (2014), Lanahan *et al.* (2013), Lanahan *et al.* (2010), Lanahan *et al.* (2014), Manickam *et al.* (2011), Nakayama *et al.* (2013), Yamada *et al.* (2014), Zhang *et al.* (2013)). Therefore the deterministic trafficking models are studied in Chapter 4 in order to understand how localisation of phosphorylated dimers affect different signalling responses. In particular, in Section 4.1, the trafficking VEGFR2/VEGF-A model is studied where two types of isoforms, VEGF-A_{165} and VEGF-A_{121} are considered as a stimulus. Two hypotheses are explored to analyse the most probable location of phosphorylated dimers within a cell causing ERK phosphorylation, which can lead to cell proliferation, migration and

homoeostasis. In Section 4.2 a VEGFR/VEGF-A trafficking model with two receptors VEGFR1 and VEGFR2 is considered. For this model the aim is to answer the question related with the synthesis of new receptors from the Golgi apparatus. To be precise, several hypotheses are tested to find the most probable localisation of phosphorylated dimers causing perturbation of receptor synthesis upon ligand stimulation.

The data used in Chapter 4 are provided by the group of Dr Sreenivasan Ponnambalam from School of Molecular and Cellular Biology at the University of Leeds. It is shown in this thesis how experimental data, obtained from *western blot*, can be used for modelling, and I discuss the problems one can encounter when dealing with this type of data.

Additionally in Chapter 5 I once more make use of Bayesian methods to parametrise thymic development models studied previously during my master project (see Sawicka *et al.* (2014)). The experimental data, which have not been used before for modelling in this form, are used in order to learn about the insides of T cell maturation processes in the thymus. All biological introduction for these models is provided within Chapter 5.

Chapter 2

Mathematical background

2.1 Probability theory

This section details the important concepts and definitions of probability theory which are required in this thesis, based on work presented by Allen (2003) and Taylor & Karlin (2014). Probability theory is needed to introduce the stochastic processes which are used to model the biological phenomena described in this work.

2.1.1 Probability space

Let S be a set or any collection of objects, which is referred to as *sample space*. For example, the sample space could be the set of all possible outcomes of a random experiment. A *sample point* is an element of S whereas an *event* is a subset of S. For any experiment, the probability space is defined as $(S, \mathcal{A}, Prob)$, where S is the sample space, $\mathcal{A}$ is the collection of events in S, and $Prob$ is a *probability measure* defined on $\mathcal{A}$.

Let $\mathcal{A}$ be a collection of subsets of S. $\mathcal{A}$ is called a σ-algebra and the ordered pair $(S, \mathcal{A})$ is called a measurable space if $\mathcal{A}$ has the following properties,

(i) $\mathcal{A}$ contains the sample space S, that is $S \in \mathcal{A}$;

(ii) If $B \in \mathcal{A}$, then the complement of B, denoted B^c, is in $\mathcal{A}$, *i.e.*

$$B \in \mathcal{A} \Rightarrow B^c = \{s \in S : s \notin B\} \in \mathcal{A};$$

(iii) For any sequence $\{B_n\}_{n=1}^{+\infty}$, with $B_n \in \mathcal{A}\ \forall n \geq 1$, the union $\cup_{n=1}^{+\infty} B_n \in \mathcal{A}$.

Hence the probability measure $Prob$ is defined on $\mathcal{A}$ as follows.

Definition 2.1. Let $(S, \mathcal{A})$ be a measurable space. Let $Prob$ be a real-valued set function defined on the σ-algebra $\mathcal{A}$. The set function $Prob : \mathcal{A} \to [0, 1]$ is called a probability measure if it has the following properties:

(i) $Prob(B) \geq 0$ for all $B \in \mathcal{A}$.

(ii) $Prob(S) = 1$.

(iii) If $B_i \cap B_j = \emptyset$ for integers $i, j \geq 1$, where $i \neq j$, then

$$Prob(\cup_{i=1}^{+\infty} B_i) = \sum_{i=1}^{+\infty} Prob(B_i),$$

where $B_i \in \mathcal{A}$ for $i \geq 1$.

The ordered triple $(S, \mathcal{A}, Prob)$ defines a *probability space*.

Definition 2.2. A *partition* of a sample space is simply the decomposition of the sample space into a collection of mutually exclusive events with positive probability. That is $\{B_1, \ldots, B_n\}$ forms a partition of S if

(i) $S = B_1 \cup B_2 \cup \ldots \cup B_n = \bigcup_{i=1}^{n} B_i$,

(ii) $B_i \cap B_j = \emptyset,\ \forall i \neq j$,

(iii) $Prob(B_i) > 0,\ \forall i$.

2.1.2 Conditional probability and independence

Other important concepts to be defined are *conditional probability* and *independence*. Let $(S, \mathcal{A}, Prob)$ be a probability space. Let B_1 and B_2 be two events from $\mathcal{A}$. The conditional probability of event B_1 given event B_2 is defined as

$$Prob(B_1|B_2) = \frac{Prob(B_1 \cap B_2)}{Prob(B_2)},$$

assuming that $Prob(B_2) > 0$. Two events B_1 and B_2 are independent if and only if $Prob(B_1|B_2) = Prob(B_1)$ or $Prob(B_2|B_1) = Prob(B_2)$. In other words the events B_1 and B_2 are independent if and only if $Prob(B_1 \cap B_2) = Prob(B_1)Prob(B_2)$. Now one can write the following *theorem of total probability.*

Theorem 2.3 (Theorem of total probability)**.** *Suppose that there is a partition* $\{B_1, \ldots, B_n\}$ *of a sample space* S*, then for any event* A *in the sample space* S*,*

$$Prob(A) = \sum_{i=1}^{n} Prob(A|B_i)Prob(B_i).$$

One can use Theorem 2.3 to formulate *Bayes theorem.*

Theorem 2.4 (Bayes theorem)**.** *Suppose that there is a partition* $\{B_1, \ldots, B_n\}$ *of a sample space* S *and there is an event* A *such that* $Prob(A) > 0$*. Then, for* $1 \leq j \leq n$ *the probability of* B_j *given* A *is*

$$Prob(B_j|A) = \frac{Prob(A|B_j)Prob(B_j)}{Prob(A)} = \frac{Prob(A|B_j)Prob(B_j)}{\sum_{i=1}^{n} Prob(A|B_i)Prob(B_i)}.$$

Bayes theorem is the most important concept used in parameter inference methods described in Section 2.4.

2.1.3 Random variables and state space

A variable whose values depend on the possible outcomes in S is called a random variable. This idea is central to probability theory and can be defined as follows. Let $(S, \mathcal{A})$ be a measurable space. A random variable X is a real-valued function defined on the sample space S,

$$X : S \to \mathbb{R},$$

such that $\forall a \in \mathbb{R}$

$$X^{-1}(-\infty, a] = \{s \in S : X(s) \leq a\} \in \mathcal{A}.$$

The measurable space $\mathcal{S}_X$ such that,

$$\mathcal{S}_X = \{x \in \mathbb{R} : X(s) = x \text{ for some } s \in S\},$$

is called the *state space* of X. The random variable X is called a *discrete random variable* if the state space of X is finite or countably finite, whereas if the state space is infinite, the random variable X is said to be a *continuous random variable*. The random variable can be also *mixed type* if it has some properties of both a discrete and a continuous random variable.

2.1.4 Cumulative distribution function

The cumulative distribution function (c.d.f.) of the random variable X is the function $F : \mathbb{R} \to [0, 1]$, with domain $\mathbb{R}$ and range $[0, 1]$, defined by

$$F(x) = Prob(X \leq x).$$

The function $F(\cdot)$ is non-decreasing, right continuous and satisfies

$$\lim_{x \to -\infty} F(x) = 0 \qquad \text{and} \qquad \lim_{x \to +\infty} F(x) = 1.$$

The cumulative distribution function describes how the probabilities accumulate.

2.1.5 Probability mass function and probability density function

Functions that define the probability measure for discrete and continuous random variables are called the *probability mass function* (p.m.f.) and the *probability density function* (p.d.f.), respectively. Suppose X is a discrete random variable on a state space $\mathcal{S}_X$. The function $p(x) = Prob(X = x)$ that is defined for each $x \in \mathcal{S}_X$ is called the probability mass function. The p.m.f. has the following properties which result from Definition 2.1,

$$\sum_{x \in \mathcal{S}_X} p(x) = 1 \qquad \text{and} \qquad Prob(X \in B) = \sum_{x \in B} p(x), \tag{2.1}$$

for any $B \subset \mathcal{S}_X$. Additionally the c.m.f. of a discrete random variable satisfies

$$F(x) = \sum_{a \leq x} p(a),$$

and $F(x) = 0$ if $x < \inf\{a \in \mathcal{S}_X\}$.

On the other hand, suppose X is a continuous random variable with c.d.f. $F(\cdot)$ and there exists a non-negative, integrable function $f : \mathbb{R} \to [0, +\infty)$, such that

$$F(x) = \int_{-\infty}^{x} f(y)dy.$$

The function $f(\cdot)$ is called the probability density function (p.d.f.) of X. Analogously to Equation (2.1)

$$\int_{-\infty}^{+\infty} f(x)dx = 1 \qquad \text{and} \qquad Prob(X \in B) = \int_{x \in B} f(x)dx.$$

2.1.6 Joint probability distributions

Let X and Y be two random variables with state space $\mathcal{S}_X$ and $\mathcal{S}_Y$, respectively, so that the random vector (X, Y) is defined on the state space $\mathcal{S}_{XY} = \mathcal{S}_X \times \mathcal{S}_Y$ ($\times$ denotes the Cartesian product). In order to study two (or more) random variables the *joint probability mass function*, for discrete random vectors, or the *joint probability density function*, for continuous random vectors, needs to be defined.

Let X and Y be some discrete random variables, then the joint p.m.f. can be written as

$$p(x, y) = Prob(X = x, Y = y),$$

and the following equation is satisfied

$$\sum_{(x,y) \in \mathcal{S}_{XY}} p(x, y) = 1.$$

The joint p.m.f. contains all the information regarding the distributions of X and Y. This means that one can obtain the p.m.f. of X or the p.m.f. of Y from the joint p.m.f. of (X, Y) as follows,

$$p_X(x) = \sum_{y \in \mathcal{S}_Y} p(x, y), \quad p_Y(y) = \sum_{x \in \mathcal{S}_X} p(x, y).$$

$p_X(\cdot)$ and $p_Y(\cdot)$ are called the *marginal* p.m.f. of X and Y, respectively.

Let now X and Y be some continuous random variables. X and Y are called *jointly continuous* if there exists a non-negative function $f_{XY} : \mathbb{R}^2 \to [0, +\infty)$, such that, for any set $A \in \mathcal{S}_{\mathcal{X}\mathcal{Y}}$

$$Prob((X, Y) \in A) = \int\limits_{(x,y)\in A} f_{XY}(x, y)dxdy.$$

The function $f_{XY}(\cdot, \cdot)$ is called the joint probability density function of X and Y and it satisfies the following equation

$$\int\limits_{(x,y)\in\mathcal{S}_{\mathcal{X}\mathcal{Y}}} f_{XY}(x, y)dydx = 1.$$

Analogously to the discrete case one can find the *marginal probability density functions* of X and Y from their joint p.d.f.

$$f_X(x) = \int\limits_{y\in\mathcal{S}_{\mathcal{Y}}} f_{XY}(x, y)dy, \quad f_Y(y) = \int\limits_{x\in\mathcal{S}_{\mathcal{X}}} f_{XY}(x, y)dx,$$

where $f_X(\cdot)$ and $f_Y(\cdot)$ are the marginal p.d.f. of X and Y, respectively.

2.1.7 Expectation, standard deviation and covariance

The *expectation*, the *standard deviation* and the *covariance* are fundamental concepts to characterise the p.d.f. of a random variable. Suppose X is a discrete random variable with p.m.f. $p(\cdot)$ defined on a discrete state space $\mathcal{S}_{\mathcal{X}}$, then the expectation of X is defined as,

$$E(X) = \sum_{x\in\mathcal{S}_X} xp(x).$$

Suppose X is a continuous random variable with p.d.f. $f(\cdot)$ defined on a continuous state space $\mathcal{S}_{\mathcal{X}}$. Then the expectation of X, denoted $E(X)$ is defined as

$$E(X) = \int\limits_{\mathcal{S}_{\mathcal{X}}} xf(x)dx.$$

In general, given a random variable X, the expectation $E(X^k)$ for $k \in \mathbb{N}$ is called the kth moment of X. The kth moment about the mean (or kth central moment) is defined as,

$$E(X - E(X))^k.$$

The variance of the random variable X, denoted $Var(X)$ is defined as,

$$Var(X) = E(X - E(X))^2.$$

Suppose Y is also a continuous random variable, then the law of total variance or variance decomposition formula, (see Weiss (2006)) says that

$$Var(Y) = E(Var(Y|X)) + Var(E(Y|X)). \tag{2.2}$$

The standard deviation of X is the square root of the variance, $\sigma = \sqrt{Var(X)}$. The covariance of two random variables X and Y characterise the dependence of the random variables on each other and is defined as

$$Cov(X, Y) = E\left((X - E(X))(Y - E(Y))\right).$$

If $Cov(X, Y) = 0$, then X and Y are said to be uncorrelated.

2.1.8 Generating functions

The *generating function* describes an infinite sequence of numbers by treating them as the coefficients of a series expansion. The sum of this infinite series is called the generating function. Generation function representation of the probability mass function of the random variable is called *probability generating function* and it is defined as follows.

Definition 2.5. Let X be a discrete random variable defined on a state space $\mathcal{S}_X$ with p.m.f. $p(\cdot)$, then for $z \in \mathbb{R}$ the probability generating function (p.g.f.) of X is defined as

$$\mathcal{P}_X(z) = E(z^X) = \sum_{x \in \mathcal{S}_X} p(x) z^x.$$

Let X be a continuous random variable with p.d.f. $f(\cdot)$, then the p.g.f. of X is

$$\mathcal{P}_X(z) = E(z^X) = \int_{\mathcal{S}_X} f(x) z^x dx.$$

A useful alternative generating function in the study of stochastic processes is the *moment generating function*.

Definition 2.6. The moment generating function (m.g.f.) of a discrete random variable X defined on a state space $\mathcal{S}_X$ with probability function $p(\cdot)$, denoted $\mathcal{M}_X(\cdot)$ is defined for $z \in \mathbb{R}$ as

$$\mathcal{M}_X(z) = E(e^{zX}) = \sum_{x \in \mathcal{S}_X} p(x)e^{xz}.$$

Let X be a continuous random variable with p.d.f. $f(\cdot)$, then the m.g.f. is given by,

$$\mathcal{M}_X(z) = E(e^{zX}) = \int_{\mathbb{R}} f(x)e^{zx}dx.$$

An alternative function that provides an alternative distribution to the moments is the *cumulant generating function*.

Definition 2.7. The cumulant generating function (c.g.f) of the random variable X is the natural logarithm of the moment generating function, denoted $\mathcal{K}_X(\cdot)$,

$$\mathcal{K}_X(t) = \log\left(\mathcal{M}_X(t)\right),$$

where $\log(\cdot)$ denotes the natural logarithm to the base of e.

The *cumulants* κ_n are obtained from a power series expansion of the c.g.f,

$$\mathcal{K}_X(t) = \sum_{n=1}^{+\infty} \kappa_n \frac{t^n}{n!}. \tag{2.3}$$

The nth cumulant can be obtained by differentiating Equation (2.3) n times and by evaluating the result at $t = 0$,

$$\kappa_n = \mathcal{K}_X^{(n)}(0).$$

2.1.9 Laplace-Stieltjes transform

Define *Laplace-Stieltjes transform* which is used later in Sections 3.4 and 3.5 of Chapter 3.

Definition 2.8. Let X be a non-negative real valued random variable with c.d.f. $F(\cdot)$. Laplace-Stieltjes transform of X (or of its c.d.f.) is defined as

$$\phi_X(s) = E(e^{-sX}) = \int_{x=0}^{+\infty} e^{-sx}dF(x), \Re(s) \geq 0.$$

The LST has the following properties,

1. $\phi_X(0) = Prob(X < +\infty)$.

2. The moments of X are given by

$$E(X^k) = (-1)^k \frac{d^k}{ds^k} \phi_X(s) \mid_{s=0}, \quad k \geq 1.$$

3. Let X and Y be independent random variables, then

$$\phi_{X+Y}(s) = \phi_X(s)\phi_Y(s).$$

2.1.10 Exponential distribution

In probability theory and statistics the *Poisson process* is a process in which events occur continuously and independently at a constant average rate. The exponential distribution describes the time between events in this process.

Definition 2.9. If a random variable X is exponentially distributed with rate parameter α then its p.d.f. is defined as,

$$f(x) = \begin{cases} \alpha e^{-\alpha x}, & x > 0, \\ 0, & x \leq 0. \end{cases}$$

The kth moment of X is given by,

$$E(X^k) = \frac{k!}{\alpha^k},$$

and its Laplace-Stieltjes transform is

$$\phi_X(s) = \int_{x=0}^{+\infty} e^{-sx} \alpha e^{-\alpha x} dx = \frac{\alpha}{\alpha + s}.$$

The exponentially distributed random variable X obeys the following memoryless property,

$$Prob(X > s + x | X > s) = Prob(X > x), \quad \forall s, x \geq 0.$$

When X is interpreted as the waiting time for an event to occur relative to some initial time, this relation implies that, if X is conditioned on a failure to observe

the event over some initial period of time s, the distribution of the remaining waiting time is the same as the original unconditional distribution.

Let $X_1, X_2, \ldots X_n$ be independent exponentially distributed random variables with rate parameters $\alpha_1, \alpha_2, \ldots, \alpha_n$. Then variable $Z = min\{X_1, X_2, \ldots, X_n\}$ is also exponentially distributed with parameter $\alpha = \alpha_1 + \alpha_2 + \ldots + \alpha_n$. The index of the variable which achieves the minimum is distributed as

$$Prob(Z = X_k) = \frac{\alpha_k}{\alpha}, \quad 1 \leq k \leq n.$$

2.2 Stochastic Processes

In probability theory, a *stochastic process* is usually defined as a collection of random variables. A *stochastic model* described by a stochastic process can be used to estimate probable outcomes when one or more model variables are changed randomly. In this section, I define a stochastic process and give some examples of the kind of processes which are used later in this thesis. I also show some methods which can help to solve stochastic equations. The theory in this section is based mainly on work presented by Allen (2003), Kulkarni (1996), Latouche & Ramaswami (1999) and He (2014).

Definition 2.10. A stochastic process $\mathcal{X}$ is a collection of random variables $\mathcal{X} = \{X(t) : t \in T\}$, where T is some index set and variables $X(t)$ take values in the state space of the stochastic process, $\mathcal{S}_\mathcal{X}$. For each realisation of the stochastic process, $\{X(t) : t \in T\}$ becomes a function defined on T that is called a sample path of the process.

A stochastic process can be multivariate, *i.e.* it can consist of a collection of random vectors,

$$\boldsymbol{X}(t) = (X_1(t), X_2(t), \ldots, X_k(t)), \text{ where } k \in \mathbb{N}.$$

2.2.1 Continuous time Markov chain

Let $\mathcal{X} = \{X(t) : t \in [0, +\infty)\}$ be a collection of discrete random variables with values in a discrete state space $\mathcal{S}_\mathcal{X}$, which can be finite or infinite, and where

the index set is continuous, $t \in [0, +\infty)$. The stochastic process $\mathcal{X}$ is called a *continuous time Markov chain* (CTMC) if for any sequence of real numbers satisfying $0 \leq t_0 < t_1 < \ldots < t_n < t_{n+1}$,

$$\begin{aligned} &Prob\left(X(t_{n+1}) = i_{n+1} | X(t_0) = i_0, X(t_1) = i_1, \ldots, X(t_n) = i_n\right) \\ &\quad = Prob\left(X(t_{n+1}) = i_{n+1} | X(t_n) = i_n\right), \end{aligned} \tag{2.4}$$

where $i_0, i_1, \ldots, i_{n+1} \in \mathcal{S}_{\mathcal{X}}$. The condition defined in Equation (2.4) is known as the *Markov property* and intuitively means that the state transition from i_n to i_{n+1} depends only on the value of the state at time t_n and does not depend on the history of the process. Each random variable $X(t)$ has an associated probability distribution,

$$p_i(t) = Prob(X(t) = i), \text{ where } i \in \mathcal{S}_{\mathcal{X}}.$$

2.2.2 Transition probabilities

Transition probabilities define a relation between the random variables $X(t)$ and $X(s)$, where $s < t$, in the following way,

$$p_{ij}(t, s) = Prob(X(t) = j | X(s) = i), \text{ for } i, j \in \mathcal{S}_{\mathcal{X}}.$$

The CTMC $\mathcal{X}$ is called *homogeneous* if the transition probabilities depend only on the length of the interval $t - s$; that is, if

$$p_{ij}(t, s) = p_{ij}(t - s) = Prob(X(t - s) = j | X(0) = i).$$

In this case the matrix of transition probabilities is called the *transition matrix*,

$$\boldsymbol{P}(t) = (p_{ij}(t))_{i,j \in \mathcal{S}_{\mathcal{X}}}.$$

The transition matrix $\boldsymbol{P}(t)$ is a stochastic matrix for all $t \geq 0$; that is, elements of each row sum up to 1. This is because the sum of transition probabilities from a state i to any state must be equal to one.

2.2.3 Chapman-Kolgomorov equations

The transition probabilities are solutions of the *Chapman-Kolgomorov* equations for all $s, t \in [0, +\infty)$,

$$\sum_{k \in \mathcal{S}_X} p_{kj}(s) p_{ik}(t) = p_{ij}(s+t),$$

which can written in matrix form as,

$$\boldsymbol{P}(s)\boldsymbol{P}(t) = \boldsymbol{P}(s+t).$$

2.2.4 Infinitesimal generator matrix

Assume that transition probabilities $p_{ij}(t)$ are continuous and differentiable for $t \geq 0$, $p_{ij}(0) = 0$ for $i \neq j$ and $p_{ii}(0) = 1$. Transition rates for the stochastic process are defined as,

$$q_{ij} = \begin{cases} \lim\limits_{\Delta t \to 0^+} \dfrac{p_{ij}(\Delta t) - p_{ij}(0)}{\Delta t} = \lim\limits_{\Delta t \to 0^+} \dfrac{p_{ij}(\Delta t)}{\Delta t} & \text{if } i \neq j, \\ \lim\limits_{\Delta t \to 0^+} \dfrac{p_{ii}(\Delta t) - p_{ii}(0)}{\Delta t} = \lim\limits_{\Delta t \to 0^+} \dfrac{p_{ii}(\Delta t) - 1}{\Delta t} & \text{if } i = j. \end{cases}$$

These transition rates can be stored in a matrix, which is called the *infinitesimal generator matrix* $\boldsymbol{Q} = (q_{ij})_{i,j \in \mathcal{S}_X}$. The matrix $\boldsymbol{Q}$ encodes all the information about the process. Note that $\sum\limits_{i,j \in \mathcal{S}_X} p_{ij}(\Delta t) = 1$, hence

$$1 - p_{ii}(\Delta t) = \sum_{\substack{i \neq j \\ j \in \mathcal{S}_X}} p_{ij}(\Delta t) = \sum_{\substack{i \neq j \\ j \in \mathcal{S}_X}} \left(q_{ij} \Delta t + o(\Delta t) \right).$$

Thus the elements on the diagonal of $\boldsymbol{Q}$ can be written as

$$q_{ii} = \lim_{\Delta t \to 0^+} \frac{1}{\Delta t} \sum_{\substack{i \neq j \\ j \in \mathcal{S}_X}} \left(q_{ij} \Delta t + o(\Delta t) \right) = - \sum_{\substack{i \neq j \\ j \in \mathcal{S}_X}} q_{ij}$$

so that elements at each row of $\boldsymbol{Q}$ sum up to zero and the matrix $\boldsymbol{Q}$ is said to be *conservative*. The notation $o(\cdot)$ is the Landau order symbol such that

$$\lim_{\Delta t \to 0^+} \frac{o(\Delta t)}{\Delta t} = 0.$$

2.2.5 Kolgomorov differential equations

Applying the Chapman-Kolgomorov equations to the transition probability $p_{ij}(t+\Delta t)$, dividing by Δt, and considering $\Delta t \to 0$ leads to the system of differential equations,

$$\frac{dp_{ij}(t)}{dt} = \sum_{k \in \mathcal{S}_X} q_{kj} p_{ik}(t), \qquad \forall i, j \in \mathcal{S}_X$$

called the *forward Kolgomorov differential equation*, which can also be expressed in matrix form as

$$\frac{d\boldsymbol{P}(t)}{dt} = \boldsymbol{Q}\boldsymbol{P}(t). \tag{2.5}$$

Equation (2.5) is often referred to as the *master equation* (ME) or the *chemical master equation* (CME) of the stochastic process.

2.2.6 Stationary probability distribution

For a CTMC $\mathcal{X}$ with the infinitesimal generator matrix $\boldsymbol{Q}$ and the transition matrix $\boldsymbol{P}(t)$, a steady state of Equation (2.5) is a *stationary probability distribution* $\boldsymbol{\pi} = (\pi_i \in [0,1] : i \in \mathcal{S}_X)$ which verifies

$$\boldsymbol{Q}\boldsymbol{\pi} = \mathbf{0}, \text{ and } \sum_{i \in \mathcal{S}_X} \pi_i = 1.$$

This condition is equivalent to

$$\boldsymbol{P}(t)\boldsymbol{\pi} = \boldsymbol{\pi}, \quad \forall t \geq 0, \quad \sum_{i \in \mathcal{S}_X} \pi_i = 1.$$

Under some conditions, value $\pi_i = \lim_{t \to +\infty} Prob(X(t) = i)$ represents the long-term probability of process $\mathcal{X}$ being at state i, for each $i \in \mathcal{S}_X$ (see Allen (2003)).

2.2.7 Generating function techniques

In general, it is not always possible to find a solution for Equation (2.5) and to obtain the transition matrix $\boldsymbol{P}(t)$ for a CTMC $\mathcal{X}$. This problem is directly related to the computation of the exponential of a matrix, since a theoretical solution for Equation (2.5) is given by $\boldsymbol{P}(t) = \boldsymbol{P}(0)e^{\boldsymbol{Q}t}$ (see Allen (2003)). One method for trying to obtain $\boldsymbol{P}(t)$ is based on the generating functions defined in Subsection

2.1.8. In this method, a partial differential equation is derived from Equation (2.5) so that the solution of this equation is a generating function. I show this method for a multi-variate random variable as the stochastic models in this thesis are usually described in terms of multi-variate continuous time Markov processes (CTMP).

Consider a multi-variate CTMP $\mathcal{X} = \{\boldsymbol{X}(t) : t \in [0, +\infty)\}$, defined in terms for $k \in \mathbb{N}$ different random variables $\boldsymbol{X}(t) = (X_1(t), X_2(t), \ldots, X_k(t))$ with state space $\mathcal{S}_{\mathcal{X}_1} \times \ldots \times \mathcal{S}_{\mathcal{X}_k}$. For an initial state $\boldsymbol{X}(0) = (x_1, x_2, \ldots, x_k)$ denote the p.g.f. of that CTMP as,

$$\mathcal{P}_{\mathcal{X}}(\boldsymbol{z}, t) = \sum_{n_1 \in \mathcal{S}_{\mathcal{X}_1}} \ldots \sum_{n_k \in \mathcal{S}_{\mathcal{X}_k}} Prob(\boldsymbol{X}(t) = \boldsymbol{n}) z_1^{n_1} \ldots z_k^{n_k}, \tag{2.6}$$

where $\boldsymbol{z} = (z_1, z_2, \ldots, z_k)$, $\boldsymbol{n} = (n_1, n_2, \ldots, n_k)$ and

$$Prob(\boldsymbol{X}(t) = \boldsymbol{n}) = Prob(X_1(t) = n_1, X_2(t) = n_2, \ldots, X_k(t) = n_k | \boldsymbol{X}(0)).$$

Similarly denote the moment generating function of $\mathcal{X}$, where $\boldsymbol{\theta} = (\theta_1, \theta_2, \ldots, \theta_k)$ as,

$$\mathcal{M}(\boldsymbol{\theta}, t) = \mathcal{P}(e^{\boldsymbol{\theta}}, t) = \sum_{n_1 \in \mathcal{S}_{\mathcal{X}_1}} \ldots \sum_{n_k \in \mathcal{S}_{\mathcal{X}_k}} Prob(\boldsymbol{X}(t) = \boldsymbol{n}) e^{n_1\theta_1} \ldots e^{n_k\theta_k}. \tag{2.7}$$

By differentiating Equation (2.7) with respect to time t, one can obtain a partial differential equation for the moment generating function of the CTMP $\mathcal{X}$. This partial differential equation can be used to derive ordinary differential equations for the mean and higher-order moments of $\boldsymbol{X}(t)$. In general, differentiating Equation (2.7) with respect to $\theta_1^{n_1}, \ldots, \theta_k^{n_k}$, where $n_1 + \ldots + n_k = N$, and interchanging the order of the differentiation yields a partial differential equation for $\frac{\partial^{N+1}\mathcal{M}}{\partial t \partial \theta_1^{n_1} \ldots \partial \theta_k^{n_k}}$. Evaluating this differential equation at $\theta_1 = \ldots = \theta_k = 0$ and using the fact that

$$\left.\frac{\partial^N \mathcal{M}}{\partial \theta_1^{n_1} \ldots \partial \theta_k^{n_k}}\right|_{\theta_1 = \ldots = \theta_k = 0} = E(X_1^{n_1}(t) \ldots X_k^{n_k}(t)),$$

an ordinary differential equation for the kth moment $E(X_1^{n_1}(t) \ldots X_k^{n_k}(t))$ may be obtained. This technique is applied in Subsection 3.3.1 of Chapter 3.

2.2.8 Moment closure methods

Moment closure is an approximation method used to estimate moments of a stochastic process. Consider a CTMP $\mathcal{X}$, with $\boldsymbol{X}(t) = (X_1(t), X_2(t), \ldots, X_k(t))$. Let $\boldsymbol{m} = (m_1, m_2, \ldots, m_k)$, where $m_1, m_2, \ldots, m_k \in \mathbb{N}$. Denote by $\mu^{(\boldsymbol{m})}(t)$ the $\boldsymbol{m}$th moment as,

$$\mu^{(\boldsymbol{m})}(t) = E(X_1^{m_1}(t)X_2^{m_2}(t)\ldots X_k^{m_k}(t)).$$

One may construct a vector $\boldsymbol{\mu}(t)$ containing all moments of $\boldsymbol{X}(t)$ up to order n. The integer n is called the *order of truncation* (see Hespanha (2008a)). The evolution of $\boldsymbol{\mu}(t)$ is determined by a differential equation of the form,

$$\frac{d\boldsymbol{\mu}(t)}{dt} = \boldsymbol{A}\boldsymbol{\mu}(t) + \boldsymbol{B}\bar{\boldsymbol{\mu}}(t), \qquad \boldsymbol{\mu}(t) \in \mathbb{R}^N, \bar{\boldsymbol{\mu}}(t) \in \mathbb{R}^{\bar{N}}, \tag{2.8}$$

where $N, \bar{N} \in \mathbb{N}$ and $\bar{\boldsymbol{\mu}}(t)$ is a vector containing moments of order larger than n. The dimension N in Equation (2.8) is always larger than n since there are many moments of each order. *Moment closure* is the procedure of approximating the exact (open) moment dynamics by an approximate (closed) equation of the form,

$$\frac{d\boldsymbol{v}(t)}{dt} = \boldsymbol{A}\boldsymbol{v}(t) + \boldsymbol{B}\phi(\boldsymbol{v}(t)), \qquad \boldsymbol{v}(t) \in \mathbb{R}^N, \tag{2.9}$$

where $\phi(\boldsymbol{v}(t))$ is a column vector that approximates the moments in $\bar{\boldsymbol{\mu}}(t)$. The function $\phi(\cdot)$ is called the *moment closure function*. The goal of any moment closure method is to construct $\phi(\cdot)$ so that the solution $\boldsymbol{v}(t)$ of Equation (2.9) is close to the solution $\boldsymbol{\mu}(t)$ of Equation (2.8). There are three main approaches to construct the moment closure function (see Hespanha (2008a), Gillespie (2009b)),

1. Matching-based methods, which directly attempt to match the solutions of Equations (2.8) and (2.9).

2. Distribution-based methods, based on constructing $\phi(\cdot)$ by making reasonable assumptions on the statistical distribution of the variable $\boldsymbol{X}(t)$.

3. Large volume methods, which construct $\phi(\cdot)$ by assuming that reactions take place in a large volume.

In this thesis, I use the zero cumulants method (see Hespanha (2008a)), which is a distribution-based method, and the van Kampen approximation (see Van Kampen (1992)), which is a large volume method.

Zero cumulants method

The zero cumulants methods assumes that all multi-variable cumulants of the population $\boldsymbol{X}(t)$ with order larger than the order of truncation n are negligible (see Hespanha (2008a)). This makes the distribution of $\boldsymbol{X}(t)$ as close as possible to a Gaussian distribution, which has all cumulants of order higher than two equal to zero. The cumulant can be expressed as

$$\kappa^{(\boldsymbol{m})}(t) = \mu^{(\boldsymbol{m})}(t) + \sum_{\sum_i \bar{m}_i < \sum_i m_i} \alpha_{\bar{\boldsymbol{m}}} \mu^{(\bar{\boldsymbol{m}})}(t), \tag{2.10}$$

where the summation is over moments $\mu^{(\bar{\boldsymbol{m}})}(t)$ of order strictly smaller than $\sum_i m_i$ and values $\alpha_{\bar{\boldsymbol{m}}}$ are appropriately selected constants. This shows that the cumulant $\kappa^{(\boldsymbol{m})}(t)$ depends only on the moment $\mu^{(\boldsymbol{m})}(t)$ and lower-order moments $\mu^{(\bar{\boldsymbol{m}})}(t)$, so by setting $\kappa^{(\boldsymbol{m})}(t) = 0$ one obtains an expression for $\mu^{(\boldsymbol{m})}(t)$ as a function of lower-order moments. The procedure to compute the zero-cumulants moment closure function $\phi(\cdot)$ consists of setting to zero all cumulants corresponding to the moments that do not appear in $\boldsymbol{\mu}(t)$ and then solving Equations (2.10) for the moments in $\bar{\boldsymbol{\mu}}(t)$.

van Kampen approximation

The van Kampen approximation, like any other moment-closure method, aims to obtain the time evolution of the different order moments for the random variables of the CTMPs under consideration. It is possible to obtain a system of differential equations for the different order moments of the random variables considered. However, this system of differential equations relates any order moment of a studied variable to its immediately posterior order moment, which yields an infinite system of differential equations. The main assumption of the van Kampen approximation is that the distribution of the stochastic fluctuations around a steady state follows a multi-variate normal distribution, which allows to

close the order moment hierarchy. The van Kampen approximation, also called linear noise approximation, is developed in Van Kampen (1992) in Chapter X and can be applied when the matrices $\boldsymbol{A}, \boldsymbol{B}$ in Equation (2.8) depend on some parameter Ω that can be assumed large, *i.e.*,

$$\frac{d\boldsymbol{\mu}(t)}{dt} = \boldsymbol{A}(\Omega)\boldsymbol{\mu}(t) + \boldsymbol{B}(\Omega)\bar{\boldsymbol{\mu}}(t),$$

with Ω large. This form of moment closure results is exact in the limit as $\Omega \to +\infty$. Typically, Ω is the volume on which the chemical reactions take place.

Both methods, the zero cumulant and the van Kampen approximation are fully described in the example in Subsection 3.3.1 and Subsection 3.3.2 of Chapter 3.

2.2.9 First-passage time

Consider a CTMC $\mathcal{X} = \{X(t) : t \geq 0\}$ on the state space $\mathcal{S}_\mathcal{X} = \{0, 1, 2, \ldots\}$ with infinitesimal generator matrix $\boldsymbol{Q} = (q_{ij})_{i,j \in \mathcal{S}_\mathcal{X}}$. Assume that one is interested in the random variable

$$T = \inf\{t \geq 0 : X(t) = 0\};$$

that is the first time at which $\mathcal{X}$ enters into state 0, for some initial state $X(0) \neq 0$. T is called the *first-passage time* to 0 and represents the first time at which the variable $X(t)$ gets into state 0. Define the matrix $\boldsymbol{R}(t) = (r_{ij}(t))_{i,j \geq 1}$ where

$$r_{ij}(t) = Prob(T > t, X(t) = j | X(0) = i), \text{ for } t \geq 0.$$

Then the complementary c.d.f. of T conditioned on $X(0) = i$ is given by

$$r_i(t) = Prob(T > t | X(0) = i) = \sum_{j=1}^{+\infty} r_{ij}(t).$$

It can be shown that the matrix function $\boldsymbol{R}(t)$ with the initial condition $\boldsymbol{R}(0) = \boldsymbol{I}$ satisfies the set of differential equations

$$\frac{d\boldsymbol{R}(t)}{dt} = \boldsymbol{M}\boldsymbol{R}(t) = \boldsymbol{R}(t)\boldsymbol{M},$$

where $\boldsymbol{I}$ is the identity matrix and $\boldsymbol{M} = (q_{ij})_{i,j \geq 1}$ is a sub-matrix of the generator matrix $\boldsymbol{Q} = (q_{ij})_{i,j \geq 0}$. In particular matrix $\boldsymbol{M}$ is obtained by deleting the row and the column corresponding to state 0.

2.2.10 Phase-type distribution

Assume now that $\mathcal{S}_X = \{0, \ldots, K\}$ and 0 is an absorbing state for the CTMC $\mathcal{X}$, so that $q_{0j} = 0 \ \forall j \geq 1$. This means that once process $\mathcal{X}$ enters in state 0, it remains in this state forever and that its infinitesimal generator can be expressed as

$$\boldsymbol{Q} = \begin{pmatrix} 0 & \mathbf{0} \\ \boldsymbol{t} & \boldsymbol{M} \end{pmatrix},$$

where $\boldsymbol{t}$ is a column vector such that

$$\boldsymbol{M}\mathbf{1} + \boldsymbol{t} = \mathbf{0},$$

and $\mathbf{1}$ is a column vector of ones. In this case T, which is the first-passage time to 0, is usually referred to as the absorption time of the CTMC $\mathcal{X}$. One can define an initial distribution $\boldsymbol{\alpha} = (\alpha_1, \alpha_2, \ldots, \alpha_K)$ with $\alpha_j = Prob(X(0) = j)$ and $\sum_{i=1}^{K} \alpha_i = 1$ where $K \in \mathbb{N}$. Then the absorption time T is known to follow a *phase-type* distribution denoted as $PH(\boldsymbol{\alpha}, \boldsymbol{M})$ with c.d.f.

$$Prob(T \leq t) = 1 - \boldsymbol{\alpha} e^{\boldsymbol{M}t} \mathbf{1},$$

where $\boldsymbol{M} = (q_{i,j})_{1 \leq i,j \leq K}$.

2.2.11 Birth-and-death process

Consider CTMC $\mathcal{X} = \{X(t) : t \geq 0\}$ on the state space $\mathcal{S}_X = \{0, 1, 2 \ldots\}$ (alternatively, one can also consider a finite state space). Assume now that events in process $\mathcal{X}$ can be births or deaths, moving the process from each state n to state $n + 1$ with rate λ_n (birth) or to state $n - 1$ with rate μ_n (death), as shown in Figure 2.1.

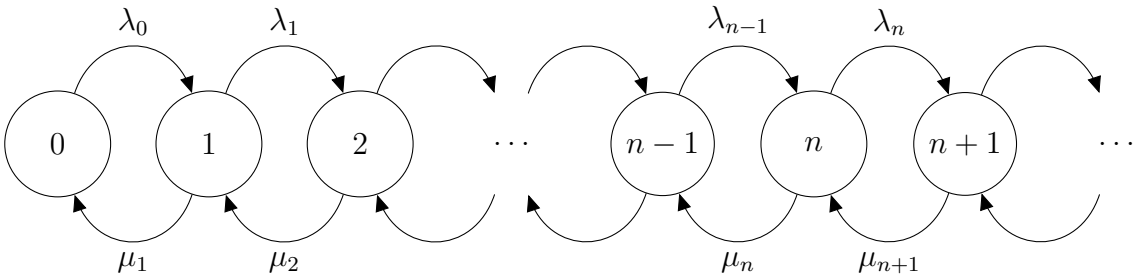

Figure 2.1: State diagram for a birth-and-death process.

Then the stochastic process $\mathcal{X}$ with transition probabilities defined as

$$\begin{aligned} p_{ij}(\Delta t) &= Prob(X(t+\Delta t)=j|X(t)=i) \\ &= \begin{cases} \lambda_i \Delta t + o(\Delta t), & \text{if } j = i+1, \\ \mu_i \Delta t + o(\Delta t), & \text{if } j = i-1, \\ 1-(\lambda_i+\mu_1)\Delta t + o(\Delta t) & \text{if } j = i, \\ o(\Delta t), & \text{otherwise,} \end{cases} \end{aligned}$$

is called *birth-and-death* process, where $i, j \in \mathcal{S}_{\mathcal{X}}$ and $o(\cdot)$ is the Landau order symbol defined in Subsection 2.2.4. The corresponding infinitesimal generator of a birth-and-death process is then the following tridiagonal matrix

$$\boldsymbol{Q} = \begin{pmatrix} -\lambda_0 & \lambda_0 & 0 & 0 & \cdots \\ \mu_1 & -(\lambda_1+\mu_1) & \lambda_1 & 0 & \cdots \\ 0 & \mu_2 & -(\lambda_2+\mu_2) & \lambda_2 & \cdots \\ 0 & 0 & \mu_3 & -(\lambda_3+\mu_3) & \cdots \\ \vdots & \vdots & \vdots & \vdots & \ddots \end{pmatrix}. \tag{2.11}$$

2.2.12 Quasi-birth-and-death process

A *quasi-birth-and-death* (QBD) process is a bivariate Markov process with a state space $\mathcal{S}_{\mathcal{X}} = \{(i,j) : i \geq 0, j = 1, 2, \ldots, M_i\}$ where i is called the *level* of the process, j is called the *phase* of the process, and M_i are integers that can be finite or infinite. The process is restricted in level jumps only to its nearest neighbours but is unrestricted in the phase dimension. More precisely, from state $(i,j) \in \mathcal{S}_{\mathcal{X}}$ the process may transition to states of the form $(i,k), (i-1,k)$ or $(i+1,k)$, but not to states of the form $(i \pm n, k)$ where $n \geq 2$. Clearly, the QBD process is an extension of the standard birth-and-death process whose state space containing levels formed by a single phase. Suppose $\mathcal{X} = \{\boldsymbol{X}(t) = (X(t), J(t)) : t \geq 0\}$ is a CTMP on the state space $\mathcal{S}$. With a suitable ordering of the states,

$$L(0) \prec L(1) \prec \ldots \prec L(n), \text{ where } L(k) = \{(k,0), \ldots, (k, M_k)\}$$

the infinitesimal generator matrix of $\mathcal{X}$ has the tridiagonal-by-block structure (similar to the matrix defined by Equation (2.11)),

$$\boldsymbol{Q} = \begin{pmatrix} \boldsymbol{A}_{0,0} & \boldsymbol{A}_{0,1} & \boldsymbol{0} & \boldsymbol{0} & \cdots \\ \boldsymbol{A}_{1,0} & \boldsymbol{A}_{1,1} & \boldsymbol{A}_{1,2} & \boldsymbol{0} & \cdots \\ \boldsymbol{0} & \boldsymbol{A}_{2,1} & \boldsymbol{A}_{2,2} & \boldsymbol{A}_{2,3} & \cdots \\ \boldsymbol{0} & \boldsymbol{0} & \boldsymbol{A}_{3,2} & \boldsymbol{A}_{3,3} & \cdots \\ \vdots & \vdots & \vdots & \vdots & \ddots \end{pmatrix}$$

where sub-matrices $\boldsymbol{A}_{k,k'}$ contain the infinitesimal transition rates of the transitions from states at level $L(k)$ to states at level $L(k')$, with $k' \in \{k-1, k, k+1\}$. For each $k \geq 0$, the diagonal elements of $\boldsymbol{A}_{k,k}$ are strictly negative, and the off-diagonal elements of $\boldsymbol{A}_{k,k}$ are non-negative. The matrices $\boldsymbol{A}_{k,k'}$ where $k \neq k'$ are non-negative. For $k \geq 1$, the matrix $\boldsymbol{A}^{(k)} = \boldsymbol{A}_{k,k-1} + \boldsymbol{A}_{k,k} + \boldsymbol{A}_{k,k+1}$ has zero row sums as does the matrix $\boldsymbol{A}_{0,0} + \boldsymbol{A}_{0,1}$. The structure of the generator matrix $\boldsymbol{Q}$ reveals that its transitions are restricted to nearest neighbours in the levels and unrestricted (in general) across the phase dimension.

The processes described in Sections 3.4 and 3.5 in Chapter 3 are studied analytically using QBD representation in order to consider a number of specifically defined stochastic descriptors.

2.2.13 The Gillespie algorithm

In probability theory, the *Gillespie algorithm* allows to generate numerical simulations of the stochastic processes under consideration. It was presented by Gillespie (1976) where the algorithm was used to simulate chemical or biochemical systems of reactions efficiently and accurately using limited computational power. Since a CTMP can be seen as a sequence of competitions of exponential random variables (see Gillespie (1976)), the Gillespie algorithm is based on the properties presented in Subsection 2.1.10. For a CTMP $\mathcal{X}$ with a space of states $\mathcal{S}_{\mathcal{X}}$ and with the infinitesimal generator matrix $\boldsymbol{Q} = (q_{ij})_{i,j \in \mathcal{S}_{\mathcal{X}}}$, the Gillespie algorithm can be described by Algorithm 1.

Define two counters to represent time, t, and the state of the process, n. Set $t = 0$ and $n = n_0$, where n_0 is the initial state of the CTMP $\mathcal{X}$. Choose a time to end the process, T_{max}. Repeat the following steps until $t > T_{max}$,

1. Calculate the transition rate to each state that can be reached from n in a single jump, that is q_{nj} for all $j \in \mathcal{S}_{\mathcal{X}}$.
   Let $\alpha = \sum_{j \neq n} q_{nj}$ be the sum of these transition rates.
2. Draw a random number τ from an exponential distribution with parameter α, representing the time until process $\mathcal{X}$ leaves n.
3. Update the time t, to $t + \tau$.
4. Draw a uniformly distributed random number u from the interval $[0, 1]$.
5. Partition the interval $[0, 1]$ by the relative size of each transition probability, $1/q_{nj}, j \in \mathcal{S}_{\mathcal{X}}$.
6. Determine which sub-interval u falls within.
7. Update n based on the corresponding transition probability determined by u.
8. Record the time and state of the process as a vector, (t, n).

Algorithm 1: by Gillespie (1976) for simulating a CTMP.

2.3 Global sensitivity analysis

Mathematical models describing some systems in biology or physics usually have some unknown parameters, and which need to be estimated from data. In order to know which parameters need more statistical effort when being estimated, one needs to assess which parameters have more impact in the output of a given data set. In this Section I briefly describe a global sensitivity analysis method called the *Sobol algorithm*, which can help to identify the most relevant parameters of the model under study. The Sobol algorithm is used in practice in Sections 4.1 and 4.2 of Chapter 3 of this thesis.

Saltelli *et al.* (2004), Campolongo & Cariboni (2007) and Wu *et al.* (2013) described in detail the Sobol algorithm. This method is a variance-based global sen-

sitivity analysis technique capable of estimating the influence of individual parameters, or a group of parameters, on some output variables of a non-linear model. Consider a model of the relationship between the parameters $\boldsymbol{\theta} = (\theta_1, \theta_2, \ldots, \theta_k)$ and the output variable $Y = f(\boldsymbol{\theta})$ which depends on those parameters. The main idea of Sobol's method is to decompose the output variance into the contributions associated with each input factor. In order to quantify the importance of an input factor θ_i on the variance of Y, imagine that one can fix it at its true value, θ_i^*. To answer the question of how much would this assumption change the variance of Y one can first compute the following conditional variance

$$Var(Y|\theta_i = \theta_i^*),$$

where the variance is taken over the $(k-1)$ dimensional parameter space consisting in all the parameters of $\boldsymbol{\theta}$ except θ_i. As the true value θ_i^* is unknown, one can look at the average of the above variance over all possible values θ_i^* of θ_i,

$$E(Var(Y|\theta_i)).$$

and take the factor with the smallest $E(Var(Y|\theta_i))$. By the law of total variance (see Equation (2.2)) the variance of Y can be written as,

$$Var(Y) = E(Var(Y|\theta_i)) + Var(E(Y|\theta_i)). \tag{2.12}$$

Given that $Var(Y)$ is a constant, betting on the lowest $E(Var(Y|\theta_i))$ is equivalent to betting the highest $Var(E(Y|\theta_i))$. Therefore by dividing Equation (2.12) by $Var(Y)$ one can obtain the *first order sensitivity index* S_i for the parameter θ_i as follows,

$$1 = \frac{E(Var(Y|\theta_i = \theta_i^*))}{Var(Y)} + \frac{Var(E(Y|\theta_i = \theta_i^*))}{Var(Y)}, \tag{2.13}$$

hence

$$S_i = \frac{Var(E(Y|\theta_i))}{Var(Y)},$$

so that $S_i \leq 1$.

As proved by Sobol (1993) if the function $f(\cdot)$ is integrable over $[0,1]^k$ then it can be decomposed into terms of increasing dimensionality as follows ,

$$Y = f(\boldsymbol{\theta}) = f_0 + \sum_{i=1}^{k} f_i(\theta_i) + \sum_{j>i}^{k} f_{i,j}(\theta_i, \theta_j) + \ldots + f_{1,2,\ldots,k}(\theta_1, \theta_2, \ldots, \theta_k),$$

where each term is a function only of the factors in its index, *i.e.* $f_i = f_i(\theta_i)$, $f_{i,j} = f_{i,j}(\theta_i, \theta_j)$ and so on. Moreover Sobol (1993) demonstrated that if each term in this expansion has a zero mean, then the total variance of an output variable can be decomposed and represented as,

$$Var(Y) = \int f(\boldsymbol{\theta})^2 d\boldsymbol{\theta} - f_0 = \sum_{i=1}^{k} V_i + \sum_{i}^{k} \sum_{j>i}^{k} V_{i,j} + \ldots + V_{1,2,\ldots,k}, \tag{2.14}$$

where $V_i, V_{i,j}, \ldots, V_{1,2,\ldots,k}$ denote the variance of $f_i, f_{ij}, f_{1,2,\ldots,k}$, respectively, that is

$$\begin{aligned} V_i &= Var(E(Y|\theta_i)), \\ V_{i,j} &= Var(E(Y|\theta_i, \theta_j)) - V_i - V_j, \\ &\ldots \\ V_{1,2,\ldots,k} &= Var(Y) - \sum_{i=1}^{k} V_i - \sum_{1 \le i < j \le k} V_{i,j} - \ldots - \sum_{1 \le i_1 \le \ldots i_{k-1} \le k} V_{i_1,\ldots,i_k}, \end{aligned}$$

where, for simplicity, the indices for the variance and the mean were omitted. Homma & Saltelli (1996) introduced an additional index, the *total-order sensitivity index*, S_{Ti}, that accounts for all the contributions to the output variation due to factor θ_i (*i.e.* first-order index plus all its interactions):

$$S_{Ti} = \sum_{p \# i} S_i,$$

where $\#i$ indicates all the indexes associated to the factor θ_i. Using Equation (2.14) it can be shown that,

$$S_{Ti} = 1 - \frac{Var(E(Y|\boldsymbol{\theta}_{\sim \boldsymbol{i}})}{Var(Y)},$$

where $\boldsymbol{\theta}_{\sim \boldsymbol{i}}$ denotes all elements of $\boldsymbol{\theta}$ except θ_i. If $S_i = S_{T_i} = 0$ then $f(\boldsymbol{\theta})$ does not depend on θ_i, while $S_i = S_{T_i} = 1$ indicates that $f(\boldsymbol{\theta})$ depends solely on θ_i. The Sobol method captures the effects of individual parameters as well as their interactions and it provides quantitative information on the contribution of each parameter to the sensitivity of the mathematical model.

Sobol algorithm is performed using SALib library in python in this thesis.

2.4 Bayesian approximation methods

In this section I show Bayesian statistical inference methods for estimating the probability distribution of the parameters of a mathematical model on the basis of experimental data. The algorithms presented in this section are described in detail by Toni *et al.* (2009), Wegmann *et al.* (2009), Boys *et al.* (2008), Marjoram *et al.* (2003), Wilkinson (2011), Beaumont *et al.* (2002) and many others.

2.4.1 Bayesian inference

Let X be defined on a sample space S_X and X is an outcome of a model which can differ among various possible hypotheses H_i, where $i = 1, 2, \ldots, n$ and H_i form a partition (see Definition 2.2). One can then compute the probabilities of an outcome $X = x$ given each chosen hypothesis, $Prob(X = x|H_i)$, where $i = 1, 2, \ldots, n$ and $x \in S_X$. However usually what is observed is an outcome $X = x^*$ and therefore it is interesting to find the probabilities of the hypotheses conditional on that outcome, $Prob(H_i|X = x^*)$. This probability can be computed from Bayes theorem (see Theorem 2.4) as follows,

$$Prob(H_i|X = x^*) = \frac{Prob(X = x^*|H_i)Prob(H_i)}{\sum_{j=1}^{n} Prob(X = x^*|H_j)Prob(H_j)}, \quad i = 1, \ldots, n,$$

where $Prob(H_i)$ is called the *prior* belief about the hypothesis H_i and $Prob(H_i|X = x^*)$ is called the *posterior* belief about the hypothesis H_i based on the occurrence of $X = x^*$. The probabilities $Prob(X = x^*|H_i)$ are known as *likelihoods* and are often written as $L(H_i; x^*)$.

Let now X be a discrete outcome and $\boldsymbol{\theta}$ represent a continuum of hypotheses, which might be for example related to the possible values of a given parameter of the model. The prior beliefs must now be represented by density functions $\pi(\theta)$, where $\theta \in \boldsymbol{\theta}$. In the continuum limit, Bayes theorem becomes,

$$\pi(\theta|X = x^*) = \frac{\pi(\theta)Prob(X = x^*|\theta)}{\int_{\theta^* \in \boldsymbol{\theta}} Prob(X = x^*|\theta^*)\pi(\theta^*)d\theta^*}. \tag{2.15}$$

In this case the likelihood function is $L(\theta; x^*) = Prob(X = x^*|\theta)$. Equation (2.15) can be rewritten in simpler form, as

$$\pi(\theta|X = x^*) \propto \pi(\theta)L(\theta; x^*),$$

meaning that the posterior distribution ($\pi(\theta|X = x^*)$) is proportional to the prior distribution ($\pi(\theta)$) times the likelihood.

In the following subsections I introduce two algorithms which can help in estimating the posterior distribution, in particular, the ABC algorithm which does not require computing the likelihood function.

2.4.2 The ABC algorithm

The *approximate Bayesian computation* (ABC) algorithm has its root in the rejection algorithm to generate samples from a probability distribution. Imagine there is a model $\mathcal{M}$ with a parameter θ described by a prior $\pi(\theta)$, and the data $\mathcal{D}$ defined by $\pi(\mathcal{D}|\theta)$. It is clear that a simple algorithm for simulating from the desired posterior $\pi(\theta|\mathcal{D})$ can be obtained as follows. First sample from the joint distribution $\pi(\theta, \mathcal{D})$ by sampling $\theta^* \sim \pi(\theta)$ and then $\mathcal{D}^* \sim \pi(\mathcal{D}|\theta^*)$. This gives a sample $(\theta^*, \mathcal{D}^*)$ from the joint distribution. A simple rejection algorithm which rejects the proposed pair unless $\mathcal{D}^*$ matches the true data $\mathcal{D}$ clearly gives a sample from the required posterior distribution. This algorithm is exact, and for discrete $\mathcal{D}$ will have a non-zero acceptance rate. However, in most of the cases, the rejection rate will be intolerably high. In particular, the acceptance rate will typically be zero for continuous valued $\mathcal{D}$. Therefore the ABC algorithm, reported here as Algorithm 2, generates $n \in \mathbb{N}$ samples from a distribution which is not the true posterior distribution of interest, but a distribution which is hoped to be close to the real posterior distribution of interest.

1. Set $i = 1$.
2. Generate $\theta^* \sim \pi(\theta)$.
3. Simulate new data $\mathcal{D}^*$ from the model $\mathcal{M}$ with parameter θ^*.
4. Calculate the distance $\delta(\mathcal{D}, \mathcal{D}^*)$.
5. Accept θ^* if $\delta(\mathcal{D}, \mathcal{D}^*) \leq \epsilon$, where $\epsilon \in \mathbb{R}$ such that $\epsilon \geq 0$ is a tolerance level for the distance $\delta(\cdot, \cdot)$. Set $i = i + 1$. If $i < n$ return to Step 2, otherwise end the algorithm.

Algorithm 2: Approximate Bayesian computation for a distance $\delta(\cdot, \cdot)$.

For a suitable and small enough choice of ϵ this will closely approximate the true posterior. However, smaller choices of ϵ will lead to higher rejection rates. This is a particular problem in the context of highly variable or high-dimensional $\mathcal{D}$, where it is often unrealistic to expect a close match between all components of $\mathcal{D}$ and the simulated data $\mathcal{D}^*$, even for a good choice of θ^*.

2.4.3 MCMC methods

A more sophisticated class of algorithms comprises *Markov chain Monte Carlo* (MCMC). Imagine a model $\mathcal{M}$, describing the data $\mathcal{D}$, determined by a parameter θ. MCMC algorithm constructs a Markov chain of parameter values $(\theta_1, \theta_2, \ldots, \theta_n)$ where the next parameter combination θ_{i+1} is chosen by proposing a random move conditional on the last parameter combination θ_i, and accepting conditional on the likelihood and proposal ratio and where $L(\theta_i; \mathcal{D}) \propto Prob(\mathcal{D}|\theta_i)$ for all $i \geq 1$. Note that proposal for θ_1 is sampled from an *empirical* prior distribution π, that is $\theta_1 \sim \pi$ and the transition kernel is also built using π in this thesis (see Subsection 4.1.2 in Chapter 4 for details). Given that certain conditions are met (see Andrieu *et al.* (2003)), the Markov chain of parameter values will eventually converge to the target posterior distribution. The advantage of MCMC method is that the time needed to obtain acceptable convergence is typically short because the sampling effort is concentrated in the areas of high likelihood

of the posterior density. The ABC algorithm is based on the assumption that the distance function would pick up all important information about the posterior distribution (sufficient summary statistics) whereas MCMC algorithm converges to posterior distribution by its construction. MCMC is recommended to use, instead of the ABC, if the ratio of likelihood function can be calculated and can be used in combination with the ABC algorithm in order to find the empirical distribution used as transition kernel (see Wegmann *et al.* (2009)). MCMC algorithm, as used in this thesis, to find nth long chain is described by Algorithm 3.

1. Set $i = 1$.
2. Sample the parameter θ_i from the empirical prior distribution π.
3. Propose to move θ_i to θ_{i+1} according to a transition kernel $q(\theta_i \to \theta_{i+1})$.
4. Calculate the following value

$$h = \min\left(1, \frac{Prob(\mathcal{D}|\theta_{i+1})\pi(\theta_{i+1})q(\theta_{i+1} \to \theta_i)}{Prob(\mathcal{D}|\theta_i)\pi(\theta_i)q(\theta_i \to \theta_{i+1})}\right)$$

Move to θ_{i+1} with probability h, and remain at θ_i otherwise. Set $i = i + 1$. If $i < n$ go to Step 3 otherwise end the algorithm.

Algorithm 3: Markov chain Monte Carlo.

Chapter 3

Cell surface binding VEGF-VEGFR models

In this chapter I focus on the binding kinetics of VEGFR/VEGF-A on the cell surface. The aim is to study the dynamics of VEGFR1, VEGFR2 and VEGF-A. First a mathematical model is introduced in which monomeric receptors, VEGFR2, can bind a bivalent ligand, VEGF-A. I assume that receptor dimerisation is ligand induced and dimers are considered to be instantaneously phosphorylated. The phosphorylation can be considered as an intrinsic characteristic of the cross-linked VEGFR2 dimers which leads to a cellular response. Therefore the time to initiate the signalling cascade can be identified with the time to reach a given threshold number of phosphorylated dimers (see Alarcón & Page (2006)). The model is called the *instantaneous phosphorylation* R_2 model (IP R_2 model). An alternative model can be constructed where phosphorylation and de-phosphorylation of dimers are considered as new reactions in the process. This second model is called the *delayed phosphorylation* R_2 model (DP R_2 model). Finally, and in order to study the role of VEGFR1 in the dynamics of VEGFR2 and VEGF-A, two stochastic models (IP R_1/R_2 model and DP R_1/R_2 model) are introduced, which are extensions of the IP R_2 model and the DP R_2 model, respectively, in the presence of VEGFR1. The analysis of these models would lead to the study of multi-variate stochastic processes, in particular multi-variate CTMPs.

As stated in by Alarcón & Page (2006), the analytical treatment of multi-variate stochastic processes is usually extremely difficult, and numerical approaches,

such as Gillespie simulations or some approximative techniques for dealing with the corresponding master equation, are often used instead (see Subsections 2.2.8 and 2.2.13). However I show in this chapter that it is still possible to carry out an analytical study of these processes without solving the master equation. To this aim, I make use of a matrix-analytic technique to consider a number of quantities of interest (usually referred to as summary statistics or stochastic descriptors). This approach, which has its origins in the seminal work by Neuts (1994), allows studying the stochastic descriptors of interest for moderate concentrations of ligands and receptors, as discussed in Section 3.4. Matrix-analytic techniques have been applied in Mathematical Biology before by Gómez-Corral & López García (2012a,b) (competition model between two species of individuals).

This chapter is organised as follows. In Section 3.1, four stochastic models are introduced to describe the binding dynamics of receptor monomers and dimers on the surface of endothelial cells. These models include phosphorylation or competition for ligand availability. In Section 3.2, parameter estimation is carried out following arguments described by Lauffenburger & Linderman (1993). The stochastic formulation of the studied models allows finding the probability density function for the population counts of the different molecular species involved. It is often done through various Monte Carlo techniques described in detail by Hespanha (2008a), and the algorithm proposed by Gillespie (1976) at relatively low significant computational cost. Since one is often interested in computing only the first and second order statistical moments of the population count, much time and effort can be saved by applying approximative methods (see Subsection 2.2.8) to directly compute these low-order moments, without actually having to solve for the probability density function. The application of moment closure methods and Gillespie simulations are discussed in Section 3.3 to study the transient behaviour of the Markov processes under consideration, when dealing with the master equation. Matrix-analytic techniques are applied in Section 3.4 and Section 3.5 in order to study different stochastic descriptors of interest in the VEGF-A/VEGFR system. One special property of this method is that a sensitivity analysis for the effect of binding, dissociation and phosphorylation rates on the stochastic descriptors can be carried out. Additionally in Section 3.5 three

different hypotheses on how to account for signal formation in the process are studied.

3.1 Stochastic models of VEGF-VEGFR binding on the cell membrane

In this section, I introduce four different stochastic models for the binding kinetics of a receptor with a bivalent ligand, taking place on the membrane of a cell. I consider a bivalent ligand that can bind to plasma membrane receptors, creating receptor-with-ligand bound monomers. The free pole of the ligand in a bound monomer can then bind to free receptors during the diffusion of these molecules on the cell surface, creating bound dimers consisting of two receptors bound to the ligand. It is assumed that two free receptors are not able to create a *pre-dimer* without ligand. Dimerisation of receptors is only possible upon ligands stimulation in all studied models in this thesis, which is called ligand-induced dimerisation (LID) (see Mac Gabhann & Popel (2007)). I point out here that the consideration of receptor pre-dimerisation does not significantly affect the dynamics of these processes, specially under low ligand concentrations (as found by Mac Gabhann & Popel (2007)). The impact in the system dynamics of pre-dimers may only occur, in some cases, under highly saturated situations. Moreover, when analysing the interaction between receptor VEGFR and ligand VEGF-A, there is experimental support for this hypothesis stated by Ruch *et al.* (2007): free VEGFR is observed (electron microscopy) in monomeric form on the cell surface.

The study of the number of bound monomer and bound dimer molecules on the cell surface over time can be viewed as the analysis of the transient behaviour of a specific Markov process, a problem which, in general, is not solvable in closed form as said by Kulkarni (1996) (see Section 3.3). Therefore, one typically carries out Gillespie simulations, or applies moment-closure techniques (see Gillespie (1976) and Hespanha (2008a)) to deal with the master equation of the Markov process under study (see Section 3.3 and Subsection 2.2.13).

3.1.1 Instantaneous phosphorylation model with VEGFR2 (IP R_2 model)

Consider the simplest model describing one receptor type binding with one ligand type on the plasma membrane. Here only VEGFR2 is considered so in the notation of the molecules containing receptor, a subscript 2 is used. In Subsections 3.1.3 and 3.1.4 models with two different receptors, VEGFR1 and VEGFR2, are considered.

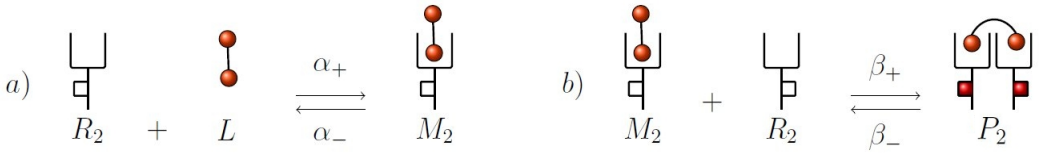

Figure 3.1: Schematic of the IP R_2 model. *a*) Formation and dissociation of bound monomers (M_2). *b*) Formation and dissociation of bound dimers (P_2), which instantaneously phosphorylate (represented by red phosphorylated residues in the intra-cellular tail of the receptors).

The standard description for the binding kinetics of free bivalent ligand L to free receptor R_2 to form bound monomer M_2 involves association and dissociation rates. Assume ligand induced dimerisation, with binding rate α_+, and dissociation rate α_-. Then the free pole of bound ligand in the monomer M_2 can bind the second receptor R_2 creating a bound phosphorylated dimer P_2 with rate β_+. That reaction is reversible and one of the receptors in the bound phosphorylated dimer complex can dissociate with rate β_-. I assume constant number of ligand n_L and constant number of receptors n_{R_2}. Consider a CTMP $\mathfrak{X}_{\text{IP } R_2} = \{\boldsymbol{X}(t) : t \geq 0\}$ where the state vector $\boldsymbol{X}(t) \in \mathcal{S}_{\text{IP } R_2} \subset (\mathbb{N} \cup \{0\})^2$ is a collection of discrete random variables representing the number of each type of molecule at time t, $\boldsymbol{X}(t) = (M_2(t), P_2(t))$, where

$M_2(t)$ = *"number of M_2 bound monomers at time t"*,

$P_2(t)$ = *"number of P_2 bound phosphorylated dimers at time t"*.

Assuming a constant number of receptors n_{R_2} and ligands n_L means that the total number of free ligands and free receptors at any time $t \geq 0$ can be found from the following equations,

$$\begin{aligned} L(t) &= n_L - M_2(t) - P_2(t), \\ R_2(t) &= n_{R_2} - M_2(t) - 2P_2(t). \end{aligned}$$

Furthermore, from the reactions in Figure 3.1, it is clear that since $R_2(t), L(t) \geq 0$ for all $t \geq 0$,

$$\begin{aligned} M_2(t) + P_2(t) &\leq n_L, \\ M_2(t) + 2P_2(t) &\leq n_{R_2}. \end{aligned}$$

The transition probabilities (see Subsection 2.2.2) are given as,

$$P_{\boldsymbol{n}}(t) = Prob(\boldsymbol{X}(t) = \boldsymbol{n}),$$

where $\boldsymbol{n} = (n_1, n_2) \in \mathcal{S}_{\text{IP } R_2}$ and n_1, n_2 refer to M_2, P_2, respectively. The state space $\mathcal{S}_{\text{IP } R_2}$ can be identified by the implicit restrictions imposed by the reactions described in Figure 3.1. Thus, $\mathcal{S}_{\text{IP } R_2} = \{(n_1, n_2) \in (\mathbb{N} \cup \{0\})^2 : n_1 + n_2 \leq n_L, n_1 + 2n_2 \leq n_{R_2}\}$. The process $\mathcal{X}_{\text{IP } R_2}$ evolves from a given state $\boldsymbol{n}$ to a state $\boldsymbol{n'} \neq \boldsymbol{n}$ according to four possible reactions described by Figure 3.1, where $\boldsymbol{n}, \boldsymbol{n'} \in \mathcal{S}_{\text{IP } R_2}$. In particular, the possible states $\boldsymbol{n'}$ accessible from $\boldsymbol{n}$ in one jump, and the corresponding infinitesimal transition rates $q_{\boldsymbol{nn'}}$ are listed in Table 3.1.

$q_{\boldsymbol{nn'}}$ for reaction $\boldsymbol{n} = (n_1, n_2) \to \boldsymbol{n'}$	$\boldsymbol{n'}$
$2\alpha_+(n_{R_2} - n_1 - 2n_2)(n_L - n_1 - n_2)$	$(n_1 + 1, n_2)$
$\alpha_- n_1$	$(n_1 - 1, n_2)$
$\beta_+ n_1(n_{R_2} - n_1 - 2n_2)$	$(n_1 - 1, n_2 + 1)$
$2\beta_- n_2$	$(n_1 + 1, n_2 - 1)$

Table 3.1: The infinitesimal transition rates $q_{\boldsymbol{nn'}}$ of the process $\mathcal{X}_{\text{IP } R_2}$, based on the reactions shown in Figure 3.1.

As shown in Equation (2.5), the transition probabilities satisfy the master equation as follows,

$$\begin{aligned}\frac{dP_{(n_1,n_2)}(t)}{dt} &= 2\alpha_+(n_{R_2}-n_1+1-2n_2)(n_L-n_1+1-n_2)P_{(n_1-1,n_2)}(t)\\ &+ \alpha_-(n_1+1)P_{(n_1+1,n_2)}(t)+2\beta_-(n_2+1)P_{(n_1-1,n_2+1)}(t)\\ &+ \beta_+(n_1+1)(n_{R_2}-n_1-1-2n_2+2)P_{(n_1+1,n_2-1)}(t)\\ &- \{2\alpha_+(n_{R_2}-n_1-2n_2)(n_L-n_1-n_2)+\alpha_-n_1\\ &+ \beta_+n_1(n_{R_2}-n_1-2n_2)+2\beta_-n_2\}\,P_{(n_1,n_2)}(t),\end{aligned} \tag{3.1}$$

where $P_{(0,0)}(0)=1$ is the initial condition for the process $\mathcal{X}_{\text{IP }R_2}$.

3.1.2 Delayed phosphorylation model with VEGFR2 (DP R_2 model)

In the previous subsection, P_2 complexes are instantaneously phosphorylated. However, this process can be in fact a separate reaction. Thus one can consider an alternative model where dimer phosphorylation is included as an additional reaction (see Figure 3.2). The relevance of considering phosphorylation as an independent reaction can now be evaluated. Hence the model is called delayed phosphorylation R_2 (DP R_2) model. Consider a CTMP $\mathcal{X}_{\text{DP }R_2}=\{\boldsymbol{X}(t):\ t\geq 0\}$ where the state vector $\boldsymbol{X}(t)\in\mathcal{S}_{\text{DP }R_2}\subset(\mathbb{N}\cup\{0\})^3$ is a collection of discrete random variables representing the number of each type of molecule at time t, $\boldsymbol{X}(t)=(M_2(t),D_2(t),P_2(t))$, where

$$\begin{aligned}M_2(t) &= \text{“Number of bound monomers } M_2 \text{ at time } t\text{”},\\ D_2(t) &= \text{“Number of bound, non-phosphorylated dimers } D_2 \text{ at time } t\text{”},\\ P_2(t) &= \text{“Number of bound, phosphorylated dimers } P_2 \text{ at time } t\text{”}.\end{aligned}$$

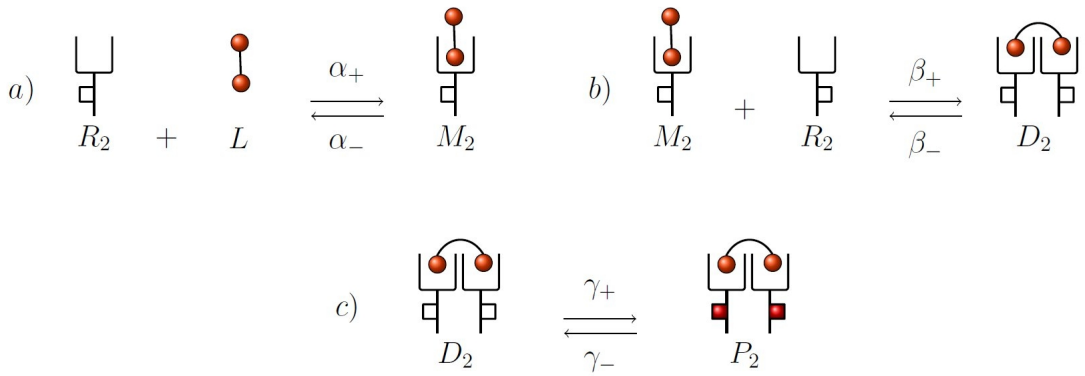

Figure 3.2: Schematic of the DP R_2 model. *a*) Formation and dissociation of bound monomers (M_2). *b*) Formation and dissociation of non-phosphorylated dimers (D_2). *c*) Formation and de-phosphorylation of phosphorylated dimers (P_2) (represented by red phosphorylated residues in the intra-cellular tail of the receptors).

It is assumed as before that the number of receptors n_{R_2} and the number of ligands n_L are constant. This implies that the total number of free ligands and free receptors at any time $t \geq 0$ can be found from the following equations,

$$\begin{aligned} L(t) &= n_L - M_2(t) - D_2(t) - P_2(t), \\ R_2(t) &= n_{R_2} - M_2(t) - 2D_2(t) - 2P_2(t). \end{aligned}$$

Therefore from reactions in Figure 3.2, it is clear that for all $t \geq 0$

$$\begin{aligned} M_2(t) + D_2(t) + P_2(t) &\leq n_L, \\ M_2(t) + 2D_2(t) + 2P_2(t) &\leq n_{R_2}, \end{aligned}$$

and the space of states $\mathcal{S}_{\text{DP } R_2}$ of $\mathcal{X}_{\text{DP } R_2}$ is defined as $\mathcal{S}_{\text{DP } R_2} = \{(n_1, n_2, n_3) \in (\mathbb{N} \cup \{0\})^3 : n_1 + n_2 \leq n_L, n_1 + 2n_2 + 2n_3 \leq n_{R_2}\}$. There are six possible reactions involved in the DP R_2 model, listed in Table 3.2 together with their corresponding infinitesimal transition rates $q_{\boldsymbol{nn'}}$, where $\boldsymbol{n}, \boldsymbol{n'} \in \mathcal{S}_{\text{DP } R_2}$.

$q_{\boldsymbol{nn'}}$ for reaction $\boldsymbol{n} = (n_1, n_2, n_3) \to \boldsymbol{n'}$	$\boldsymbol{n'}$
$2\alpha_+(n_{R_2} - n_1 - 2n_2 - 2n_3)(n_L - n_1 - n_2 - n_3)$	$(n_1 + 1, n_2, n_3)$
$\alpha_- n_1$	$(n_1 - 1, n_2, n_3)$
$\beta_+ n_1(n_{R_2} - n_1 - 2n_2 - 2n_3)$	$(n_1 - 1, n_2 + 1, n_3)$
$2\beta_- n_2$	$(n_1 + 1, n_2 - 1, n_3)$
$\gamma_+ n_2$	$(n_1, n_2 + 1, n_3 - 1)$
$\gamma_- n_3$	$(n_1, n_2 - 1, n_3 + 1)$

Table 3.2: The infinitesimal transition rates $q_{\boldsymbol{nn'}}$ of the process $\mathcal{X}_{\text{DP } R_2}$, based on the reactions shown in Figure 3.2

.

Hence the master equation of the process $\mathcal{X}_{\text{DP } R_2}$, for $\boldsymbol{n} = (n_1, n_2, n_3)$, can be written as follows,

$$\begin{aligned}
\frac{dP_{\boldsymbol{n}}(t)}{dt} = \; & 2\alpha_+(n_{R_2} - n_1 + 1 - 2n_2 - 2n_3)(n_L - n_1 + 1 - n_2 - n_3)P_{(n_1-1,n_2,n_3)}(t) \\
+ \; & \alpha_-(n_1 + 1)P_{(n_1+1,n_2,n_3)}(t) + 2\beta_-(n_2 + 1)P_{(n_1-1,n_2+1,n_3)}(t) \\
+ \; & \beta_+(n_1 + 1)(n_{R_2} - n_1 - 1 - 2n_2 + 2 - 2n_3)P_{(n_1+1,n_2-1,n_3)}(t) \\
+ \; & \gamma_+(n_2 + 1)P_{(n_1,n_2+1,n_3-1)}(t) + \gamma_-(n_3 + 1)P_{(n_1,n_2-1,n_3+1)}(t) \\
- \; & \{2\alpha_+(n_{R_2} - n_1 - 2n_2 - 2n_3)(n_L - n_1 - n_2 - n_3) + \alpha_- n_1 \\
+ \; & \beta_+ n_1(n_{R_2} - n_1 - 2n_2 - 2n_3) + 2\beta_- n_2 + \gamma_+ n_2 + \gamma_- n_3\} P_{(n_1,n_2,n_3)}(t),
\end{aligned} \tag{3.2}$$

where $P_{(0,0,0)}(0) = 1$ is the initial condition for this process.

3.1.3 Competition between VEGFR1 and VEGFR2 assuming instantaneous phosphorylation (IP R_1/R_2 model)

In Subsections 3.1.1 and 3.1.2 the interactions only between bivalent ligands VEGF-A and VEGFR2 receptors on the cell surface are analysed. However, both VEGFR1 and VEGFR2 are expressed on endothelial cells, and can bind VEGF-A (see Mac Gabhann & Popel (2004)).

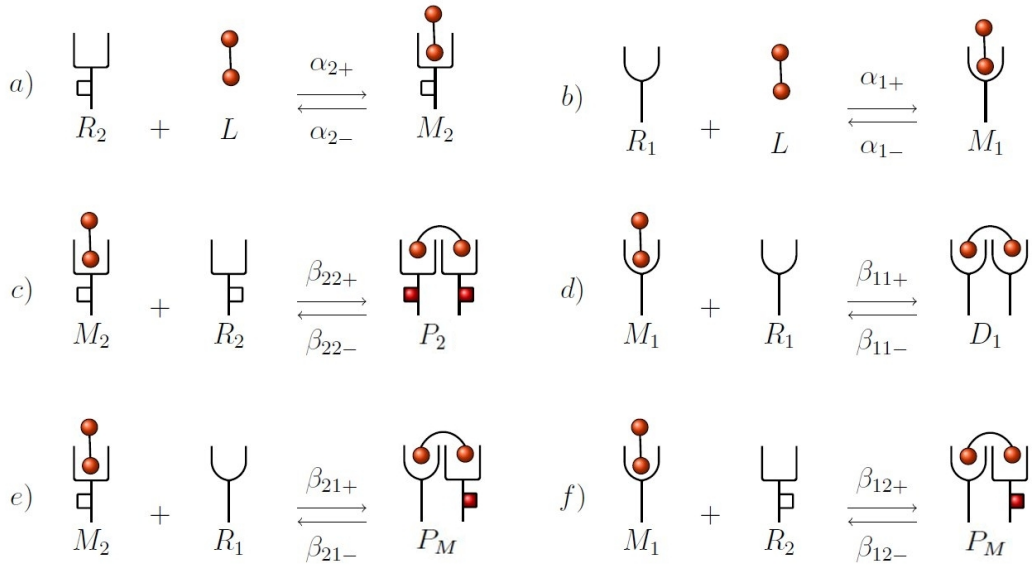

Figure 3.3: Schematic of the IP R_1/R_2 model. a) Formation and dissociation of bound monomers (M_2). b) Formation and dissociation of bound monomers (M_1). c) Formation and dissociation of bound homodimers (P_2). $d) - f$) Analogous reactions for homodimers (D_1) and heterodimers (P_M). VEGFR2 involved in a bound dimer becomes instantaneously phosphorylated which is represented by red phosphorylated residues in the intra-cellular tail of the receptors.

VEGFR1 has a greater binding affinity to VEGF-A than VEGFR2. However, it is VEGFR2 phosphorylation which generates strong signal and it is required for the homoeostasis of normal endothelial cells (see Alarcón & Page (2007) and Casaletto & McClatchey (2012)). Therefore the reaction of VEGFR1 phosphorylation is not considered in this thesis. VEGFR1 competes with VEGFR2 for ligand, and it is assumed that these receptors induce different signalling pathways. Finally, VEGFR1 and VEGFR2 are found at different copy numbers in a variety of cell lines by Imoukhuede & Popel (2011, 2012). Previous studies show that the heterogeneity in these two receptor numbers contributes to a major complexity of the VEGF-A signal transduction process, and should be studied further (see Mac Gabhann & Popel (2007)).

The IP R_1/R_2 model is constructed by assuming as before that all ligands (L) are bivalent (with two binding sites) and dimerisation of the receptors is possible

under ligand binding only, *i.e.* two free receptors are not able to dimerise. There are two kinds of receptors, VEGFR1 (R_1) and VEGFR2 (R_2) being considered. In this model two types of bound monomers can be formed, M_1 and M_2, as a result of the ligand binding to VEGFR1 and VEGFR2, respectively. Then, ligand induced receptor dimerisation leads to the formation of homodimers, D_1 and P_2, or heterodimers P_M. VEGFR2 homodimers P_2 and heterodimers P_M are instantaneously phosphorylated (P_M only on one site as VEGFR1 does not phosphorylate as noted before). Figure 3.3 shows all possible reactions with their rates between receptors, ligands and bound complexes. Consider a CTMP $\mathcal{X}_{\text{IP } R_1/R_2} = \{\boldsymbol{X}(t) : t \geq 0\}$ where the state vector $\boldsymbol{X}(t) \in \mathcal{S}_{\text{IP } R_1/R_2} \subset (\mathbb{N} \cup \{0\})^5$ is a collection of discrete random variables representing the number of each type of molecule at time t, $\boldsymbol{X}(t) = (M_1(t), M_2(t), D_1(t), P_2(t), P_M(t))$, where

$$
\begin{aligned}
M_1(t) &= \text{“Number of bound monomers } M_1 \text{ at time } t\text{”},\\
M_2(t) &= \text{“Number of bound monomers } M_2 \text{ at time } t\text{”},\\
D_1(t) &= \text{“Number of bound, non-phosphorylated homodimers } D_1 \text{ at time } t\text{”},\\
P_2(t) &= \text{“Number of bound, phosphorylated homodimers } P_2 \text{ at time } t\text{”},\\
P_M(t) &= \text{“Number of bound, phosphorylated heterodimers } P_M \text{ at time } t\text{”}.
\end{aligned}
$$

The number of VEGFR1 (n_{R_1}), the number of VEGFR2 (n_{R_2}) and the number of ligands (n_L) are assumed to be constant. Hence the total number of free ligands and free receptors at any time $t \geq 0$ can be found from the following equations,

$$
\begin{aligned}
L(t) &= n_L - M_1(t) - M_2(t) - D_1(t) - P_2(t) - P_M(t),\\
R_1(t) &= n_{R_1} - M_1(t) - 2D_1(t) - P_M(t),\\
R_2(t) &= n_{R_2} - M_2(t) - 2P_2(t) - P_M(t).
\end{aligned}
$$

Therefore from reactions in Figure 3.3, it is clear that for all $t \geq 0$,

$$
\begin{aligned}
M_1(t) + M_2(t) + D_1(t) + P_2(t) + P_M(t) &\leq n_L,\\
M_1(t) + 2D_1(t) + P_M(t) &\leq n_{R_1},\\
M_2(t) + 2P_2(t) + P_M(t) &\leq n_{R_2},
\end{aligned}
$$

and the space of states $\mathcal{S}_{\text{IP } R_1/R_2}$ of the process $\mathcal{X}_{\text{IP } R_1/R_2}$ is defined as $\mathcal{S}_{\text{IP } R_1/R_2} = \{(n_1, n_2, n_3, n_4, n_5) \in (\mathbb{N} \cup \{0\})^5 : n_1+n_2+n_3+n_4+n_5 \leq n_L, n_1+2n_3+n_5 \leq n_{R_1}, n_2 + 2n_4 + n_5 \leq n_{R_2}\}$. There are twelve reactions involved in the IP R_1/R_2

model, listed in Table 3.3 together with their corresponding infinitesimal transition rates $q_{\boldsymbol{nn'}}$, where $\boldsymbol{n}, \boldsymbol{n'} \in \mathcal{S}_{\text{IP } R_1/R_2}$.

$q_{\boldsymbol{nn'}}$ for reaction $\boldsymbol{n} = (n_1, n_2, n_3, n_4, n_5) \to \boldsymbol{n'}$	$\boldsymbol{n'}$
$2\alpha_{1+}(n_L - n_1 - n_2 - n_3 - n_4 - n_5)(n_{R_1} - n_1 - 2n_3 - n_5)$	$(n_1 + 1, n_2, n_3, n_4, n_5)$
$\alpha_{1-} n_1$	$(n_1 - 1, n_2, n_3, n_4, n_5)$
$\beta_{11+} n_1(n_{R_1} - n_1 - 2n_3 - n_5)$	$(n_1 - 1, n_2, n_3 + 1, n_4, n_5)$
$2\beta_{11-} n_3$	$(n_1 + 1, n_2, n_3 - 1, n_4, n_5)$
$\beta_{12+} n_1(n_{R_2} - n_2 - 2n_4 - n_5)$	$(n_1 - 1, n_2, n_3, n_4, n_5 + 1)$
$\beta_{12-} n_5$	$(n_1 + 1, n_2, n_3, n_4, n_5 - 1)$
$2\alpha_{2+}(n_L - n_1 - n_2 - n_3 - n_4 - n_5)(n_{R_2} - n_2 - 2n_4 - n_5)$	$(n_1, n_2 + 1, n_3, n_4, n_5)$
$\alpha_{2-} n_2$	$(n_1, n_2 - 1, n_3, n_4, n_5)$
$\beta_{22+} n_2(n_{R_2} - n_2 - 2n_4 - n_5)$	$(n_1, n_2 - 1, n_3, n_4 + 1, n_5)$
$2\beta_{22-} n_4$	$(n_1, n_2 + 1, n_3, n_4 - 1, n_5)$
$\beta_{21+} n_2(n_{R_1} - n_1 - 2n_3 - n_5)$	$(n_1, n_2 - 1, n_3, n_4, n_5 + 1)$
$\beta_{21-} n_5$	$(n_1, n_2 + 1, n_3, n_4, n_5 - 1)$

Table 3.3: The infinitesimal transition rates $q_{\boldsymbol{nn'}}$ of the process $\mathcal{X}_{\text{IP } R_1/R_2}$, based on the reactions shown in Figure 3.3.

Dynamics of the IP R_1/R_2 model can be described by the master equation in general form

$$\frac{dP_{\boldsymbol{n}}(t)}{dt} = \sum_{\substack{\boldsymbol{n'} \neq \boldsymbol{n} \\ \boldsymbol{n'} \in \mathcal{S}_{\text{IP } R_1/R_2}}} q_{\boldsymbol{n'n}} \, P_{\boldsymbol{n'}}(t) - \sum_{\substack{\boldsymbol{n'} \neq \boldsymbol{n} \\ \boldsymbol{n'} \in \mathcal{S}_{\text{IP } R_1/R_2}}} q_{\boldsymbol{nn'}} \, P_{\boldsymbol{n}}(t), \tag{3.3}$$

for all $\boldsymbol{n} \in \mathcal{S}_{\text{IP } R_1/R_2}$, where,

$$q_{\boldsymbol{nn}} = - \sum_{\substack{\boldsymbol{n'} \neq \boldsymbol{n} \\ \boldsymbol{n'} \in \mathcal{S}_{\text{IP } R_1/R_2}}} q_{\boldsymbol{nn'}}$$

and the initial condition is $P_{(0,0,0,0,0)}(0) = 1$.

3.1.4 Competition between VEGFR1 and VEGFR2 assuming delayed phosphorylation (DP R_1/R_2 model)

Here a variant of the IP R_1/R_2 model is introduced, denoted by the DP R_1/R_2 model (as the DP R_2 model for the IP R_2 model in Subsection 3.1.2) in which

phosphorylation is not assumed to be instantaneous. In this case, the dimeric bound complexes, D_2 and D_M, can become phosphorylated, P_2 and P_M, complexes, respectively. As noted in previous subsection, bound homodimers D_1 are not become phosphorylated. The complete set of reactions for the DP R_1/R_2 model is given in Figure 3.4.

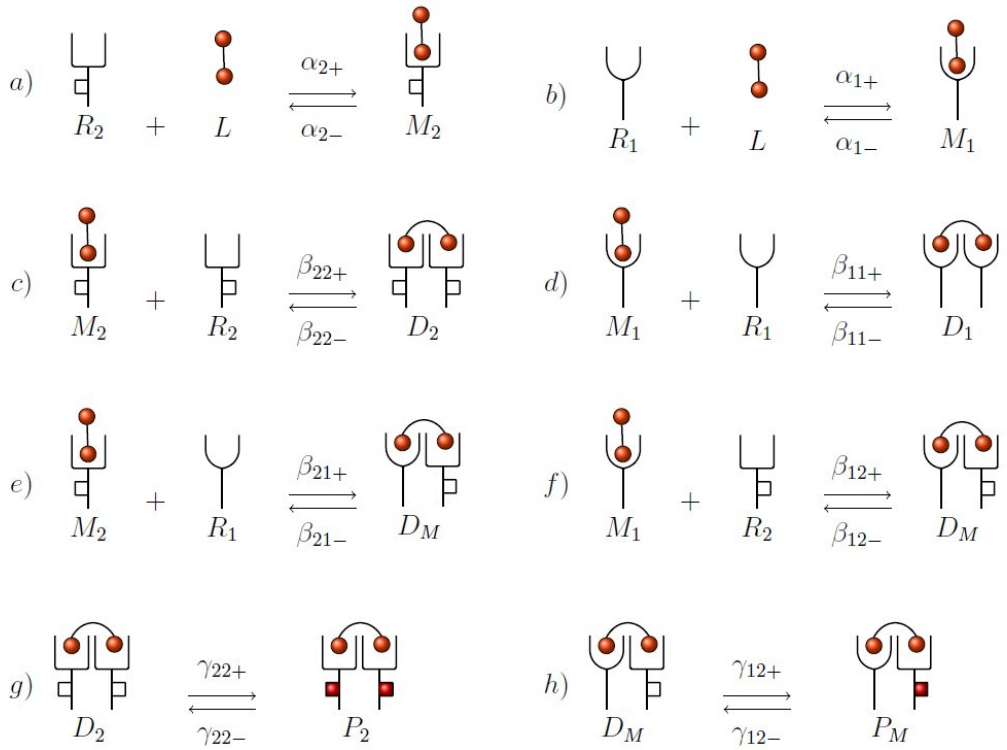

Figure 3.4: Schematic of the DP R_1/R_2 model. Reactions $a) - b)$ are like those in Figure 3.3 for IP R_1/R_2 model. Reactions $c) - f)$ describe the formation of non-phosphorylated dimers. Reactions $g)$ and $h)$ represent, respectively, phosphorylation of homodimers D_2 and heterodimers D_M.

The infinitesimal transition rates can be obtained in a similar way to the IP R_1/R_2 model, and an analogous master equation to Equation (3.3) could be written, which is omitted here.

3.2 Parameter estimation

It was noted by Berg & Purcell (1977), Berezhkovskii & Szabo (2013), Shoup & Szabo (1982), Keizer (1985), DeLisi (1980), Lauffenburger & Linderman (1996) and many others that the rate at which a biomolecular chemical reaction occurs is determined by two factors, one chemical and the other physical. Thus for the models in Section 3.1, the reaction of receptor-ligand binding or receptor dimerisation can be that type of biomolecular reaction. A local electron density can be a chemical factor determining the intrinsic rate of reaction when reactants approach close to one other (*i.e.* the ligand is in close proximity to bind the free receptor). Physical factors, such as diffusion, can determine the rate at which these potentially reactive encounters occur. The biomolecular constant, such as binding rate or dimerisation rate can be written in terms of these factors.

Consider ligand L and receptor R which can form monomer M in free solution. The reaction of binding can be written as follows, based on the assumption that it occurs in two steps,

$$R + L \underset{k_{d_L}}{\overset{k_{d_L}}{\rightleftarrows}} \overline{RL} \underset{k_-}{\overset{k_+}{\rightleftarrows}} M,$$

where k_{d_L} is the diffusion rate, k_+, k_- are reaction intrinsic rates, and $\overline{RL}$ denotes receptor and ligand in close enough proximity to start intrinsic reaction. The concentration of $\overline{RL}$ is usually small compare to R, L and M. Hence, by using steady-state approximation, as suggested by Eigen (1974), one gets $\frac{d\overline{RL}}{dt} = 0$. The dynamics of monomers can be described by the ordinary differential equation (ODE),

$$\frac{dM(t)}{dt} = \frac{k_{d_L} k_+}{k_{d_L} + k_+} R(t)L(t) - \frac{k_{d_L} k_-}{k_{d_L} + k_+} M(t),$$

with the initial condition $M(0) = 0$, where $L(t)$, $R(t)$ and $M(t)$ denote the number of ligands L, receptors R and monomers M, respectively, at time t. Hence receptor-ligand binding reaction can be described as

$$R + L \underset{q_{\text{off}}}{\overset{q_{\text{on}}}{\rightleftarrows}} M,$$

where

$$q_{\text{on}} = \frac{k_{d_L} k_+}{k_{d_L} + k_+}, \quad q_{\text{off}} = \frac{k_{d_L} k_-}{k_{d_L} + k_+},$$

are forward and backward binding and dissociation rates. Using the classic work of Smoluchowski (1917) the association rate constant for purely diffusion-controlled reaction of two molecules R and L is directly given by the diffusion rate k_{d_L}. If ligand is in free solution having diffusion constant equal to D_L, and receptor is on the membrane of a cell with radius a, one can get $k_{d_L} = 4\pi D_L a$ as explained in detail by Erickson *et al.* (1987) or Lauffenburger & Linderman (1993). Therefore the overall $q_{\text{on}}^{\text{cell}}, q_{\text{off}}^{\text{cell}}$ rates for the entire cell can be found as,

$$q_{\text{on}}^{\text{cell}} = \frac{4\pi D_L a k_+^{\text{cell}}}{4\pi D_L a + k_+^{\text{cell}}}, \quad q_{\text{off}}^{\text{cell}} = \frac{4\pi D_L a k_-^{\text{cell}}}{4\pi D_L a + k_+^{\text{cell}}},$$

where $k_+^{\text{cell}} = n_R^T k_+$, $k_-^{\text{cell}} = n_R^T k_-$ and n_R^T denotes the total number of receptors per cell. Hence it is possible to compute the forward and backward binding rates for single reaction by dividing $q_{\text{on}}^{\text{cell}}, q_{\text{off}}^{\text{cell}}$ by total number of receptors n_R^T,

$$q_{\text{on}} = \frac{4\pi D_L a k_+}{4\pi D_L a + k_+ n_R^T}, \quad q_{\text{off}} = \frac{4\pi D_L a k_-}{4\pi D_L a + k_+ n_R^T}.$$

In Subsections 3.2.1 and 3.2.2 I show how that approach can be implemented in order to find the rates in the binding models described in Section 3.1 with one or two receptor types.

3.2.1 One receptor type

First I show how to estimate parameters α_+, α_-, β_+ and β_- $[s^{-1}]$ which represent binding or unbinding of a single type of receptor (or monomer) to a bivalent ligand. The focus here is on the dynamics for a fraction $0 < f < 1$ of a cell. From the equilibrium dissociation constant $K_d[mm^{-3}mol]$ given by $K_d = k_{\text{off}}/k_{\text{on}}$ of the receptor and ligand under consideration, it is possible to obtain the biophysical binding rate $k_{\text{on}}[mol^{-1}mm^3s^{-1}]$. Therefore the transition rates α_+ and α_- are given by

$$\alpha_+ = \frac{k_{\text{on}}}{N_A\, f\, h\, s_c}, \quad \alpha_- = k_{\text{off}},$$

where $h[mm]$ is the *height* of the experimental volume, $s_c[mm^2]$ is the total area of the cell surface, and $N_A[mol^{-1}]$ is Avogadro's number.

Note that the binding process between the receptor and the ligand, such as reaction *a)* in Figure 3.1, can be considered as a one-step process, with $q_{\text{on}}[mm^3s^{-1}]$ the association constant and $q_{\text{off}}[s^{-1}]$ the dissociation constant, as explained before. Constants q_{on} and q_{off} are directly related to the biophysical rates k_{on} and k_{off} as follows,

$$q_{\text{on}} = k_{\text{on}}/N_A, \quad q_{\text{off}} = k_{\text{off}}.$$

As mentioned before the focus is on a particular fraction $0 < f < 1$ of the cell, so that the radius of this target surface is given by

$$r = \sqrt{\frac{n_R s_c}{n_R^T \pi}},$$

where n_R^T is the total number of receptors on the cell surface, and $n_R = f n_R^T$ is the number of receptors present on the target surface, which amounts to the assumption of an homogeneous spatial distribution of receptors on the cell surface (see Ewan *et al.* (2006a), Mittar *et al.* (2009)), neglecting receptor clustering, which might be initiated upon ligand simulation (see Almqvist *et al.* (2004)).

Consider now the binding as a two-step process described above in this section, see Figure 3.5 *a)*, where the intrinsic forward rate is denoted as $k_+^{3D}[mm^3s^{-1}]$ to emphasise that this process takes place in 3D space.

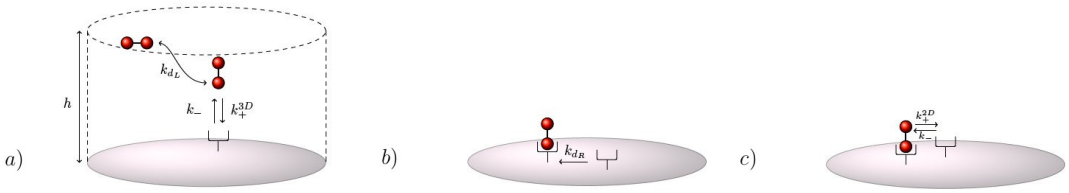

Figure 3.5: *a)* Two-step binding and unbinding of receptor and ligand: k_{d_L} is the ligand transport rate, k_+^{3D} and k_- are the intrinsic binding and unbinding rates, respectively, and h is the *height* of the experimental volume; *b)* Diffusive transport of surface receptor: k_{d_R} is the transport rate for both receptor R and bound monomer M; *c)* Once in the reaction zone of M, R can bind with rate k_+^{2D} (which is a *2D version* of k_+^{3D}) or unbind with rate k_-.

As a fraction of the cell is targeted and not the entire cell, the contributions of the rates k_+^{3D} and k_- to the overall association and dissociation rates, q_{on} and q_{off}, respectively, are given by

$$q_{\text{on}} = \frac{4\pi D_L r k_+^{3D}}{4\pi D_L r + n_R k_+^{3D}}, \quad q_{\text{off}} = \frac{4\pi D_L r k_-}{4\pi D_L r + n_R k_+^{3D}}. \tag{3.4}$$

Note here that q_{on} is a *per receptor* rate.

Denote the overall rate of an unoccupied receptor which binds a free pole, of bound to the other receptor, ligand by k_c and the unbinding rate of this type by k_u, on the cell membrane. A similar argument (Figure 3.5 *b)* and *c)*) to the one presented above applies when computing $k_c[mm^2 s^{-1}]$ or $k_u[s^{-1}]$ (see Lauffenburger & Linderman (1993)), which occurs with rates

$$k_c = \frac{k_+^{2D} k_{d_R}}{k_{d_R} + k_+^{2D}}, \quad k_u = \frac{k_- k_{d_R}}{k_{d_R} + k_+^{2D}}, \tag{3.5}$$

where the transport rate $k_{d_R}[mm^2 s^{-1}]$ (Figure 3.5 *b)*) is given by $k_{d_R} = \frac{2\pi D}{\log \frac{w}{b}}$. The diffusion constant $D = D_R + D_M[mm^2 s^{-1}]$ is the sum of diffusivities of the receptor and the bound monomer on the cell membrane (which are assumed the same $D_R = D_M$), $b[mm]$ is the characteristic length of the receptor, and $w[mm]$ is one-half the mean distance between receptors, given by

$$w = \sqrt{\frac{s_c}{\pi\, n_R^T}}.$$

k_+^{3D} and k_- can be found from Equation (3.4). Once k_+^{3D} is in hand, this $3D$ intrinsic binding rate allows to compute its 2D version, k_+^{2D}, as

$$k_+^{2D} = \frac{k_+^{3D}}{th}$$

where $th[mm]$ is the cell membrane thickness, as suggested by Lauffenburger & Linderman (1993). Once k_+^{2D} is computed, the rate constants k_c and k_u can be found by means of Equation (3.5), and they are identified with or directly related to the rates β_+ and β_-, respectively, as follows

$$\beta_+ = \frac{k_c}{f\, s_c}, \quad \beta_- = k_u.$$

3.2.2 Two receptor types (VEGFR1 and VEFGR2)

In this subsection the values of the parameters for the IP R_1/R_2 and the DP R_1/R_2 models are established. In this case, there are two types of receptors (VEGFR1 and VEGFR2) in the system, R_1 and R_2, with the same diffusion coefficient D_R. Since the amount of each type of receptor on the cell surface is significantly different (see Imoukhuede & Popel (2011), Imoukhuede & Popel (2012)), the average distance w between two given receptors, considered in the previous subsection, depends here on the particular pair of receptors under study. This changes the diffusion rate k_{d_R} of each possible reaction in Figures 3.3 and 3.4.

Let k_d^{ij} be the transport rate for receptor R_j diffusing towards monomer M_i (Figure 3.5 *b)*), with $i, j \in \{1, 2\}$. The probability of monomer M_i meeting receptor R_j can be approximated by

$$p_j = \frac{n_{R_j}^T}{n_{R_1}^T + n_{R_2}^T},$$

where $n_{R_j}^T$ is the total number of receptors R_j per cell. It is assumed that the diffusion of a free receptor is much higher than a bound monomer, regardless the type of the molecule, so the probability p_j does not depends on the monomer (*i.e.* does not depend on the index i). In the same way, the average distance between receptors R_i and R_j can be written as

$$w_{ij} = \begin{cases} \sqrt{\dfrac{s_c}{\pi\, n_{R_i}^T}}, & \text{if} \quad i = j, \\ \sqrt{\dfrac{s_c}{\pi\, (n_{R_1}^T + n_{R_2}^T)}}, & \text{if} \quad i \neq j. \end{cases}$$

Finally, the diffusion rates are then given by

$$k_d^{ij} = \begin{cases} \dfrac{2\pi D_R}{\log \frac{w_{ii}}{b}}, & \text{if} \quad i = j, \\ \dfrac{2\pi D_R}{\log \frac{w_{ij}}{b}} p_i, & \text{if} \quad i \neq j. \end{cases}$$

Having that the rates of the IP R_1/R_2 and the DP R_1/R_2 models can be easily obtain from,

$$\beta_{ij+} = \frac{k_c^{ij}}{f s_c}, \quad \beta_{ij-} = k_u^{ij},$$

where

$$k_c^{ij} = \frac{k_+^{2D} k_d^{ij}}{k_d^{ij} + k_+^{2D}}, \quad k_u^{ij} = \frac{k_- k_d^{ij}}{k_d^{ij} + k_+^{2D}}.$$

Finally, the binding rates α_{i+}, α_{i-} are found in the same way as for a single receptor.

3.2.3 Sensitivity analysis for physiological parameters and kinetic rates

In this subsection the interest is in studying how key rates k_+^{3D}, k_-, k_c, and k_u depend on some of the other parameters. The aim is to analyse in what follows how these four kinetic rates depend on *physiological* parameters such as the area s_c of the cell, the total number n_R^T of receptors, the ligand diffusion coefficient D_L, the receptor diffusion coefficient D_R, and the receptor length b. The sensitivity analysis is carried out which allows identifying the most relevant parameter(s) of the model.

Physiological parameter	Sign of partial derivatives
Area of the cell surface, s_c	$\frac{\partial k_+^{3D}}{\partial s_c}, \frac{\partial k_-}{\partial s_c}, \frac{\partial k_c}{\partial s_c}, \frac{\partial k_u}{\partial s_c} < 0$
Total number of receptors, n_R^T	$\frac{\partial k_+^{3D}}{\partial n_R^T}, \frac{\partial k_-}{\partial n_R^T}, \frac{\partial k_c}{\partial n_R^T}, \frac{\partial k_u}{\partial n_R^T} > 0$
Diffusion coefficients, D_L and D_R	$\frac{\partial k_+^{3D}}{\partial D_L}, \frac{\partial k_-}{\partial D_L} < 0, \quad \frac{\partial k_c}{\partial D_R}, \frac{\partial k_u}{\partial D_R} > 0$
Receptor length, b	$\frac{\partial k_c}{\partial b}, \frac{\partial k_u}{\partial b} > 0$

Table 3.4: Signs of partial derivatives.

One can obtain the partial derivatives of these four rates with respect to the physiological parameters. The effect of a given parameter on a kinetic rate is determined by the sign of the corresponding partial derivative, which is reported in Table 3.4. As the cell surface increases, it becomes more difficult to find nearby receptors, thus binding/unbinding rates (intrinsic and overall) decrease.

On the other hand, when the number of receptors increases, it is easier to find nearby receptors, so that the association and dissociation rates are larger for increasing receptor numbers. If the diffusion coefficient of the ligand increases, k_{d_L} also increases and thus, the overall binding rate decreases. Yet, if the diffusion coefficient of the ligand increases, the probability of dimerisation is greater, and overall rates grow. Finally, by increasing the receptor length, the average time to find a free receptor decreases.

In order to compare the magnitudes of the different partial derivatives in Table 3.4, they need to be normalised by the introduction of *sensitivity coefficients*. The sensitivity coefficient (also called *elasticity*) of a given dependent parameter with respect to an independent one can be calculated from the corresponding partial derivative. Specifically, if a parameter y depends on the parameter z as $y = f(z)$, where $f(\cdot)$ is a certain function, one can define their associated sensitivity coefficient as $\frac{\partial y}{\partial z}\,\frac{z^*}{y^*}$, where z^* is the actual value of the parameter z and $y^* = f(z^*)$. Quotient $\frac{z^*}{y^*}$ is then introduced to normalise the partial derivative, leading to an elasticity. For example, given the definition of k_+^{3D}

$$k_+^{3D} \;=\; \frac{q_{\text{on}}\; 4\pi D_L \sqrt{\frac{n_R\; s_c}{n_R^T\,\pi}}}{4\pi D_L \sqrt{\frac{n_R\; s_c}{n_R^T\,\pi}} - q_{\text{on}}\; n_R},$$

the following partial derivatives can be computed:

$$\frac{\partial k_+^{3D}}{\partial D_L} \;=\; -\frac{q_{\text{on}}^2 4\pi n_R \sqrt{\frac{n_R\; s_c}{n_R^T\,\pi}}}{(4\pi D_L \sqrt{\frac{n_R\; s_c}{n_R^T\,\pi}} - q_{\text{on}} n_R)^2}, \qquad \frac{\partial k_+^{3D}}{\partial n_R^T} \;=\; \frac{q_{\text{on}}^2 4\pi D_L \sqrt{\frac{n_R s_c}{n_R^T \pi}}\, n_R}{2 n_R^T (4\pi D_L \sqrt{\frac{n_R s_c}{n_R^T \pi}} - q_{\text{on}} n_R)^2},$$

$$\frac{\partial k_+^{3D}}{\partial s_c} \;=\; -\frac{q_{\text{on}}^2 n_R 4\pi D_L \frac{n_R}{n_R^T \pi}}{2\sqrt{\frac{n_R s_c}{n_R^T \pi}} (4\pi D_L \sqrt{\frac{n_R s_c}{n_R^T \pi}} - q_{\text{on}} n_R)^2}.$$

Then, regardless of the particular values of the parameters, it can be shown that

$$\left|\frac{\partial k_+^{3D}}{\partial D_L}\,\frac{D_L}{k_+^{3D}}\right| \;>\; \left|\frac{\partial k_+^{3D}}{\partial n_R^T}\,\frac{n_R^T}{k_+^{3D}}\right| \;=\; \left|\frac{\partial k_+^{3D}}{\partial s_c}\,\frac{s_c}{k_+^{3D}}\right|.$$

Similar arguments to the previous ones yield the following inequalities:

$$\left|\frac{\partial k_-}{\partial D_L}\frac{D_L}{k_-}\right| > \left|\frac{\partial k_-}{\partial n_R^T}\frac{n_R^T}{k_-}\right| = \left|\frac{\partial k_-}{\partial s_c}\frac{s_c}{k_-}\right|,$$
$$\left|\frac{\partial k_{c/u}}{\partial D_R}\frac{D_R}{k_{c/u}}\right| > \left|\frac{\partial k_{c/u}}{\partial n_R^T}\frac{n_R^T}{k_{c/u}}\right| = \left|\frac{\partial k_{c/u}}{\partial b}\frac{b}{k_{c/u}}\right| > \left|\frac{\partial k_{c/u}}{\partial s_c}\frac{s_c}{k_{c/u}}\right|,$$

so that the diffusion coefficients, D_L and D_R, are the most sensitive physiological parameters having the greatest impact on the binding and dissociation rates, while the specific value of the area of the cell surface has a smallest impact. Note that the previous inequalities are obtained under the following assumptions:

- the binding rate is much smaller than the diffusion rate of the ligand,

$$q_{\text{on}} n_R << 4\pi D_L \sqrt{\frac{n_R\, s_c}{n_R^T\, \pi}},$$

- surface receptor density is low, $b^2\pi n_R << s_c$, which also implies that the average distance between receptors is larger than the length of the receptor, and

- the intrinsic binding rate is greater than the diffusion rate of the receptor, $k_+^{2D} > 2\pi D_R$.

3.3 Moment closure approximation methods

In this section I show how the solution of master equations from Section 3.1 describing the cell surface models can be found using the moment closure approximation methods.

3.3.1 Zero cumulant method

One of the methods for obtaining information about the probability distribution associated with the Markov process is the generating function technique described in Subsection 2.2.7 of Chapter 2. The partial differential equation for moment generating function can be found by differentiating Equation (2.7) with respect

to t. For example, for the IP R_2 model, the moment generating function $\mathcal{M}(\cdot,\cdot)$ satisfies the following partial differential equation,

$$\begin{aligned}
\frac{\partial \mathcal{M}(\boldsymbol{\theta},t)}{\partial t} = & \frac{\partial \mathcal{M}(\boldsymbol{\theta},t)}{\partial \theta_1}\left\{(-2\alpha_+ n_{R_2} - 2\alpha_+ n_L)(e^{\theta_1}-1) + \beta_+ n_{R_2}(e^{-\theta_1+\theta_2}-1)\right. \\
& + \left.\alpha_-(e^{\theta_1}-1)\right\} + \frac{\partial^2 \mathcal{M}(\boldsymbol{\theta},t)}{\partial \theta_1 \partial \theta_2}\left\{-2\beta_+(e^{-\theta_1+\theta_2}-1) + 6\alpha_+(e^{\theta_1}-1)\right\} \\
& + \frac{\partial \mathcal{M}(\boldsymbol{\theta},t)}{\partial \theta_2}\left\{(-2\alpha_+ n_{R_2} - 4\alpha_+ n_L)(e^{\theta_1}-1) + 2\beta_-(e^{\theta_1-\theta_2}-1)\right\} \\
& + 2\alpha_+ n_{R_2} n_L \mathcal{M}(\boldsymbol{\theta},t)(e^{\theta_1}-1) + \frac{\partial^2 \mathcal{M}(\boldsymbol{\theta},t)}{\partial \theta_2^2}\left\{4\alpha_+(e^{\theta_1}-1)\right\} \\
& + \frac{\partial^2 \mathcal{M}(\boldsymbol{\theta},t)}{\partial \theta_1^2}\left\{2\alpha_+(e^{\theta_1}-1) - \beta_+(e^{-\theta_1+\theta_2}-1)\right\},
\end{aligned} \tag{3.6}$$

where $\boldsymbol{\theta} = (\theta_1, \theta_2)$ and the boundary conditions are $\mathcal{M}((\theta_1,\theta_2),0) = 1$ and $\mathcal{M}((0,0),t) = 1$. This differential equation is used to derive differential equations satisfied by the mean and higher-order moments. By executing the procedure described in Subsection 2.2.7 of Chapter 2 on Equation (3.6), one can get the system of ordinary differential equations for the moments,

$$\begin{aligned}
\frac{dm_{10}(t)}{dt} = & \; 2\alpha_+ n_L n_{R_2} - m_{10}(t)\left(2\alpha_+(n_{R_2}+n_L) + \alpha_- + \beta_+ n_{R_2}\right) + 4m_{02}(t)\alpha_+ \\
& + m_{20}(t)\left(2\alpha_+ + \beta_+\right) - m_{01}(t)\left(2\alpha_+(n_{R_2}+2n_L) - 2\beta_-\right) \\
& + m_{11}(t)\left(6\alpha_+ + 2\beta_+\right), \\
\frac{dm_{01}(t)}{dt} = & \; m_{10}(t)\beta_+ n_{R_2} - 2m_{01}(t)\beta_- - m_{20}(t)\beta_+ - 2m_{11}(t)\beta_+, \\
\frac{dm_{11}(t)}{dt} = & \; m_{01}(t)\left(2\alpha_+ n_L n_{R_2} - 2\beta_-\right) - m_{10}(t)\beta_+ n_{R_2} + m_{20}(t)\beta_+\left(n_{R_2}+1\right) \\
& + m_{12}(t)(6\alpha_+ + 2\beta_+) + m_{02}(t)\left(-4\alpha_+ n_L - 2\alpha_+ n_{R_2} + 2\beta_-\right) \\
& + m_{21}(t)(2\alpha_+ - \beta_+) + 4m_{03}(t)\alpha_+ - m_{30}(t)\beta_+ \\
& + m_{11}(t)\left(-2\alpha_+ n_L - 2\alpha_+ n_{R_2} - \alpha_- - \beta_+ n_{R_2} + 2\beta_+ - 2\beta_-\right),
\end{aligned}$$

$$
\begin{aligned}
\frac{dm_{02}(t)}{dt} &= m_{10}(t)\beta_+ n_{R_2} + 2m_{01}(t)\beta_- - m_{20}(t)\beta_+ - 4m_{02}(t)\beta_- \\
&+ m_{11}(t)[2n_{R_2}\beta_+ - 2\beta_+] - 2m_{21}(t)\beta_+ - 4m_{12}(t)\beta_+, \\
\\
\frac{dm_{20}(t)}{dt} &= m_{10}(t)\left(4\alpha_+ n_L n_{R_2} - 2\alpha_+ n_L - 2\alpha_+ n_{R_2} + \alpha_- + \beta_+ n_{R_2}\right) + 2\alpha_+ n_L n_{R_2} \\
&+ m_{01}(t)\left(-4\alpha_+ n_L - 2\alpha_+ n_{R_2} + 2\beta_-\right) + m_{21}(t)\left(12\alpha_+ + 4\beta_+\right) \\
&+ m_{20}(t)\left(-4\alpha_+ n_L - 4\alpha_+ n_{R_2} + 2\alpha_+ - 2\alpha_- - 2\beta_+ n_{R_2} - \beta_+\right) \\
&+ 4m_{02}(t)\alpha_+ + m_{11}(t)\left(-8\alpha_+ n_L + 6\alpha_+ - 4\alpha_+ n_{R_2} - 2\beta_+ + 4\beta_-\right) \\
&+ m_{30}(t)\left(4\alpha_+ + 2\beta_+\right) + 8m_{12}(t)\alpha_+,
\end{aligned}
\tag{3.7}
$$

with the initial conditions $m_{ij}(0) = 0$ for $i, j \in \{0, 1, 2\}$ and where $m_{ij}(t) = E(M_2(t)^i P_2(t)^j)$. Equation (3.7) for $m_{10}(\cdot)$ and $m_{01}(\cdot)$ cannot be solved alone, since $m_{10}(\cdot)$ and $m_{01}(\cdot)$ also depend on $m_{20}(\cdot), m_{02}(\cdot)$ and $m_{11}(\cdot)$. In the same manner, differential equations for the second-order moments also depend on higher-order moments and so on, forming an infinite system of the differential equation. That kind of system is called *open*, or *not closed*. The zero cumulant method (distribution-based), described in Subsection 2.2.8, can be used in order to find the solution of the ODEs system given by Equation (3.7). For example, assuming that all multi-variable cumulants of population $M_2(t)$ with order larger than 2 are negligible leads to the following approximation,

$$
\begin{aligned}
E\left(M_2(t)^3\right) &= 3E\left(M_2(t)^2\right)E\left(M_2(t)\right) - 2\left(E\left(M_2(t)\right)\right)^3, \\
E\left(M_2(t)^2 P_2(t)\right) &= E\left(M_2(t)^2\right)E\left(P_2(t)\right) + 2E\left(M_2(t)\right)E\left(M_2(t)P_2(t)\right) \\
&- 2\left(E(M_2(t))\right)^2 E\left(P_2(t)\right).
\end{aligned}
\tag{3.8}
$$

Therefore in the ODEs system given by Equation (3.7), the third moments can be approximated by,

$$
\begin{aligned}
m_{30}(t) &= 3m_{20}(t)m_{10}(t) - 2m_{10}(t)^3, \\
m_{03}(t) &= 3m_{02}(t)m_{01}(t) - 2m_{01}(t)^3, \\
m_{21}(t) &= m_{20}(t)m_{01}(t) + 2m_{10}(t)m_{11}(t) - 2m_{10}(t)^2 m_{01}(t), \\
m_{12}(t) &= m_{02}(t)m_{10}(t) + 2m_{01}(t)m_{11}(t) - 2m_{01}(t)^2 m_{10}(t).
\end{aligned}
\tag{3.9}
$$

The zero cumulant technique is applied in this thesis only for the IP R_2 model to compare the closure technique with the van Kampen expansion, which is applied in the following section for all models presented in Section 3.1. The results of that numerical work are shown further in Subsection 3.3.3.

3.3.2 van Kampen approximation

An alternative moment closure method is the system-size expansion technique, based on the power-series approximation proposed by Van Kampen (1992). It can also be used on the non-linear master equations given by Equations (3.1), (3.2) or (3.3). Using the van Kampen approximation the deterministic macroscopic equation and the equation for fluctuations might be obtained. First of all the expansion parameter Ω needs to be identified, with $\Omega \gg 1$. In this study Ω represents the volume of the system, so that fluctuations are of order $\Omega^{\frac{1}{2}}$.

Consider a CTMP $\mathcal{X} = \{\boldsymbol{X}(t) : t \geq 0\}$ defined on a state space $\mathcal{S}_{\mathcal{X}}$ with $P_{\boldsymbol{n}}(t) = Prob(\boldsymbol{X}(t) = \boldsymbol{n})$ for $\boldsymbol{n} = (n_1, n_2, \ldots) \in \mathcal{S}_{\mathcal{X}}$. The variable $\boldsymbol{X}(t)$ can be written as a sum of "mean" number $\boldsymbol{x}(t)$ (macroscopic concentration of order Ω) and fluctuation $\boldsymbol{\xi}(t)$ of order $\Omega^{\frac{1}{2}}$, that is

$$\boldsymbol{X}(t) = \Omega \boldsymbol{x}(t) + \Omega^{\frac{1}{2}} \boldsymbol{\xi}(t), \tag{3.10}$$

for all $t \geq 0$, where $\boldsymbol{X}(t) = (X_1(t), X_2(t), \ldots)$, $\boldsymbol{x}(t) = (x_1(t), x_2(t), \ldots)$ and $\boldsymbol{\xi}(t) = (\xi_1(t), \xi_2(t), \ldots)$. This conversion of variables implies that for all $t \geq 0$ $P_{\boldsymbol{n}}(t)$ transforms to a function $\Psi(t)$ as follows,

$$P_{\boldsymbol{n}}(t) = Prob(\boldsymbol{X}(t) = \boldsymbol{n}) = Prob(\Omega \boldsymbol{x}(t) + \Omega^{\frac{1}{2}} \boldsymbol{\xi}(t) = \boldsymbol{n}) = \Psi(\boldsymbol{\xi}(t), t). \tag{3.11}$$

Hence, the transformation of derivatives is found from the following equations,

$$\begin{aligned} \frac{\partial \Psi}{\partial \boldsymbol{\xi}(t)} &= \Omega^{\frac{1}{2}} \frac{\partial P_{\boldsymbol{n}}(t)}{\partial \boldsymbol{n}}, \\ \frac{\partial \Psi}{\partial t} &= \frac{\partial P_{\boldsymbol{n}}(t)}{\partial t} + \Omega \frac{\partial P_{\boldsymbol{n}}(t)}{\partial \boldsymbol{n}} \frac{d\boldsymbol{x}(t)}{dt}, \end{aligned}$$

therefore,

$$\frac{\partial P_{\boldsymbol{n}}(t)}{\partial t} = \frac{\partial \Psi}{\partial t} - \Omega^{\frac{1}{2}} \frac{\partial \Psi}{\partial \boldsymbol{\xi}(t)} \frac{d\boldsymbol{x}(t)}{dt}. \tag{3.12}$$

Using the transformation defined above I show in the following subsections how to carry out the van Kampen approximation for all the models described in Section 3.1.

I introduce here the operator $\mathbb{E}$ which is needed to perform the van Kampen linear noise approximation. Let $\mathbb{E}$ be the operator changing n_i into $n_i \pm 1$ for any

function $f(\cdot)$ and $i \geq 1$, that is $\mathbb{E}f(n_i) = f(n_i + 1)$ and $\mathbb{E}^{-1}f(n_i) = f(n_i - 1)$. This means that for all $t \geq 0$ the operator $\mathbb{E}$ changes $\xi_i(t)$ into $\xi_i(t) + \Omega^{\frac{1}{2}}$, that is

$$\begin{aligned} \mathbb{E}(\xi_i(t)) = &\quad \mathbb{E}_i(\xi_i(t)) = \xi_i(t) + \Omega^{\frac{1}{2}}, \\ \mathbb{E}^{-1}(\xi_i(t)) = &\quad \mathbb{E}_i^{-1}(\xi_i(t)) = \xi_i(t) - \Omega^{\frac{1}{2}}, \end{aligned}$$

where

$$\begin{aligned} \mathbb{E}_i &= 1 + \Omega^{-\frac{1}{2}} \frac{\partial}{\partial \xi_i(t)} + \tfrac{1}{2}\Omega^{-1} \frac{\partial^2}{\partial \xi_i^2(t)} + \dots, \\ \mathbb{E}_i^{-1} &= 1 - \Omega^{-\frac{1}{2}} \frac{\partial}{\partial \xi_i(t)} + \tfrac{1}{2}\Omega^{-1} \frac{\partial^2}{\partial \xi_i^2(t)} + \dots. \end{aligned} \tag{3.13}$$

van Kampen approximation for the IP R_2 model

Consider the CTMP $\mathcal{X}_{\text{IP } R_2}$ with the state space $\mathcal{S}_{\text{IP } R_2}$, defined in Subsection 3.1.1. By using the transformation defined by Equations (3.10) and (3.11) one can rewrite the master equation (3.1) in the form of Equation (3.12), as follows

$$\frac{dP_{\boldsymbol{n}}(t)}{dt} = \frac{\partial \Psi}{\partial t} - \Omega^{\frac{1}{2}} \sum_{i=1}^{2} \frac{\partial \Psi}{\partial \xi_i(t)} \frac{dx_i(t)}{dt}, \tag{3.14}$$

where $\boldsymbol{\xi}(t) = (\xi_1(t), \xi_2(t))$ and $\boldsymbol{x}(t) = (x_1(t), x_2(t))$ for $t \geq 0$. Rewrite now Equation (3.1) in terms of the operators $\mathbb{E}_i$ and $\mathbb{E}_i^{-1}$ given by Equation (3.13),

$$\begin{aligned} \frac{dP_{\boldsymbol{n}}(t)}{dt} &= (\mathbb{E}_1^{-1} - 1)\left\{2\alpha_+(n_{R_2} - n_1 - 2n_2)(n_L - n_1 - n_2)P_{\boldsymbol{n}}(t)\right\} \\ &+ (\mathbb{E}_1 - 1)\left\{\alpha_- n_1 P_{\boldsymbol{n}}(t)\right\} + (\mathbb{E}_1^{-1}\mathbb{E}_2 - 1)\left\{2\beta_- n_2 P_{\boldsymbol{n}}(t)\right\} \\ &+ (\mathbb{E}_1\mathbb{E}_2^{-1} - 1)\left\{\beta_+ n_1(n_{R_2} - n_1 - 2n_2)P_{\boldsymbol{n}}(t)\right\}. \end{aligned} \tag{3.15}$$

Note that the following expressions can be simplified,

$$\mathbb{E}_i\mathbb{E}_j^{-1} = 1 + \Omega^{-\frac{1}{2}}\left(\frac{\partial}{\partial \xi_i(t)} - \frac{\partial}{\partial \xi_j(t)}\right) + \frac{1}{2}\Omega^{-1}\left(\frac{\partial^2}{\partial \xi_i^2(t)} + \frac{\partial^2}{\partial \xi_j^2(t)} - 2\frac{\partial^2}{\partial \xi_i(t)\partial \xi_j(t)}\right) + \cdots.$$

The rates α_+ and β_+ are involved in non-linear terms of $q_{\boldsymbol{nn'}}$ (see Table 3.1). Therefore α_+ and β_+ require reduction of the volume of the system as follows

$$\alpha_+ = a_+\Omega^{-1}, \quad \beta_+ = b_+\Omega^{-1}. \tag{3.16}$$

n_L and n_{R_2} represent the total numbers of ligands and receptors, respectively, in the model. These two quantities need to be rescaled to macroscopic concentration expressed in the order of Ω, that is

$$n_L = N_L\Omega, \quad n_{R_2} = N_{R_2}\Omega. \tag{3.17}$$

By introducing the rescaled parameters to Equation (3.15) and compare the terms $-\Omega^{\frac{1}{2}}\dfrac{\partial\Psi}{\partial\xi_i(t)}$ for $i \in \{1,2\}$ with the analogue terms in Equation (3.14) one can get the macroscopic description of the IP R_2 model,

$$\begin{aligned}
\frac{dx_1(t)}{dt} &= 2a_+(N_L - x_1(t) - x_2(t))(N_{R_2} - x_1(t) - 2x_2(t)) \\
&- b_+x_1(t)(N_{R_2} - x_1(t) - 2x_2(t)) - \alpha_-x_1(t) + 2\beta_-x_2(t), \\
\frac{dx_2(t)}{dt} &= b_+x_1(t)(N_{R_2} - x_1(t) - 2x_2(t)) - 2\beta_-x_2(t),
\end{aligned} \tag{3.18}$$

with the initial conditions $x_1(0) = 0, x_2(0) = 0$ (as the initial condition of the process $\mathcal{X}_{\text{IP }R_2}$ says that $Prob\,((X_1(0), X_2(0)) = (0,0)) = 1$ which induces that $(\xi_1(0), \xi_2(0)) = (0,0)$). This implies that for all $t \geq 0$ the deterministic variable $x_1(t)$ represents the evolution of the monomers M_2 whereas $x_2(t)$ represents the evolution of the phosphorylated dimers P_2. Moreover, by comparing all terms of order Ω^0, the following Fokker-Planck equation can be obtained,

$$\frac{\partial\Psi}{\partial t} = -\sum_{i,j=1}^{2} A_{ij}\frac{\partial}{\partial\xi_i(t)}(\xi_j(t)\Psi) + \frac{1}{2}\sum_{i,j=1}^{2} B_{ij}\frac{\partial^2\Psi}{\partial\xi_i(t)\partial\xi_j(t)}, \tag{3.19}$$

where all elements of the matrices $\boldsymbol{A} = (A_{ij})_{i,j\in\{1,2\}}$ and $\boldsymbol{B} = (B_{ij})_{i,j\in\{1,2\}}$ are given by Equation (3.20).

$$\begin{aligned}
A_{11} &= -2a_+(N_L - x_1^* - x_2^*) - 2a_+(N_{R_2} - x_1^* - 2x_2^*) - \alpha_- - b_+(N_{R_2} - 2x_1^* - 2x_2^*), \\
A_{12} &= -4a_+(N_L - x_1^* - x_2^*) - 2a_+(N_{R_2} - x_1^* - 2x_2^*) + 2b_+x_1^* + 2\beta_-, \\
A_{21} &= b_+(N_{R_2} - 2x_1^* - 2x_2^*), \\
A_{22} &= -2b_+x_1^* - 2\beta_-,
\end{aligned}$$

$$\begin{aligned} B_{11} &= 2a_+(N_L - x_1^* - x_2^*)(N_{R_2} - x_1^* - 2x_2^*) + \alpha_- x_1^* + b_+ x_1^*(N_{R_2} - x_1^* - 2x_2^*), \\ &+ 2\beta_- x_2^*, \\ B_{12} &= B_{21} = -b_+ x_1^*(N_{R_2} - x_1^* - 2x_2^*) - 2\beta_- x_2^*, \\ B_{22} &= b_+ x_1^*(N_{R_2} - x_1^* - 2x_2^*) + 2\beta_- x_2^*, \end{aligned} \tag{3.20}$$

and where (x_1^*, x_2^*) denotes the steady state of the ODEs system given by Equation (3.18). From the Fokker-Planck equation given by Equation (3.19) it is possible to obtain the equations for the mean value of the fluctuations $\boldsymbol{\xi}(t)$ as well as the correlations of these fluctuations for all $t \geq 0$. By multiplying Equation (3.19) by $\xi_k(t)$, and integrating the obtained expression over $\xi_k(t)$ one can get the following equations

$$\frac{dE(\xi_k(t))}{dt} = \sum_{i=1}^{2} A_{ki} E(\xi_i(t)), \tag{3.21}$$

for all $t \geq 0$ and $k \in \{1, 2\}$, where $E(\xi_k(0)) = 0$ is the initial condition for this ODEs system. On the other hand, by multiplying Equation (3.19) by $\xi_i(t)\xi_j(t)$ and integrating the obtained expression over $\xi_i(t)\xi_j(t)$ one can get the equation for the second moments, $\xi_i(t)\xi_j(t)$, that is

$$\frac{dE(\xi_i(t)\xi_j(t))}{dt} = \sum_{k=1}^{2} A_{ik} E(\xi_k(t)\xi_j(t)) + \sum_{k=1}^{2} A_{jk} E(\xi_i(t)\xi_k(t)) + B_{ij}, \tag{3.22}$$

for all $t \geq 0$ and $i, j \in \{1, 2\}$, where $E(\xi_i(0)\xi_j(0)) = 0$ is the initial condition for this ODEs system. Results of zero cumulant method are compared with results of the van Kampen approximation in Subsection 3.3.3 for the IP R_2 model. As the results of both methods give similar approximations I use only the van Kampen approximation for the DP R_2, the IP R_1/R_2 and the DP R_1/R_2 models.

van Kampen approximation for the DP R_2 model

Using the van Kampen approximation, as for the IP R_2 model, the deterministic description of the DP R_2 model is obtained,

$$\begin{aligned}
\frac{dx_1(t)}{dt} &= 2a_+(N_L - x_1(t) - x_2(t) - x_3(t))(N_{R_2} - x_1(t) - 2x_2(t) - 2x_3(t)) \\
&- \alpha_- x_1(t) + 2\beta_- x_2(t) - b_+ x_1(t)(N_{R_2} - x_1(t) - 2x_2(t) - 2x_3(t)), \\
\frac{dx_2(t)}{dt} &= b_+ x_1(t)(N_{R_2} - x_1(t) - 2x_2(t) - 2x_3(t)) - 2\beta_- x_2(t) - \gamma_+ x_2(t) \\
&+ \gamma_- x_3(t), \\
\frac{dx_3(t)}{dt} &= \gamma_+ x_2(t) - \gamma_- x_3(t),
\end{aligned} \tag{3.23}$$

with the initial condition $x_1(0) = x_2(0) = x_3(0) = 0$ which is consequence of the initial condition for Equation (3.2) (see the previous subsection where this issue is explained in detail for the IP R_2 model), and for all $t \geq 0$ the deterministic variables $x_1(t), x_2(t)$ and $x_3(t)$ represent the evolution of the monomers M_2, the bound dimers D_2 and the phosphorylated dimers P_2, respectively. The parameters α_+, β_+, n_L and n_{R_2} require the same rescaling as for the IP R_2 model (see Equations (3.16) and (3.17)). Accordingly it is possible to write down Equations (3.21) and (3.22) for the moments, where the matrix $\boldsymbol{A} = (A_{ij})_{i,j\in\{1,2,3\}}$ is given by,

$$\begin{aligned}
A_{11} &= -2a_+(N_L - x_1^* - x_2^* - x_3^*) - 2a_+(N_{R_2} - x_1^* - 2x_2^* - 2x_3^*) \\
&- b_+(N_{R_2} - x_1 - 2x_2^* - 2x_3^*) + b_+ x_1^* - \alpha_-, \\
A_{12} &= -4a_+(N_L - x_1^* - x_2^* - x_3^*) - 2a_+(N_{R_2} - x_1^* - 2x_2^* - 2x_3^*) + 2b_+ x_1^* \\
&+ 2\beta_-, \\
A_{13} &= -4a_+(N_L - x_1^* - x_2^* - x_3^*) - 2a_+(N_{R_2} - x_1^* - 2x_2^* - 2x_3^*) + 2b_+ x_1^*, \\
A_{21} &= b_+(N_{R_2} - x_1^* - 2x_2^* - 2x_3^*) - b_+ x_1^*, \\
A_{22} &= -2b_+ x_1^* - 2\beta_- - \gamma_+,
\end{aligned}$$

$$
\begin{aligned}
A_{23} &= -2b_+x_1^* + \gamma_-,\\
A_{31} &= 0,\\
A_{32} &= \gamma_+,\\
A_{33} &= -\gamma_-,
\end{aligned}
$$

and the matrix $\boldsymbol{B} = (B_{ij})_{i,j\in\{1,2,3\}}$ is given by

$$
\begin{aligned}
B_{11} &= 2(N_L - x_1^* - x_2^* - x_3^*)(N_{R_2} - x_1^* - 2x_2^* - 2x_3^*) + \alpha_- x_1^* + 2\beta_- x_2^*,\\
&+ b_+x_1^*(N_{R_2} - x_1^* - 2x_2^* - 2x_3^*)\\
B_{22} &= b_+x_1^*(N_{R_2} - x_1^* - 2x_2^* - 2x_3^*) + 2\beta_- x_2^* + \gamma_- x_3^* + \gamma_+ x_2^*,\\
B_{33} &= \gamma_- x_3^* + \gamma_+ x_2^*,\\
B_{12} &= B_{21} = -b_+x_1^*(N_{R_2} - x_1^* - 2x_2^* - 2x_3^*) - 2\beta_- x_2^*,\\
B_{13} &= B_{31} = 0,\\
B_{23} &= B_{32} = -\gamma_- x_3^* - \gamma_+ x_2^*,
\end{aligned}
$$

where (x_1^*, x_2^*, x_3^*) is the steady state of the ODEs system given by Equation (3.23).

van Kampen approximation for the IP R_1/R_2 model

Consider the IP R_1/R_2 model described in Subsection 3.1.3. The following rates are involved in non-linear terms of $q_{\boldsymbol{nn'}}$ (see Table 3.3) and these rates require reduction of the volume of the system as follows,

$$
\begin{aligned}
&\alpha_{1+} = a_{1+}\Omega^{-1}, \quad \alpha_{2+} = a_{2+}\Omega^{-1}, \quad \beta_{11+} = b_{11+}\Omega^{-1},\\
&\beta_{12+} = b_{12+}\Omega^{-1}, \quad \beta_{21+} = b_{21+}\Omega^{-1}, \quad \beta_{22+} = b_{22+}\Omega^{-1}.
\end{aligned}
\tag{3.24}
$$

As for the IP R_2 model, the parameters representing the total number of ligands and receptors need to be rescaled to match macroscopic representation expressed in the order of Ω, that is

$$
n_L = N_L\Omega, \quad n_{R_1} = N_{R_1}\Omega, \quad n_{R_2} = N_{R_2}\Omega. \tag{3.25}
$$

In the case of the IP R_1/R_2 model the deterministic variables $x_1(t), x_2(t), x_3(t)$, $x_4(t)$ and $x_5(t)$ represent the evolution of the monomers M_1, M_2, the bound

homodimers D_1, P_2 and the bound heterodimers P_M, respectively, and they are described by the following system of the ordinary equations,

$$\begin{aligned}
\frac{dx_1(t)}{dt} &= 2a_{1+}(N_{R_1} - x_1(t) - 2x_3(t) - x_5(t))(N_L - x_1(t) - x_2(t) - x_3(t) \\
&- x_4(t) - x_5(t)) - b_{11+}x_1(t)(N_{R_1} - x_1(t) - 2x_3(t) - x_5(t)) + \beta_{12-}x_5(t) \\
&- b_{12+}x_1(t)(N_{R_2} - x_2(t) - 2x_4(t) - x_5(t)) - \alpha_{1-}x_1(t) + 2\beta_{11-}x_3(t), \\
\frac{dx_2(t)}{dt} &= 2a_{2+}(N_{R_2} - x_2(t) - 2x_4(t) - x_5(t))(N_L - x_1(t) - x_2(t) - x_3(t) \\
&- x_4(t) - x_5(t)) - b_{22+}x_2(N_{R_2} - x_2(t) - 2x_4(t) - x_5(t)) + \beta_{21-}x_5(t) \\
&- b_{21+}x_2(t)(N_{R_1} - x_1(t) - 2x_3(t) - x_5(t)) - \alpha_{2-}x_2(t) + 2\beta_{22-}x_4(t), \\
\frac{dx_3(t)}{dt} &= -2\beta_{11-}x_3(t) + b_{11+}x_1(t)(N_{R_1} - x_1(t) - 2x_3(t) - x_5(t)), \\
\frac{dx_4(t)}{dt} &= b_{22+}x_2(t)(N_{R_2} - x_2(t) - 2x_4(t) - x_5(t)) - 2\beta_{22-}x_4(t), \\
\frac{dx_5(t)}{dt} &= b_{12+}x_1(t)(N_{R_2} - x_2(t) - 2x_4(t) - x_5(t)) + b_{21+}x_2(t)(N_{R_1} - x_1(t) \\
&- 2x_3(t) - x_5(t)) - \beta_{12-}x_5(t) - \beta_{21-}x_5(t),
\end{aligned} \tag{3.26}$$

for all $t \geq 0$, where the initial conditions are determined by the initial condition for Equation (3.3), that is $x_i(0) = 0$ for $1 \leq i \leq 5$. Denote by $(x_1^*, x_2^*, x_3^*, x_4^*, x_5^*)$ the steady state of this ODEs system. From Equation (3.19) the equations for the moments are obtained from Equations (3.21) and (3.22). The matrices $\boldsymbol{A} = (A_{ij})_{1\leq i,j\leq 5}$ and $\boldsymbol{B} = (B_{ij})_{1\leq i,j\leq 5}$ are such that $B_{ij} = B_{ji}$ and $A_{ij} = 0$, $B_{ij} = 0$, except for

$$\begin{aligned}
A_{11} &= -2a_{1+}\left((N_L - x_1^* - x_2^* - x_3^* - x_4^* - x_5^*) + (N_{R_1} - x_1^* - 2x_3^* - x_5^*)\right) - \alpha_{1-} \\
&- b_{11+}(N_{R_1} - x_1^* - 2x_3^* - x_5^*) - b_{12+}(N_{R_2} - x_2^* - 2x_4^* - x_5^*) + b_{11+}x_1^*, \\
A_{12} &= b_{12+}x_1^* - 2a_{1+}(N_{R_1} - x_1^* - 2x_3^* - x_5^*), \\
A_{13} &= -2a_{1+}\left(2(N_L - x_1^* - x_2^* - x_3^* - x_4^* - x_5^*) + (N_{R_1} - x_1^* - 2x_3^* - x_5^*)\right) \\
&+ 2b_{11+}x_1^* + 2\beta_{11-}, \\
A_{14} &= 2b_{12+}x_1 - 2a_{1+}(N_{R_1} - x_1^* - 2x_3^* - x_5^*), \\
A_{15} &= -2a_{1+}\left((N_L - x_1^* - x_2^* - x_3^* - x_4^* - x_5^*) + (N_{R_1} - x_1^* - 2x_3^* - x_5^*)\right) \\
&+ b_{11+}x_1^* + b_{12+}x_1^* + \beta_{12-},
\end{aligned}$$

$$
\begin{aligned}
A_{21} &= b_{21+}x_2^* - 2a_{2+}(N_{R_2} - x_2^* - 2x_4^* - x_5^*),\\
A_{22} &= -2a_{2+}\left((N_L - x_1^* - x_2^* - x_3^* - x_4^* - x_5^*) + (N_{R_2} - x_2^* - 2x_4^* - x_5^*)\right) - \alpha_{2-}\\
&- b_{21+}(N_{R_1} - x_1^* - 2x_3^* - x_5^*) - b_{22+}(N_{R_2} - x_2^* - 2x_4^* - x_5^*) + b_{22+}x_2^*,\\
A_{23} &= 2b_{21+}x_2^* - 2a_{2+}(N_{R_2} - x_2^* - 2x_4^* - x_5^*),\\
A_{24} &= -2a_{2+}\left(2(N_L - x_1^* - x_2^* - x_3^* - x_4^* - x_5^*) + (N_{R_2} - x_2^* - 2x_4^* - x_5^*)\right)\\
&+ 2b_{22+}x_2^* + 2\beta_{22-},\\
A_{25} &= -2a_{2+}\left((N_L - x_1^* - x_2^* - x_3^* - x_4^* - x_5^*) + (N_{R_2} - x_2^* - 2x_4^* - x_5^*)\right)\\
&+ b_{21+}x_2^* + b_{22+}x_2^* + \beta_{21-},\\
A_{31} &= b_{11+}(N_{R_1} - x_1^* - 2x_3^* - x_5^*) - b_{11+}x_1^*,\\
A_{33} &= -2b_{11+}x_1^* - 2\beta_{11-},\\
A_{35} &= -b_{11+}x_1^*,\\
A_{42} &= b_{22+}(N_{R_2} - x_2^* - 2x_4^* - x_5^*) - b_{22+}x_2^*,\\
A_{44} &= -2b_{22+}x_2^* - 2\beta_{22-},\\
A_{45} &= -b_{22+}x_2^*,\\
A_{51} &= -b_{21+}x_2^* + b_{12+}(N_{R_2} - x_2^* - 2x_4^* - x_5^*),\\
A_{52} &= -b_{12+}x_1^* + b_{21+}(N_{R_1} - x_1^* - 2x_3^* - x_5^*),\\
A_{53} &= -2b_{21+}x_2^*,\\
A_{54} &= -2b_{12+}x_1^*,\\
A_{55} &= -b_{12+}x_1^* - b_{21+}x_2^* - \beta_{12-} - \beta_{21-},
\end{aligned}
$$

and for the matrix $\boldsymbol{B}$,

$$
\begin{aligned}
B_{11} &= 2a_{1+}(N_L - x_1^* - x_2^* - x_3^* - x_4^* - x_5^*)(N_{R_1} - x_1^* - 2x_3^* - x_5^*) + \alpha_{1-}x_1^*\\
&+ \beta_{12-}x_5^* + b_{11+}x_1^*(N_{R_1} - x_1^* - 2x_3^* - x_5^*) + b_{12+}x_1^*(N_{R_2} - x_2^* - 2x_4^* - x_5^*)\\
&+ 2\beta_{11-}x_3^*,\\
B_{13} &= -b_{11+}x_1^*(N_{R_1} - x_1^* - 2x_3^* - x_5^*) - 2\beta_{11-}x_3^*,
\end{aligned}
$$

$$
\begin{aligned}
B_{15} &= -b_{12+}x_1^*(N_{R_2} - x_2^* - 2x_4^* - x_5^*) - \beta_{12-}x_5^*,\\
B_{22} &= 2a_{2+}(N_L - x_1^* - x_2^* - x_3^* - x_4^* - x_5^*)(N_{R_2} - x_2^* - 2x_4^* - x_5^*) + \alpha_{2-}x_2^*\\
&+ b_{21+}x_2^*(N_{R_1} - x_1^* - 2x_3^* - x_5^*) + b_{22+}x_2^*(N_{R_2} - x_2^* - 2x_4^* - x_5^*) + 2\beta_{22-}x_4^*\\
&+ \beta_{21-}x_5^*,\\
B_{24} &= -b_{22+}x_2^*(N_{R_2} - x_2^* - 2x_4^* - x_5^*) - 2\beta_{22-}x_4^*,\\
B_{33} &= b_{11+}x_1^*(N_{R_1} - x_1^* - 2x_3^* - x_5^*) + 2\beta_{11-}x_3^*,\\
B_{35} &= -b_{21+}x_2^*(N_{R_1} - x_1^* - 2x_3^* - x_5^*) - \beta_{21-}x_5^*,\\
B_{44} &= b_{22+}x_2^*(N_{R_2} - x_2^* - 2x_4^* - x_5^*) + 2\beta_{22-}x_4^*,\\
B_{55} &= b_{12+}x_1^*(N_{R_2} - x_2^* - 2x_4^* - x_5^*) + b_{21+}x_2^*(N_{R_1} - x_1^* - 2x_3^* - x_5^*) + \beta_{12-}x_5^*\\
&+ \beta_{21-}x_5^*.
\end{aligned}
$$

van Kampen approximation for the DP R_1/R_2 model

The DP R_1/R_2 model requires the same scaling of parameters as the IP R_1/R_2 model given by Equations (3.24) and (3.25). There are seven variables in the DP R_1/R_2 model $x_1(t), x_2(t), x_3(t), x_4(t), x_5(t), x_6(t)$ and $x_7(t)$ which represent the evolution of the monomers M_1, M_2, the bound homodimers D_1, D_2, the bound heterodimers D_M, the phosphorylated dimers P_2 and the phosphorylated heterodimers P_M, respectively, which are described by the following ODEs system,

$$
\begin{aligned}
\frac{dx_1(t)}{dt} &= 2a_{1+}(N_{R_1} - x_1(t) - 2x_3(t) - x_5(t) - x_7(t))(N_L - x_1(t) - x_2(t)\\
&- x_3(t) - x_4(t) - x_5(t) - x_6(t) - x_7(t)) - b_{11+}x_1(t)(N_{R_1} - x_1(t)\\
&- 2x_3(t) - x_5(t) - x_7(t)) - \alpha_{1-}x_1(t) + 2\beta_{11-}x_3(t) + \beta_{12-}x_5(t)\\
&- b_{12+}x_1(t)(N_{R_2} - x_2(t) - 2x_4(t) - x_5(t) - 2x_6(t) - x_7(t)),\\
\frac{dx_2(t)}{dt} &= 2a_{2+}(N_{R_2} - x_2(t) - 2x_4(t) - x_5(t) - 2x_6(t) - x_7(t))\,(N_L - x_1(t)\\
&- x_2(t) - x_3(t) - x_4(t) - x_5(t) - x_6(t) - x_7(t)) + 2\beta_{22-}x_4(t)\\
&- b_{22+}x_2(t)(N_{R_2} - x_2(t) - 2x_4(t) - x_5(t) - 2x_6(t) - x_7(t)) - \alpha_{2-}x_2(t)\\
&- b_{21+}x_2(t)(N_{R_1} - x_1(t) - 2x_3(t) - x_5(t) - x_7(t)) + \beta_{21-}x_5(t),\\
\frac{dx_3(t)}{dt} &= -2\beta_{11-}x_3(t) + b_{11+}x_1(t)(N_{R_1} - x_1(t) - 2x_3(t) - x_5(t) - x_7(t)),
\end{aligned}
$$

$$\begin{aligned}
\frac{dx_4(t)}{dt} &= b_{22+}x_2(t)(N_{R_2} - x_2(t) - 2x_4(t) - x_5(t) - 2x_6(t) - x_7(t)) \\
&- 2\beta_{22-}x_4(t) - \gamma_{22+}x_4(t) + \gamma_{22-}x_6(t), \\
\frac{dx_5(t)}{dt} &= b_{12+}x_1(t)(N_{R_2} - x_2(t) - 2x_4(t) - x_5(t) - 2x_6(t) - x_7(t)) - \beta_{12-}x_5(t) \\
&- \beta_{21-}x_5(t) + b_{21+}x_2(t)(N_{R_1} - x_1(t) - 2x_3(t) - x_5(t) - x_7(t)) \\
&- \gamma_{12+}x_5(t) + \gamma_{12-}x_7(t) \\
\frac{dx_6(t)}{dt} &= \gamma_{22+}x_4(t) - \gamma_{22-}x_6(t), \\
\frac{dx_7(t)}{dt} &= \gamma_{12+}x_5(t) - \gamma_{12-}x_7(t),
\end{aligned} \tag{3.27}$$

for all $t \geq 0$, where the initial conditions are $x_i(0) = 0$ for $1 \leq i \leq 7$. Denote by $(x_1^*, x_2^*, x_3^*, x_4^*, x_5^*, x_6^*, x_7^*)$ the steady state of this ODEs system. The moments can be obtained from Equations (3.21) and (3.22) where $\boldsymbol{A} = (A_{ij})_{1\leq i,j\leq 7}$ and $\boldsymbol{B} = (B_{ij})_{1\leq i,j\leq 7}$. The elements A_{ij} and B_{ij} for $i, j \leq 5$ are the same as in the IP R_1/R_2 model except for the following contributions which must be added: $\Delta A_{44} = -\gamma_{22+}$, $\Delta A_{55} = -\gamma_{12+}$, and $\Delta B_{44} = \gamma_{22-}x_6^* + \gamma_{22+}x_4^*$, $\Delta B_{55} = \gamma_{12-}x_7^* + \gamma_{12+}x_5^*$. There are seven variables in the DP R_1/R_2 model, therefore the expressions describing the number of free ligand or free receptor in time have to be updated in the matrices $\boldsymbol{A}$, $\boldsymbol{B}$ of the IP R_1/R_2 model in the following way,

$$\begin{aligned}
&(N_L - x_1^* - x_2^* - x_3^* - x_4^* - x_5^*) &&\to (N_L - x_1^* - x_2^* - x_3^* - x_4^* - x_5^* - x_6^* - x_7^*), \\
&(N_{R_1} - x_1^* - 2x_3^* - x_5^*) &&\to (N_{R_1} - x_1^* - 2x_3^* - x_5^* - x_7^*), \\
&(N_{R_2} - x_2^* - 2x_4^* - x_5^*) &&\to (N_{R_2} - x_2^* - 2x_4^* - x_5^* - 2x_6^* - x_7^*),
\end{aligned}$$

Additionally for $i \geq 6$ or $j \geq 6$, $A_{ij} = 0$ and $B_{ij} = B_{ji} = 0$, except for the following

$$\begin{aligned}
A_{16} &= 2b_{12+}x_1^* - 2a_{1+}(N_{R_1} - x_1^* - 2x_3^* - x_5^* - x_7^*), \\
A_{17} &= b_{11+}x_1^* + b_{12+}x_1^* - 2a_{1+}((N_L - x_1^* - x_2^* - x_3^* - x_4^* - x_5^* - x_6^* - x_7^*) \\
&+ (N_{R_1} - x_1^* - 2x_3^* - x_5^* - x_7^*)), \\
A_{26} &= 2b_{22+}x_2^* - 2a_{2+}(2(N_L - x_1^* - x_2^* - x_3^* - x_4^* - x_5^* - x_6^* - x_7^*) \\
&+ (N_{R_2} - x_2^* - 2x_4^* - x_5^* - 2x_6^* - x_7^*)),
\end{aligned}$$

$$
\begin{aligned}
A_{27} &= b_{21+}x_2^* + b_{22+}x_2^* - 2a_{2+}((N_L - x_1^* - x_2^* - x_3^* - x_4^* - x_5^* - x_6^* - x_7^*) \\
&+ (N_{R_2} - x_2^* - 2x_4^* - x_5^* - 2x_6^* - x_7^*)),
\end{aligned}
$$

$$A_{37} = -b_{11+}x_1^*,$$

$$A_{46} = -2b_{22+}x_2^* + \gamma_{22-},$$

$$A_{47} = -b_{22+}x_2^*,$$

$$A_{56} = -2b_{12+}x_1^*,$$

$$A_{57} = \gamma_{12-} - b_{12+}x_1^* - b_{21+}x_2^*,$$

$$A_{64} = \gamma_{22+},$$

$$A_{66} = -\gamma_{22-},$$

$$A_{75} = \gamma_{12+},$$

$$A_{77} = -\gamma_{12-},$$

and

$$B_{46} = -\gamma_{22-}x_6^* - \gamma_{22+}x_4^*,$$

$$B_{57} = -\gamma_{12-}x_7^* - \gamma_{12+}x_5^*,$$

$$B_{66} = \gamma_{22-}x_6^* + \gamma_{22+}x_4^*,$$

$$B_{77} = \gamma_{12-}x_7^* + \gamma_{12+}x_5^*.$$

3.3.3 Results

Firstly I show in Table 3.5 values of the physiological parameters used in the models described in Section 3.1. Secondly the comparison between two moment closure methods, the zero cumulant and the van Kampen approximation, is done for the IP R_2 model. In the next step I compare the IP R_2 model with the IP R_1/R_2 model and the DP R_2 model with the DP R_1/R_2 model. For these models, the objective is to analyse the dynamics of the different receptors and complexes for different VEGF-A ligand concentrations, and to study the competition effect that the presence of VEGFR1 has in the dynamics of VEGFR2.

Parameters values

Rates involved in the IP R_2, the DP R_2, the IP R_1/R_2 and the DP R_1/R_2 models (Figures 3.1, 3.2, 3.3 and 3.4, respectively) have been obtained by following the approach described in Subsections 3.2.1 and 3.2.2 with physiological parameters taken from the literature. In particular, physiological parameters are given in Table 3.5, and computed rates corresponding to the IP R_2 and the DP R_2 models are given in Table 3.6, whereas computed rates corresponding to the IP R_1/R_2 and the DP R_1/R_2 models are given in Tables 3.7 and 3.8 assuming three different initial number for VEGFR1 receptors per cell.

Physiological parameter	Value	Reference
Endothelial cell surface area, s_c	$10^{-3}\ mm^2$	Mac Gabhann & Popel (2007)
VEGF-A diffusion coefficient at 4 °C, D_L	$5.2 \times 10^{-5} mm^2 s^{-1}$	Mac Gabhann *et al.* (2005)
VEGFR1 and VEGFR2 diffusion coefficient, D_R	$10^{-8} mm^2 s^{-1}$	Linderman & Lauffenburger (2013)
VEGFR1 and VEGFR2 radius, b	$5 \times 10^{-7}\ mm$	Alarcón & Page (2006)
Average membrane thickness of ECs, th	$10^{-4}\ mm$	Aird (2007)
Height of the experimental volume, h	$1\ mm$	Mac Gabhann & Popel (2007)
Dissociation rate, k_{off}	$1.32 \times 10^{-3} s^{-1}$	Mac Gabhann & Popel (2007)
Equilibrium dissociation constant, K_d for VEGFR1	$30\ pM$	Mac Gabhann & Popel (2007)
Equilibrium dissociation constant, K_d for VEGFR2	$150\ pM$	Mac Gabhann & Popel (2007)
Phosphorylation rate for D complexes, γ_+	$3.67 \times 10^{-3}\ s^{-1}$	Lauffenburger & Linderman (1993)
De-phosphorylation rate for P complexes, γ_-	$9.17 \times 10^{-4}\ s^{-1}$	Lauffenburger & Linderman (1993)

Table 3.5: Physiological parameters

I consider the subset of endothelial cells, called human umbilical vein endothelial cells (HUVECs), which have been characterised to express (on average) 5800 VEGFR2 receptors per cell as reported by Imoukhuede & Popel (2012). The focus is on 4% of the cell surface ($f = 0.04$) for computational reasons, so that in this area the total number of VEGFR2 receptors is $n_{R_2} = 232$. Based on the fact that HUVECs express a total number of 1800 ± 100 VEGFR1 receptors per cell (see Imoukhuede & Popel (2012)) three values were chosen to study the impact of receptor competition, $1600, 1800$ and 2000 VEGFR1 receptors per cell. These numbers correspond to $64, 72$ and 80 VEGFR1 receptors present on 4% fraction of the cell. Therefore Table 3.7 contains the kinetics rates for different initial number of VEGFR1 receptors.

α_+	α_-	β_+	β_-	γ_+	γ_-
3.65×10^{-7}	1.32×10^{-3}	2.16×10^{-4}	7.80×10^{-5}	3.67×10^{-3}	9.17×10^{-4}

Table 3.6: Kinetic rates (in s^{-1}) for the IP R_2 and the DP R_2 models, where $n_{R_1} = 0$, considering 4% of the cell.

	$n_{R_1} = 64$	$n_{R_1} = 72$	$n_{R_1} = 80$
α_{1+}	1.83×10^{-6}	1.83×10^{-6}	1.83×10^{-6}
α_{1-}	1.32×10^{-3}	1.32×10^{-3}	1.32×10^{-3}
α_{2+}	3.65×10^{-7}	3.65×10^{-7}	3.65×10^{-7}
α_{2-}	1.32×10^{-3}	1.32×10^{-3}	1.32×10^{-3}
β_{11+}	2.07×10^{-4}	2.09×10^{-4}	2.11×10^{-4}
β_{11-}	1.50×10^{-5}	1.51×10^{-5}	1.52×10^{-5}
β_{12+}	1.74×10^{-4}	1.70×10^{-4}	1.67×10^{-4}
β_{12-}	6.30×10^{-5}	6.16×10^{-5}	6.02×10^{-5}
β_{21+}	5.04×10^{-5}	5.53×10^{-5}	6.00×10^{-5}
β_{21-}	3.64×10^{-6}	4.00×10^{-6}	4.33×10^{-6}
β_{22+}	2.16×10^{-4}	2.16×10^{-4}	2.16×10^{-4}
β_{22-}	7.80×10^{-5}	7.80×10^{-5}	7.80×10^{-5}

Table 3.7: Kinetic rates (in s^{-1}) for the IP R_1/R_2 and the DP R_1/R_2 models considering 4% of the cell.

The phosphorylation rate of the D_M complexes in the DP R_1/R_2 model is taken to be $\gamma_{21+} = 0.5\gamma_{22+}$, since only VEGFR2 is assumed to become phosphorylated (VEGFR1 phosphorylation is neglected as per Casaletto & McClatchey (2012)), and the de-phosphorylation rate of P_M complexes is taken to be $\gamma_{21-} = \gamma_{22-}$.

γ_{21+}	γ_{21-}	γ_{22+}	γ_{22-}
1.833×10^{-3}	9.167×10^{-4}	3.667×10^{-3}	9.167×10^{-4}

Table 3.8: Phosphorylation and de-phosphorylation rates (in s^{-1}) for the IP R_1/R_2 and the DP R_1/R_2 models considering 4% of the cell.

Moment closure methods for the IP R_2 model

Results for the zero cumulant method (denoted by ZC on Figures 3.6 and 3.7) are compared with results for the van Kampen approximation (denoted by VK on Figures 3.6 and 3.7) for the IP R_2 model. Figures 3.6 and 3.7 show results of these moment closure techniques using rates described in Table 3.6 for four different initial ligand concentrations $c_l \in \{0.25nM, 0.1nM, 1nM, 2.5nM\}$, which approximately corresponds to $n_L \in \{0.25n_{R_2}, 10n_{R_2}, 100n_{R_2}, 250n_{R_2}\}$, where n_{R_2} is the number of VEGFR2. Only 4% of the cell is considered in this experiment. Blue curves show the solution of the deterministic representation of the IP R_2 model defined by Equations (3.18). Black curves show the sampled stochastic simulation computed using the Gillespie algorithm described in Subsection 2.2.13 of Chapter 2. Shaded area on these Figures represents the mean ± two standard deviations for the van Kampen approximation and the zero cumulant method. As both approximation work well only the van Kampen approximation is used for the DP R_2, the IP R_1/R_2 and the DP R_1/R_2 models.

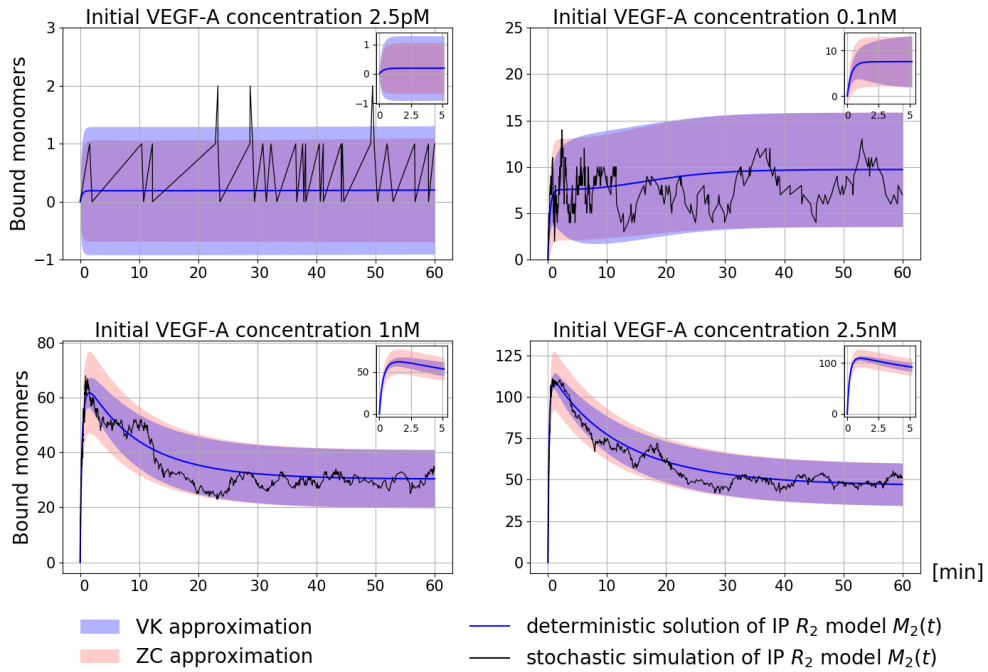

Figure 3.6: Comparison of moment closure techniques for the IP R_2 model for bound monomers M_2.

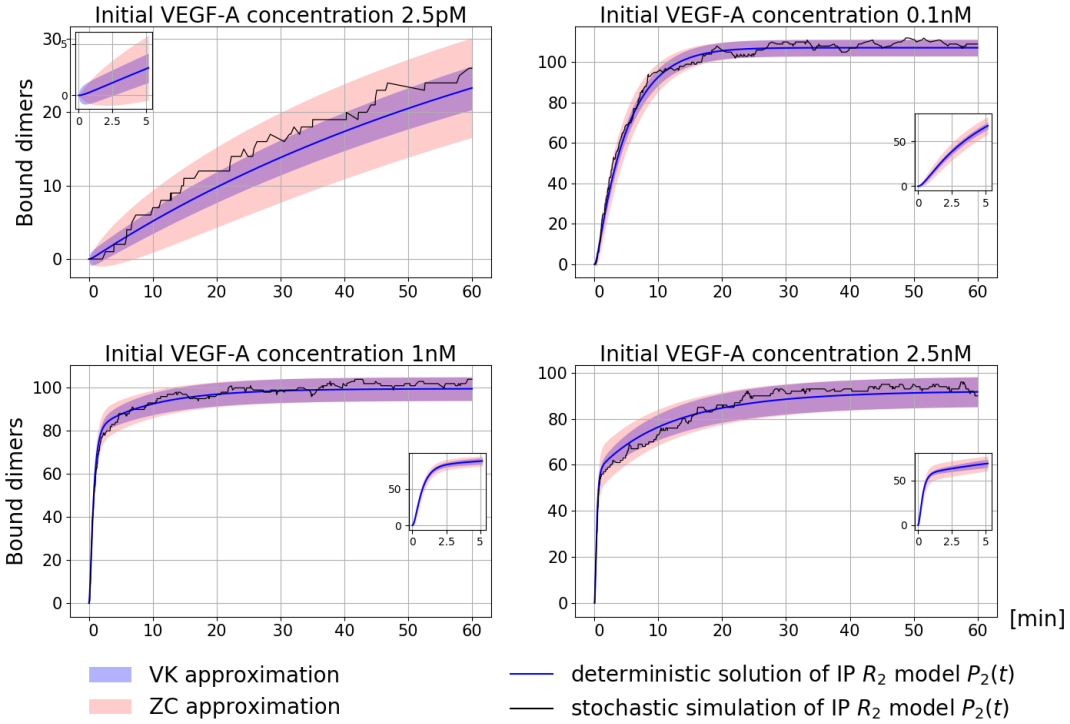

Figure 3.7: Comparison of moment closure techniques for the IP R_2 model for bound dimers P_2.

Immediate phosphorylation: IP R_2 and IP R_1/R_2 models

In order to analyse the dynamics of the stochastic process in the presence of VEGFR1 receptors, in Figure 3.8 the means of the random variables in the IP R_2 and the IP R_1/R_2 models as a function of time are plotted with shaded area showing two standard deviations. The time course has been generated with the van Kampen approximation, where the following VEGF-A ligand copy numbers are considered $n_L \in \{0.1n_{R_2},\ 0.25n_{R_2},\ 0.5n_{R_2},\ 10n_{R_2},\ 50n_{R_2},\ 100n_{R_2},\ 250n_{R_2},\ 625n_{R_2}, 1250n_{R_2}\}$, which approximately correspond to concentrations $c_L \in \{1pM,\ 2.5pM,\ 5pM,\ 0.1nM,\ 0.5nM,\ 1nM,\ 2.5nM,\ 6.25nM,\ 12.5nM\}$.

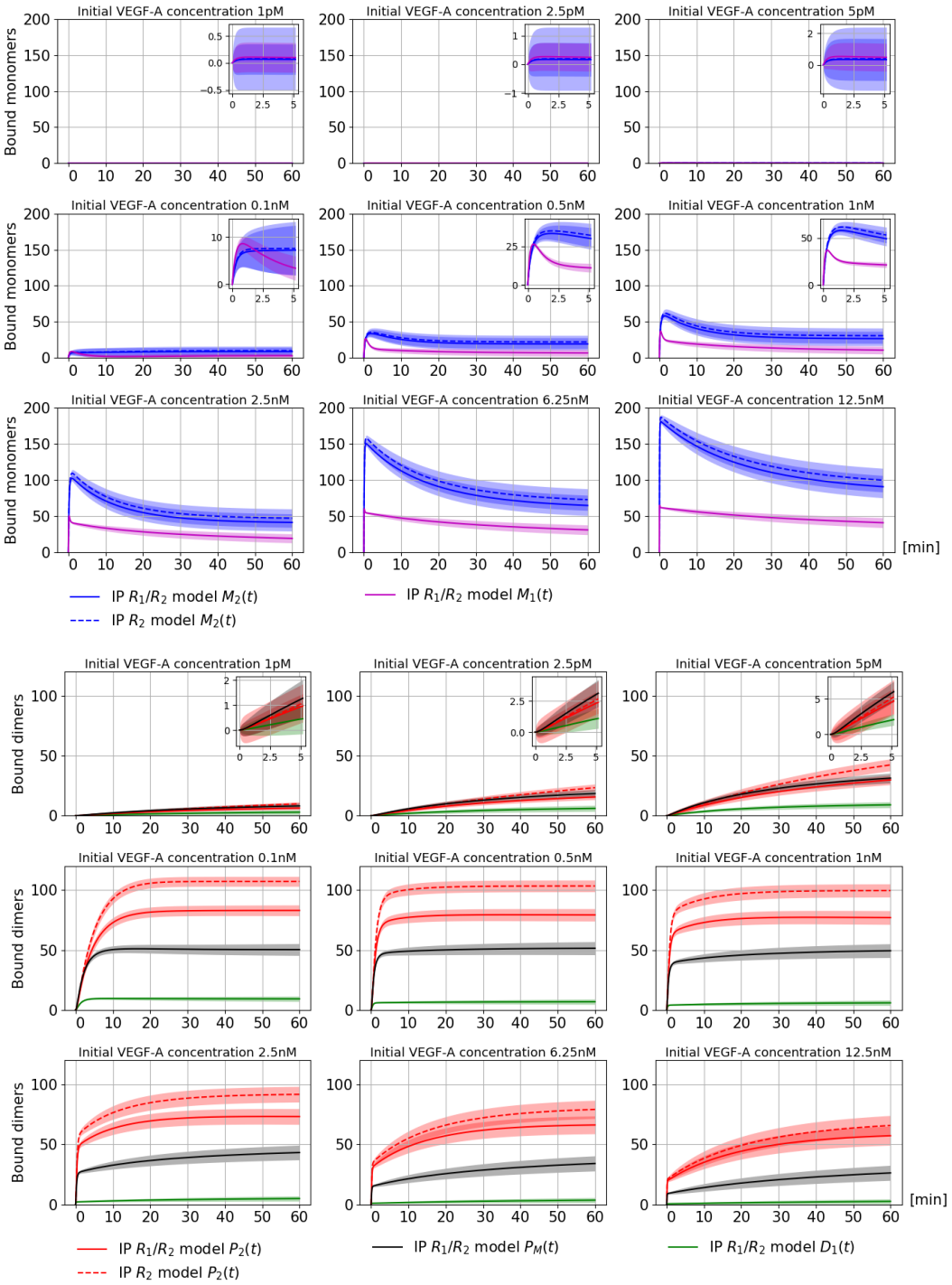

Figure 3.8: The van Kampen approximation of the IP R_2 and the IP R_1/R_2 models for different initial ligand concentrations $c_L \in \{1pM, 2.5pM, 5pM, 0.1nM, 0.5nM, 1nM, 2.5nM, 6.25nM, 12.5nM\}$. *Dashed* lines correspond to the IP R_2 model and *solid* lines correspond to the IP R_1/R_2 whereas the shaded areas show the mean $\pm$ two standard deviations. Time course showed on *top* for monomers and on *bottom* for dimers.

For low ligand concentrations the number of dimers grows as the VEGF-A concentration is increased. For these concentrations the steady state has not been reached in the first 60 *min* of the numerical simulation. However, higher concentrations result in saturated situations, where the difference between the number of P_2 complexes with and without considering VEGFR1 receptors becomes stable. In fact, this saturation results in lower numbers of P_2 complexes for ligand concentrations higher than $c_L \sim 2.5nM$. Thus, concentrations around $0.1nM - 2.5nM$ may be considered as the optimum ones. For ligand concentrations of order $c_L = \{6.25nM, 12.5nM\}$, the system exhibits a reduction in the number of dimers, which is caused by the rapid formation of monomeric bound complexes (see Figure 3.8). By analysing the formation of monomers as a function of time under optimal ligand concentrations a peak of monomeric complexes in the first 5 minutes can be observed. It is followed by a decrease of P_2 complexes. For high ligand concentrations, the steady state value for monomeric complexes increases, so that formation of dimers is effectively blocked.

Delayed phosphorylation: DP R_2 and DP R_1/R_2 models

In Figure 3.9, the Gillespie simulations are carried out to obtain the dynamics of the system in the DP R_2 and the DP R_1/R_2 models for different ligand concentrations, as before, $c_L \in \{1pM, 2.5pM, 5pM, 0.1nM, 0.5nM, 1nM, 2.5nM, 6.25nM, 12.5nM\}$. For high ligand concentrations, phosphorylation events occur within 10-20 minutes of ligand stimulation as observed by Alarcón & Page (2007), Ewan *et al.* (2006a) and Tan *et al.* (2013a). The number of non-active dimers (D_1, D_M, D_2) is, in general, lower than the number of active dimers P_M and P_2, in steady state. When enough ligand stimulation is given ($c_L \in \{0.1nM, 0.5nM, 1nM, 2.5nM, 6.25nM, 12.5nM\}$) the curves corresponding to dimers D_2 and D_M show a peak at early times, which is eventually lost once these complexes become phosphorylated, as can be seen in the sudden increase for P_2 and P_M complexes. Similar comments can be made regarding monomer formation (see Figure 3.9): a peak is seen during the first 5 minutes, slightly before the dimeric peak. This clearly indicates a *two-step* (monomer and non-phosphorylated dimer) formation

process, which is required for the subsequent creation of phosphorylated complexes on the cell surface. The optimum ligand concentration, c_L, for phosphorylated dimers in steady state is approximately given by the range $0.1nM - 2.5nM$. As depicted in Figure 3.8, for higher ligand concentrations monomeric complexes are more likely to be formed than either non-phosphorylated or phosphorylated dimeric complexes. In this case, the peak for non-phosphorylated dimers D_2 and D_M is reduced, which is explained by the larger numbers of monomeric bound complexes formed (see Figure 3.9). When focusing on the number of dimers at $t = 60\ min$, one can observe an approximately 20% decrease for the number of P_2 dimers in the DP R_2 model with respect to the IP R_2 model, for small ligand concentrations $c_L \in \{1pM, 2.5pM, 5pM\}$. As c_L grows, the difference between the number of P_2 dimers drops down to 16%. The final aspect to study is the influence of competition between VEGFR1 and VEGFR2 receptors for the ligand, VEGF-A, on the number of dimers. Theses results indicate that there is a 35% decrease in the number of P_2 complexes in the IP R_1/R_2 model with instantaneous phosphorylation for small ligand concentration, $c_L = 1pM$ with respect to the IP R_2 model.

As the ligand concentration increases, this difference drops down to 22%, so that the competition between VEGFR1 and VEGFR2 receptors is, again, reduced when enough ligand stimulation is given. In the model with delayed phosphorylation, there is a 15% decrease in the number of the dimers P_2 in the DP R_1/R_2 model compared to the DP R_2 model, for small ligand concentration, $c_L = 1pM$. As the concentration of ligand is increased, this difference also drops down to $1 - 2\%$.

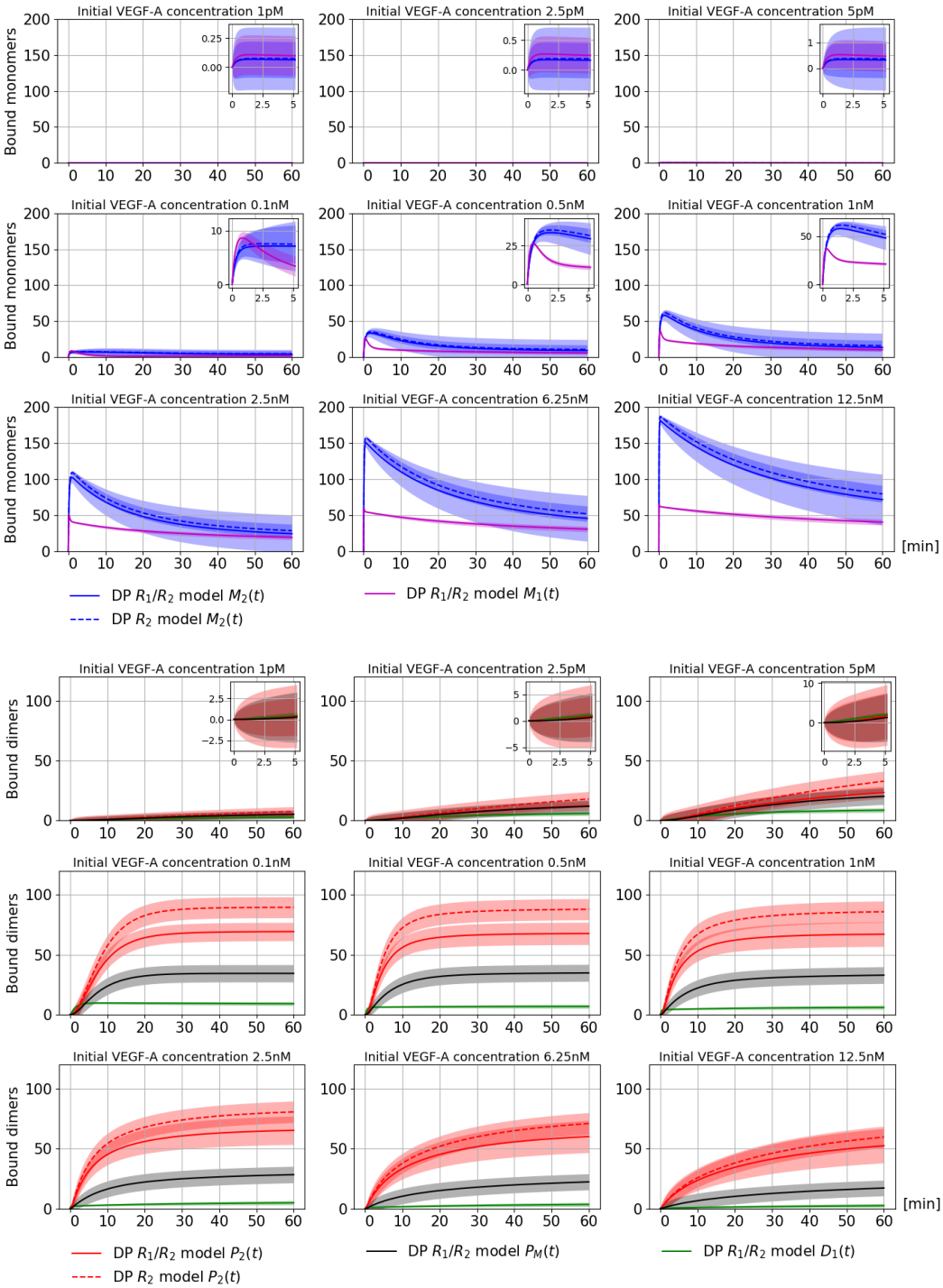

Figure 3.9: The van Kampen approximation of the DP R_2 and the DP R_1/R_2 models for different initial ligand concentrations $c_L \in \{1pM, 2.5pM, 5pM, 0.1nM, 0.5nM, 1nM, 2.5nM, 6.25nM, 12.5nM\}$. *Dashed* lines correspond to the DP R_2 model and *solid* lines correspond to the DP R_1/R_2 whereas the shaded areas show mean $\pm$ two standard deviations. Time course showed on *top* for monomers and on *bottom* for dimers.

3.3.4 Discussion

A particular assumption in the DP R_2 model and the DP R_1/R_2 model is that dissociation of phosphorylated dimers requires de-phosphorylation as a first step. An alternative model that allows for dissociation of phosphorylated dimers would need to include the following three reactions,

- $P_2 \rightarrow R_2 + M_2$,
- $P_M \rightarrow R_2 + M_1$,
- $P_M \rightarrow R_1 + M_2$.

Results for this alternative model are shown in Figure 3.10, where the most significant difference with respect to Figure 3.9 is the lower number of P_2 complexes after 20 minutes under optimal ligand concentrations (0.5nM - 1nM). This small effect, which is more prominent in the DP R_2 model than in the DP R_1/R_2 model, can be explained by the new de-phosphorylation pathway of P_2 complexes (by direct dissociation) that arises with the new reactions. However, no significant differences are identified (see Figure 3.9 and Figure 3.10), which suggests that the consideration of these additional reactions does not dramatically change the dynamics or the steady state of the system, with or without VEGFR1 receptors.

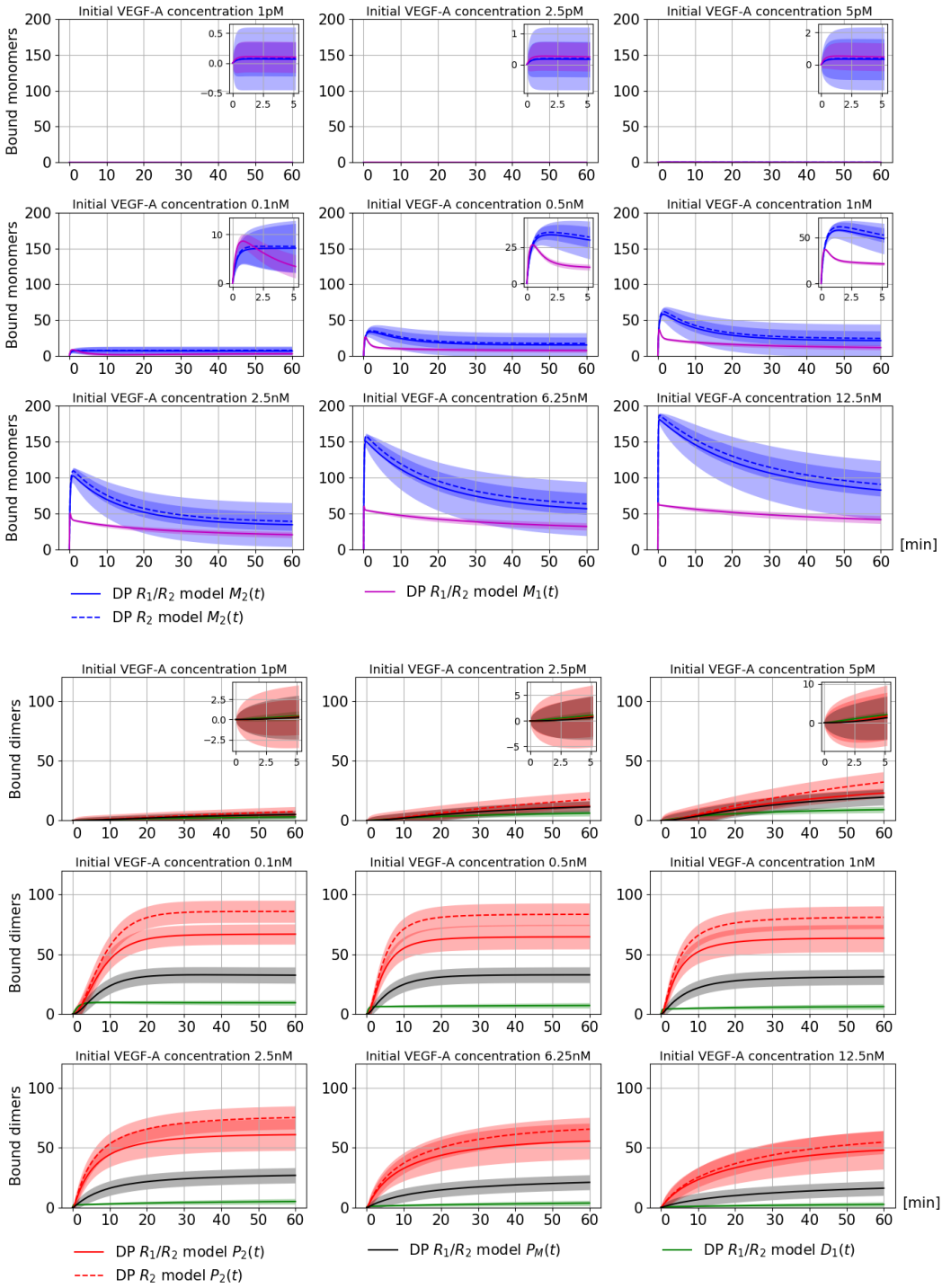

Figure 3.10: Generalisation of the DP R_2 and the DP R_1/R_2 models to include dissociation of phosphorylated dimers. This figure is analogous to Figure 3.9.

3.4 Quantifying the phosphorylation timescales

For the IP R_2 and the DP R_2 models, the aim in this section is to quantify the time to reach a given signalling threshold on the cell membrane. This signalling is directly identified in the models with the number of activated (either instantaneously or in a delayed fashion) complexes at any given time. Moreover, the steady-state distribution of the system is computed. Finally, a sensitivity analysis is developed for both models, in order to understand how the binding, dissociation, phosphorylation and de-phosphorylation rates affect the dynamics of the ligand/receptor system.

The study of the number of bound monomer, non-phosphorylated and phosphorylated bound dimer molecules on the cell surface over time can be viewed as the analysis of the transient behaviour of a specific Markov process, a problem which, in general, is not solvable in closed form Kulkarni (1996). Therefore, one typically carries out the Gillespie simulations (see Gillespie (1977)), or applies moment-closure techniques (see Gillespie (2009a), Hespanha (2008b)) to deal with the master equation of the Markov process under study. In this section alternative procedures are applied in order to analyse, in an exact way, the quantities of interest mentioned above. In particular, by representing the time to reach a signal threshold as a continuous random variable, and by conveniently structuring the space of states of the continuous time Markov processes under study, one can identify this time as the absorption time in an auxiliary absorbing continuous time Markov process. The Laplace-Stieltjes transform is computed for this random variable, as well as the steady-state probabilities of the process under study, by making use of first-step arguments and matrix-analytic arguments. Moreover, a novel local sensitivity analysis for the Markov processes under study is adapted and applied in Subsection 3.4.3, by generalising arguments given by Caswell (2011). This analysis allows one to identify how the stochastic descriptors considered in Subsection 3.4.1 and Subsection 3.4.2 (time to signalling formation and steady-state probabilities), are affected by the binding, dissociation, phosphorylation and de-phosphorylation rates.

3.4.1 IP R_2 model

Consider the IP R_2 model described by the process $\mathcal{X}_{\text{IP } R_2}$ defined on the state space $\mathcal{S}_{\text{IP } R_2}$ which was studied in Subsection 3.1.1. Note that given $(M_2(t), P_2(t)) = (n_1, n_2)$ at some time instant $t \geq 0$, then

- if $2n_L \leq n_{R_2}$: $n_1 + n_2 \leq n_L \Rightarrow n_1 + 2n_2 \leq n_{R_2}$, and
- if $n_{R_2} \leq n_L$: $n_1 + 2n_2 \leq n_{R_2} \Rightarrow n_1 + n_2 \leq n_L$,

so that three different specifications of the space of states $\mathcal{S}_{\text{IP } R_2}$ are obtained, depending on the particular values of n_{R_2} and n_L. In particular:

- if $2n_L \leq n_{R_2}$, then $\mathcal{S}_{\text{IP } R_2} = \{(n_1, n_2) \in (\mathbb{N} \cup \{0\})^2 : \ n_1 + n_2 \leq n_L\}$,
- if $n_{R_2} < 2n_L < 2n_{R_2}$, then $\mathcal{S}_{\text{IP } R_2} = \{(n_1, n_2) \in (\mathbb{N} \cup \{0\})^2 : \ n_1 + n_2 \leq n_L, \ n_1 + 2n_2 \leq n_{R_2}\}$, and
- if $n_{R_2} \leq n_L$, then $\mathcal{S}_{\text{IP } R_2} = \{(n_1, n_2) \in (\mathbb{N} \cup \{0\})^2 : \ n_1 + 2n_2 \leq n_{R_2}\}$.

Although one can deal with each of these cases in a similar manner, the focus here is on the case $2n_L \leq n_{R_2}$, since this is the case under physiological conditions for VEGFR2 (see Kut *et al.* (2007)), which is the receptor analysed in numerical results in Subsection 3.3.3. In this case, $\mathcal{X}_{\text{IP } R_2}$ is defined over $\mathcal{S}_{\text{IP } R_2} = \{(n_1, n_2) \in (\mathbb{N} \cup \{0\})^2 : \ n_1 + n_2 \leq n_L\}$. The objectives in this section amount to study two descriptors of interest:

1. Starting from any state $(n_1, n_2) \in \mathcal{S}_{\text{IP } R_2}$, the time to reach a number $N > n_2$ of P_2 complexes.
2. Starting from any state $(n_1, n_2) \in \mathcal{S}_{\text{IP } R_2}$, the stationary distribution of the process.

Descriptor 2 allows obtaining the theoretical state of the system at steady-state, thus enabling to analyse the long-term dynamics of the process. Descriptor 1 represents the time to reach some pre-defined threshold number of signalling complexes, or equivalently a pre-defined signal threshold for cell activation (see Alarcón & Page (2006), Starbuck *et al.* (1990)). One of the aims here is to analyse

how this time depends on the number of ligand and receptor molecules on the cell surface. Moreover, the sensitivity analysis carried out in Subsection 3.4.3 allows for analysing as well the impact that small perturbations for each kinetic rate in the system has on these descriptors of interest. The analysis carried out in this section is based on the use of levels for the organisation of the state space, Laplace-Stieltjes transforms, first-step arguments and auxiliary absorbing Markov processes (see Subsection 2.2.9). First organise the space of states $\mathcal{S}_{\text{IP } R_2}$, which contains

$$\#\mathcal{S}_{\text{IP } R_2} = \frac{(n_L+1)(n_L+2)}{2}$$

states, by levels (groups of states) as

$$\mathcal{S}_{\text{IP } R_2} = \bigcup_{k=0}^{n_L} L(k),$$

where $L(k) = \{(n_1, n_2) : n_2 = k\}$, $0 \leq k \leq n_L$, so that $J(k) = \#L(k) = n_L - k + 1$. That is, a level $L(k)$ comprises all the possible states (n_1, n_2) of the process with a total number of P_2 complexes equal to k. Moreover, these levels are ordered as

$$L(0) \prec L(1) \prec \cdots \prec L(n_L),$$

and states inside a level, $L(k) = \{(0,k), (1,k), \ldots, (n_L - k, k)\}$, $0 \leq k \leq n_L$, are ordered as

$$(0,k) \prec (1,k) \prec \cdots \prec (n_L - k, k).$$

It is clear that from a state (n_1, n_2) at level $L(n_2)$, the process can only move to states at the same level, $L(n_2)$, and to states at adjacent levels, $L(n_2 - 1)$ and $L(n_2+1)$. That is, if the state of the system is (n_1, n_2) (and then, the process is at level $L(n_2)$), the only possible transitions are to $(n_1 - 1, n_2)$ (if a bound monomer dissociates, in which case the process remains at level $L(n_2)$), to $(n_1 + 1, n_2)$ (if a bound monomer is formed, leaving the process at level $L(n_2)$), to $(n_1 + 1, n_2 - 1)$ (if a bound dimer dissociates, and the process then decreases to level $L(n_2 - 1)$), or to $(n_1 - 1, n_2 + 1)$ (if a bound dimer is created, increasing the level of the process to $L(n_2 + 1)$).

The organisation of $\mathcal{S}_{\text{IP }R_2}$, previously proposed, becomes crucial in order to obtain a convenient structure for the infinitesimal generator $\boldsymbol{Q}$ of $\mathcal{X}_{\text{IP }R_2}$, the matrix containing the transition rates in the Markov process. In particular, the resulting $\boldsymbol{Q}$ has the quasi-birth-and-death type (see Subsection 2.2.12) tridiagonal by blocks structure

$$\boldsymbol{Q} = \begin{pmatrix} \boldsymbol{A}_{0,0} & \boldsymbol{A}_{0,1} & \mathbf{0}_{J(0)\times J(2)} & \cdots & \mathbf{0}_{J(0)\times J(n_L-1)} & \mathbf{0}_{J(0)\times J(n_L)} \\ \boldsymbol{A}_{1,0} & \boldsymbol{A}_{1,1} & \boldsymbol{A}_{1,2} & \cdots & \mathbf{0}_{J(1)\times J(n_L-1)} & \mathbf{0}_{J(1)\times J(n_L)} \\ \mathbf{0}_{J(2)\times J(0)} & \boldsymbol{A}_{2,1} & \boldsymbol{A}_{2,2} & \cdots & \mathbf{0}_{J(2)\times J(n_L-1)} & \mathbf{0}_{J(2)\times J(n_L)} \\ \vdots & \vdots & \vdots & \ddots & \vdots & \vdots \\ \mathbf{0}_{J(n_L-1)\times J(0)} & \mathbf{0}_{J(n_L-1)\times J(1)} & \mathbf{0}_{J(n_L-1)\times J(2)} & \cdots & \boldsymbol{A}_{n_L-1,n_L-1} & \boldsymbol{A}_{n_L-1,n_L} \\ \mathbf{0}_{J(n_L)\times J(0)} & \mathbf{0}_{J(n_L)\times J(1)} & \mathbf{0}_{J(n_L)\times J(2)} & \cdots & \boldsymbol{A}_{n_L,n_L-1} & \boldsymbol{A}_{n_L,n_L} \end{pmatrix}, \tag{3.28}$$

where sub-matrices $\boldsymbol{A}_{k,k'}$ contain the infinitesimal transition rates of the transitions from states at level $L(k)$ to states at level $L(k')$, with $k' \in \{k-1, k, k+1\}$. In particular, matrices $\boldsymbol{A}_{k,k'}$ in Equation (3.28) are obtained as follows:

- For $1 \leq k \leq n_L$,

$$(\boldsymbol{A}_{k,k-1})_{ij} = \begin{cases} 2\beta_- k, & \text{if } j = i+1, \\ 0, & \text{otherwise,} \end{cases}$$

  where $0 \leq i \leq n_L - k$, $0 \leq j \leq n_L - k + 1$.

- For $0 \leq k \leq n_L$,

$$(\boldsymbol{A}_{k,k})_{ij} = \begin{cases} 2\alpha_+(n_{R_2} - i - 2k)(n_L - i - k), & \text{if } j = i+1 \\ \alpha_- i, & \text{if } j = i-1 \\ -\left(2\alpha_+(n_{R_2} - i - 2k)(n_L - i - k)\right. & \\ \left. +\alpha_- i + 2\beta_- k + \beta_+ i(n_{R_2} - i - 2k)\right), & \text{if } j = i \\ 0, & \text{otherwise.} \end{cases}$$

  where $0 \leq i \leq n_L - k$, $0 \leq j \leq n_L - k$.

- For $0 \leq k \leq n_L - 1$,

$$(\boldsymbol{A}_{k,k+1})_{ij} = \begin{cases} \beta_+ i(n_{R_2} - i - 2k), & \text{if } j = i-1, \\ 0, & \text{otherwise,} \end{cases}$$

  where $0 \leq i \leq n_L - k$, $0 \leq j \leq n_L - k - 1$.

The time to obtain a number $N > 0$ of P_2 complexes is considered. In particular, given an initial state of the process (n_1, n_2), and a certain threshold $N > 0$, one can consider the random variable

$$\begin{aligned} T_{(n_1,n_2)}(N) &= \text{“Time to reach a number } N \text{ of } P_2 \text{ complexes in } \mathcal{X}_{IP\ R_2}, \\ &\quad \text{if the process starts at } (n_1, n_2) \in \mathcal{S}_{IP\ R_2}\text{.”} \\ &= \inf\{t \geq 0 : P_2(t) = N\}. \end{aligned}$$

Observe here that this time is 0 for $N \leq n_2$. In order to study this descriptor for $N > n_2$, one can use an auxiliary CTMP, $\mathcal{X}_{\text{IP } R_2}(N)$, which depends on the threshold value N. Define $\mathcal{X}_{\text{IP } R_2}(N)$ over $\mathcal{S}_{\text{IP } R_2}(N)$ with

$$\mathcal{S}_{\text{IP } R_2}(N) = \mathcal{C}(N) \cup \{\bar{N}\},$$

where $\mathcal{C}(N) = \cup_{k=0}^{N-1} L(k)$, and $\bar{N}$ is a macro-state obtained by lumping together all states in the set $\cup_{k=N}^{n_L} L(k)$. Regarding the transition rates of this auxiliary CTMP, the transitions of $\mathcal{X}_{\text{IP } R_2}$ between states in $\mathcal{C}(N)$ are retained, and $\bar{N}$ is considered as an absorbing macro-state, so that once $\mathcal{X}_{\text{IP } R_2}(N)$ enters $\bar{N}$, it does not leave this state. Transitions from states in level $L(N-1)$ to states in $L(N)$ of the original process $\mathcal{X}_{\text{IP } R_2}$, become transitions from states in level $L(N-1)$ to the macro-state $\bar{N}$ in $\mathcal{X}_{\text{IP } R_2}(N)$, where their infinitesimal transition rates are directly obtained from the original ones as follows:

$$q_{(n_1,n_2)\bar{N}} = \sum_{(n_1',n_2') \in L(N)} q_{(n_1,n_2)(n_1',n_2')}, \quad \forall (n_1, n_2) \in L(N-1).$$

Process $\mathcal{X}_{\text{IP } R_2}(N)$ can be seen as process $\mathcal{X}_{\text{IP } R_2}$ until N of P_2 complexes are formed. Then, $\mathcal{X}_{\text{IP } R_2}(N)$ ends since $\bar{N}$ is an absorbing state for this auxiliary process. With $\mathcal{X}_{\text{IP } R_2}(N)$ so defined, it is clear that the time taken to obtain a number N of P_2 complexes in the original process $\mathcal{X}_{\text{IP } R_2}$ is equal to the time until absorption at $\bar{N}$ in the absorbing process $\mathcal{X}_{\text{IP } R_2}(N)$, which is known to follow a continuous phase-type (PH) distribution, (see Subsection 2.2.10). Analysing the exact distribution of a continuous phase-type random variable is, in general, a difficult problem. In this case, it would imply obtaining the exponential matrix $\exp(\boldsymbol{T}(N)) = \sum_{n=0}^{+\infty} \frac{\boldsymbol{T}(N)^n}{n!}$,where $\boldsymbol{T}(N)$ is a specific sub-matrix of the infinitesimal generator of $\mathcal{X}_{\text{IP } R_2}(N)$. Here, the Laplace-Stieltjes transform of $T_{(n_1,n_2)}(N)$

is used instead, which completely determines its distribution, and which allows for obtaining any l-th order moment $E\left(T_{(n_1,n_2)}(N)^l\right)$. Moreover, the l-th order moment can be efficiently calculated by using the $(l-1)$-th order moment, proceeding recursively, with the computational effort devoted to obtaining inverses of square blocks $\boldsymbol{A}_{k,k}$, which have dimension $J(k) = n_L - k + 1$. Again, the proposed organisation of states is crucial for the construction of an efficient algorithm. By defining the Laplace-Stieltjes transform of $T_{(n_1,n_2)}(N)$ as

$$\phi^N_{(n_1,n_2)}(z) \;=\; E\left(e^{-zT_{(n_1,n_2)}(N)}\right), \quad \Re(z) \geq 0,$$

which uniquely determines the distribution of $T_{n_1,n_2}(N)$. The different l-th order moments of $T_{(n_1,n_2)}(N)$ are given by differentiation of the Laplace-Stieltjes transform,

$$E\left(T_{(n_1,n_2)}(N)^l\right) \;=\; (-1)^l \frac{d^l}{dz^l}\phi^N_{(n_1,n_2)}(z)\bigg|_{z=0}, \quad \forall l \geq 1.$$

In order to compute the Laplace-Stieltjes transform $\phi^N_{(n_1,n_2)}(z)$, one can make use of a first-step argument, as follows. If the process, $\mathcal{X}_{\text{IP } R_2}(N)$, is at a given time in state $\boldsymbol{n} = (n_1, n_2)$, then $\boldsymbol{n} \to \boldsymbol{n'}$ denotes the event of the next transition of the process being to state $\boldsymbol{n'} = (n'_1, n'_2)$. Then, from the theory of Markov processes, it is well known that

$$Prob\left(\boldsymbol{n} \to \boldsymbol{n'}\right) \;=\; \frac{q_{\boldsymbol{nn'}}}{\sum\limits_{\substack{\boldsymbol{n''} \neq \boldsymbol{n} \\ \boldsymbol{n''} \in \mathcal{S}_{\text{IP } R_2}(N)}} q_{\boldsymbol{nn''}}} .$$

hence, $\phi^N_{\boldsymbol{n}}(z)$ is equal to

$$\sum_{\substack{\boldsymbol{n'} \neq \boldsymbol{n} \\ \boldsymbol{n'} \in \mathcal{S}_{\text{IP } R_2}(N)}} E\left(e^{-z\, T_{\boldsymbol{n}(N)}} | \boldsymbol{n} \to \boldsymbol{n'}\right) Prob\left(\boldsymbol{n} \to \boldsymbol{n'}\right) ,$$

where

$$E\left(e^{-z\, T_{\boldsymbol{n}}(N)} | \boldsymbol{n} \to \boldsymbol{n'}\right) \;=\; E\left(e^{-z\, t_{\boldsymbol{nn'}}}\; e^{-z\, T_{\boldsymbol{n'}}(N)}\right) ,$$

for

$$t_{\boldsymbol{nn'}} \sim \exp(\kappa), \qquad \text{where } \kappa = \sum_{\substack{\boldsymbol{n'} \neq \boldsymbol{n} \\ \boldsymbol{n'} \in \mathcal{S}_{\text{IP } R_2}(N)}} q_{\boldsymbol{nn'}}.$$

$t_{\boldsymbol{n}\boldsymbol{n}'}$ is the time until the event (or transition) $\boldsymbol{n} \to \boldsymbol{n}'$ occurs, which is independent of $T_{\boldsymbol{n}'}(N)$. Finally, since $E\left(e^{-z\,X}\right) = a/(a+z)$ if $X \sim \exp(a)$, it can be concluded that

$$\begin{aligned}
\phi^N_{(n_1,n_2)}(z) &= (1-\delta_{n_1+n_2,n_L})\tfrac{2\alpha_+(n_{R_2}-n_1-2n_2)(n_L-n_1-n_2)}{z+A_{(n_1,n_2)}}\phi^N_{(n_1+1,n_2)}(z) \\
&+ (1-\delta_{n_1,0}) \times \tfrac{\alpha_- n_1}{z+A_{(n_1,n_2)}}\phi^N_{(n_1-1,n_2)}(z) \\
&+ (1-\delta_{n_1,0})\tfrac{\beta_+ n_1(n_{R_2}-n_1-2n_2)}{z+A_{(n_1,n_2)}}\left(\delta_{n_2,N-1} + (1-\delta_{n_2,N-1})\phi^N_{(n_1-1,n_2+1)}(z)\right) \\
&+ (1-\delta_{n_2,0})\tfrac{2\beta_- n_2}{z+A_{(n_1,n_2)}}\phi^N_{(n_1+1,n_2-1)}(z),
\end{aligned} \tag{3.29}$$

where from now on $A_{(n_1,n_2)} = 2\alpha_+(n_{R_2}-n_1-2n_2)(n_L-n_1-n_2) + \alpha_- n_1 + \beta_+ n_1(n_{R_2}-n_1-2n_2) + 2\beta_- n_2$. Equation (3.29) relates the Laplace-Stieltjes transforms corresponding to all the states of $\mathcal{S}_{\text{IP }R_2}(N)$, so that a system of linear equations is obtained. By organising the Laplace-Stieltjes transforms in vectors by levels as follows

$$\boldsymbol{g}^N(z) = (\boldsymbol{g}^N_0(z)^T, \boldsymbol{g}^N_1(z)^T, \boldsymbol{g}^N_2(z)^T, \ldots, \boldsymbol{g}^N_{N-1}(z)^T)^T,$$

with $\boldsymbol{g}^N_k(z) = (\phi^N_{(0,k)}(z), \phi^N_{(1,k)}(z), \phi^N_{(2,k)}(z), \ldots, \phi^N_{(n_L-k,k)}(z))^T$, for $0 \le k \le N-1$, then the system given in Equation (3.29) can be expressed in matrix form as

$$\boldsymbol{g}^N(z) = \boldsymbol{A}^N(z)\,\boldsymbol{g}^N(z) + \mathbf{a}^N(z), \tag{3.30}$$

with the matrix $\boldsymbol{A}^N(z)$ given by

$$\begin{pmatrix}
\boldsymbol{A}_{0,0}(z) & \boldsymbol{A}_{0,1}(z) & \mathbf{0}_{J(0)\times J(2)} & \cdots & \mathbf{0}_{J(0)\times J(N-2)} & \mathbf{0}_{J(0)\times J(N-1)} \\
\boldsymbol{A}_{1,0}(z) & \boldsymbol{A}_{1,1}(z) & \boldsymbol{A}_{1,2}(z) & \cdots & \mathbf{0}_{J(1)\times J(N-2)} & \mathbf{0}_{J(1)\times J(N-1)} \\
\mathbf{0}_{J(2)\times J(0)} & \boldsymbol{A}_{2,1}(z) & \boldsymbol{A}_{2,2}(z) & \cdots & \mathbf{0}_{J(2)\times J(N-2)} & \mathbf{0}_{J(2)\times J(N-1)} \\
\vdots & \vdots & \vdots & \ddots & \vdots & \vdots \\
\mathbf{0}_{J(N-2)\times J(0)} & \mathbf{0}_{J(N-2)\times J(1)} & \mathbf{0}_{J(N-2)\times J(2)} & \cdots & \boldsymbol{A}_{N-2,N-2}(z) & \boldsymbol{A}_{N-2,N-1}(z) \\
\mathbf{0}_{J(N-1)\times J(0)} & \mathbf{0}_{J(N-1)\times J(1)} & \mathbf{0}_{J(N-1)\times J(2)} & \cdots & \boldsymbol{A}_{N-1,N-2}(z) & \boldsymbol{A}_{N-1,N-1}(z)
\end{pmatrix},$$

and the vector $\boldsymbol{a}^N(z) = \left(\mathbf{0}^T_{J(0)}, \mathbf{0}^T_{J(1)}, \ldots, \mathbf{0}^T_{J(N-2)}, \boldsymbol{a}_{N-1}(z)^T\right)^T$. Sub-matrices $\boldsymbol{A}_{k,k'}(z)$ and sub-vector $\boldsymbol{a}_{N-1}(z)$ in Equation (3.30) are given by:

- $(\boldsymbol{a}_{N-1}(z))_i = \frac{\beta_+ i(n_{R_2}-i-2(N-1))}{z+A_{(i,N-1)}}$, for $0 \le i \le n_L - N + 1$.

- For $1 \leq k \leq n_L$,

$$\left(\boldsymbol{A}_{k,k-1}(z)\right)_{ij} = \begin{cases} \frac{2\beta_- k}{z+A_{(i,k)}}, & \text{if } j = i+1, \\ 0, & \text{otherwise,} \end{cases}$$

  where $0 \leq i \leq n_L - k$, $0 \leq j \leq n_L - k + 1$.

- For $0 \leq k \leq n_L$,

$$\left(\boldsymbol{A}_{k,k}(z)\right)_{ij} = \begin{cases} \frac{2\alpha_+(n_{R_2}-i-2k)(n_L-i-k)}{z+A_{(i,k)}}, & \text{if } j = i+1, \\ \frac{\alpha_- i}{z+A_{(i,k)}}, & \text{if } j = i-1, \\ 0, & \text{otherwise,} \end{cases}$$

  where $0 \leq i \leq n_L - k$, $0 \leq j \leq n_L - k$.

- For $0 \leq k \leq n_L - 1$,

$$\left(\boldsymbol{A}_{k,k+1}(z)\right)_{ij} = \begin{cases} \frac{\beta_+ i(n_{R_2}-i-2k)}{z+A_{(i,k)}}, & \text{if } j = i-1, \\ 0, & \text{otherwise,} \end{cases}$$

  where $0 \leq i \leq n_L - k$, $0 \leq j \leq n_L - k - 1$.

Exploiting the special block structure of $\boldsymbol{A}^N(z)$, allows for an efficient solution of Equation (3.30), in a recursive manner through a specialised block-Gaussian elimination process, leading to Algorithm 4 (Part 1). The calculation of the Laplace-Stieltjes transforms in Algorithm 4 (Part 1) has its own merit, since it determines the distribution of the random variable under consideration.

PART 1

$\boldsymbol{H}_0^N(z) = \boldsymbol{I}_{J(0)} - \boldsymbol{A}_{0,0}(z)$
for $k = 1, \ldots, N-1$ **do**
  $\boldsymbol{H}_k^N(z) = \boldsymbol{I}_{J(k)} - \boldsymbol{A}_{k,k}(z) - \boldsymbol{A}_{k,k-1}(z) \times \boldsymbol{H}_{k-1}^N(z)^{-1}\boldsymbol{A}_{k-1,k}(z)$
end
$\boldsymbol{g}_{N-1}^N(z) = \boldsymbol{H}_{N-1}^N(z)^{-1}\boldsymbol{a}_{N-1}(z)$
$\boldsymbol{m}_{N-1}^{N,(0)} = \boldsymbol{g}_{N-1}^N(0)$
for $k = N-2, \ldots, 1, 0$ **do**
  $\boldsymbol{g}_k^N(z) = \boldsymbol{H}_k^N(z)^{-1}\boldsymbol{A}_{k,k+1}(z)\boldsymbol{g}_{k+1}^N(z)$
  $\boldsymbol{m}_k^{N,(0)} = \boldsymbol{g}_k^N(0)$
end

PART 2

$\boldsymbol{m}_{N-1}^{N,(0)} = \boldsymbol{g}_{N-1}^N(0)$
for $k = N-2, \ldots, 1, 0$ **do**
  $\boldsymbol{m}_k^{N,(0)} = \boldsymbol{g}_k^N(0)$
end
for $p = 1, \ldots, l$ **do**
  $\boldsymbol{P}_0^{N,(p)} = \sum_{k=1}^{p} \binom{p}{k}(-1)^k \left(\boldsymbol{A}_{0,0}^{(k)}(0)\boldsymbol{m}_0^{N,(p-k)} + \boldsymbol{A}_{0,1}^{(k)}(0)\boldsymbol{m}_1^{N,(p-k)}\right)$
  for $j = 1, \ldots, N-1$ **do**
    $\boldsymbol{P}_j^{N,(p)} = \boldsymbol{A}_{j,j-1}(0)\boldsymbol{H}_{j-1}^N(0)^{-1}\boldsymbol{P}_{j-1}^{N,(p)}$
    $+ \sum_{k=1}^{p} \binom{p}{k}(-1)^k \left(\boldsymbol{A}_{j,j-1}^{(k)}(0)\boldsymbol{m}_{j-1}^{N,(p-k)} + \boldsymbol{A}_{j,j}^{(k)}(0)\boldsymbol{m}_j^{N,(p-k)}\right.$
    $\left. +(1-\delta_{j,N-1}) \times \boldsymbol{A}_{j,j+1}^{(k)}(0)\boldsymbol{m}_{j+1}^{N,(p-k)}\right)$
  end
  $\boldsymbol{m}_{N-1}^{N,(p)} = \boldsymbol{H}_{N-1}^N(0)^{-1}\left(\boldsymbol{P}_{N-1}^{N,(p)} + (-1)^p\boldsymbol{a}_{N-1}^{(p)}(0)\right)$
  for $j = N-2, \ldots, 1, 0$ **do**
    $\boldsymbol{m}_j^{N,(p)} = \boldsymbol{H}_j^N(0)^{-1}\left(\boldsymbol{P}_j^{N,(p)} + \boldsymbol{A}_{j,j+1}(0)\boldsymbol{m}_{j+1}^{N,(p)}\right)$
  end
end

Algorithm 4: to obtain the Laplace-Stieltjes transforms $\boldsymbol{g}^N(z)$ and the l-th order moments $\boldsymbol{m}^{N,(l)}$.

Moreover, the calculation of the distribution function of $T_{(n_1,n_2)}(N)$ by numerical inversion of the transform is possible, although computationally expensive, and is not developed here (see Abate & Whitt (1992)).

Once the Laplace-Stieltjes transforms are in hand, the different l-th order moments can be obtained by successive differentiation of the system given by Equation (3.30). In particular, one can write

$$\boldsymbol{m}^{N,(l)} = \sum_{p=0}^{l}(-1)^p\binom{l}{p}\left.\frac{d^p}{dz^p}\boldsymbol{A}^N(z)\right|_{z=0}\boldsymbol{m}^{N,(l-p)} + (-1)^l\left.\frac{d^l}{dz^l}\boldsymbol{a}^N(z)\right|_{z=0} \quad (3.31)$$

where $\boldsymbol{m}^{N,(l)}$ is the column vector containing the desired moments $E\left(T_{(n_1,n_2)}(N)^l\right)$, for $(n_1,n_2)\in\mathcal{C}(N)$. These moments are organised in sub-vectors by levels as

$$\boldsymbol{m}^{N,(l)} = (\boldsymbol{m}_0^{N,(l)T}, \boldsymbol{m}_1^{N,(l)T}, \boldsymbol{m}_2^{N,(l)T}, \ldots, \boldsymbol{m}_{N-1}^{N,(l)T})^T,$$

where for $0\leq k\leq N-1$

$$\boldsymbol{m}_k^{N,(l)} = \left(E\left(T_{(0,k)}(N)^l\right), E\left(T_{(1,k)}(N)^l\right), E\left(T_{(2,k)}(N)^l\right), \ldots, E\left(T_{(n_L-k,k)}(N)^l\right)\right)^T,$$

Note that the notation $\boldsymbol{m}^{N,(0)} = \boldsymbol{g}^N(0) = \boldsymbol{e}_{\#\mathcal{C}(N)}$ is implicit in Equation (3.31). That is, the moment of order $l=0$ is the Laplace-Stieltjes transform for $z=0$. Finally, the system given by Equation (3.31) is rewritten as follows:

$$\boldsymbol{m}^{N,(l)} = \boldsymbol{A}^N(0)\boldsymbol{m}^{N,(l)} + \sum_{p=1}^{l}\binom{l}{p}(-1)^p\boldsymbol{A}^{N,(p)}(0)\boldsymbol{m}^{N,(l-p)} + (-1)^l\boldsymbol{a}^{N,(l)}(0). \quad (3.32)$$

It is clear that the direct calculation of the inverse $(\boldsymbol{I}_{\#\mathcal{C}(N)} - \boldsymbol{A}^N(0))^{-1}$ involved in the solution of Equation (3.32) can be avoided by working by levels and solving Equation (3.32) in a similar way to Algorithm 4 (Part 1). By starting with the known moment of order $p=0$, one can proceed recursively by calculating $\boldsymbol{m}^{N,(p)}$ from $\boldsymbol{m}^{N,(p-1)}$, until the desired order $p=l$ is reached, leading to Algorithm 4 (Part 2). Matrix $\boldsymbol{A}^{N,(p)}(0)$ in Equation (3.32) is given by

$$\begin{pmatrix}
\boldsymbol{A}_{0,0}^{(p)}(0) & \boldsymbol{A}_{0,1}^{(p)}(0) & \boldsymbol{0}_{J(0)\times J(2)} & \cdots & \boldsymbol{0}_{J(0)\times J(N-2)} & \boldsymbol{0}_{J(0)\times J(N-1)} \\
\boldsymbol{A}_{1,0}^{(p)}(0) & \boldsymbol{A}_{1,1}^{(p)}(0) & \boldsymbol{A}_{1,2}^{(p)}(0) & \cdots & \boldsymbol{0}_{J(1)\times J(N-2)} & \boldsymbol{0}_{J(1)\times J(N-1)} \\
\boldsymbol{0}_{J(2)\times J(0)} & \boldsymbol{A}_{2,1}^{(p)}(0) & \boldsymbol{A}_{2,2}^{(p)}(0) & \cdots & \boldsymbol{0}_{J(2)\times J(N-2)} & \boldsymbol{0}_{J(2)\times J(N-1)} \\
\vdots & \vdots & \vdots & \ddots & \vdots & \vdots \\
\boldsymbol{0}_{J(N-2)\times J(0)} & \boldsymbol{0}_{J(N-2)\times J(1)} & \boldsymbol{0}_{J(N-2)\times J(2)} & \cdots & \boldsymbol{A}_{N-2,N-2}^{(p)}(0) & \boldsymbol{A}_{N-2,N-1}^{(p)}(0) \\
\boldsymbol{0}_{J(N-1)\times J(0)} & \boldsymbol{0}_{J(N-1)\times J(1)} & \boldsymbol{0}_{J(N-1)\times J(2)} & \cdots & \boldsymbol{A}_{N-1,N-2}^{(p)}(0) & \boldsymbol{A}_{N-1,N-1}^{(p)}(0)
\end{pmatrix}$$

and matrix $\boldsymbol{a}^{N,(p)}(0)$ is given by,

$$\boldsymbol{a}^{N,(p)}(0) \;=\; \begin{pmatrix} \mathbf{0}_{J(0)} \\ \mathbf{0}_{J(1)} \\ \vdots \\ \mathbf{0}_{J(N-2)} \\ \boldsymbol{a}^{(p)}_{N-1}(0) \end{pmatrix},$$

where expressions for $\boldsymbol{a}^{(p)}_{N-1}(0)$ and $\boldsymbol{A}^{(p)}_{k,k'}(0)$, for $p \geq 1$, are as follows:

- $\left(\boldsymbol{a}^{(p)}_{N-1}(0)\right)_i \;=\; (-1)^p p! \frac{\beta_+ i(n_{R_2}-i-2(N-1))}{A^{p+1}_{(i,N-1)}}$, for $0 \leq i \leq n_L - N + 1$.
- For $1 \leq k \leq n_L$, $p \geq 1$,

$$\left(\boldsymbol{A}^{(p)}_{k,k-1}(0)\right)_{ij} \;=\; \begin{cases} (-1)^p p! \frac{2\beta_- k}{A^{p+1}_{(i,k)}}, & \text{if } j = i+1, \\ 0, & \text{otherwise,} \end{cases}$$

  where $0 \leq i \leq n_L - k$, $0 \leq j \leq n_L - k + 1$.

- For $0 \leq k \leq n_L$, $p \geq 1$,

$$\left(\boldsymbol{A}^{(p)}_{k,k}(0)\right)_{ij} \;=\; \begin{cases} (-1)^p p! \frac{2\alpha_+(n_{R_2}-i-2k)(n_L-i-k)}{A^{p+1}_{(i,k)}}, & \text{if } j = i+1, \\ (-1)^p p! \frac{\alpha_- i}{A^{p+1}_{(i,k)}}, & \text{if } j = i-1, \\ 0, & \text{otherwise,} \end{cases}$$

  where $0 \leq i \leq n_L - k$, $0 \leq j \leq n_L - k$.

- For $0 \leq k \leq n_L - 1$, $p \geq 1$,

$$\left(\boldsymbol{A}^{(p)}_{k,k+1}(0)\right)_{ij} \;=\; \begin{cases} (-1)^p p! \frac{\beta_+ i(n_{R_2}-i-2k)}{A^{p+1}_{(i,k)}}, & \text{if } j = i-1, \\ 0, & \text{otherwise,} \end{cases}$$

  where $0 \leq i \leq n_L - k$, $0 \leq j \leq n_L - k - 1$.

Finally, the long term behaviour of the process is given by the stationary distribution of the CTMP; that is, by probabilities

$$\pi_{(n_1,n_2)} \;=\; \lim_{t \to +\infty} Prob((M(t), P(t)) = (n_1, n_2)), \quad \forall (n_1, n_2) \in \mathcal{S}_{\text{IP } R_2},$$

which do not depend on the initial state. This distribution can be stored in a row vector $\boldsymbol{\pi} = (\boldsymbol{\pi}_0, \boldsymbol{\pi}_2, \ldots, \boldsymbol{\pi}_{n_L})$, where the row sub-vector $\boldsymbol{\pi}_k$ contains the ordered probabilities $\pi_{(n_1,n_2)}$ for states at level $L(k)$. Solving the system

$$\boldsymbol{\pi}\boldsymbol{Q} = \mathbf{0}^T_{\#\mathcal{S}_{\text{IP } R_2}} \quad \text{and} \quad \boldsymbol{\pi}\boldsymbol{e}_{\#\mathcal{S}_{\text{IP } R_2}} = 1,$$

where $\boldsymbol{e}_{\#\mathcal{S}_{\text{IP } R_2}}$ represents vector of ones with length equal to number of elements in $\mathcal{S}_{\text{IP } R_2}$, and adapting the arguments presented by Latouche & Ramaswami (1999) in Chapter 10, one can obtain Algorithm 5. With $\boldsymbol{\pi}$ in hand, the long term mean number of M_2 and P_2 complexes can be obtained as

$$\pi_M = \text{“Mean number of } M_2 \text{ complexes in steady-state”} = \sum_{k=0}^{n_L} k \left(\sum_{j=0}^{n_L} (\boldsymbol{\pi}_j)_k \right),$$

$$\pi_P = \text{“Mean number of } P_2 \text{ complexes in steady-state”} = \sum_{k=0}^{n_L} k \left(\boldsymbol{\pi}_k \boldsymbol{e}_{J(k)} \right).$$

$\boldsymbol{H}_0 = \boldsymbol{A}_{0,0}$
for $k = 1, \ldots, n_L - 1$ **do**
  $\boldsymbol{H}_k = \boldsymbol{A}_{k,k} - \boldsymbol{A}_{k,k-1}\boldsymbol{H}_{k-1}^{-1}\boldsymbol{A}_{k-1,k}$
end
$\boldsymbol{\pi}^*_{n_L} = 1$
for $k = n_L - 1, \ldots, 0$ **do**
  $\boldsymbol{\pi}^*_k = -\boldsymbol{\pi}^*_{k+1}\boldsymbol{A}_{k+1,k}\boldsymbol{H}_k^{-1}$
end
for $k = 0, \ldots, n_L$ **do**
  $\boldsymbol{\pi}_k = \frac{1}{\sum_{j=0}^{n_L} \boldsymbol{\pi}^*_j \boldsymbol{e}_{J(r)}} \boldsymbol{\pi}^*_k$
end

Algorithm 5: to obtain the stationary distribution $\boldsymbol{\pi}$.

3.4.2 DP R_2 model

In the previous subsection the IP R_2, which assumes P_2 complexes were instantaneously phosphorylated, was studied. Here the DP R_2 model described by the process $\mathcal{X}_{\text{DP } R_2}$ defined on the state space $\mathcal{S}_{\text{DP } R_2}$, assuming two-step process for P_2 phosphorylation, presented in Subsection 3.1.2 is considered. In what follows, the arguments of the previous subsection are adopted to this model. This allows

evaluating the relevance of considering phosphorylation as an independent reaction, and serving as an example of how to include new reactions in this type of models, while adapting the matrix-analytic arguments. Assuming as previously that $2n_L \leq n_{R_2}$, it is straightforward to show that for all $t \geq 0$

$$M_2(t) + D_2(t) + P_2(t) \leq n_L, \qquad \Rightarrow \quad M_2(t) + 2D_2(t) + 2P_2(t) \leq n_{R_2},$$

so that the space of state of the process $\mathcal{X}_{\text{DP } R_2}$ becomes simply $\mathcal{S}_{\text{DP } R_2} = \{(n_1, n_2, n_3\} \in (\mathbb{N} \cup \{0\})^3 : \ n_1 + n_2 + n_3 \leq n_L\}$. The following descriptors, analogous to those of the previous section, are studied:

1. Starting from any state $(n_1, n_2, n_3) \in \mathcal{S}_{\text{DP } R_2}$, the time to reach a number $N > n_3$ of P complexes.

2. Starting from any state $(n_1, n_2, n_3) \in \mathcal{S}_{\text{DP } R_2}$, the stationary distribution of the system.

To study these descriptors, the level structure for the state space is used again, that is, $\mathcal{S}_{\text{DP } R_2}$ is split in levels as follows:

$$\mathcal{S}_{\text{DP } R_2} \quad = \quad \bigcup_{k=0}^{n_L} \hat{L}(k),$$

where $\hat{L}(k) = \{(n_1, n_2, n_3) \in \mathcal{S}_{\text{DP } R_2} : \ n_3 = k\}$, for $0 \leq k \leq n_L$, so that

$$\hat{J}(k) \quad = \quad \#\hat{L}(k) \quad = \quad \frac{(n_L - k + 1)(n_L - k + 2)}{2}.$$

The three-dimensionality of the process implies that each level $\hat{L}(k)$ may be split into different sub-levels, as follows:

$$\hat{L}(k) \quad = \quad \bigcup_{r=0}^{n_L - k} l(k; r),$$

with $l(k; r) = \{(n_1, n_2, n_3) \in \mathcal{S}_{\text{DP } R_2} : \ n_2 = r, \ n_3 = k\}$, for $0 \leq r \leq n_L - k$, $0 \leq k \leq n_L$, and $J(k; r) = \#l(k; r) = n_L - r - k + 1$. That is,

$$l(k; r) \quad = \quad \{(0, r, k), (1, r, k), \ldots, (n_L - r - k, r, k)\},$$

where $0 \leq r \leq n_L - k,\ 0 \leq k \leq n_L$ and states in $l(k;r)$ are ordered as indicated above. The given order of states and the organisation by levels and sub-levels, thus, yield an infinitesimal generator similar to Equation (3.28), where quantities $J(k)$ and matrices $\boldsymbol{A}_{k,k'}$ are replaced by $\hat{J}(k)$ and $\hat{\boldsymbol{A}}_{k,k'}$, respectively. A matrix $\hat{\boldsymbol{A}}_{k,k'}$ contains the ordered infinitesimal transition rates corresponding to transitions from states at level $\hat{L}(k)$ to states at level $\hat{L}(k')$. Each matrix $\hat{\boldsymbol{A}}_{k,k'}$ is formed by sub-blocks $\boldsymbol{B}^{k,k'}_{r,r'}$ which contain the infinitesimal transition rates corresponding to transitions from states at sub-level $l(k;r) \subset \hat{L}(k)$ to states at sub-level $l(k';r') \subset \hat{L}(k')$. It can be observed that the dimension of the matrix $\hat{\boldsymbol{A}}_{k,k'}$ is $\hat{J}(k) \times \hat{J}(k') = \frac{(n_L-k+1)(n_L-k+2)}{2} \times \frac{(n_L-k'+1)(n_L-k'+2)}{2}$, while the dimension of the sub-block $\boldsymbol{B}^{k,k'}_{r,r'}$ inside $\hat{\boldsymbol{A}}_{k,k'}$ is $J(k;r)\times J(k';r') = (n_L-r-k+1)\times(n_L-r'-k'+1)$. Expressions for these matrices are as follows:

- For $0 \leq k \leq n_L$

$$\hat{\boldsymbol{A}}_{k,k} = \begin{pmatrix} \boldsymbol{B}^{k,k}_{0,0} & \boldsymbol{B}^{k,k}_{0,1} & \mathbf{0} & \dots & \mathbf{0} & \mathbf{0} \\ \boldsymbol{B}^{k,k}_{1,0} & \boldsymbol{B}^{k,k}_{1,1} & \boldsymbol{B}^{k,k}_{1,2} & \dots & \mathbf{0} & \mathbf{0} \\ \mathbf{0} & \boldsymbol{B}^{k,k}_{2,1} & \boldsymbol{B}^{k,k}_{2,2} & \dots & \mathbf{0} & \mathbf{0} \\ \vdots & \vdots & \vdots & \ddots & \vdots & \vdots \\ \mathbf{0} & \mathbf{0} & \mathbf{0} & \dots & \boldsymbol{B}^{k,k}_{n_L-k-1,n_L-k-1} & \boldsymbol{B}^{k,k}_{n_L-k-1,n_L-k} \\ \mathbf{0} & \mathbf{0} & \mathbf{0} & \dots & \boldsymbol{B}^{k,k}_{n_L-k,n_L-k-1} & \boldsymbol{B}^{k,k}_{n_L-k,n_L-k} \end{pmatrix},$$

- For $0 \leq k \leq n_L - 1$,

$$\hat{\boldsymbol{A}}_{k,k+1} = \begin{pmatrix} \mathbf{0} & \mathbf{0} & \mathbf{0} & \dots & \mathbf{0} & \mathbf{0} \\ \boldsymbol{B}^{k,k+1}_{1,0} & \mathbf{0} & \mathbf{0} & \dots & \mathbf{0} & \mathbf{0} \\ \mathbf{0} & \boldsymbol{B}^{k,k+1}_{2,1} & \mathbf{0} & \dots & \mathbf{0} & \mathbf{0} \\ \vdots & \vdots & \vdots & \ddots & \vdots & \vdots \\ \mathbf{0} & \mathbf{0} & \mathbf{0} & \dots & \mathbf{0} & \mathbf{0} \\ \mathbf{0} & \mathbf{0} & \mathbf{0} & \dots & \boldsymbol{B}^{k,k+1}_{n_L-k,n_L-k-1} & \mathbf{0} \end{pmatrix},$$

- For $1 \leq k \leq n_L$,

$$\hat{\boldsymbol{A}}_{k,k-1} = \begin{pmatrix} \mathbf{0} & \boldsymbol{B}^{k,k-1}_{0,1} & \mathbf{0} & \dots & \mathbf{0} & \mathbf{0} \\ \mathbf{0} & \mathbf{0} & \boldsymbol{B}^{k,k-1}_{1,2} & \dots & \mathbf{0} & \mathbf{0} \\ \mathbf{0} & \mathbf{0} & \mathbf{0} & \dots & \mathbf{0} & \mathbf{0} \\ \vdots & \vdots & \vdots & \ddots & \vdots & \vdots \\ \mathbf{0} & \mathbf{0} & \mathbf{0} & \dots & \boldsymbol{B}^{k,k-1}_{n_L-k-1,n_L-k} & \mathbf{0} \\ \mathbf{0} & \mathbf{0} & \mathbf{0} & \dots & \mathbf{0} & \boldsymbol{B}^{k,k-1}_{n_L-k,n_L-k+1} \end{pmatrix}.$$

Note that, although dimensions of matrices $\mathbf{0}$ are omitted for the ease of notation, the dimension of each matrix $\mathbf{0}$, representing transitions from states at sub-level $l(k;r)$ to states at sub-level $l(k';r')$, is $J(k;r) \times J(k';r')$. The expressions for the matrices $\boldsymbol{B}_{r,r'}^{k,k'}$ are given as follows:

- For $0 \leq r \leq n_L - k$, $0 \leq k \leq n_L$,

$$\left(\boldsymbol{B}_{r,r}^{k,k}\right)_{ij} = \begin{cases} \alpha_- i, & \text{if } j = i-1, \\ -A_{(i,r,k)}, & \text{if } j = i, \\ 2\alpha_+(n_{R_2} - i - 2r - 2k)(n_L - i - r - k), & \text{if } j = i+1, \\ 0, & \text{otherwise,} \end{cases}$$

  where $0 \leq i \leq n_L - r - k$, $0 \leq j \leq n_L - r - k$, and, from now on, $A_{(i,r,k)} = 2\alpha_+(n_{R_2} - i - 2r - 2k)(n_L - i - r - k) + \alpha_- i + \beta_+ i(n_{R_2} - i - 2r - 2k) + 2\beta_- r + \gamma_+ r + \gamma_- k$.

- For $0 \leq r \leq n_L - k - 1$, $0 \leq k \leq n_L$,

$$\left(\mathbf{B}_{r,r+1}^{k,k}\right)_{ij} = \begin{cases} \beta_+ i(n_{R_2} - i - 2r - 2k), & \text{if } j = i-1, \\ 0, & \text{otherwise,} \end{cases}$$

  where $0 \leq i \leq n_L - r - k$, $0 \leq j \leq n_L - r - k - 1$.

- For $1 \leq r \leq n_L - k$, $0 \leq k \leq n_L$,

$$\left(\boldsymbol{B}_{r,r-1}^{k,k}\right)_{ij} = \begin{cases} 2\beta_- r, & \text{if } j = i+1, \\ 0, & \text{otherwise,} \end{cases}$$

  where $0 \leq i \leq n_L - r - k$, $0 \leq j \leq n_L - r - k + 1$.

- For $1 \leq r \leq n_L - k$, $0 \leq k \leq n_L - 1$,

$$\left(\boldsymbol{B}_{r,r-1}^{k,k+1}\right)_{ij} = \begin{cases} \gamma_+ r, & \text{if } j = i, \\ 0, & \text{otherwise,} \end{cases}$$

  where $0 \leq i \leq n_L - r - k$, $0 \leq j \leq n_L - r - k$.

- For $0 \leq r \leq n_L - k$, $1 \leq k \leq n_L$,

$$\left(\boldsymbol{B}_{r,r+1}^{k,k-1}\right)_{ij} = \begin{cases} \gamma_- k, & \text{if } j = i, \\ 0, & \text{otherwise,} \end{cases}$$

  where $0 \leq i \leq n_L - r - k$, $0 \leq j \leq n_L - r - k$.

For an initial state $(n_1, n_2, n_3) \in \mathcal{S}_{\text{DP } R_2}$ and a number $N > 0$, the following random variable is studied,

$$\begin{aligned} T_{(n_1,n_2,n_3)}(N) &= \text{“Time to reach a number } N \text{ of } P_2 \text{ complexes in } \mathcal{X}_{DP\ R_2}, \\ &\quad \text{if the process starts at } (n_1, n_2, n_3) \in \mathcal{S}_{DP\ R_2}.\text{”} \\ &= \inf\{t \geq 0 : P_2(t) = N\}. \end{aligned}$$

N is omitted in the notation for convenience. Again, this time is 0 for $N \leq n_3$. For $N > n_3$, an argument similar to that of Subsection 3.4.1 is used, so that the analysis of an auxiliary absorbing CTMP requires the study of $T_{(n_1,n_2,n_3)}$ as an absorption time in the auxiliary process.

In order to obtain the different l-th order moments in an efficient way, define the Laplace-Stieltjes transform of $T_{(n_1,n_2,n_3)}$ as

$$\xi_{(n_1,n_2,n_3)}(z) = E\left(e^{-zT_{(n_1,n_2,n_3)}}\right), \quad \Re(z) \geq 0,$$

and the different l-th order moments of $T_{(n_1,n_2,n_3)}$ can be obtained as

$$E\left(T^l_{(n_1,n_2,n_3)}\right) = (-1)^l \frac{d^l}{dz^l} \xi_{(n_1,n_2,n_3)}(z)\Big|_{z=0}, \quad \forall l \geq 1.$$

By a first-step argument, the following system is obtained,

$$\hat{\boldsymbol{g}}(z) = \hat{\boldsymbol{A}}(z)\, \hat{\boldsymbol{g}}(z) + \hat{\boldsymbol{a}}(z), \tag{3.33}$$

where the Laplace-Stieltjes transforms are stored in vectors $\hat{\boldsymbol{g}}(z)$, following the order given by levels and sub-levels, and where the expressions for matrices $\hat{\boldsymbol{A}}(z)$ and $\hat{\boldsymbol{a}}(z)$ are omitted for brevity. By successive differentiation of the system in Equation (3.33), the different l-th order moments $E\left(T^l_{(n_1,n_2,n_3)}\right)$ are obtained through an adapted version of Algorithm 4, with the l-th order moments stored in the vectors $\hat{\boldsymbol{m}}^{(l)}$. Note that in the adapted version of Algorithm 4 to solve Equation (3.33), which is omitted, one needs to deal with inverses of matrices with dimension $\hat{J}(k) = \#\hat{L}(k)$. The complexity of transitions between states does not seem to allow to gain further efficiency in the algorithms by working with inverses of matrices with the dimensions of the given sub-levels. However, in the special case $\gamma_- = 0$, that is, when de-phosphorylation is neglected, it is possible

to improve the procedures so that the highest computational effort is placed on inverting matrices with the dimensions of sub-levels instead of levels, which would yield to an alternative algorithm, which is not described here. Finally, the focus here is on the stationary distribution of the process, that is, probabilities

$$\hat{\pi}_{(n_1,n_2,n_3)} = \lim_{t\to+\infty} Prob((M_2(t), D_2(t), P_2(t)) = (n_1, n_2, n_3)),$$

which do not depend on the initial state of the system for all $(n_1, n_2, n_3) \in \mathcal{S}_{\text{DP } R_2}$. Similar arguments to those considered in Subsection 3.4.1 which allow obtaining the stationary distribution in a row vector $\hat{\boldsymbol{\pi}} = (\hat{\boldsymbol{\pi}}_0, \hat{\boldsymbol{\pi}}_2, \ldots, \hat{\boldsymbol{\pi}}_{n_L})$, where $\hat{\boldsymbol{\pi}}_k = \left(\hat{\boldsymbol{\pi}}_0^k, \hat{\boldsymbol{\pi}}_2^k, \ldots, \hat{\boldsymbol{\pi}}_{n_L-k}^k\right)$, and where row sub-vectors $\hat{\boldsymbol{\pi}}_r^k$ contain, in an ordered manner, steady-state probabilities of states at sub-levels $l(k;r)$. An adapted version of Algorithm 5 can be obtained, where the matrices $\boldsymbol{A}_{j,j'}$, in Equation (3.29), would be now replaced by the matrices $\hat{\boldsymbol{A}}_{k,k'}$ previously defined. Once these vectors are in hand, it is clear that

$$\begin{aligned}
\hat{\pi}_M &= \text{“Mean number of } M_2 \text{ complexes in steady-state”} \\
&= \sum_{i=0}^{n_L} i \left(\sum_{k=0}^{n_L-i} \sum_{r=0}^{n_L-i-k} (\hat{\boldsymbol{\pi}}_r^k)_i \right), \\
\hat{\pi}_D &= \text{“Mean number of } D_2 \text{ complexes in steady-state”} \\
&= \sum_{r=0}^{n_L} r \left(\sum_{k=0}^{n_L-r} \sum_{i=0}^{n_L-r-k} (\hat{\boldsymbol{\pi}}_r^k)_i \right), \\
\hat{\pi}_P &= \text{“Mean number of } P_2 \text{ complexes in steady-state”} \\
&= \sum_{k=0}^{n_L} k \left(\sum_{r=0}^{n_L-k} \sum_{i=0}^{n_L-r-k} (\hat{\boldsymbol{\pi}}_r^k)_i \right).
\end{aligned}$$

3.4.3 Local sensitivity analysis

The objective of this section is to develop a local sensitivity analysis to understand the effect that each of the (binding, dissociation, phosphorylation or de-phosphorylation) rates ($\alpha_+, \alpha_-, \beta_+, \beta_-, \gamma_+$ and γ_-) has on the stochastic descriptors introduced in Subsections 3.4.1 and 3.4.2, in a given neighbourhood of parameter space. This selected neighbourhood of parameter space may be obtained from a parameter estimation of in vitro and in silico experiments, as

shown in Subsection 3.3.3. The aim then is to obtain the partial derivatives of the descriptors with respect to each parameter, so that these derivatives provide a measure of the effect of a perturbation of the parameters on the descriptors.

Sensitivity analysis for CTMP with absorbing states has been recently developed by Caswell (2011). Although Markov processes considered in this paper are, in general, non-absorbing, arguments presented by Caswell (2011) can be clearly generalised for the CTMPs considered here. For that aim, consider a given matrix $\boldsymbol{A}_{m\times n}(\boldsymbol{\theta})$, that depends on $\boldsymbol{\theta} = (\alpha_+, \alpha_-, \beta_+, \beta_-, \gamma_+, \gamma_-)$, the parameter's vector, and its element-by-element derivative with respect to $\theta_i \in \{\alpha_+, \alpha_-, \beta_+, \beta_-, \gamma_+, \gamma_-\}$, $\boldsymbol{A}^{(\theta_i)}(\boldsymbol{\theta})$. It is then possible to calculate the derivative of $\boldsymbol{A}^{-1}(\boldsymbol{\theta})$ with respect to θ_i from $\boldsymbol{A}^{(\theta_i)}(\boldsymbol{\theta})$ as (see Magnus & Neudecker (1985); Neudecker & Magnus (1988))

$$(\boldsymbol{A}^{-1})^{(\theta_i)}(\boldsymbol{\theta}) \;=\; -\boldsymbol{A}^{-1}(\boldsymbol{\theta})\boldsymbol{A}^{(\theta_i)}(\boldsymbol{\theta})\boldsymbol{A}^{-1}(\boldsymbol{\theta}). \tag{3.34}$$

One can make use of this and other basic matrix calculus properties, as discussed by Caswell (2011), to obtain Algorithm 6 and Algorithm 7. Note that $\boldsymbol{m}_k^{N,(r,\theta_i)}$ and $\boldsymbol{A}_{k,k'}^{(r,\theta_i)}(0)$ in Algorithm 6, which corresponds to the IP R_2 model, represent the derivatives of $\boldsymbol{m}_k^{N,(r)}$ and $\boldsymbol{A}_{k,k'}^{(r)}(0)$, respectively, with respect θ_i, for $\theta_i \in \{\alpha_+, \alpha_-, \beta_+, \beta_-\}$. Finally, explicit expressions for matrices in these algorithms, consisting on the element-by-element partial derivative of the matrices defined in Subsections 3.4.1 and 3.4.2, with respect to any parameter, $\theta_i \in \{\alpha_+, \alpha_-, \beta_+, \beta_-, \gamma_+, \gamma_-\}$, are not reported here.

It is clear that, since the descriptors are stored in the vectors $\boldsymbol{m}^{N,(l)}$, $\hat{\boldsymbol{m}}^{(l)}$ (time to reach a threshold number of P_2 complexes in the IP and the DP R_2 models, respectively) and quantities π_j and $\hat{\pi}_j$ (mean number of j complexes in steady-state in the IP R_2 model ($j \in \{M_2, P_2\}$) and the DP R_2 model ($j \in \{M_2, D_2, P_2\}$), respectively), the objective in Algorithm 6 and Algorithm 7 is to obtain the derivative vectors $\boldsymbol{m}^{N,(l,\theta_i)}$, $\hat{\boldsymbol{m}}^{(l,\theta_i)}$, $\boldsymbol{\pi}^{(\theta_i)}$ and $\hat{\boldsymbol{\pi}}^{(\theta_i)}$. The first two vectors contain the derivatives of the l-th order moments of the time to reach a given threshold number of P complexes, and the last two yield the derivatives of quantities π_j and $\hat{\pi}_j$, with respect to each rate $\theta_i \in \{\alpha_+, \alpha_-, \beta_+, \beta_-, \gamma_+, \gamma_-\}$.

$\boldsymbol{H}_0^{N,(\theta_i)}(0) = -\boldsymbol{A}_{0,0}^{(\theta_i)}(0)$
for $k = 1, \ldots, N-1$ **do**
  $\boldsymbol{H}_k^{N,(\theta_i)}(0) = -\boldsymbol{A}_{k,k}^{(\theta_i)}(0) - \Big(\boldsymbol{A}_{k,k-1}^{(\theta_i)}(0)\boldsymbol{H}_{k-1}^{N}(0)^{-1}\boldsymbol{A}_{k-1,k}(0)$
  $-\boldsymbol{A}_{k,k-1}(0)\boldsymbol{H}_{k-1}^{N}(0)^{-1} \times \boldsymbol{H}_{k-1}^{N,(\theta_i)}(0)\boldsymbol{H}_{k-1}^{N}(0)^{-1}\boldsymbol{A}_{k-1,k}(0)$
  $+\boldsymbol{A}_{k,k-1}(0)\boldsymbol{H}_{k-1}^{N}(0)^{-1}\boldsymbol{A}_{k-1,k}^{(\theta_i)}(0)\Big)$
end
$\boldsymbol{m}_{N-1}^{N,(0,\theta_i)} = -\boldsymbol{H}_{N-1}^{N}(0)^{-1}\boldsymbol{H}_{N-1}^{N,(\theta_i)}(0)\boldsymbol{H}_{N-1}^{N}(0)^{-1}\boldsymbol{a}_{N-1}(0) +$
$\boldsymbol{H}_{N-1}^{N}(z)^{-1}\boldsymbol{a}_{N-1}^{,(\theta_i)}(z)$
for $k = N-2, \ldots, 1, 0$ **do**
  $\boldsymbol{m}_k^{N,(0,\theta_i)} = -\boldsymbol{H}_k^{N}(0)^{-1}\boldsymbol{H}_k^{N,(\theta_i)}(0)\boldsymbol{H}_k^{N}(0)^{-1}\boldsymbol{A}_{k,k+1}(0)\boldsymbol{m}_{k+1}^{N,(0)}$
  $+\boldsymbol{H}_k^{N}(0)^{-1}\boldsymbol{A}_{k,k+1}^{(\theta_i)}(0) \times \boldsymbol{m}_{k+1}^{N,(0)} + \boldsymbol{H}_k^{N}(0)^{-1}\boldsymbol{A}_{k,k+1}(0)\boldsymbol{m}_{k+1}^{N,(0,\theta_i)}$
end
for $j = 1, \ldots, r$ **do**
  $\boldsymbol{P}_0^{N,(j,\theta_i)} = \sum_{k=1}^{j}\binom{j}{k}(-1)^k\Big(\boldsymbol{A}_{0,0}^{(k,\theta_i)}(0)\boldsymbol{m}_0^{N,(j-k)} + \boldsymbol{A}_{0,0}^{(k)}(0)\boldsymbol{m}_0^{N,(j-k,\theta_i)}$
  $+\boldsymbol{A}_{0,1}^{(k,\theta_i)}(0)\boldsymbol{m}_1^{N,(j-k)} + \boldsymbol{A}_{0,1}^{(k)}(0)\boldsymbol{m}_1^{N,(j-k,\theta_i)}\Big)$
  for $p = 1, \ldots, N-1$ **do**
    $\boldsymbol{P}_p^{N,(j,\theta_i)} = \boldsymbol{A}_{p,p-1}^{(\theta_i)}(0)\boldsymbol{H}_{p-1}^{N}(0)^{-1}\boldsymbol{P}_{p-1}^{N,(j)}$
    $-\boldsymbol{A}_{p,p-1}(0)\boldsymbol{H}_{p-1}^{N}(0)^{-1}\boldsymbol{H}_{p-1}^{N,(\theta_i)}(0) \times \boldsymbol{H}_{p-1}^{N}(0)^{-1}\boldsymbol{P}_{p-1}^{N,(j)}$
    $+\boldsymbol{A}_{p,p-1}(0)\boldsymbol{H}_{p-1}^{N}(0)^{-1}\boldsymbol{P}_{p-1}^{N,(j,\theta_i)} + \sum_{k=1}^{j}\binom{i}{k}(-1)^k \times \Big(\boldsymbol{A}_{p,p-1}^{(k,\theta_i)}(0)\boldsymbol{m}_{p-1}^{N,(j-k)}$
    $+\boldsymbol{A}_{p,p-1}^{(k)}(0)\boldsymbol{m}_{p-1}^{N,(j-k,\theta_i)} + \boldsymbol{A}_{p,p}^{(k,\theta_i)}(0)\boldsymbol{m}_p^{N,(j-k)} + \boldsymbol{A}_{p,p}^{(k)}(0)\boldsymbol{m}_p^{N,(j-k,\theta_i)}$
    $+(1-\delta_{p,N-1})\Big(\boldsymbol{A}_{p,p+1}^{(k,\theta_i)}(0)\boldsymbol{m}_{p+1}^{N,(j-k)} + \boldsymbol{A}_{p,p+1}^{(k)}(0) \times \boldsymbol{m}_{p+1}^{N,(j-k,\theta_i)}\Big)\Big)$;
  end

  $\boldsymbol{m}_{N-1}^{N,(j,\theta_i)} = -\boldsymbol{H}_{N-1}^{N}(0)^{-1}\boldsymbol{H}_{N-1}^{N,(\theta_i)}(0)\boldsymbol{H}_{N-1}^{N}(0)^{-1}\Big(\boldsymbol{P}_{N-1}^{N,(j)} + (-1)^j\boldsymbol{a}_{N-1}^{,(j)}(0)\Big)$
  $+\boldsymbol{H}_{N-1}^{N}(0)^{-1}\Big(\boldsymbol{P}_{N-1}^{N,(j,\theta_i)} + (-1)^j\boldsymbol{a}_{N-1}^{,(j,\theta_i)}(0)\Big)$
  for $p = N-2, \ldots, 1, 0$ **do**
    $\boldsymbol{m}_p^{N,(j,\theta_i)} = -\boldsymbol{H}_p^{N}(0)^{-1}\boldsymbol{H}_p^{N,(\theta_i)}(0)\boldsymbol{H}_p^{N}(0)^{-1}\Big(\boldsymbol{P}_p^{N,(j)} + \boldsymbol{A}_{p,p+1}(0)\boldsymbol{m}_{p+1}^{N,(j)}\Big)$
    $+\boldsymbol{H}_p^{N}(0)^{-1} \times \Big(\boldsymbol{P}_p^{N,(j,\theta_i)} + \boldsymbol{A}_{p,p+1}^{(\theta_i)}(0)\boldsymbol{m}_{p+1}^{N,(j)} + \boldsymbol{A}_{p,p+1}(0)\boldsymbol{m}_{p+1}^{N,(j,\theta_i)}\Big)$
  end
end

Algorithm 6: to obtain the derivative of the r-th order moments $E\left(T_{(n_1,n_2)}(N)^r\right)$ with respect $\theta_i \in \{\alpha_+, \alpha_-, \beta_+, \beta_-\}$.

$$
\begin{aligned}
&\boldsymbol{H}_0^{(\theta_i)} = \boldsymbol{A}_{0,0}^{(\theta_i)} \\
&\textbf{for } k = 1, \ldots, n_L - 1 \textbf{ do} \\
&\quad \boldsymbol{H}_k^{(\theta_i)} = \boldsymbol{A}_{k,k}^{(\theta_i)} - \Big(\boldsymbol{A}_{k,k-1}^{(\theta_i)} \boldsymbol{H}_{k-1}^{-1} \boldsymbol{A}_{k-1,k} - \boldsymbol{A}_{k,k-1} \boldsymbol{H}_{k-1}^{-1} \boldsymbol{H}_{k-1}^{(\theta_i)} \boldsymbol{H}_{k-1}^{-1} \boldsymbol{A}_{k-1,k} \\
&\quad + \boldsymbol{A}_{k,k-1} \boldsymbol{H}_{k-1}^{-1} \boldsymbol{A}_{k-1,k}^{(\theta_i)} \Big) \\
&\textbf{end} \\
&\boldsymbol{\pi}_{n_L}^{*,(\theta_i)} = 0 \\
&\textbf{for } k = n_L - 1, \ldots, 1, 0 \textbf{ do} \\
&\quad \boldsymbol{\pi}_k^{*,(\theta_i)} = - \Big(\boldsymbol{\pi}_{k+1}^{*,(\theta_i)} \boldsymbol{A}_{k+1,k} \boldsymbol{H}_k^{-1} + \boldsymbol{\pi}_{k+1}^{*} \boldsymbol{A}_{k+1,k}^{(\theta_i)} \boldsymbol{H}_k^{-1} \\
&\quad - \boldsymbol{\pi}_{k+1}^{*} \boldsymbol{A}_{k+1,k} \boldsymbol{H}_k^{-1} \boldsymbol{H}_k^{(\theta_i)} \boldsymbol{H}_k^{-1} \Big) \\
&\textbf{end} \\
&\textbf{for } k = 0, \ldots, n_L \textbf{ do} \\
&\quad \boldsymbol{\pi}_k^{(\theta_i)} = \frac{1}{\boldsymbol{\pi}^* \boldsymbol{e}_{\#\mathbb{S}}} \Big(\boldsymbol{\pi}_k^{*,(\theta_i)} - \boldsymbol{\pi}_k \boldsymbol{\pi}^{*,(\theta_i)} \boldsymbol{e}_{\#\mathbb{S}} \Big) \\
&\textbf{end} \\
&\pi_M^{(\theta_i)} = \sum_{k=0}^{n_L} k \left(\sum_{j=0}^{n_L} (\boldsymbol{\pi}_j^{(\theta_i)})_k \right) \\
&\pi_P^{(\theta_i)} = \sum_{k=0}^{n_L} k \left(\boldsymbol{\pi}_k^{(\theta_i)} \boldsymbol{e}_{J(k)} \right)
\end{aligned}
$$

Algorithm 7: to obtain the derivative of π_M and π_P with respect $\theta_i \in \{\alpha_+, \alpha_-, \beta_+, \beta_-\}$.

3.4.4 Results

Here I develop a number of numerical results in order to illustrate the analytical work carried out in Subsection 3.4.1 and 3.4.2. In particular, the focus here is on the interaction between VEGFR2 receptors and VEGF-A ligands on the surface of human vascular endothelial cells, an interaction initiating signalling cascades that can cause diverse cellular responses such as cell motility, division or death (*i.e.,* apoptosis).

One can analyse the stochastic descriptors of interest when the IP R_2 or the DP R_2 models are considered for this interaction. This allows studying the impact of considering phosphorylation as a separate reaction in the process (delayed phosphorylation), to quantify timescales for signalling formation under different ligand concentrations, and to analyse the impact that each kinetic rate in these

processes has in these stochastic descriptors.

Time to reach a signal threshold

In Figure 3.11, $E\left(T_{(0,0)}(N)\right)$ (for the IP R_2 model) and $E\left(T_{(0,0,0)}(N)\right)$ (for the DP R_2 model) are plotted, for values $0 \leq N \leq n_L$, where $n_L \in \{23, 58, 116\}$ is the number of ligands considered, which corresponds to 10%, 25% and 50% of the total number of VEGFR2, respectively, and to ligand concentrations $c_L \in \{1pM,$ $2.5pM,$ $5pM\}$.

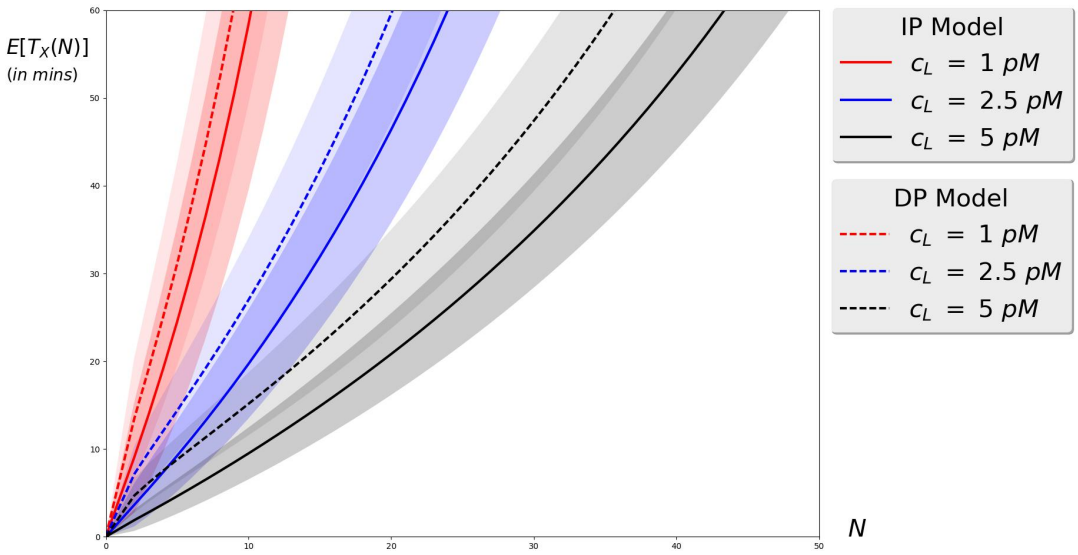

Figure 3.11: $E\left(T_{\boldsymbol{x}}(N)\right)$ for (from *left* to *right*) ligand concentrations $c_L \in \{1pM,$ $2.5pM,$ $5pM\}$, for the IP R_1 model (*solid* curves) and the DP R_2 model (*dashed* curves). IP R_2 model: $\boldsymbol{x} = (0, 0)$. DP R_2 model: $\boldsymbol{x} = (0, 0, 0)$.

The number of ligands considered in these three cases verifies the condition $2n_L \leq n_{R_2}$, assumed in the analysis of $T_{(0,0)}(N)$, as discussed in Subsection 3.4.1. $T_{(0,0)}(N)$ is the continuous random variable that represents the time to reach a total number, N, of phosphorylated bound dimers P_2, given the initial state $(0, 0)$, in the IP R_2 model where instantaneous phosphorylation is considered (for details, see Subsection 3.4.1), while $T_{(0,0,0)}(N)$ is its DP R_2 model counterpart.

Figures in this subsection have been restricted to times up to 60 min, to describe the early time dynamics on the cell surface. The long-term behaviour of the system can be analysed by means of the steady-state distribution. In Figure 3.11, *solid* curves represent values of $E\left(T_{(0,0)}(N)\right)$, while dashed curves represent values of $E\left(T_{(0,0,0)}(N)\right)$, obtained by means of Algorithm 4. Shaded areas have been obtained for both models by considering $E\left(T_{\mathbf{x}}(N)\right) \pm SD\left(T_{\boldsymbol{x}}(N)\right)$, where $SD(X)$ represents the standard deviation of the random variable X, obtained from Algorithm 4.

In Figure 3.11, a monotonic behaviour can be easily identified. For a fixed value of N in the IP R_2 model, $E\left(T_{(0,0)}(N)\right)$ is always smaller for larger ligand concentrations, c_L. Indeed, an increase in the amount of available ligand to bind receptors implies reaching the given signalling threshold (encoded by the value of N) in a shorter time. The behaviour for $E\left(T_{(0,0,0)}(N)\right)$ is similar to that observed for $E\left(T_{(0,0)}(N)\right)$, so that the consideration of delayed phosphorylation in the DP R_2 model does not seem to qualitatively affect the main features of the descriptor under consideration. This is related to the fact that the most likely fate of a bound monomer is to produce signal before its dissociation, regardless of including or not this additional reaction. However, the consideration of phosphorylation as an independent reaction in the process clearly amounts to a delay in the time to reach the threshold N, in comparison with the time to reach the threshold N, and every curve is displaced to the left. For example, for the ligand concentration given by $c_L = 1pM$, the mean time $E\left(T_{(0,0)}(N)\right)$ to reach a threshold $N = 5$ (20% of n_L) of phosphorylated bound dimers is ~ 25 min under the IP R_2 model. When the phosphorylation of bound complexes is explicitly considered (th DP R_2 model), this mean time increases up to ~ 31 min.

Stationary distribution

The asymptotic behaviour of curves in Figure 3.11 is directly related to the maximum signalling threshold that is, in fact, reached by the process in the short- and mid-term. From a purely mathematical perspective, any state within $\mathcal{S}_{\text{IP } R_2}$ or $\mathcal{S}_{\text{DP } R_2}$ in the IP R_2 and the DP R_2 models, respectively, is reached as $t \to +\infty$,

since $\mathcal{S}_{\text{IP } R_2}$ and $\mathcal{S}_{\text{DP } R_2}$ are the irreducible finite class of states for process $\mathcal{X}_{\text{IP } R_2}$ and $\mathcal{X}_{\text{DP } R_2}$.

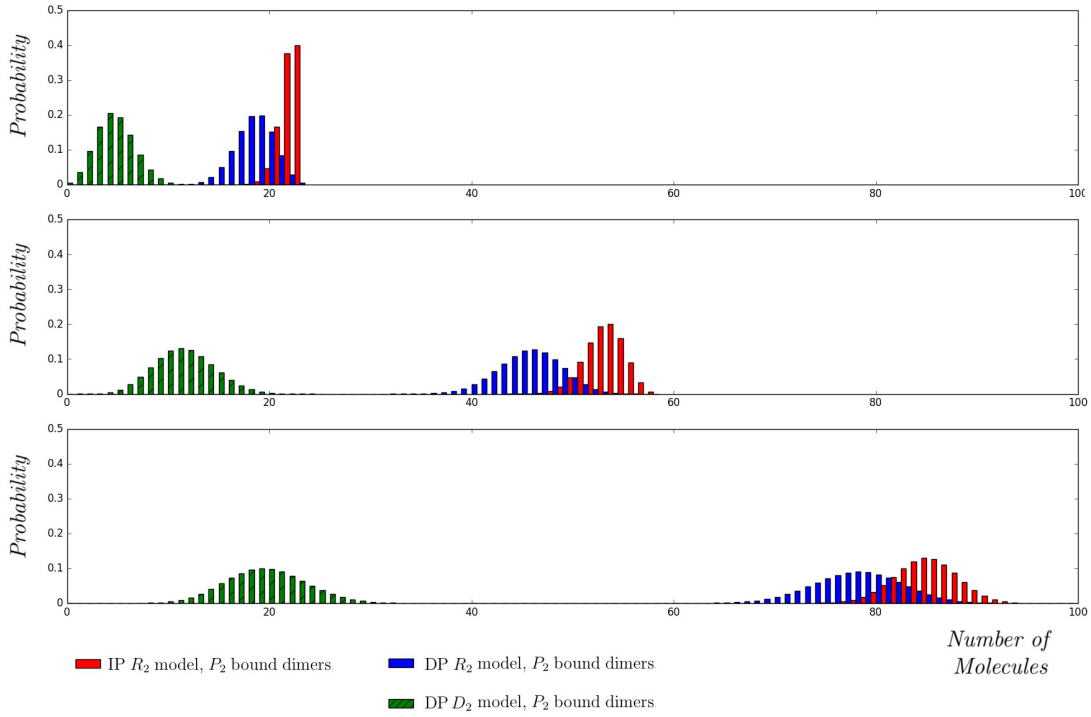

Figure 3.12: Distribution of the number of bound dimers in steady state for processes $\mathcal{X}_{\text{IP } R_2}$ (the IP R_2 model, P_2 bound dimers, *red*) and $\mathcal{X}_{\text{DP } R_2}$ (the DP R_2 model, D_2 and P_2 bound dimers, *green* and *blue*) for (from *top* to *bottom*) ligand concentrations $c_L \in \{1pM, 2.5pM, 5pM\}$.

However, according to the numerical results, there exists a sub-set of (high) signalling thresholds that is not reached in practice by $\mathcal{X}_{\text{IP } R_2}$ ($\mathcal{X}_{\text{DP } R_2}$). This signalling threshold is directly related to the steady-state distribution of this process, which can be computed from Algorithm 5, and which measures the potential of the system to reach any signalling threshold under different ligand concentrations for both models.

In Figure 3.12, the distribution of the number of (phosphorylated and non-phosphorylated) bound dimers at steady-state, for the IP R_2 and the DP R_2 models, is plotted for different ligand concentrations $c_L \in \{1pM, 2.5pM, 5pM\}$.

Under low ligand concentrations, near all the n_L available ligands are forming phosphorylated bound dimers in steady-state. This is specially the case in the IP R_2 model, where no non-phosphorylated bound dimers exist. In the DP R_2 model, a small number of non-phosphorylated bound dimers can be found in steady-state. These non-phosphorylated bound dimers in steady-state explain why the distribution of the number of phosphorylated bound dimers in steady-state is displaced to the left when phosphorylation is considered as a separate reaction in the DP R_2 model, in comparison with the same distribution in the IP R_2 model.

Local sensitivity analysis

The effect of the binding, dissociation, phosphorylation and de-phosphorylation rates on the descriptors considered in this subsection, can be estimated by means of the sensitivity analysis proposed in Subsection 3.4.3. In Tables 3.9 and 3.10 the sensitivity coefficients (*i.e.,* normalised derivatives), also called elasticities, of the descriptors $E\left(T_{(0,0)}(N)\right)$, $E\left(T_{(0,0,0)}(N)\right)$, π_P and $\hat{\pi}_P$ are presented, when N is chosen to be 25% of the total number of ligands n_L, and for different concentrations of ligands c_L. As expected, the effect of each rate on any descriptor increases with increasing values of ligand concentration c_L. It is also worth noting that the elasticities of the mean number of phosphorylated complexes in steady state are equal, with opposite sign, with respect binding and dissociation rates (*e.g.,* $\dfrac{\partial \pi_P}{\partial \alpha_+} \Big/ \dfrac{\pi_P}{\alpha_+} = -\dfrac{\partial \pi_P}{\partial \alpha_-} \Big/ \dfrac{\pi_P}{\alpha_-}$), which means that this characteristic only depends on ratios $\dfrac{\alpha_+}{\alpha_-}$, $\dfrac{\beta_+}{\beta_-}$ and $\dfrac{\gamma_+}{\gamma_-}$, and not on each particular rate. This can be easily understood by noting that, from a deterministic perspective the steady state corresponding to the DP R_2 model can be obtained as the solution of

$$\begin{aligned} 2\frac{\alpha_+}{\alpha_-} R_2^* L^* - M_2^* &= 0, \\ \cdot\frac{\beta_+}{\beta_-} M_2^* R_2^* - 2D_2^* &= 0, \\ \frac{\gamma_+}{\gamma_-} D_2^* - P_2^* &= 0, \end{aligned}$$

which does only depend on these ratios. Note here that, according to results in Tables 3.9 and 3.10, the rate α_+ plays an important role in all the descriptors.

This is related to the fact that, once a ligand is trapped to form a bound monomer, its most probable fate is to produce signal before dissociation of the corresponding dimer occurs.

Elasticity	c_L	α_+	α_-	β_+	β_-
$\frac{\frac{\partial E\left(T_{(0,0)}(N)\right)}{\partial\theta}}{\frac{E\left(T_{(0,0)}(N)\right)}{\theta}}$	$1pM$	-9.98×10^{-1}	1.61×10^{-2}	-2.17×10^{-2}	3.42×10^{-3}
	$2.5pM$	-9.99×10^{-1}	1.78×10^{-2}	-2.36×10^{-2}	4.60×10^{-3}
	$5pM$	-1.00	2.01×10^{-2}	-2.66×10^{-2}	6.02×10^{-3}
$\frac{\frac{\partial E\left(T_{(0,0,0)}(N)\right)}{\partial\theta}}{\frac{E\left(T_{(0,0,0)}(N)\right)}{\theta}}$	$1pM$	-8.47×10^{-1}	1.22×10^{-2}	-1.73×10^{-2}	2.12×10^{-3}
	$2.5pM$	-8.60×10^{-1}	1.33×10^{-2}	-1.84×10^{-2}	2.59×10^{-3}
	$5pM$	-8.72×10^{-1}	1.51×10^{-2}	-2.07×10^{-2}	3.30×10^{-3}
$\frac{\frac{\partial\pi_P}{\partial\theta}}{\frac{\pi_P}{\theta}}$	$1pM$	3.45×10^{-2}	-3.45×10^{-2}	3.82×10^{-2}	-3.82×10^{-2}
	$2.5pM$	6.67×10^{-2}	-6.67×10^{-2}	7.17×10^{-2}	-7.17×10^{-2}
	$5pM$	1.03×10^{-1}	-1.03×10^{-1}	1.10×10^{-1}	-1.10×10^{-1}
$\frac{\frac{\partial\hat{\pi}_P}{\partial\theta}}{\frac{\hat{\pi}_P}{\theta}}$	$1pM$	7.31×10^{-3}	-7.31×10^{-3}	8.08×10^{-3}	-8.08×10^{-3}
	$2.5pM$	1.73×10^{-2}	-1.73×10^{-2}	1.85×10^{-2}	-1.85×10^{-2}
	$5pM$	5.88×10^{-2}	-5.88×10^{-2}	6.12×10^{-2}	-6.12×10^{-2}

Table 3.9: Elasticities of the stochastic descriptors $E\left(T_{(0,0)}(N)\right)$ and $E\left(T_{(0,0,0)}(N)\right)$ and descriptors π_P and $\hat{\pi}_P$, with respect to each parameter $\theta_i \in \{\alpha_+, \alpha_-, \beta_+, \beta_-\}$ for different ligand concentrations $c_L \in \{1pM, 2.5pM, 5pM\}$.

Elasticity	c_L	γ_+	γ_-
$\dfrac{\dfrac{\partial E\left(T_{(0,0,0)}(N)\right)}{\partial\theta}}{\dfrac{E\left(T_{(0,0,0)}(N)\right)}{\theta}}$	$1pM$	-2.26×10^{-1}	8.82×10^{-2}
	$2.5pM$	-2.68×10^{-1}	1.36×10^{-1}
	$5pM$	-2.99×10^{-1}	1.76×10^{-1}
$\dfrac{\dfrac{\partial\hat{\pi}_P}{\partial\theta}}{\dfrac{\hat{\pi}_P}{\theta}}$	$1pM$	2.06×10^{-1}	-2.06×10^{-1}
	$2.5pM$	2.15×10^{-1}	-2.15×10^{-1}
	$5pM$	2.49×10^{-1}	-2.49×10^{-1}

Table 3.10: Elasticities of the stochastic descriptors $E\left(T_{(0,0)}(N)\right)$ and $E\left(T_{(0,0,0)}(N)\right)$ and descriptors π_P and $\hat{\pi}_P$, with respect to each parameter $\theta_i \in \{\gamma_+, \gamma_-\}$ for different ligand concentrations $c_L \in \{1pM, 2.5pM, 5pM\}$.

3.4.5 Discussion

In Section 3.4 the aim was to measure the timescales for signalling formation for two different stochastic models for receptor-ligand interaction (instantaneous phosphorylation, the IP R_2 model, and delayed phosphorylation, the DP R_2 model), and to analyse the long-term dynamics of these systems. Bound dimers become instantaneously phosphorylated in the IP R_2 model, while in the DP R_2 model phosphorylation is considered a new and independent reaction. In these two models, matrix-analytic techniques have been applied to study the time to reach a threshold number of phosphorylated bound dimers P_2 on the cell membrane, and the steady-state distribution of the corresponding CTMPs. These times are identified as absorption times in conveniently defined auxiliary CTMPs, and their Laplace-Stieltjes transforms and different order moments have been computed algorithmically by means of a first-step analysis, while exploiting the quasi-birth-and-death structure of the infinitesimal generators associated to these processes. Moreover, the construction of the DP R_2 model, as an extension of the IP R_2 model in Subsection 3.1.2 allows analysing the role played by phosphorylation events and showing how different reactions may be incorporated while adapting the matrix-analytic approach. A particular feature of this ana-

lytic approach is that it allows one to analyse the role played by each kinetic rate in these processes, by means of the computation of the partial derivatives of the descriptors under analysis with respect to the corresponding parameters.

The numerical results in Subsection 3.4.4 are related to the interaction between receptor VEGFR2 and ligand VEGF-A, in human vascular endothelial cells. The analysis of these results shows how including phosphorylation as a separate reaction only seems to quantitatively affect the timescales for signal formation, but does not qualitatively change the dynamics of these processes. The small qualitative impact of including phosphorylation as a new reaction can be better clarified by analysing the fate of a bound monomer in the processes from an individual perspective. In particular, a single ligand can be considered, that has been captured by a receptor forming a bound monomer and only the dynamics of this new complex is analysed, neglecting the other dynamics related to the other ligands and receptors in the system. Thus, the focus is on the *fate* of this complex (causing or not signalling before the bound monomer dissociates), which directly depends on the kinetic rates and is controlled by the stochastic processes illustrated in Figure 3.13.

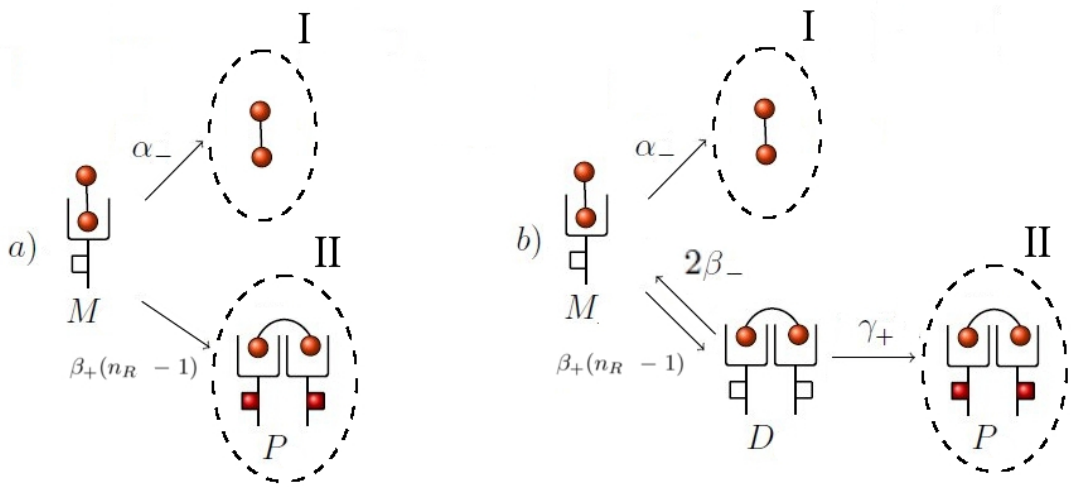

Figure 3.13: Individual bound monomer fate under a) the IP R_2 model, and b) the DP R_2 model. Fate I: dissociation before signal; Fate II: signal before dissociation.

Hence, the following probability

$$p_{signal} \quad = \quad \textit{“probability of the complex signalling before dissociation”},$$

can be obtained for both models in an analytical way, by using the parameters' values reported in Table 3.6, where $n_{R_2} = 232$ as only 4% of the cell is considered,

- IP R_2 model (instantaneous phosphorylation):

$$p_{signal} \quad = \quad \frac{\beta_+(n_{R_2}-1)}{\alpha_- + \beta_+(n_{R_2}-1)} \quad = \quad 0.9742.$$

- DP R_2 model (delayed phosphorylation):

$$\begin{aligned} p_{signal} \quad &= \quad \left(1 - \frac{\beta_+(n_{R_2}-1)2\beta_-}{(\alpha_- + \beta_+(n_{R_2}-1))(2\beta_- + \gamma_+)}\right)^{-1} \\ &\times \quad \frac{\gamma_+\beta_+(n_{R_2}-1)}{(2\beta_- + \gamma_+)(\alpha_- + \beta_+(n_{R_2}-1))} \quad = \quad 0.9393. \end{aligned}$$

On the other hand, if the focus is on the time until the signal occurs, that is

$$\begin{aligned} \tau_{signal} \quad = \quad &\textit{“mean time for complex to form signalling,} \\ &\textit{conditioned on this occurring”}, \end{aligned}$$

then this mean time can be obtained for both models in an analytical way:

- IP R_2 model (instantaneous phosphorylation):

$$\tau_{signal} \quad = \quad \frac{1}{\alpha_- + \beta_+(n_{R_2}-1)} \quad = \quad 9.5356s.$$

- DP R_2 model (delayed phosphorylation):

$$\tau_{signal} \quad = \quad \frac{2\beta_- + \gamma_+}{(\alpha_- + \beta_+(n_{R_2}-1))\gamma_+} + \frac{1}{\gamma_+} \quad = \quad 283.1053s.$$

This implies that ligands tend to form signal with probability near one once they are captured to form a bound monomer, and the phosphorylation/de-phosphorylation reactions can only cause a delay on this occurring.

The total number of VEGFR2s per cell varies according to Ewan *et al.* (2006a), Ewan *et al.* (2006b), Napione *et al.* (2012) and could be tenfold higher than the numbers, reported by Imoukhuede & Popel (2012), used in this section. A larger number of VEGFR2 receptors on the cell surface would, however, only quantitatively change the results. Finally, the sensitivity analysis carried out for the descriptors enables to show how the monomeric formation rate, α_+, plays a crucial role in these models, with an effect which can be more than twice the effect of any other rate for some of the descriptors which were considered.

Finally, numerical results presented in Subsection 3.4.4 allowed quantifying the effect of different ligand concentrations. Increasing ligand concentration decreases the times to reach any signalling threshold, while increases the maximum potential signalling thresholds to be reached. However, too high ligand concentrations can result in saturated situations, where the phosphorylation of bound dimers is reduced and monomeric bound complexes are enhanced.

3.5 Alternative Signalling Hypotheses

The analysis carried out in Section 3.4 for analysing the timescales of signal generation is complemented here, by means of studying a continuous stochastic descriptor for the process under different *signalling hypotheses*. In this section, a stochastic descriptor and a matrix-analytic method is used in the context of a stochastic model for the interaction between the receptor VEGFR2 and the soluble dimeric ligand VEGF-A on the surface of a human umbilical vein endothelial cell. The bivalent nature of the ligand molecule allows the formation of both monomeric and dimeric ligand-receptor complexes. The assumption is that only dimeric complexes can signal and thus, they will be considered the signalling units of the process. The aim is to study the timescales of signal generation. Different hypotheses are considered for how this signal is produced and *stored*. To this end, the time to reach a particular signalling threshold is defined here as a random variable, identified with a first-passage time of the underlying continuous-time Markov process, and its different order moments are computed in an algorithmic manner.

3.5.1 The stochastic model

The focus here is on the following hypotheses, which have been previously considered in the literature:

(DS) The signalling unit of the process is the number of bound dimers in the system (as shown in Subsection 3.4.1 or by Alarcón & Page (2006)) or **Dimer Signalling Hypothesis**.

(AS) Each cell is seen as a *counter*, which keeps track of the signals generated by the dimers. Thus, signals generated from bound dimers are *accumulated* (see Currie *et al.* (2012)) or **Accumulative Signalling Hypothesis**.

(ASD-λ) The signal is accumulated as in the **AS** hypothesis, but a linear signal decay with rate $\lambda > 0$ is introduced (see Starbuck *et al.* (1990)) or **Accumulative Signalling with Decay Hypothesis**.

In Subsection 3.5.2, these three hypotheses are compared by analysing a unique stochastic descriptor: the time to reach a signalling threshold. This is identified with a first-passage time (or absorption time) in the theory of stochastic processes, which follows a continuous phase-type distribution. Signal generation is tracked by means of an extended CTMP, whose transitions directly depend on the signalling hypothesis under consideration. The probabilistic descriptor is then analysed by means of an algorithmic approach, which requires the introduction of a matrix formalism.

3.5.2 A probabilistic performance measure: time to reach a signalling threshold

Consider an additional variable $S(t)$ for the IP R_2 model, defined in Subsection 3.1.1, which represents the amount of signal at time $t \geq 0$. The introduction of this variable leads to extended CTMP $\mathcal{X}^{ext} = \{\mathbf{X}^{ext}(t) = (M_2(t), P_2(t), S(t)) : t \geq 0\}$. The transitions and the state space of $\mathcal{X}^{ext}$ directly depend on the signalling hypothesis (**DS**, **AS** or **ASD-λ**) under consideration. Since the interest here is in the timescales of signal generation, the aim is to analyse the random variable $T^S_{(n_1,n_2,s)}$, which amounts to the time to reach a signalling threshold $S \geq s$, given

the initial state of the process (n_1, n_2, s), with $T^S_{(n_1,n_2,S)} = 0$; that is, $T^S_{(n_1,n_2,s)} = inf\{t \geq 0 : S(t) = S \mid (M_2(0), P_2(0), S(0)) = (n_1, n_2, s)\}$.

The **DS** hypothesis implies considering $S(t) = P_2(t)$ for all $t \geq 0$, so that the amount of signalling in the process increases and decreases directly following the formation and dissociation of dimers. This particular case was analysed in detail in Subsection 3.4.1.

Under hypotheses **AS** and **ASD-λ**, the signal is accumulated according to the formation of new dimers, while it decays with rate $\lambda \geq 0$ ($\lambda = 0$ corresponds to the **AS** hypothesis). This implies that $\mathcal{X}^{ext}$ has state space given by $\mathcal{S}^{ext} = \{(n_1, n_2, s) \in \mathbb{N}_0^3 : \ n_1 + n_2 \leq n_L, \ s \geq 0\}$, with transitions and infinitesimal transition rates given in Table 3.11.

$q_{\boldsymbol{n}\boldsymbol{n}'}$ for reaction $\boldsymbol{n} = (n_1, n_2, s) \to \boldsymbol{n}'$	$\boldsymbol{n}'$
$2\alpha_+(n_L - n_1 - n_2)(n_{R_2} - n_1 - 2n_2)$	$(n_1 + 1, n_2, s)$
$\alpha_- n_1$	$(n_1 - 1, n_2, s)$
$\beta_+ n_1(n_{R_2} - n_1 - 2n_2)$	$(n_1 - 1, n_2 + 1, s + 1)$
$2\beta_- n_2$	$(n_1 + 1, n_2 - 1, s)$
λs	$(n_1, n_2, s - 1)$

Table 3.11: The infinitesimal transition rates $q_{\boldsymbol{n}\boldsymbol{n}'}$ of the process $\mathcal{X}^{ext}$.

Since the aim is to study the random variable $T^S_{(n_1,n_2,s)}$ that represents the time to reach a signalling threshold $S \geq s$, the focus is on the dynamics of process $\mathcal{X}^{ext}$ before this signalling threshold is reached. This means that one can consider $\mathcal{S}^{ext} = \mathcal{S}^S \cup \mathcal{S}_0^S$ with $\mathcal{S}^S = \{(n_1, n_2, s) \in \mathbb{N}_0^3 : n_1 + n_2 \leq n_L, \ 0 \leq s \leq S - 1\}$ and $\mathcal{S}_0^S = \{(n_1, n_2, S) \in \mathbb{N}_0^3 : n_1 + n_2 \leq n_L\}$. States within $\mathcal{S}_0^S$ are considered as absorbing from now on (the process $\mathcal{X}^{ext}$ ends once the signalling threshold S is reached), and states (n_1, n_2, s) with $s > S$ are not included. Then, $\mathcal{S}^S$ is a finite irreducible class of transient states, from where the absorbing set $\mathcal{S}_0^S$ is accessible. $T^S_{(n_1,n_2,s)}$ for $(n_1, n_2, s) \in \mathcal{S}^S$ can be seen as the time to reach $\mathcal{S}_0^S$ (see Kulkarni (1996), Section 6.7), and is well-known to follow a continuous phase-type distribution (see He (2014), Chapter 1). Thus, its probability density function is given by

$$f_{T^S_{(n_1,n_2,s)}}(t) \ = \ -\boldsymbol{q}_0 \, e^{\boldsymbol{M}t} \, \boldsymbol{M} \, \boldsymbol{e}_{\#\mathcal{S}^S} \ , \quad t \geq 0 \ ,$$

where $\boldsymbol{q}_0$ is a row vector with the initial distribution of $\mathcal{X}^{ext}$ in $\mathcal{S}^S$, $\boldsymbol{e}_j$ represents a column vector of ones with dimension j, $\#\mathcal{S}^S$ is the cardinality of $\mathcal{S}^S$, and $\boldsymbol{M}$ is the sub-matrix of the infinitesimal generator of $\mathcal{X}^{ext}$ corresponding to transitions between states within the irreducible class of transient states $\mathcal{S}^S$.

The practical computation of $f_{T^S_{(n_1,n_2,s)}}(t)$ is restricted by the computational difficulties of calculating the exponential of the matrix $\boldsymbol{M}$ (see Moler & Van Loan (2003)). Thus, the different order moments of $T^S_{(n_1,n_2,s)}$ are computed instead. Consider the Laplace-Stieltjes transform of $T^S_{(n_1,n_2,s)}$, as follows

$$\phi^S_{(n_1,n_2,s)}(z) \;=\; E\left(e^{-z\,T^S_{(n_1,n_2,s)}}\right)\,, \quad \Re(z)\geq 0\,,$$

which uniquely determines the distribution of $T^S_{(n_1,n_2,s)}$. The different order moments of $T^S_{(n_1,n_2,s)}$ are given by differentiation of the Laplace-Stieltjes transform, that is

$$w^{S,l}_{(n_1,n_2,s)} \;=\; E\left((T^S_{(n_1,n_2,s)})^l\right) \;=\; (-1)^l \frac{d^l}{dz^l}\phi^S_{(n_1,n_2,s)}(z)\bigg|_{z=0}\,, \quad l\geq 1\,.$$

To simplify notation, the superscript S is omitted. A first-step argument can be applied in order to obtain a system of linear equations for the Laplace-Stieltjes transform $\phi_{(n_1,n_2,s)}(z)$, given a state $\boldsymbol{n}=(n_1,n_2,s)$ such that $\boldsymbol{n}\in\mathcal{S}^S$ (see Subsection 3.4.1), hence

$$\begin{aligned}(z+\Delta_{\boldsymbol{n}})\,\phi_{\boldsymbol{n}}(z) \;&=\; 2\alpha_+(n_L-n_1-n_2)(n_{R_2}-n_1-2n_2)\phi_{(n_1+1,n_2,s)}(z)\\ &+\; \alpha_- n_1\phi_{(n_1-1,n_2,s)}(z)+\beta_+ n_1(n_{R_2}-n_1-2n_2)\phi_{(n_1-1,n_2+1,s+1)}(z)\\ &+\; 2\beta_- n_2\phi_{(n_1+1,n_2-1,s)}(z)+\lambda s\phi_{(n_1,n_2,s-1)}(z),\quad \boldsymbol{n}\in\mathcal{S}^S\,,\end{aligned} \tag{3.35}$$

with $\Delta_{\boldsymbol{n}} = 2\alpha_+(n_L-n_1-n_2)(n_{R_2}-n_1-2n_2)+\alpha_- n_1+\beta_+ n_1(n_{R_2}-n_1-2n_2)+2\beta_- n_2+\lambda s$, and with boundary conditions $\phi_{(n_1,n_2,S)}(z)=1$ for states $(n_1,n_2,S)\in\mathcal{S}^S_0$. Once the system of equations given by Equation (3.35) is obtained, an analogous system for computing the moments $w^l_{\boldsymbol{n}}$ can be obtained by direct differentiation of Equation (3.35), as follows

$$\begin{aligned}\Delta_{\boldsymbol{n}} w^l_{\boldsymbol{n}} \;=\;& 2\alpha_+(n_L-n_1-n_2)(n_R-n_1-2n_2)w^l_{(n_1+1,n_2,s)}+\alpha_- n_1 w^l_{(n_1-1,n_2,s)}+\beta_+ n_1\\ &\times(n_R-n_1-2n_2)w^l_{(n_1-1,n_2+1,s+1)}+2\beta_- n_2 w^l_{(n_1+1,n_2-1,s)}+\lambda s w^l_{(n_1,n_2,s-1)}\\ &+l w^{l-1}_{(n_1,n_2,s)}\,,\quad l\geq 1\,,\quad \boldsymbol{n}\in\mathcal{S}^S\,,\end{aligned} \tag{3.36}$$

with boundary conditions $w^{l}_{(n_1,n_2,S)} = 0$ for all $(n_1, n_2, S) \in \mathcal{S}^S_0$ and $w^{0}_{(n_1,n_2,s)} = 1$ for all $(n_1, n_2, s) \in \mathcal{S}^S$. The system given by Equation (3.36) implies that the moment of order r, for a given initial state $(n_1, n_2, s) \in \mathcal{S}^S$, can be directly computed from the moment of order $r-1$, starting with $w^{r=0}_{(n_1,n_2,s)} = \phi_{(n_1,n_2,s)}(0) = 1$ and until the desired order l is reached.

The system given by Equation (3.36) can be solved by constructing and inverting its corresponding coefficient matrix. However, the number of states in $\mathcal{S}^S$ requires working in an efficient manner. Therefore, the level structures for the state space is used again (see Subsection 3.4.1). In particular, $\mathcal{S}^{ext}$ can be organised by *levels*

$$\mathcal{S}^{ext} \;=\; \mathcal{S}^S \cup \mathcal{S}^S_0 \,, \quad \mathcal{S}^S \;=\; \bigcup_{k=0}^{S-1} L(k) \,, \quad \mathcal{S}^S_0 \;=\; L(S) \,,$$

with $L(k) = \{(n_1, n_2, s) \in \mathcal{S}^{ext} : \; s = k\}$, and by *sub-levels*

$$L(k) \;=\; \bigcup_{r=0}^{n_L} L(k; r) \,, \quad 0 \leq k \leq S \,,$$

with $L(k; r) = \{(n_1, n_2, s) \in \mathcal{S}^{ext} : \; n_1 = k, \; n_2 = r\}$. The structure introduced by levels and sub-levels guarantees that the infinitesimal generator of $\mathcal{X}^{ext}$ is three-diagonal-by-blocks (as in Equation (3.28)), and given by

$$\boldsymbol{Q} \;=\; \begin{pmatrix} \boldsymbol{Q}_{0,0} & \boldsymbol{Q}_{0,1} & \mathbf{0}_J & \dots & \mathbf{0}_J & \mathbf{0}_J \\ \boldsymbol{Q}_{1,0} & \boldsymbol{Q}_{1,1} & \boldsymbol{Q}_{1,2} & \dots & \mathbf{0}_J & \mathbf{0}_J \\ \mathbf{0}_J & \boldsymbol{Q}_{2,1} & \boldsymbol{Q}_{2,2} & \dots & \mathbf{0}_J & \mathbf{0}_J \\ \vdots & \vdots & \vdots & \ddots & \vdots & \vdots \\ \mathbf{0}_J & \mathbf{0}_J & \mathbf{0}_J & \dots & \boldsymbol{Q}_{S-1,S-1} & \boldsymbol{Q}_{S-1,S} \\ \mathbf{0}_J & \mathbf{0}_J & \mathbf{0}_J & \dots & \mathbf{0}_J & \mathbf{0}_J \end{pmatrix} . \tag{3.37}$$

The square matrix $\boldsymbol{Q}_{k,k'}$ contains those infinitesimal transition rates, in an ordered manner, corresponding to transitions from states in $L(k)$ to states in $L(k')$, so that it has dimension $\#L(k) \times \#L(k') = J \times J$, with $J = \frac{(n_L+1)(n_L+2)}{2}$. Matrices $\mathbf{0}_J$ are square matrices of zeros with dimension J. Given the structure by sub-levels and the transitions of the process (see Table 3.11), matrices $\boldsymbol{Q}_{k,k-1}$, $\boldsymbol{Q}_{k,k}$

and $\boldsymbol{Q}_{k,k+1}$ can be written as follows

$$\boldsymbol{Q}_{k,k} = \begin{pmatrix} \boldsymbol{Q}_{k,k}^{0,0} & \mathbf{0}_{J(0)\times J(1)} & \mathbf{0}_{J(0)\times J(2)} & \cdots & \mathbf{0}_{J(0)\times J(n_L-1)} & \mathbf{0}_{J(0)\times J(n_L)} \\ \boldsymbol{Q}_{k,k}^{1,0} & \boldsymbol{Q}_{k,k}^{1,1} & \mathbf{0}_{J(1)\times J(2)} & \cdots & \mathbf{0}_{J(1)\times J(n_L-1)} & \mathbf{0}_{J(1)\times J(n_L)} \\ \mathbf{0}_{J(2)\times J(0)} & \boldsymbol{Q}_{k,k}^{2,1} & \boldsymbol{Q}_{k,k}^{2,2} & \cdots & \mathbf{0}_{J(2)\times J(n_L-1)} & \mathbf{0}_{J(2)\times J(n_L)} \\ \vdots & \vdots & \vdots & \ddots & \vdots & \vdots \\ \mathbf{0}_{J(n_L)\times J(0)} & \mathbf{0}_{J(n_L)\times J(1)} & \mathbf{0}_{J(n_L)\times J(2)} & \cdots & \boldsymbol{Q}_{k,k}^{n_L,n_L-1} & \boldsymbol{Q}_{k,k}^{n_L,n_L} \end{pmatrix} ,$$

for $0 \leq k \leq S-1$, $\boldsymbol{Q}_{k,k-1} = diag(\boldsymbol{Q}_{k,k-1}^{0,0}, \ldots, \boldsymbol{Q}_{k,k-1}^{n_L,n_L})$ with $1 \leq k \leq S-1$, and

$$\boldsymbol{Q}_{k,k+1} = \begin{pmatrix} \mathbf{0}_{J(0)\times J(0)} & \boldsymbol{Q}_{k,k+1}^{0,1} & \mathbf{0}_{J(0)\times J(2)} & \cdots & \mathbf{0}_{J(0)\times J(n_L-1)} & \mathbf{0}_{J(0)\times J(n_L)} \\ \mathbf{0}_{J(1)\times J(0)} & \mathbf{0}_{J(1)\times J(1)} & \boldsymbol{Q}_{k,k+1}^{1,2} & \cdots & \mathbf{0}_{J(1)\times J(n_L-1)} & \mathbf{0}_{J(1)\times J(n_L)} \\ \mathbf{0}_{J(2)\times J(0)} & \mathbf{0}_{J(2)\times J(1)} & \mathbf{0}_{J(2)\times J(2)} & \cdots & \mathbf{0}_{J(2)\times J(n_L-1)} & \mathbf{0}_{J(2)\times J(n_L)} \\ \vdots & \vdots & \vdots & \ddots & \vdots & \vdots \\ \mathbf{0}_{J(n_L)\times J(0)} & \mathbf{0}_{J(n_L)\times J(1)} & \mathbf{0}_{J(n_L)\times J(2)} & \cdots & \mathbf{0}_{J(n_L)\times J(n_L-1)} & \boldsymbol{Q}_{k,k+1}^{n_L-1,n_L} \end{pmatrix} ,$$

for $0 \leq k \leq S-1$, with $J(r) = n_L - r + 1$. In the previous expressions, $diag(\boldsymbol{A}_1, \ldots, \boldsymbol{A}_p)$ is a diagonal-by-blocks matrix with blocks $\boldsymbol{A}_1$, …, $\boldsymbol{A}_p$ in the diagonal, and the matrices $\mathbf{0}_{a\times b}$ are matrices of zeros with dimension $a \times b$. The sub-matrix $\boldsymbol{Q}_{k,k'}^{r,r'}$ contains those infinitesimal transition rates corresponding to transitions from states in $L(k;r)$ to states in $L(k';r')$. By ordering states within $L(k;r)$ as indicated below and making use of the transitions described in Table 3.11

$$(0,r,k) \prec (1,r,k) \prec \cdots \prec (n_L - r - 1, r, k) \prec (n_L - r, r, k) ,$$

the following can be obtained

$$\left(\boldsymbol{Q}_{k,k}^{r,r}\right)_{ij} = \begin{cases} 2\alpha_+(n_L - i - r)(n_{R_2} - i - 2r) , & \text{if } j = i+1 , \\ \alpha_- i , & \text{if } j = i-1 , \\ -\Delta_{(i,r,k)} , & \text{if } j = i , \\ 0 , & \text{otherwise} , \end{cases}$$

for $0 \leq i, j \leq n_L - r$,

$$\left(\boldsymbol{Q}_{k,k}^{r,r-1}\right)_{ij} = \begin{cases} 2\beta_- r , & \text{if } j = i+1 , \\ 0 , & \text{otherwise} , \end{cases}$$

for $0 \leq i \leq n_L - r$, $0 \leq j \leq n_L - r + 1$,

$$\left(\boldsymbol{Q}_{k,k+1}^{r,r+1}\right)_{ij} = \begin{cases} \beta_+ i(n_{R_2} - i - 2r) , & \text{if } j = i-1 , \\ 0 , & \text{otherwise} , \end{cases}$$

for $0 \leq i \leq n_L - r$, $0 \leq j \leq n_L - r - 1$, and

$$\left(\boldsymbol{Q}^{r,r}_{k,k-1}\right)_{ij} = \begin{cases} \lambda k\,, & \text{if } j = i\,, \\ 0\,, & \text{otherwise}\,, \end{cases}$$

for $0 \leq i, j \leq n_L - r$.

The system of equations given by Equation (3.36) can be rewritten in matrix form, by storing the moments $w^l_{(n_1,n_2,s)}$ for $(n_1, n_2, s) \in \mathcal{S}^S$ in a column vector $\boldsymbol{w}^l$. Hence, $\boldsymbol{w}^l$ is equal to

$$\begin{pmatrix} \boldsymbol{w}^l_0 \\ \boldsymbol{w}^l_1 \\ \vdots \\ \boldsymbol{w}^l_{S-2} \\ \boldsymbol{w}^l_{S-1} \end{pmatrix} = \begin{pmatrix} \boldsymbol{A}_{0,0} & \boldsymbol{A}_{0,1} & \boldsymbol{0}_J & \dots & \boldsymbol{0}_J \\ \boldsymbol{A}_{1,0} & \boldsymbol{A}_{1,1} & \boldsymbol{A}_{1,2} & \dots & \boldsymbol{0}_J \\ \boldsymbol{0}_J & \boldsymbol{A}_{2,1} & \boldsymbol{A}_{2,2} & \dots & \boldsymbol{0}_J \\ \vdots & \vdots & \vdots & \ddots & \vdots \\ \boldsymbol{0}_J & \boldsymbol{0}_J & \boldsymbol{0}_J & \dots & \boldsymbol{A}_{S-1,S-1} \end{pmatrix} \begin{pmatrix} \boldsymbol{w}^l_0 \\ \boldsymbol{w}^l_1 \\ \vdots \\ \boldsymbol{w}^l_{S-2} \\ \boldsymbol{w}^l_{S-1} \end{pmatrix} + \begin{pmatrix} \boldsymbol{b}^{l-1}_0 \\ \boldsymbol{b}^{l-1}_1 \\ \vdots \\ \boldsymbol{b}^{l-1}_{S-2} \\ \boldsymbol{b}^{l-1}_{S-1} \end{pmatrix} \quad (3.38)$$

which is directly related to the QBD structure of $\boldsymbol{Q}$ (Equation (3.37)). In particular, each matrix $\boldsymbol{A}_{k,k'}$ is obtained from the matrix $\boldsymbol{Q}_{k,k'}$ by dividing each row i (corresponding to a given state (n_1, n_2, s)) by $\Delta_{(n_1,n_2,s)}$, except for the case $(\boldsymbol{A}^{r,r}_{k,k})_{ii} = 0$, for $0 \leq i \leq n_L - r$, $0 \leq k \leq S - 1$ and $0 \leq r \leq n_L$. Furthermore, the sub-vectors $\boldsymbol{b}^l_k$ are obtained from $\boldsymbol{w}^l_k$ by multiplying each row i (corresponding to a particular state (n_1, n_2, s)) by $(l + 1)/\Delta_{(n_1,n_2,s)}$. Equation (3.38) clearly shows how the moment of order l is obtained from the moment of order $l - 1$, with $\boldsymbol{w}^0 = \boldsymbol{e}_{\#\mathcal{S}^S}$ a column vector of ones with dimension $\#\mathcal{S}^S$. Finally, Equation (3.38) can be solved by a forward-elimination backward-substitution method suggested by Ciarlet *et al.* (1989), making use of Algorithm 8. Matrix $\boldsymbol{I}_J$ in Algorithm 8 represents the identity matrix of dimension J.

$p = 0$
$\boldsymbol{w}_k^p = \boldsymbol{e}_J,\ 0 \leq k \leq S-1$
for $k = 0, \ldots, S-1$ **do**
  for $i = 0, \ldots, J-1$ **do**
    $(\boldsymbol{b}_k^p)_i = \frac{p+1}{\Delta_{(n_1,n_2,s)}} (\boldsymbol{w}_k^p)_i$
  end
end
$\boldsymbol{H}_0 = \mathbf{I}_J - \boldsymbol{A}_{0,0}$
for $k = 1, \ldots, S-1$ **do**
  $\boldsymbol{H}_k = \mathbf{I}_J - \boldsymbol{A}_{k,k} - \boldsymbol{A}_{k,k-1} \boldsymbol{H}_{k-1}^{-1} \boldsymbol{A}_{k-1,k}$
end
for $p = 1, \ldots, l$ **do**
  $\mathbf{J}_0^p = \boldsymbol{b}_0^{p-1}$
end
for $k = 1, \ldots, S-1$ **do**
  $\mathbf{J}_k^p = \boldsymbol{A}_{k,k-1} \boldsymbol{H}_{k-1}^{-1} \mathbf{J}_{k-1}^p + \boldsymbol{b}_k^{p-1}$
end
$\boldsymbol{w}_{S-1}^p = \boldsymbol{H}_{S-1}^{-1} \mathbf{J}_{S-1}^p$
for $k = S-2, \ldots, 0$ **do**
  $\boldsymbol{w}_k^p = \boldsymbol{H}_k^{-1} \left(\boldsymbol{A}_{k,k+1} \boldsymbol{w}_{k+1}^p + \mathbf{J}_k^p \right)$
end
for $k = 0, \ldots, S-1$ **do**
  for $i = 0, \ldots, J-1$ **do**
    $(\boldsymbol{b}_k^p)_i = \frac{p+1}{\Delta_{(n_1,n_2,s)}} (\boldsymbol{w}_k^p)_i$
  end
end

Algorithm 8: for solving Equation (3.38).

3.5.3 Local sensitivity analysis

The aim in this section is to analyse how the kinetic rates contribute to the signal generation. In particular, a local sensitivity (perturbation) analysis is developed, which allows to study how the time $T^S_{(n_1,n_2,s)}$ changes with small perturbations of the parameters $(\alpha_+, \alpha_-, \beta_+, \beta_-, \lambda)$, as it was shown for the ***DS*** hypothesis in Subsection 3.4.3. Since $T^S_{(n_1,n_2,s)}$ has been identified with an absorption time the

partial derivatives

$$\frac{\partial E\left((T^S_{(n_1,n_2,s)})^l\right)}{\partial\theta}\,, \tag{3.39}$$

can be computed for $\theta \in \{\alpha_+, \alpha_-, \beta_+, \beta_-, \lambda\}$, and for any $l \geq 1$. The arguments by Caswell (2011) can be applied and adapted to Algorithm 8. Given a matrix $\boldsymbol{B}(\theta)$ that depends on a parameter θ, one can write an equation analogous to Equation (3.34), as follows

$$\frac{\partial\left(\boldsymbol{B}(\theta)^{-1}\right)}{\partial\theta} \;=\; -\boldsymbol{B}(\theta)^{-1}\frac{\partial\boldsymbol{B}(\theta)}{\partial\theta}\boldsymbol{B}(\theta)^{-1}\,.$$

Thus, Algorithm 9 can be obtained by directly differentiating matrices and vectors in Algorithm 8. Then, the desired partial derivatives $\partial E\left((T^S_{(n_1,n_2,s)})^l\right)/\partial\theta$ are computed and stored in the vectors $\boldsymbol{w}_k^{l,(\theta)}$ for $\theta \in \{\alpha_+, \alpha_-, \beta_+, \beta_-, \lambda\}$. In Algorithm 9, the derivatives of the matrices $\boldsymbol{A}_{k,k'}$ with respect to θ, $\boldsymbol{A}^{(\theta)}_{k,k'}$, are computed by direct element-by-element differentiation. Moreover, the derivative of $\Delta_{(n_1,n_2,s)} = 2\alpha_+(n_L - n_1 - n_2)(n_{R_2} - n_1 - 2n_2) + \alpha_- n_1 + \beta_+ n_1(n_{R_2} - n_1 - 2n_2) + 2\beta_- n_2 + \lambda s$ with respect to θ, $\Delta^{(\theta)}_{(n_1,n_2,s)}$, is given by

$$\Delta^{(\theta)}_{(n_1,n_2,s)} \;=\; \begin{cases} 2(n_L - n_1 - n_2)(n_{R_2} - n_1 - 2n_2)\,, & \text{if } \theta = \alpha_+\,, \\ n_1\,, & \text{if } \theta = \alpha_-\,, \\ n_1(n_{R_2} - n_1 - 2n_2)\,, & \text{if } \theta = \beta_+\,, \\ 2n_2\,, & \text{if } \theta = \beta_-\,, \\ s\,, & \text{if } \theta = \lambda\,. \end{cases}$$

$p = 0$
$\boldsymbol{b}_k^{p,(\theta)} = \mathbf{0}_J,\ 0 \leq k \leq S-1$
$\boldsymbol{H}_0^{(\theta)} \;=\; -\boldsymbol{A}_{0,0}^{(\theta)}$
for $k = 1, \ldots, S-1$ **do**
  $\boldsymbol{H}_k^{(\theta)} \;=\; -\boldsymbol{A}_{k,k}^{(\theta)} - \boldsymbol{A}_{k,k-1}^{(\theta)}\boldsymbol{H}_{k-1}^{-1}\boldsymbol{A}_{k-1,k}$
  $+\boldsymbol{A}_{k,k-1}\boldsymbol{H}_{k-1}^{-1}\boldsymbol{H}_{k-1}^{(\theta)}\boldsymbol{H}_{k-1}^{-1}\boldsymbol{A}_{k-1,k}$
  $-\boldsymbol{A}_{k,k-1}\boldsymbol{H}_{k-1}^{-1}\boldsymbol{A}_{k-1,k}^{(\theta)}$
end
... continue on the next page

for $p = 1, \ldots, l$ **do**
  $\boldsymbol{J}_0^{p,(\theta)} = \boldsymbol{b}_0^{p-1,(\theta)}$
  for $k = 1, \ldots, S-1$ **do**
    $\boldsymbol{J}_k^{p,(\theta)} = \boldsymbol{A}_{k,k-1}^{(\theta)} \boldsymbol{H}_{k-1}^{-1} \boldsymbol{J}_{k-1}^{p} - \boldsymbol{A}_{k,k-1}$
    $\times \boldsymbol{H}_{k-1}^{-1} \boldsymbol{H}_{k-1}^{(\theta)} \boldsymbol{H}_{k-1}^{-1} \boldsymbol{J}_{k-1}^{p}$
    $+ \boldsymbol{A}_{k,k-1} \boldsymbol{H}_{k-1}^{-1} \boldsymbol{J}_{k-1}^{p,(\theta)} + \boldsymbol{b}_k^{p-1,(\theta)}$
  end
  $\boldsymbol{w}_{S-1}^{p,(\theta)} = -\boldsymbol{H}_{S-1}^{-1} \boldsymbol{H}_{S-1}^{(\theta)} \boldsymbol{H}_{S-1}^{-1} \boldsymbol{J}_{S-1}^{p}$
  $+ \boldsymbol{H}_{S-1}^{-1} \boldsymbol{J}_{S-1}^{p,(\theta)}$
  for $k = S-2, \ldots, 0$ **do**
    $\boldsymbol{w}_k^{p,(\theta)} = -\boldsymbol{H}_k^{-1} \boldsymbol{H}_k^{(\theta)} \boldsymbol{H}_k^{-1} \left(\boldsymbol{A}_{k,k+1} \boldsymbol{w}_{k+1}^{p} \right.$
    $\left. + \boldsymbol{J}_k^{p} \right) + \boldsymbol{H}_k^{-1} \left(\boldsymbol{A}_{k,k+1}^{(\theta)} \boldsymbol{w}_{k+1}^{p} \right.$
    $\left. + \boldsymbol{A}_{k,k+1} \boldsymbol{w}_{k+1}^{p,(\theta)} + \boldsymbol{J}_k^{p,(\theta)} \right)$
  end
  for $k = 0, \ldots, S-1$ **do**
    for $i = 0, \ldots, J-1$ **do**
      $(\boldsymbol{b}_k^{p,(\theta)})_i = \frac{(p+1)}{\Delta^2_{(n_1,n_2,s)}} \left((\boldsymbol{w}_k^{p,(\theta)})_i \Delta_{(n_1,n_2,s)} \right.$
      $\left. - (\boldsymbol{w}_k^{p})_i \Delta^{(\theta)}_{(n_1,n_2,s)} \right)$
    end
  end
end

Algorithm 9: to obtain the derivative of the l-th order moments $E\left((T^S_{(n_1,n_2,s)})^l \right)$ with respect to $\theta \in \{\alpha_+, \alpha_-, \beta_+, \beta_-, \lambda\}$.

3.5.4 Results

A series of numerical experiments related to those developed in Section 3.4 for a HUVEC are carried out in this section. For computational convenience, receptor-ligand dynamics are restricted to 4% of the cell surface, as in Section 3.4 so that $n_R = 232$, if a HUVEC contains, on average, 5800 VEGFR2 receptors. Given ligand-limiting conditions, I take $n_L \in \{23, 58, 116\}$, so that $2n_L \leq n_R$. These correspond to soluble ligand concentrations approximately equal to $c_L \in \{1pM, 2.5pM, 5pM\}$. The kinetic rates $\theta \in \{\alpha_+, \alpha_-, \beta_+, \beta_-\}$ are given in Table 3.6 (γ_+ and γ_- are not used). In Figure 3.14 the mean time $E\left(T^S_{(0,0,0)}\right)$ ($\pm$ standard

deviation) to reach a signalling threshold S is plotted, as a function of S, for the **DS** (which corresponds to the results reported in Section 3.4.4) and the **AS** hypotheses, for different ligand concentrations. First it can be noted that the asymptotic behaviour of the curves corresponding to the **DS** hypothesis is directly related to the biological interpretation of $T^S_{(0,0,0)}$. Since $T^S_{(0,0,0)}$ represents the time to reach a signalling threshold S, with $S(t) = P_2(t)$ under the **DS** hypothesis, it is clear that $S(t)$ can only take values in the interval $0 \leq s \leq n_L$. This is not the case in the **AS** hypothesis, where $S(t)$ can take any value $s \geq 0$, so that an almost linear behaviour is obtained for $E\left(T^S_{(0,0,0)}\right)$ as a function of S. As the number of ligands, n_L, increases and thus, the ligand concentration increases, signal generation is faster and the time required to reach a signalling threshold decreases. For example, $E\left(T^S_{(0,0,0)}\right)$ for $c_L = 1pM$ and the **DS** hypothesis, is approximately 2.5 times higher than for $c_L = 2.5pM$, for $S = 5$.

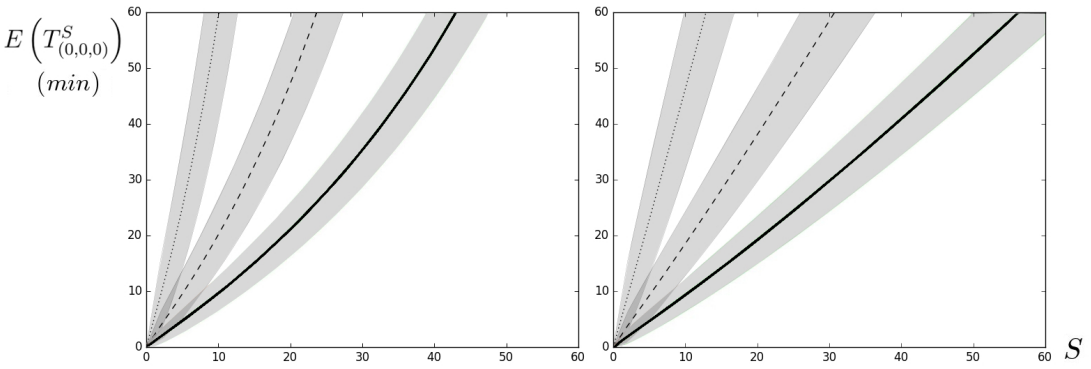

Figure 3.14: Mean time $E\left(T^S_{(0,0,0)}\right)$ ($\pm$ standard deviation) to reach a signalling threshold S, as a function of S, for the **DS** (*left*), see Figure 3.11 and the **AS** (*right*) hypotheses, and for ligand concentrations $c_L = 1pM$ (*dotted*), $c_L = 2.5pM$ (*dashed*) and $c_L = 5pM$ (*solid*).

In Figure 3.15 the mean time $E\left(T^S_{(0,0,0)}\right)$ ($\pm$ standard deviation) is plotted, when the **ASD-λ** hypothesis is considered, for different decay rates $\lambda \in \{10^{-4}, 0.5 \times 10^{-3}\}$. Numerical results of Figure 3.15, together with additional ones corresponding to different values of λ and not reported here show that, as expected, in the limit $\lambda \to 0$, the behaviour under the **ASD-λ** hypothesis tends

to the behaviour observed in Figure 3.14 for the **AS** hypothesis. The process under the **ASD-**λ hypothesis should be seen as an intermediate regime between the **DS** and the **AS** case, for moderate values of the decay rate λ. Thus, a similar asymptotic behaviour for $E\left(T^S_{(0,0,0)}\right)$ can be observed in Figure 3.15 for the **ASD-**λ hypothesis to the observed for the **DS** case in Figure 3.14. For higher values of the decay signal λ, the signalling threshold S is reached slowly, regardless of the ligand concentration. In particular, the results displayed in Figure 3.15 suggest that concentration would play a more important role if cellular mechanisms led to low signal decay rates. For higher values of λ, ligand concentration becomes less important.

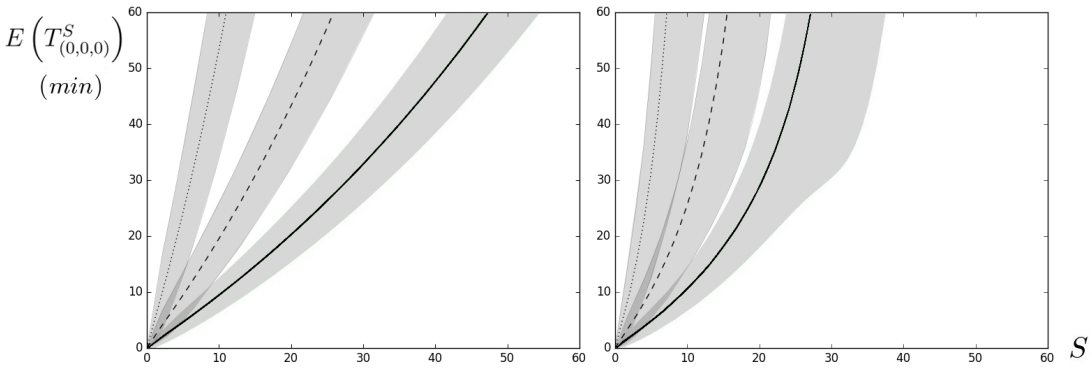

Figure 3.15: Mean time $E\left(T^S_{(0,0,0)}\right)$ ($\pm$ standard deviation) to reach a signalling threshold S, as a function of S, under the **ASD-**λ hypothesis for ligand concentrations $c_L = 1pM$ (*dotted*), $c_L = 2.5pM$ (*dashed*) and $c_L = 5pM$ (*solid*) and for $\lambda = 10^{-4}s^{-1}$ (*left*) and $\lambda = 0.5 \times 10^{-3}s^{-1}$ (*right*).

The impact of the different kinetic rates in the descriptor, for each hypothesis considered, can be analysed by means of the results summarised in Table 3.12. In particular, the dimensionless partial derivatives (or *elasticities*) $\left(\partial E\left(T^S_{(0,0,0)}\right)/\partial\theta\right) \times \left(\theta/E\left(T^S_{(0,0,0)}\right)\right)$ are computed for the parameters $\theta \in \{\alpha_+, \alpha_-, \beta_+, \beta_-, \lambda\}$, for concentration $c_L = 2.5pM$, and for the **DS** (see Tables 3.9 and 3.10), **AS** and **ASD-**λ hypotheses.

Signalling hypothesis	α_+	α_-	β_+	β_-	λ
DS	-9.93×10^{-1}	3.15×10^{-2}	-4.31×10^{-2}	4.82×10^{-3}	–
ASD-λ $\lambda = 0$	-8.71×10^{-1}	2.65×10^{-2}	-4.17×10^{-2}	-1.14×10^{-1}	–
ASD-λ $\lambda = 10^{-4}$	-9.39×10^{-1}	2.93×10^{-2}	-4.41×10^{-2}	-1.43×10^{-1}	9.60×10^{-2}
ASD-λ $\lambda = 0.5 \times 10^{-3}$	-1.47×10^{0}	6.02×10^{-2}	-7.53×10^{-2}	-5.90×10^{-1}	1.08×10^{0}

Table 3.12: Elasticities $\left(\partial E\left(T^S_{(0,0,0)}\right)/\partial\theta\right) \times \left(\theta/E\left(T^S_{(0,0,0)}\right)\right)$, where $\theta \in \{\alpha_+, \alpha_-, \beta_+, \beta_-, \lambda\}$, for the **DS**, **AS** and **ASD-λ** (with $\lambda = 10^{-4}s^{-1}$ and $\lambda = 0.5 \times 10^{-3}s^{-1}$) hypotheses. S is chosen as 25% of the total number, n_L, of ligands. Concentration $c_L = 2.5pM$.

Results of Table 3.12 lead to the following insights:

- The monomer formation rate, α_+, is the most important rate regardless of the scenario under consideration. That is, the formation of monomers in the system, which allows the subsequent formation of dimers and signal generation, is more important than, for example, the signal (or dimer) formation rate itself, β_+.

- When signal decay is considered, the decay rate λ becomes one of the most important kinetic rates in the system.

- A qualitative difference is observed for the dimer dissociation rate, β_-, between the **DS** and the rest of hypotheses. $\partial E\left(T^S_{(0,0,0)}\right)/\partial\beta_-$ is positive under the **DS** hypothesis, since β_- represents loss of signal (or bound dimeric complex). Thus, if the dimer dissociation rate increases, the time to reach a given signalling threshold also increases. On the other hand, $\partial E\left(T^S_{(0,0,0)}\right)/\partial\beta_-$ is negative under the **AS** and **ASD** hypotheses. This implies that, since signal is generated each time a dimer is formed, stable dimers would result in a disadvantage for signal generation (given that the total number of soluble molecules is fixed). Thus, dimer dissociation would

allow the formation of new dimers, so that signal could be generated in a more efficient way.

3.5.5 Discussion

In this section a matrix-analytic approach was used to compute the timescales for signal generation under different hypotheses. It was done so by studying a continuous probabilistic performance measure which results in a first-passage time, and which follows a phase-type distribution. First-passage times are not the only descriptors that can be considered, and alternative probabilistic measures can be proposed depending on the particular features of interest for the process under analysis. For example, for the stochastic process considered in this section, a discrete probabilistic descriptor that complements the analysed descriptor $T^S_{(n_1,n_2,s)}$, and that helps to understand the results, is

$$N^S_{(n_1,n_2,s)} = \textit{“Number of dimer formation events that take place before a signalling threshold } S \textit{ is reached, given the current state } (n_1,n_2,s) \textit{ of the process”.}$$

This stochastic descriptor can be seen as a discrete version of $T^S_{(n_1,n_2,s)}$. That is, $N^S_{(n_1,n_2,s)}$ represents the required number of dimer formation events in order to reach the signalling threshold S, so that $N^S_{(n_1,n_2,s)} = S$ under the **AS** hypothesis. The random variable $N^S_{(n_1,n_2,s)}$ measures the *resistance* of the system to signal generation (through signal decay for the **ASD-λ** hypothesis, or through dimer dissociation for the **DS** hypothesis), and it can be analysed in a similar way as done for $T^S_{(n_1,n_2,s)}$. In particular, if one considers the probability generating function $\mu^S_{(n_1,n_2,s)}(z) = E\left(z^{N^S_{(n_1,n_2,s)}}\right)$ for $|z| \leq 1$, the different factorial moments and the probability mass function of $N^S_{(n_1,n_2,s)}$ can be computed as

$$\begin{aligned} v^{S,l}_{(n_1,n_2,s)} &= E\left(N^S_{(n_1,n_2,s)}(N^S_{(n_1,n_2,s)}-1)\cdots(N^S_{(n_1,n_2,s)}-l+1)\right) \\ &= \left.\frac{d^l}{dz^l}\mu^S_{(n_1,n_2,s)}(z)\right|_{z=1}, \end{aligned}$$

$$Prob\left(N^S_{(n_1,n_2,s)}=a\right) = \left.\frac{1}{a!}\frac{d^a}{dz^a}\mu^S_{(n_1,n_2,s)}(z)\right|_{z=0}.$$

The probability generating function, $\mu^S_{(n_1,n_2,s)}(z)$, can be computed in a similar way to that of $\phi^S_{(n_1,n_2,s)}(z)$, by following a first-step argument, so that an analogous equation to Equation (3.35) is obtained. Successive differentiation of this equation leads to (omitting the superscript S)

$$\begin{aligned}\Delta_{\boldsymbol{n}} v^l_{\boldsymbol{n}} &= 2\alpha_+(n_L - n_1 - n_2)(n_{R_2} - n_1 - 2n_2)v^l_{(n_1+1,n_2,s)} + \alpha_- n_1 v^l_{(n_1-1,n_2,s)} + \beta_+ n_1 \\ &\quad \times(n_{R_2} - n_1 - 2n_2)v^l_{(n_1-1,n_2+1,s+1)} + 2\beta_- d v^l_{(n_1+1,n_2-1,s)} + \lambda s v^l_{(n_1,n_2,s-1)} \\ &\quad + l\beta_+ m(n_{R_2} - n_1 - 2n_2)v^{l-1}_{(n_1-1,n_2+1,s+1)}\,, \quad \boldsymbol{n} \in \mathcal{S}^S\,, \end{aligned} \tag{3.40}$$

for $l \geq 1$ and $\boldsymbol{n} = (n_1, n_2, s)$, so that a system of linear equations is obtained. The difference between Equation (3.40) and Equation (3.36) lies in the last term of both equations, where $l w^{l-1}_{(n_1,n_2,s)}$ is replaced by $l\beta_+ n_1(n_{R_2} - n_1 - 2n_2)v^{l-1}_{(n_1-1,n_2+1,s+1)}$. This implies that an adapted version of Algorithm 8 can be implemented as follows to solve the system given by Equation (3.40): vectors $\boldsymbol{w}^p_k$ (storing moments $w^p_{(n_1,n_2,s)}$ for states $(n_1, n_2, s) \in L(k)$) are replaced by vectors $\mathbf{v}^p_k$ (storing factorial moments $v^p_{(n_1,n_2,s)}$), and auxiliary vectors $\boldsymbol{b}^p_k$ (with component i obtained as $\frac{p+1}{\Delta_{(n_1,n_2,s)}}(\boldsymbol{w}^p_k)_i$) are replaced by auxiliary vectors $\mathbf{c}^p_k$ (with component i obtained as $\frac{p+1}{\Delta_{(n_1-1,n_2+1,s+1)}}(\mathbf{v}^p_{k+1})_i$).

The mean of $N^S_{(0,0,0)}$ is plotted in Figure 3.16 as done in Figure 3.15 for the mean of $T^S_{(0,0,0)}$. The qualitative behaviour displayed in Figure 3.16 is in agreement to that observed in Figure 3.15. For example, $E\left(N^S_{(0,0,0)}\right)$ displays a linear behaviour with respect to S when $\lambda \to 0$, which is related to the fact that $N^S_{(0,0,0)} = S$ under the **AS** hypothesis. The values of $E\left(N^S_{(0,0,0)}\right)$ for small values of S are much the same, do not depend on the particular value of λ or the concentration c_L. This implies that low signalling thresholds S are reached after S dimer formation events, where signal decay does not have enough time to play a role for short timescales. If the interest is in the time to reach a large signalling threshold S, then the decay rate λ plays a fundamental role, as well as the ligand concentration c_L.

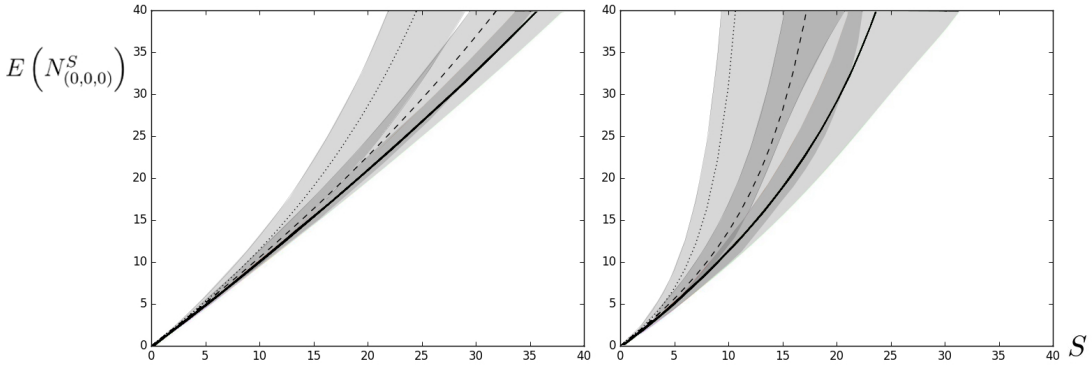

Figure 3.16: Mean number $E\left(N^S_{(0,0,0)}\right)$ ($\pm$ standard deviation) of dimer formation events to reach a signalling threshold S, as a function of S, under the **ASD-λ** hypothesis for ligand concentrations $c_L = 1pM$ (*dotted*), $c_L = 2.5pM$ (*dashed*) and $c_L = 5pM$ (*solid*) and for $\lambda = 10^{-4}s^{-1}$ (*left*) and $\lambda = 0.5 \times 10^{-3}s^{-1}$ (*right*).

The stochastic descriptor $T^S_{(n_1,n_2,s)} = inf\{t \geq 0 : S(t) = S \mid (M(0), P_2(0), S(0)) = (n_1, n_2, s)\}$ is proposed for measuring the time to reach a signalling threshold S, for different signalling hypotheses (**DS**, **AS** and **ASD-λ**) that translate into different definitions for the stochastic variable $S(t)$. Since $T^S_{(n_1,n_2,s)}$ is a random variable, the values of $E\left(T^S_{(n_1,n_2,s)}\right)$ and $SD\left(T^S_{(n_1,n_2,s)}\right)$ (standard deviation) are plotted. However, a slightly different alternative is to consider the scalar value

$$ET^S_{(n_1,n_2,s)} = inf\{t \geq 0 : E\left(S(t)\right) = S \mid (M(0), P_2(0), S(0)) = (n_1, n_2, s)\},$$

where in general $E\left(T^S_{(n_1,n_2,s)}\right) \neq ET^S_{(n_1,n_2,s)}$. Value $ET^S_{(n_1,n_2,s)}$ should be seen as the stochastic version of the deterministic counterpart $DT^S_{(n_1,n_2,s)} = inf\{t \geq 0 : S(t) = S \mid (M(0), P_2(0), S(0)) = (n_1, n_2, s)\}$ where here $S(t)$ represents the

variable of the deterministic process given by equations

$$\begin{aligned}
\frac{dM_2(t)}{dt} &= 2\alpha_+(n_L - M_2(t) - P_2(t))(n_{R_2} - M_2(t) - 2P_2(t)) + 2\beta_- P_2(t) \\
&\quad -\alpha_- M_2(t) - \beta_+ M_2(t)(n_{R_2} - M_2(t) - 2P_2(t)), \\
\frac{dP_2(t)}{dt} &= \beta_+ M_2(t)(n_{R_2} - M_2(t) - 2P_2(t)) - 2\beta_- P_2(t), \\
\frac{dS(t)}{dt} &= \begin{cases} \frac{dP_2(t)}{dt}, & \textit{under the } \textbf{DS}, \\ \beta_+ M_2(t)(n_{R_2} - M_2(t) - 2P_2(t)), & \textit{under the } \textbf{AS}, \\ \beta_+ M_2(t)(n_{R_2} - M_2(t) - 2P_2(t)) - \lambda S(t), & \textit{under the } \textbf{ASD-}\lambda. \end{cases}
\end{aligned}$$

These comments can be illustrated by comparing in Table 3.13 between values of $E\left(T^S_{(0,0,0)}\right)$, $ET^S_{(0,0,0)}$ and $DT^S_{(0,0,0)}$, for $c_L = 2.5pM$, for different signalling hypotheses and for different values of λ.

Signalling hypothesis	$E\left(T^S_{(0,0,0)}\right)$	$ET^S_{(0,0,0)}$	$DT^S_{(0,0,0)}$
DS	30.90	32.00	31.98
AS (**ASD-**λ, $\lambda = 0$)	27.43	27.50	27.58
ASD-λ, $\lambda = 10^{-4}$	29.52	30.17	30.20
ASD-λ, $\lambda = 0.5 \times 10^{-3}$	42.50	63.33	63.33

Table 3.13: Values of $E\left(T^S_{(0,0,0)}\right)$, $ET^S_{(0,0,0)}$ and $DT^S_{(0,0,0)}$ (in minutes) for **DS**, **AS** and **ASD-**λ (with $\lambda = 10^{-4}s^{-1}$, $\lambda = 0.5 \times 10^{-3}s^{-1}$) hypotheses. S is chosen as 25% of the total number n_L of ligands. Concentration $c_L = 1pM$.

$ET^S_{(0,0,0)}$ is computed by carrying out 10^5 Gillespie simulations of the stochastic process, while $DT^S_{(0,0,0)}$ is computed by simulating the deterministic process. While in those scenarios that favour signalling (*e.g.,* **AS** hypothesis) the three descriptors report similar values, those scenarios that prevent from signalling (*e.g.,* **ASD-**λ hypothesis, with $\lambda = 0.5 \times 10^{-3}s^{-1}$) report similar values for $ET^S_{(0,0,0)}$ and $DT^S_{(0,0,0)}$, but a value of $E\left(T^S_{(0,0,0)}\right)$ that significantly differs from these. This is related to the fact that $ET^S_{(n_1,n_2,s)}$ and $DT^S_{(n_1,n_2,s)}$ are the stochastic and deterministic version of the same quantity (time at which the system has an average signalling level S), while $E\left(T^S_{(n_1,n_2,s)}\right)$ has a slightly different meaning (average time until the system reaches signalling level S for the first time). This difference can be noticed from the fact that, for example for the **DS** hypothesis and for high

values of S, one may have $ET^S_{(n_1,n_2,s)} = DT^S_{(n_1,n_2,s)} = \infty$, while $E\left(T^S_{(n_1,n_2,s)}\right)$ is always finite for $0 \leq S \leq n_L$ since the stochastic process under study evolves among an irreducible class of positive recurrent states, so that every state is visited with probability one in finite mean time.

The dynamics of the process were restricted in previous results within a 4% of the cell, for computational convenience. However, one should expect similar results if the entire cell were to be considered instead. To illustrate this, the values of $E\left(T^S_{(n_1,n_2,s)}\right)$ when considering 4% or 100% of the cell are compared in Table 3.14. Results related to 4% of the cell are analytically computed, while results corresponding to 100% of the cell are computed by carrying out 10^5 Gillespie simulations of the stochastic process. When considering 100% of the cell, new binding rates $\hat{\alpha}_+ = 0.04\alpha_+$ and $\hat{\beta}_+ = 0.04\beta_+$ need to be considered (see Subsection 3.2.1). Values of $E\left(T^S_{(n_1,n_2,s)}\right)$ slightly vary only from a quantitative perspective, while the qualitative behaviour is the same when considering 4% or 100% of the cell. Thus, the conclusions in this section remain valid.

% of the cell	Signalling hypothesis	$S = 5\%$ of n_L	$S = 10\%$ of n_L	$S = 15\%$ of n_L
4%	**DS**	5.69	11.52	17.89
	AS (**ASD-**λ, $\lambda = 0$)	5.61	11.05	16.63
	ASD-λ, $\lambda = 10^{-4}$	5.67	11.37	17.43
	ASD-λ, $\lambda = 0.5 \times 10^{-3}$	5.91	12.83	21.85
100%	**DS**	5.54	11.28	17.47
	AS (**ASD-**λ, $\lambda = 0$)	5.43	10.72	16.09
	ASD-λ, $\lambda = 10^{-4}$	5.50	11.08	16.92
	ASD-λ, $\lambda = 0.5 \times 10^{-3}$	5.85	12.89	22.18

Table 3.14: Values of $E\left(T^S_{(0,0,0)}\right)$ (in minutes) when analysing 4% or 100% of the cell, for **DS**, **AS** and **ASD-**λ (with $\lambda = 10^{-4}s^{-1}$, $\lambda = 0.5 \cdot 10^{-3}s^{-1}$) hypotheses, and different values of S. Concentration $c_L = 2.5pM$.

This Section shows how to exploit the Markovian nature of the stochastic process under study in order to analyse a number of characteristics of interest in the process (*e.g.*, time to reach a signalling threshold), while sidestepping the so-

lution of the CME. The application of first-step arguments over Laplace-Stieltjes transforms and probability generating functions, corresponding to a number of random variables (stochastic descriptors, or performance measures) conveniently defined, allow us to reduce the analysis of these random variables to the solution of a number of systems of linear equations. While this approach is, in principle, feasible in any CTMC, computational limitations related to the dimensionality of the process under study imply the convenience of exploiting, if possible, the structure of the space of states of this process.

Chapter 4

VEGF-VEGFR intracellular trafficking

In Chapter 3 I focused on finding an approximation of the solution of master equations describing models on the cell surface only. As there was small number of complexes involved in these studied models it was possible to find analytical solution for the moments. In Chapter 4 I introduce more complex models involving events that happen not only on the cell surface but also inside the cell. This chapter contains more statistical work as I use experimental data in order to infer parameters of the proposed models. I use here Bayesian inference which is a flexible method and it can be used even for complex mathematical models. The data presented in this chapter were gathered by researchers at the laboratory of Dr. Sreenivasan Ponnambalam from the School of Molecular and Cellular Biology at the University of Leeds using *western blot* methodology (sometimes called the protein immunoblotting). It is a technique used in molecular biology, immunogenetics and other molecular biology disciplines to detect specific proteins in a sample of tissue homogenate or extract (see Mahmood & Yang (2012)).

This chapter is organised as follows: in Section 4.1 I provide a mathematical model, with accompanying quantitative experimental data, for binding and trafficking kinetics of vascular endothelial growth factor receptors on human umbilical vein endothelial cells. I calibrate the mathematical model of one receptor type, VEGFR2, and for two different isoforms of VEGF-A ligand to analyse how each of the isoforms can affect VEGFR2 phosphorylation. In order to study intracellular

signalling I additionally propose and test two hypotheses explaining dependence of extracellular signal-regulated kinases (ERK) phosphorylation on the localisation of the phosphorylated bound receptors in a cell. In Section 4.2 I study the mathematical model for two types of receptors, VEGFR1 and VEGFR2. The parameters of this model are calibrated using quantitative experimental data. I also analyse how the localisation of the bound phosphorylated dimers may affect the synthesis of new receptors in a cell.

4.1 A model of ERK phosphorylation induced by VEGF-A isoforms

Vascular endothelial growth factor A regulates many aspects of vascular physiology. All VEGF-A isoforms display similar binding affinity to VEGFR2 but unique receptor-ligand complexes can produce different functional outputs (see Delcombel *et al.* (2013), Keyt *et al.* (1996)). The kinetics of the endothelial response to different VEGF-A isoforms suggests that the exact location of the VEGF-A/VEGFR2 complex could have considerable implications for the controlled activation of different signalling pathways (see Ballmer-Hofer *et al.* (2011), Fearnley *et al.* (2014), Fearnley *et al.* (2015), Fearnley *et al.* (2016)). Notably, depending on the location of VEGF-A-stimulated VEGFR2 at the plasma membrane or the endosomes different enzymes could be activated that have pronounced effects on gene expression and endothelial function. Fearnley *et al.* (2014) show that VEGFR2 activation by VEGF-A programs differential phosphorylation of the residue Y1175. In particular VEGF-A_{165} isoform seems to greatly increase VEGFR2 phosphorylation at residue Y1175 when comparing it with VEGF-A_{121}. Binding of VEGF-A to VEGFR2 stimulates ERK phosphorylation and activation. Fearnley *et al.* (2014) measured phosphorylation of ERK at the residues Tr202 and Tr204 to find that VEGF-A_{165} was better in stimulating ERK than VEGF-A_{121}.

4.1.1 The experimental data for phosphorylation of VEGFR2 and ERK

In order to obtain some biological insights Fearnley *et al.* (2014) gathered some quantitative results via western blot analysis. In particular, the human umbilical vein endothelial cells were stimulated with 0.025, 0.25 and 1.25 nM of VEGF-A ligands (both isoforms, VEGF-A_{165} and VEGF-A_{121}), and some protein level measurements were obtained at different time instants within the following hour (for each ligand concentration and each isoform under consideration):

- the intensity of VEGFR2 phosphorylation at the residue Y1175,
- the intensity of ERK phosphorylation at the residues Tr202 and Tr204 (simultaneously).

All these intensities were given normalised by the levels of a control protein called (*Tubuline*), and where all the experiments were repeated four or six times. The data for the phosphorylated VEGFR2 receptors protein levels (pVEGFR2) are summarised in Table 4.1 whereas the data for the phosphorylated ERK protein levels (pERK) are summarised in Table 4.2. In particular, the experimental intensity value $ei(j, p, t, iso, c_l)$ corresponds to the jth experiment, $j \in \{1, 2, 3, 4, 5, 6\}$, when measuring the levels of protein $p \in \{\text{pVEGFR2, pERK}\}$ at time $t \in T = \{5\ min,\ 15\ min,\ 30\ min,\ 60\ min\}$ after the ligand stimulation with isoform $iso \in I = \{165, 121\}$ and using the ligand concentration $c_l \in C_L = \{0.025nM, 0.25nM,\ 1.25nM\}$. Each data point $data(j, p, t, iso, c_l)$ in Tables 4.1 and 4.2 was computed relative to a specific experiment,

$$data(j, p, t, iso, c_l) \quad = \quad \frac{ei(j, p, t, iso, c_l)}{ei(j, p, t = 5\ min, iso = 165, c_l = 1.25nM)}. \quad (4.1)$$

Table 4.2 consists of the data related only to the experiments 1, 4, 5 and 6, since the pERK observations from experiments 2 and 3 appear to deviate markedly from the other observations in the sample and were thus discarded as outliers by the experimentalists.

a)

stimulation with VEGF-A_{165}

time [min]	conc. [nM]	set 1	set 2	set 3	set 4	set 5	set 6	mean	sample SD
5	0.025	0.11	0.20	0.33	0.71	0.47	0.50	0.39	0.22
	0.25	1.27	2.23	0.88	1.42	2.00	0.79	1.43	0.58
	1.25	1.00	1.00	1.00	1.00	1.00	1.00	1.00	0.00
15	0.025	0.19	0.14	0.25	0.24	0.30	0.78	0.32	0.23
	0.25	0.76	0.80	0.92	0.21	1.12	0.63	0.74	0.31
	1.25	0.78	0.47	0.83	0.30	1.11	0.85	0.73	0.29
30	0.025	0.04	-	-	0.23	0.23	0.77	0.32	0.31
	0.25	0.17	-	-	0.32	0.26	0.88	0.41	0.32
	1.25	0.17	-	-	0.29	0.23	0.87	0.39	0.32
60	0.025	0.02	-	-	0.11	0.21	0.38	0.18	0.15
	0.25	0.10	-	-	0.16	0.28	0.55	0.27	0.20
	1.25	0.08	-	-	0.37	0.25	0.24	0.23	0.12

b)

stimulation with VEGF-A_{121}

time [min]	conc. [nM]	set 1	set 2	set 3	set 4	set 5	set 6	mean	sample SD
5	0.025	0.08	0.05	0.05	0.31	0.16	0.06	0.12	0.10
	0.25	0.17	0.17	0.07	0.68	0.18	0.10	0.23	0.23
	1.25	0.52	0.23	0.30	0.51	0.42	0.27	0.37	0.12
15	0.025	0.03	0.07	0.06	0.14	0.18	0.17	0.11	0.06
	0.25	0.10	0.09	0.15	0.35	0.37	0.50	0.26	0.17
	1.25	0.51	0.19	0.88	0.74	0.83	0.75	0.65	0.26
30	0.025	0.09	-	-	0.15	0.19	0.36	0.20	0.12
	0.25	0.37	-	-	0.45	0.27	0.51	0.40	0.10
	1.25	0.37	-	-	0.77	0.33	0.68	0.54	0.22
60	0.025	0.06	-	-	0.08	0.15	0.10	0.10	0.04
	0.25	0.08	-	-	0.15	0.21	0.22	0.16	0.07
	1.25	0.06	-	-	0.29	0.21	0.17	0.18	0.09

Table 4.1: Quantified VEGFR2 phosphorylation data: a) results for the experiments using VEGF-A_{165} as a stimulus; b) results for the experiments using VEGF-A_{121} as a stimulus. The experiments related with the data set 2 and set 3 were performed only up to 15 minutes.

a)

stimulation with VEGF-A_{165}

time $[min]$	conc. $[nM]$	set 1	set 4	set 5	set 6	mean	sample SD
5	0.025	0.223	0.430	0.498	0.345	0.374	0.119
	0.25	0.844	1.147	0.797	1.061	0.962	0.169
	1.25	1.000	1.000	1.000	1.000	1.000	0.000
15	0.025	0.728	0.534	0.771	0.926	0.740	0.161
	0.25	2.668	0.314	0.638	2.630	1.562	1.262
	1.25	2.300	0.526	0.851	2.584	1.565	1.027
30	0.025	0.147	0.342	0.807	0.159	0.364	0.309
	0.25	1.911	0.461	0.944	2.074	1.348	0.773
	1.25	1.534	0.639	0.859	1.524	1.139	0.459
60	0.025	0.097	0.214	0.396	0.152	0.215	0.130
	0.25	0.398	0.342	0.548	0.376	0.416	0.091
	1.25	0.255	0.243	0.243	0.275	0.254	0.015

b)

stimulation with VEGF-A_{121}

time $[min]$	conc. $[nM]$	set 1	set 4	set 5	set 6	mean	sample SD
5	0.025	0.070	0.147	0.073	0.129	0.105	0.039
	0.25	0.102	0.218	0.110	0.129	0.140	0.054
	1.25	0.696	0.223	0.289	0.691	0.475	0.254
15	0.025	0.215	0.087	0.193	0.323	0.205	0.097
	0.25	1.235	0.081	0.515	1.611	0.861	0.690
	1.25	2.339	0.133	0.783	2.571	1.457	1.187
30	0.025	0.141	0.094	0.380	0.180	0.199	0.126
	0.25	0.301	0.111	0.510	0.309	0.308	0.163
	1.25	1.132	0.059	0.665	0.818	0.669	0.450
60	0.025	0.069	0.069	0.120	0.131	0.097	0.033
	0.25	0.147	0.073	0.230	0.199	0.162	0.068
	1.25	0.136	0.066	0.191	0.195	0.147	0.060

Table 4.2: Quantified ERK phosphorylation data: a) results for the experiments using VEGF-A_{165} as a stimulus; b) results for the experiments using VEGF-A_{121} as a stimulus. The experiments related with the data set 2 and set 3 were not considered (see text for details).

4.1.2 Model 1: binding, trafficking

In this Section I propose a mathematical model, called Model 1, that explains how different VEGF-A isoforms can exert a different endothelial response by incorporating changes in VEGFR2 signal transduction, the membrane trafficking and the turnover. To this aim, the cell is split into three compartments (*cell surface*, *endosome* and *Golgi apparatus*), under the assumption that without ligand stimulation VEGFR2 receptors are located in these compartments following proportions 60% (surface), 20% (endosome) and 20% (Golgi apparatus) according to observations from Jopling *et al.* (2011) and personal communication with the group of Dr. Ponnambalam from the University of Leeds. Golgi apparatus, which is directly involved in receptor synthesis, is not explicitly included in the model, and synthesis of new receptors on the cell surface is assumed to occur with a constant rate for the first 60 minutes. This condition is relaxed in Section 4.2 where Golgi apparatus is considered as separate compartment. The marker $iso \in I = \{121, 165\}$ indicates that the rate for a specific reaction is isoform-dependent.

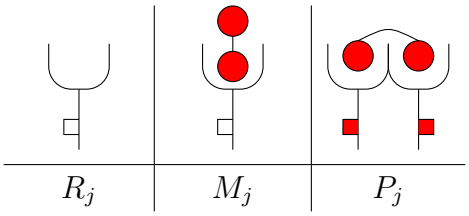

Table 4.3: Diagrams of molecules considered in Model 1. The index j denotes the localisation of each molecule; that is, $j = S$ for a molecule in the cell surface and $j = E$ for a molecule in the endosome.

The following reactions occurring according to the diagram in Figure 4.1 are considered for molecules described in Table 4.3

- binding (with rate α_+) of free receptor (R_S) with free ligand (L_S) on the cell surface, forming monomer (M_S), and dissociation (with rate α_-),
- binding (with rate β_+) of monomer (M_S) with free receptor (R_S) on the cell surface, forming phosphorylated dimer (P_S), and dissociation (with rate β_-),

- internalisation of free receptor (R_S) and monomers (M_S) with rate k_{int} and phosphorylated dimers (P_S) bound to VEGF-A$_{iso}$ with rate $k_{int}^{P,iso}$,
- recycling of free receptor (R_E) with rate k_{rec},
- dissociation of phosphorylated dimers (P_E) and monomers (M_E) (formed with VEGF-A$_{iso}$) in the endosome, occurring with the same rates than on the cell surface but multiplied by a factor $f^{iso} \geq 1$ (related to the more acidic environment of the endosome),
- degradation of free receptors (R_E) with rate k_{deg} in the endosome,
- synthesis of new free receptors (R_S) with rate k_{syn} on the cell surface.

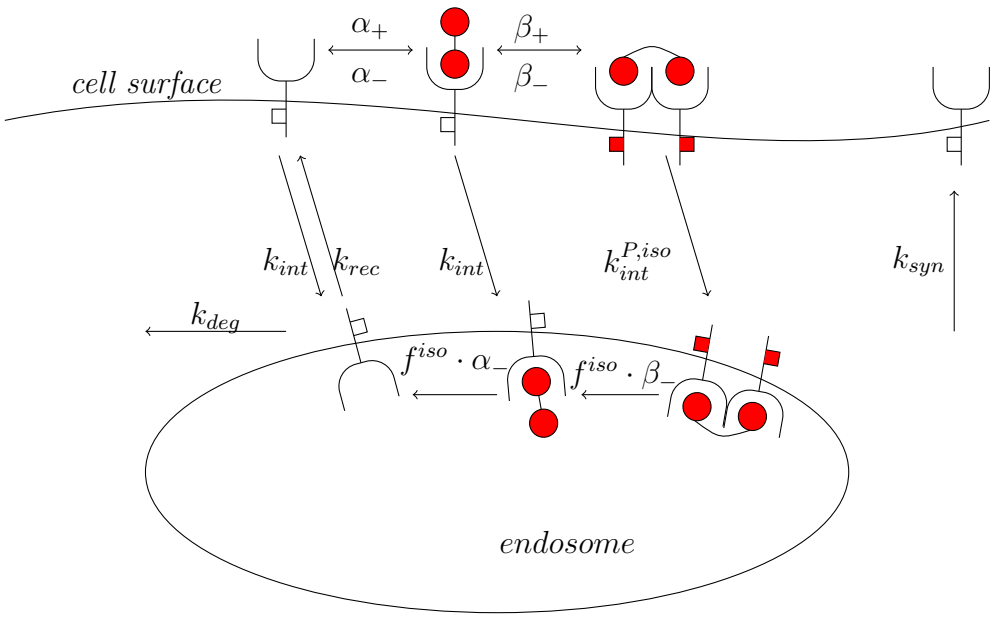

Figure 4.1: Events involved in Model 1 for binding and trafficking of the VEGFR2 receptor. Model parameters are described in the text.

The values of the binding and the dissociation rates are proposed to be identical for both isoforms. This assumption agrees with observations reported by Delcombel *et al.* (2013), where all of examined VEGF-A isoforms were able to bind to VEGFR2 with a dissociation constant within the $10^{-10} - 10^{-11} M$ range. The

internalisation of the bound monomers occurs at the same rate regardless the isoform. It is based on the assumption that the conformal change of the receptor takes place after the dimerisation. Therefore I assume that the internalisation of bound dimers occurs with a different rate for each isoform. The variables of Model 1 can be defined as follows,

$$\begin{aligned}
L_S(t) &= \text{“number of free ligands } L_S \text{ at time } t\text{”},\\
R_S(t) &= \text{“number of free receptors } R_S \text{ on the cell surface at time } t\text{”},\\
M_S(t) &= \text{“number of monomers } M_S \text{ on the cell surface at time } t\text{”},\\
P_S(t) &= \text{“number of phosphorylated dimers } P_S \text{ on the cell surface at time } t\text{”},\\
R_E(t) &= \text{“number of free receptors } R_E \text{ in the endosome at time } t\text{”},\\
M_E(t) &= \text{“number of monomers } M_E \text{ in the endosome at time } t\text{”},\\
P_E(t) &= \text{“number of phosphorylated dimers } P_E \text{ in the endosome at time } t\text{”},
\end{aligned}$$

for $t \geq 0$, where $t = 0$ represents the time instant when the ligand stimulation occurs. Dynamics of Model 1 can be described by the following equations,

$$\begin{aligned}
\frac{dL_S(t)}{dt} &= -2\alpha_+ L_S(t)R_S(t) + \alpha_- M_S(t),\\
\frac{dR_S(t)}{dt} &= -2\alpha_+ L_S(t)R_S(t) + \alpha_- M_S(t) - \beta_+ M_S(t)R_S(t) + 2\beta_- P_S(t)\\
&- k_{int}R_S(t) + k_{rec}R_E(t) + k_{syn},\\
\frac{dM_S(t)}{dt} &= 2\alpha_+ L_S(t)R_S(t) - \alpha_- M_S(t) - \beta_+ M_S(t)R_S(t) + 2\beta_- P_S(t) - k_{int}M_S(t),\\
\frac{dP_S(t)}{dt} &= \beta_+ M_S(t)R_S(t) - 2\beta_- P_S(t) - k_{int}^{P,iso}P_S(t),\\
\frac{dR_E(t)}{dt} &= k_{int}R_S(t) - k_{rec}R_E(t) - k_{deg}R_E(t) + 2f^{iso}\beta_- P_E(t) + f^{iso}\alpha_- M_E(t),\\
\frac{dM_E(t)}{dt} &= k_{int}M_S(t) + 2f^{iso}\beta_- P_E(t) - f^{iso}\alpha_- M_E(t),\\
\frac{dP_E(t)}{dt} &= k_{int}^{P,iso}P_S(t) - 2f^{iso}\beta_- P_E(t),
\end{aligned} \tag{4.2}$$

where $(L_S(0)\,, R_S(0), M_S(0), P_S(0), R_E(0), M_E(0), P_E(0)) = (n_L, n_R^S, 0, 0, n_R^E, 0, 0)$ is the initial condition based on the assumption that at $t = 0$ (that is without any ligands) monomers or dimers are not in the system. n_L, n_R^S and n_R^E are fixed numbers of ligands, receptors on the cell surface and receptors in the endosome.

Model 1 in the absence of ligand: parameters' constraints

The first aim here is to approximate some of the rates described above, for both isoforms VEGF-A_{165} and VEGF-A_{121} simultaneously, by using the data provided in Table 4.1. However, one can first reduce the dimensionality of the parameter space by computing the surface binding and the dissociation rates α_+, α_-, β_+ and β_- by following the arguments described for this particular receptor and ligand in Subsection 3.2.1. Note that rates β_+ and β_- are equal for both isoforms due to the similar value of the diffusion coefficient of VEGF-A_{165} and VEGF-A_{121} as shown by Mac Gabhann & Popel (2005). Moreover, one can consider the deterministic equations for the process without ligand stimulation,

$$\begin{aligned} \frac{dR_S(t)}{dt} &= -k_{int}R_S(t) + k_{rec}R_E(t) + k_{syn}, \\ \frac{dR_E(t)}{dt} &= k_{int}R_S(t) - k_{rec}R_E(t) - k_{deg}R_E(t), \end{aligned}$$

with the initial condition $(R_S(0), R_E(0)) = (n_R^S, n_R^E)$. The steady state (R_S^*, R_E^*) of this system is given by

$$R_S^* = \frac{k_{syn}(k_{rec} + k_{deg})}{k_{deg}k_{int}}, \quad R_E^* = \frac{k_{syn}}{k_{deg}}. \tag{4.3}$$

As explained earlier, the number of VEGFR2 on the cell surface and in the endosome at the steady state should verify the following proportion $R_S^*/R_E^* = 0.6/0.2 = 3$. Let n_R^T be the total number of receptors in the cell under no ligand stimulation, then $R_S^* + R_E^* = 0.8n_R^T$, which means that $R_S^* = 3/5n_R^T$ and $R_E^* = 1/5n_R^T$. This, together with Equation (4.3) leads to the following expressions for the synthesis and the internalisation rates,

$$k_{syn} = \frac{k_{deg}n_R^T}{5}, \quad k_{int} = \frac{1}{3}(k_{rec} + k_{deg}). \tag{4.4}$$

Global sensitivity analysis of Model 1

The experimentalists measured the total phosphorylation intensity of bound dimers which may be identified in Model 1 as a sum of dimers on the cell surface and in the endosome at any time t, for the initial ligand VEGF-A_{iso} concentration c_l, which is denoted here as $P(t, c_l, iso) = P_S(t) + P_E(t)$ for $L(0) = c_l$. Each measured value was divided by the results for VEGF-A_{165} stimulation for the initial concentration $c_l = 1.25nM$ at the time point $t = 5\ min$. Thus to compare the simulation of Model 1 with the data from Table 4.1 the following expression must be computed,

$$sim(t, c_l, iso) = \frac{P(t, c_l, iso)}{P(t = 5\ min, c_l = 1.25nM, iso = 165)}, \tag{4.5}$$

where $t \in T$, $c_l \in C_L$, $iso \in I$.

By using Sobol method, described in Section 2.3, one can learn about the impact of the parameters on the model. In particular, $sim(\cdot, \cdot, \cdot)$ defined by Equation (4.5) is used as the model output of interest, where the input is the set of parameters left to be estimated, that is $\boldsymbol{\theta} = (n_R^T, k_{rec}, k_{deg}, k_{int}^{P,165}, k_{int}^{P,121}, f^{165}, f^{121})$, where ranges considered for these parameters are defined in Table.

$n_R^T\ [molecules]$	$k_{rec}\ [s^{-1}]$	$k_{deg}\ [s^{-1}]$	$k_{int}^{P,iso}\ [s^{-1}]$	f^{iso}
$(10^3, 10^6)$	$(10^{-4}, 10^{-1})$	$(10^{-5}, 10^{-1})$	$(10^{-5}, 10^{-1})$	$(1, 10^2)$

Table 4.4: Ranges considered for $n_R^T, k_{rec}, k_{deg}, k_{int}^{P,iso}, f^{iso}$ for Model 1, when applying Sobol algorithm, where $iso \in \{121, 165\}$.

For each parameter from $\boldsymbol{\theta}$ there are 24 results obtained by performing Sobol algorithm as there are four time points, three concentrations and two isoforms being considered. The results of the sensitivity analysis are summarised in Table 4.5 and 4.6.

	S_1 mean	S_1 st deviation	S_1 range	S_T mean	S_T st deviation	S_T range
n_R^T	0.60	0.06	(0.50, 0.69)	0.82	0.05	(0.75, 0.88)
k_{rec}	0.01	0.001	(0.00, 0.03)	0.05	0.03	(0.02, 0.13)
k_{deg}	0.02	0.01	(0.00, 0.04)	0.14	0.05	(0.07, 0.25)
$k_{int}^{P,165}$	0.09	0.04	(0.05, 0.16)	0.19	0.07	(0.07, 0.31)
$k_{int}^{P,121}$	-	-	-	-	-	-
f^{165}	0.03	0.02	(0.00, 0.06)	0.12	0.03	(0.08, 0.16)
f^{121}	-	-	-	-	-	-

Table 4.5: Results of Sobol algorithm. The main effect index S_1 and the total effect index S_T for the model output $sim(\cdot, \cdot, iso = 165)$. The mean and the standard deviation were taken over all time points t and all concentrations c_l. Note that $sim(\cdot, \cdot, iso = 165)$ does not depend on $k_{int}^{P,121}$ and f^{121}.

	S_1 mean	S_1 st deviation	S_1 range	S_T mean	S_T st deviation	S_T range
n_R^T	0.05	0.03	(0.01, 0.08)	0.40	0.07	(0.30, 0.51)
k_{rec}	$< 10^{-5}$	$< 10^{-5}$	-	0.06	0.01	(0.03, 0.08)
k_{deg}	$< 10^{-5}$	$< 10^{-5}$	-	0.06	0.01	(0.04, 0.08)
$k_{int}^{P,165}$	0.01	0.01	(0.00, 0.04)	0.21	0.05	(0.12, 0.30)
$k_{int}^{P,121}$	0.31	0.07	(0.16, 0.39)	0.63	0.09	(0.48, 0.77)
f^{165}	0.01	0.01	(0.00, 0.03)	0.18	0.02	(0.14, 0.22)
f^{121}	0.06	0.05	(0.00, 0.14)	0.15	0.06	(0.08, 0.25)

Table 4.6: Results of Sobol algorithm. The main effect index S_1 and the total effect index S_T for the model output $sim(\cdot, \cdot, iso = 121)$. The mean and the standard deviation were taken over all time points t and all concentrations c_l. Note that $sim(\cdot, \cdot, iso = 121)$ depends on $k_{int}^{P,165}$ and f^{165} due to normalisation in Equation (4.5).

The parameter n_R^T is found to be the most sensitive parameter whereas k_{rec}, k_{deg} and f^{165} are found to have weak influence on the model output $sim(\cdot, \cdot, iso = 165)$. The mean total effect index of k_{rec} is close to zero, meaning that there is not much interaction going on between k_{rec} and the rest of the parameters.

As for the output $sim(\cdot, \cdot, iso = 121)$, the most sensitive parameter is $k_{int}^{P,121}$,

whereas k_{rec} and k_{deg} are found to be the least sensitive. k_{rec} and k_{deg} have low mean of the total index which suggests that there is not much interaction between each of them and the other parameters. There is lot of interaction between n_R^T and the other parameters as the mean $S_T = 0.40$.

The recycling rate k_{rec} and the degradation rate k_{deg} are the least sensitive parameters for all the outputs and therefore those rates are set in what follows from rates reported in the literature. The rest of the parameters, $\hat{\boldsymbol{\theta}} = (n_R^T, k_{int}^{P,165}, k_{int}^{P,121}, f^{165}, f^{121})$, are estimated in next subsection as they have some impact on the model output directly or by interacting with the other parameters.

Parameter inference for Model 1

The aim here is to use the data from Table 4.1 in order to estimate the remaining rates of interest $\hat{\boldsymbol{\theta}} = (n_R^T, k_{int}^{P,165}, k_{int}^{P,121}, f^{165}, f^{121})$ by using Bayesian techniques. Taking into consideration the results of the global sensitivity analysis the recycling rate k_{rec} and the degradation rate k_{deg} are fixed as $k_{rec} = 10^{-3}s^{-1}$ and $k_{deg} = 10^{-4}s^{-1}$ (see Tan *et al.* (2013c) and Mac Gabhann & Popel (2004)). This automatically leads to fixing free receptors and bound monomers internalisation rate according to Equation (4.4), that is $k_{int} = 3.67 \times 10^{-4}s^{-1}$. The prior distributions for the rest of the parameters are proposed based on the literature (see Mac Gabhann & Popel (2004), Vempati *et al.* (2010),Tan *et al.* (2013c), Anderson *et al.* (2011), French *et al.* (1995), Starbuck & Lauffenburger (1992) and Tzafriri & Edelman (2007)), so that parameters are considered in the ranges, $n_R^T \in (10^3, 10^6)$ receptors per cell, $k_{int}^{P,iso} \in (10^{-4}, 10^{-2})s^{-1}$, $f^{iso} \in (10^0, 10^2)$. Taking this into consideration, there are four different set of prior distributions proposed in Table 4.7. Each distribution has different mean and variance allowing to explore the same parameter space differently.

	Prior1	*Prior2*	*Prior3*	*Prior4*
n_R^T	$U(10^3, 10^6)$	$10^r, r \sim U(3,6)$	$10^r, r \sim U(3,6)$	$U(10^3, 10^6)$
$k_{int}^{P,165}$	$U(10^{-5}, 10^{-1})$	$10^r, r \sim U(-5,-1)$	$r^{-1}, r \sim U(10^1, 10^5)$	$10^r, r \sim U(-5,-1)$
$k_{int}^{P,121}$	$U(10^{-5}, 10^{-1})$	$10^r, r \sim U(-5,-1)$	$r^{-1}, r \sim U(10^1, 10^5)$	$10^r, r \sim U(-5,-1)$
f^{165}	$U(10^0, 10^2)$	$10^r, r \sim U(0,2)$	$10^r, r \sim U(0,2)$	$10^r, r \sim U(0,2)$
f^{121}	$U(10^0, 10^2)$	$10^r, r \sim U(0,2)$	$10^r, r \sim U(0,2)$	$10^r, r \sim U(0,2)$

Table 4.7: Proposal for prior distributions for $\hat{\boldsymbol{\theta}} = (n_R^T, k_{int}^{P,165}, k_{int}^{P,121}, f^{165}, f^{121})$.

The ABC algorithm, described in Subsection 2.4.2, is used to perform a series of $n \in \mathbb{N}$ simulations to obtain an approximation of the posterior distribution for $\hat{\boldsymbol{\theta}}$. Algorithm 10 describes in detail the ABC algorithm for Model 1, where the number of drawn samples $n = 10^6$ and the tolerance level $\epsilon = 0.001$ (which gave the acceptance ratio 0.1%). The comparison of the data with $sim(t, c_l, iso)$ defined by Equation (4.5) is done by a proper distance measure. In this particular case the Pearson distance (called normalised Euclidean distance) is used, defined as follows,

$$\delta(sim, data)^2 = \sum_{iso \in I} \sum_{c_l \in C_L} \sum_{t \in T} \frac{(sim(t, c_l, iso) - \mu_{data}(t, c_l, iso))^2}{\sigma_{data}(t, c_l, iso)}. \tag{4.6}$$

The mean $\mu_{data}(t, c_l, iso)$ and the sample variance $\sigma_{data}(t, c_l, iso)$ of the data $data(j, p = \text{pVEGFR2}, t, iso, c_l)$ defined by Equation (4.1) at the time $t \in T$ for the concentration $c_l \in C_L$ for the isoform $iso \in I$ over the series of the experiments performed in this setup (see Table 4.1) is given by the following equations,

$$\begin{aligned} \mu_{data}(t, c_l, iso) &= \sum_{j \in K} data(j, p = \text{pVEGFR2}, t, iso, c_l), \\ \sigma_{data}(t, c_l, iso) &= \frac{1}{k} \sum_{j \in K} \left(data(j, p = \text{pVEGFR2}, t, iso, c_l) - \mu_{data}(t, c_l, iso)\right)^2, \end{aligned} \tag{4.7}$$

where $K = \{1,2,3,4,5,6\}$, $k = 6$ for $t \in \{5, 15\}min$ and $K = \{1,4,5,6\}$, $k = 4$ for $t \in \{30, 60\}min$. The obtained approximation of the posterior distribution is later used as a prior distribution in the more computationally expensive MCMC algorithm, described in Subsection 2.4.3.

A1. *Let* $\pi(\hat{\boldsymbol{\theta}})$ *be one of the prior distributions, Prior1, Prior2, Prior3 or Prior4 defined in Table 4.7 for* $\hat{\boldsymbol{\theta}} = (n_R^T, k_{int}^{P,165}, k_{int}^{P,121}, f^{165}, f^{121})$.

A2. **for** $i = 1, \ldots, n$ **do**

1. *Generate* $\boldsymbol{\theta_i^*}$ *from* $\pi(\hat{\boldsymbol{\theta}})$.
2. *Generate* $sim(t, c_l, iso|\boldsymbol{\theta_i^*})$ *where* $t \in \{5\ min,\ 15\ min,\ 30\ min,\ 60\ min\}$, $c_l \in \{0.025nM, 0.25nM, 1.25nM\}$ *and* $iso \in \{165, 121\}$.
3. *Compute the distance* $\delta_i^* = \delta(sim, data|\boldsymbol{\theta_i^*})$ *from Equation (4.6).*

end

A3. *Accept, for each* $1 \leq i \leq n$, $n\epsilon$ *proposed* $\boldsymbol{\theta_i^*}$ *which result with the smallest distance* δ_i^*.

Algorithm 10: to find the approximation of posterior distribution of $\hat{\boldsymbol{\theta}}$ using the ABC method.

Figures 4.2, 4.3, 4.4 and 4.5 show the posterior distributions (in blue) obtained by Algorithm 10 for $\hat{\boldsymbol{\theta}} = (n_R^T, k_{int}^{P,165}, k_{int}^{P,121}, f^{165}, f^{121})$ using the prior distributions (in red) *Prior1, Prior2, Prior3* and *Prior4*, respectively, defined in Table 4.7. The results are shown in logarithmic scale.

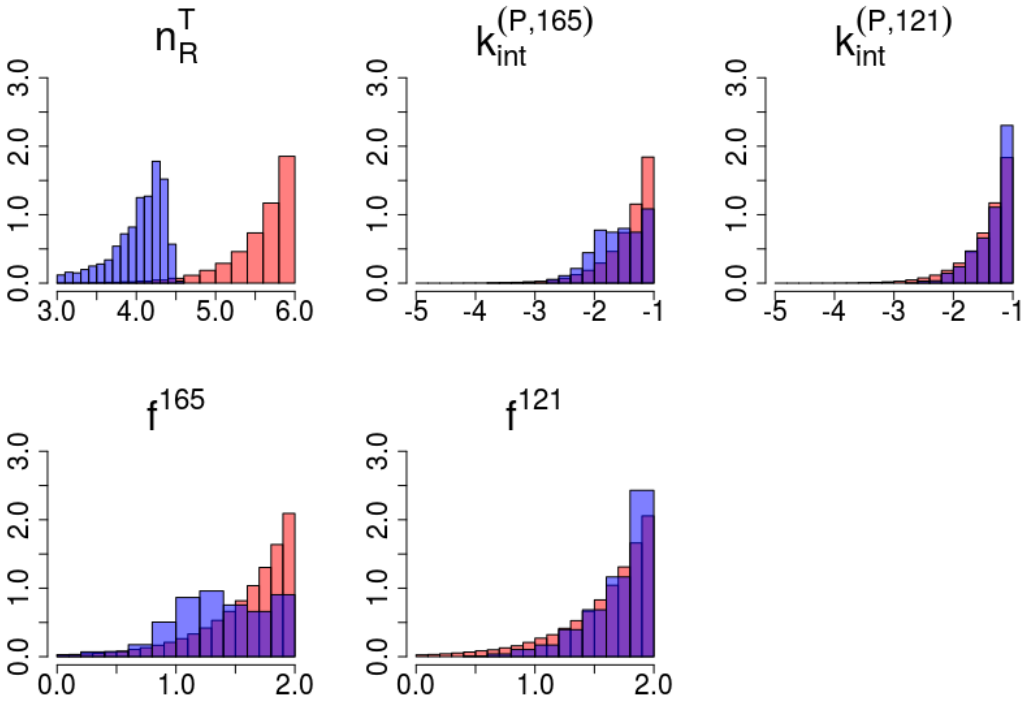

Figure 4.2: The red histograms represent sampled *Prior1*, whereas the blue histograms represent the estimated posterior distribution, called *Posterior1*, for $\hat{\boldsymbol{\theta}}$ obtained by Algorithm 10. Results are presented in logarithmic scale.

	n_R^T $[rec.\ per\ cell]$	$k_{int}^{P,165}$ $[s^{-1}]$	$k_{int}^{P,121}$ $[s^{-1}]$	f^{165}	f^{121}
Min.	1.00×10^3	2.18×10^{-4}	2.30×10^{-3}	1.14×10^0	2.85×10^0
1st Qu.	7.37×10^3	1.32×10^{-2}	3.39×10^{-2}	1.27×10^1	3.64×10^1
Median	1.30×10^4	2.68×10^{-2}	5.98×10^{-2}	2.31×10^1	6.18×10^1
Mean	1.35×10^4	3.63×10^{-2}	5.65×10^{-2}	3.38×10^1	5.89×10^1
3rd Qu.	1.93×10^4	5.78×10^{-2}	8.05×10^{-2}	5.10×10^1	8.22×10^1
Max.	3.34×10^4	9.95×10^{-2}	1.00×10^{-1}	9.98×10^1	1.00×10^2

Table 4.8: Summary statistics for the posterior distribution *Posterior1* of $\hat{\boldsymbol{\theta}} = (n_R^T, k_{int}^{P,165}, k_{int}^{P,121}, f^{165}, f^{121})$ in Figure 4.2, found by Algorithm 10 using the prior distribution *Prior1* defined in Table 4.7.

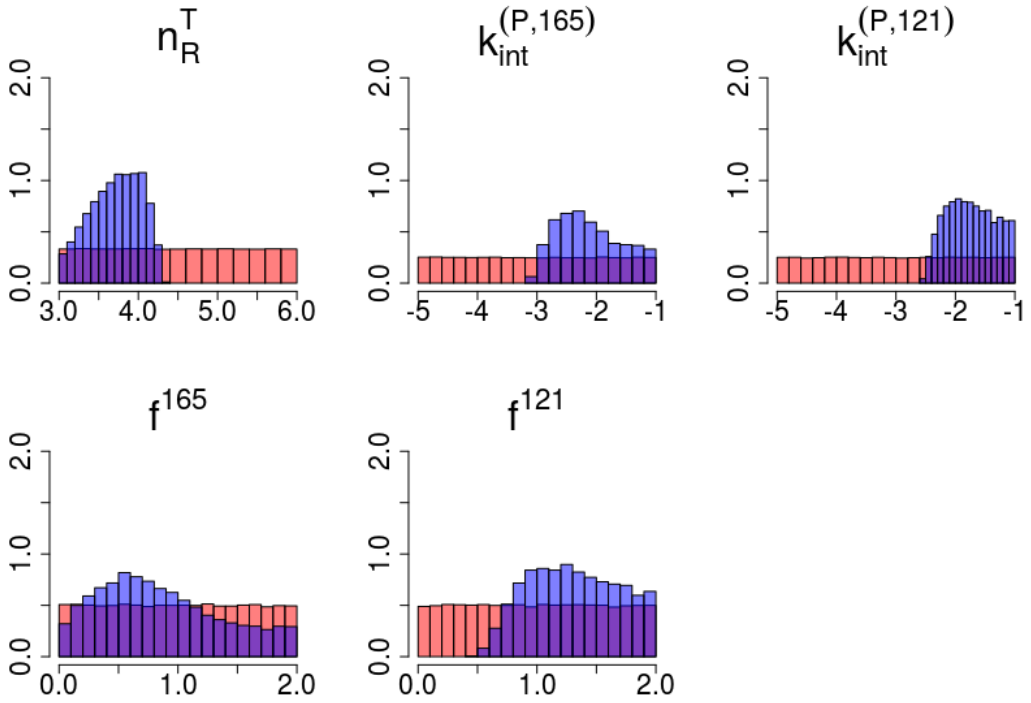

Figure 4.3: The red histograms represent sampled *Prior2*, whereas the blue histograms represent the estimated posterior distribution, called *Posterior2*, for $\hat{\boldsymbol{\theta}}$ obtained by Algorithm 10. Results are presented in logarithmic scale.

	n_R^T [*rec. per cell*]	$k_{int}^{P,165}$ $[s^{-1}]$	$k_{int}^{P,121}$ $[s^{-1}]$	f^{165}	f^{121}
Min.	1.00×10^3	7.41×10^{-4}	2.60×10^{-3}	1.00×10^0	3.03×10^0
1st Qu.	2.99×10^3	2.87×10^{-3}	8.76×10^{-3}	2.87×10^0	1.02×10^1
Median	5.53×10^3	6.57×10^{-3}	1.78×10^{-2}	6.02×10^0	1.98×10^1
Mean	6.60×10^3	1.67×10^{-2}	2.76×10^{-2}	1.50×10^1	2.91×10^1
3rd Qu.	9.47×10^3	2.01×10^{-2}	3.93×10^{-2}	1.63×10^1	4.17×10^1
Max.	2.19×10^4	1.00×10^{-1}	1.00×10^{-1}	9.96×10^1	1.00×10^2

Table 4.9: Summary statistics for the posterior distribution *Posterior2* of $\hat{\boldsymbol{\theta}} = (n_R^T, k_{int}^{P,165}, k_{int}^{P,121}, f^{165}, f^{121})$ in Figure 4.3, found by Algorithm 10 using the prior distribution *Prior2* defined in Table 4.7.

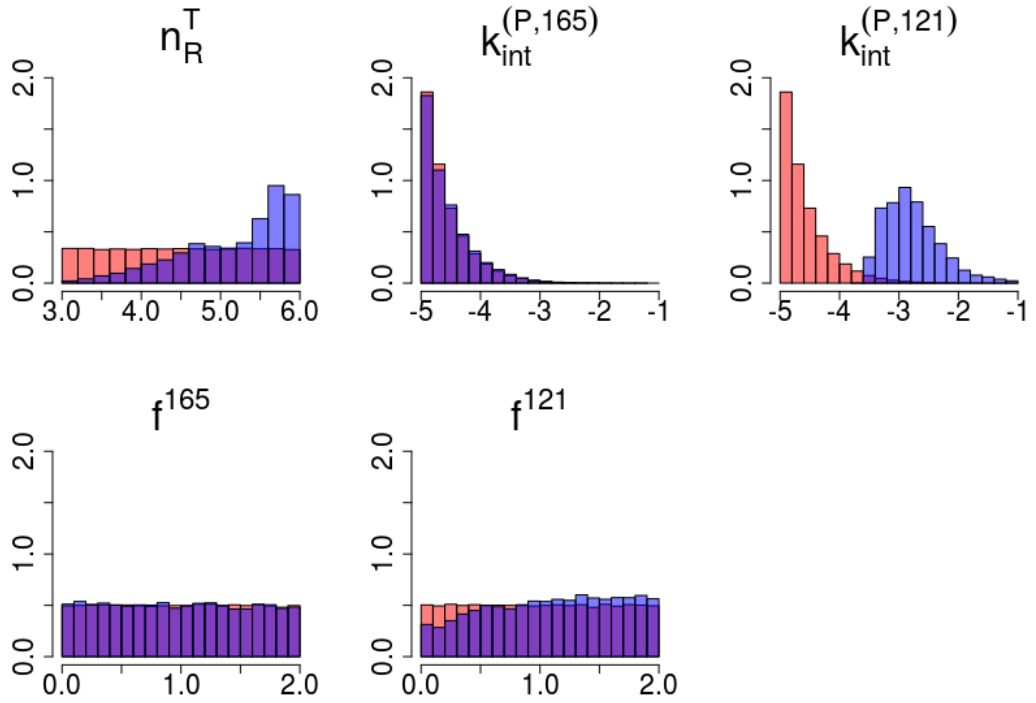

Figure 4.4: The red histograms represent sampled *Prior3*, whereas the blue histograms represent the estimated posterior distribution, called *Posterior3*, for $\hat{\boldsymbol{\theta}}$ obtained by Algorithm 10. Results are presented in logarithmic scale.

	n_R^T $[rec.\ per\ cell]$	$k_{int}^{P,165}$ $[s^{-1}]$	$k_{int}^{P,121}$ $[s^{-1}]$	f^{165}	f^{121}
Min.	1.05×10^3	1.00×10^{-5}	2.09×10^{-4}	1.00×10^0	1.00×10^0
1st Qu.	4.89×10^4	1.34×10^{-5}	7.64×10^{-4}	3.04×10^0	4.33×10^0
Median	2.36×10^5	2.05×10^{-5}	1.43×10^{-3}	9.61×10^0	1.34×10^1
Mean	3.12×10^5	6.51×10^{-5}	3.64×10^{-3}	2.10×10^1	2.43×10^1
3rd Qu.	5.27×10^5	4.16×10^{-5}	3.04×10^{-3}	3.06×10^1	3.68×10^1
Max.	1.00×10^6	4.45×10^{-2}	9.99×10^{-2}	1.00×10^2	1.00×10^2

Table 4.10: Summary statistics for the posterior distribution *Posterior3* of $\hat{\boldsymbol{\theta}} = (n_R^T, k_{int}^{P,165}, k_{int}^{P,121}, f^{165}, f^{121})$, in Figure 4.4, found by Algorithm 10 using the prior distribution *Prior3* defined in Table 4.7.

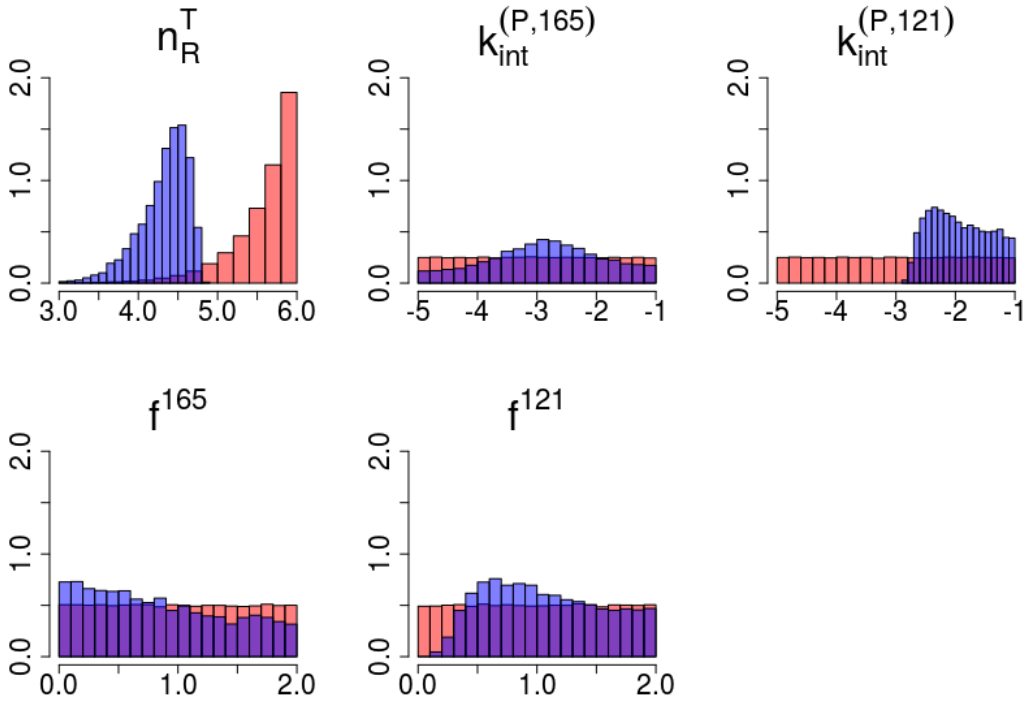

Figure 4.5: The red histograms represent sampled *Prior4*, whereas the blue histograms represent the estimated posterior distribution, called *Posterior4*, for $\hat{\boldsymbol{\theta}}$ obtained by Algorithm 10. Results are presented in logarithmic scale.

	n_R^T [*rec. per cell*]	$k_{int}^{P,165}$ $[s^{-1}]$	$k_{int}^{P,121}$ $[s^{-1}]$	f^{165}	f^{121}
Min.	1.03×10^3	1.00×10^{-5}	1.33×10^{-3}	1.00×10^0	1.22×10^0
1st Qu.	1.41×10^4	2.96×10^{-4}	4.60×10^{-3}	2.27×10^0	4.56×10^0
Median	2.44×10^4	1.45×10^{-3}	1.06×10^{-2}	5.93×10^0	1.04×10^1
Mean	2.56×10^4	8.79×10^{-3}	2.15×10^{-2}	1.64×10^1	2.13×10^1
3rd Qu.	3.57×10^4	6.62×10^{-3}	3.05×10^{-2}	2.04×10^1	2.86×10^1
Max.	6.70×10^4	1.00×10^{-1}	1.00×10^{-1}	9.99×10^1	1.00×10^2

Table 4.11: Summary statistics for the posterior distributions *Posterior4* of $\hat{\boldsymbol{\theta}} = (n_R^T, k_{int}^{P,165}, k_{int}^{P,121}, f^{165}, f^{121})$ in Figure 4.5, found by Algorithm 10 using the prior distribution *Prior4* defined in Table 4.7.

Prior3 and *Posterior3* are very similar (see Figure 4.4) suggesting that the data with the prior distribution do not introduce any new information about the parameters. Using *Prior1, Prior2* or *Prior4* reveals some information regarding the initial number of receptors per cell n_R^T which intends to be of the order $10^3 - 10^4$. The mean and the median of the internalisation rates, for both isoforms, are of the order $10^{-3} - 10^{-2}$ for *Posterior1*, *Posterior2* and *Posterior4*. The internalisation rate of the phosphorylated dimers P_S, bound with VEGF-A_{165}, is lower than the one of complexes built with VEGF-A_{121}. Thus, fewer molecules with VEGF-A_{165} are internalised per second in comparison to those with VEGF-A_{121}. The dissociation constant for the bound dimers in the endosome is greater for VEGF-A_{121} than for VEGF-A_{165}. This suggests that the dissociation takes place faster for the dimers bound with VEGF-A_{121} in the endosome. Overall, the results suggest that dimers bound with VEGF-A_{121} tend to be quickly internalised, dissociated and finally degraded. This conclusion agrees with the results reported by Fearnley *et al.* (2014).

The deterministic evolution of the phosphorylated dimers (both on the cell surface and in the endosome), in the model defined by Equation (4.2), is plotted in Figures 4.6, 4.7, 4.8 and 4.9. The plots show the median at each time point over the simulations computed using all accepted $\hat{\boldsymbol{\theta}}$. Similarly, the shaded area is found between the 5th and the 95th percentile at each time point over the simulations computed using all accepted $\hat{\boldsymbol{\theta}}$. One can notice that the number of bound dimers is always greater for VEGF-A_{165} in comparison with VEGF-A_{121}, which leads to the conclusion that VEGF-A_{165} is better in phosphorylation. According to the results of the experiment the optimal initial concentration giving the highest phosphorylation peak is $c_l = 0.25nM$. One can see similar behaviour in the simulation using *Posterior2* (Figure 4.7) and *Posterior4* (Figure 4.9) for the time point $t = 5$ *min*. However the phosphorylation peak appears within first 360 seconds for this concentration in the simulated results. It is not definite from this analysis which initial ligand concentration is optimal to get the maximal total number of the phosphorylated dimers.

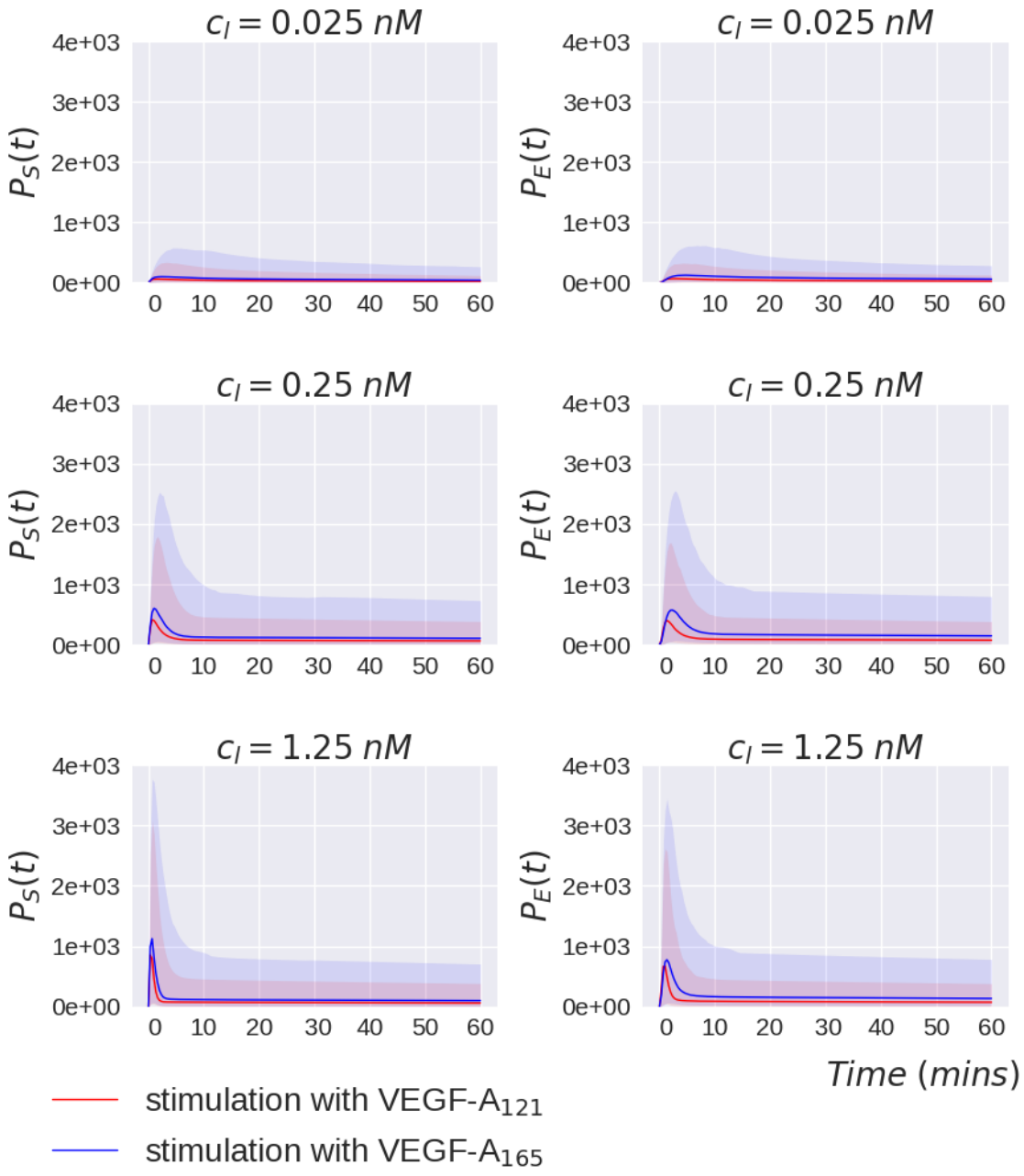

Figure 4.6: Numerical solution of Equation (4.5) using the parameters from *Posterior1*: phosphorylated dimers on the cell surface (*left* column) and in the endosome (*right* column) bound with VEGF-A_{121} and VEGF-A_{165}. The shaded area is found between the 5th and the 95th percentile at each time point over the simulations computed using all accepted $\hat{\boldsymbol{\theta}}$.

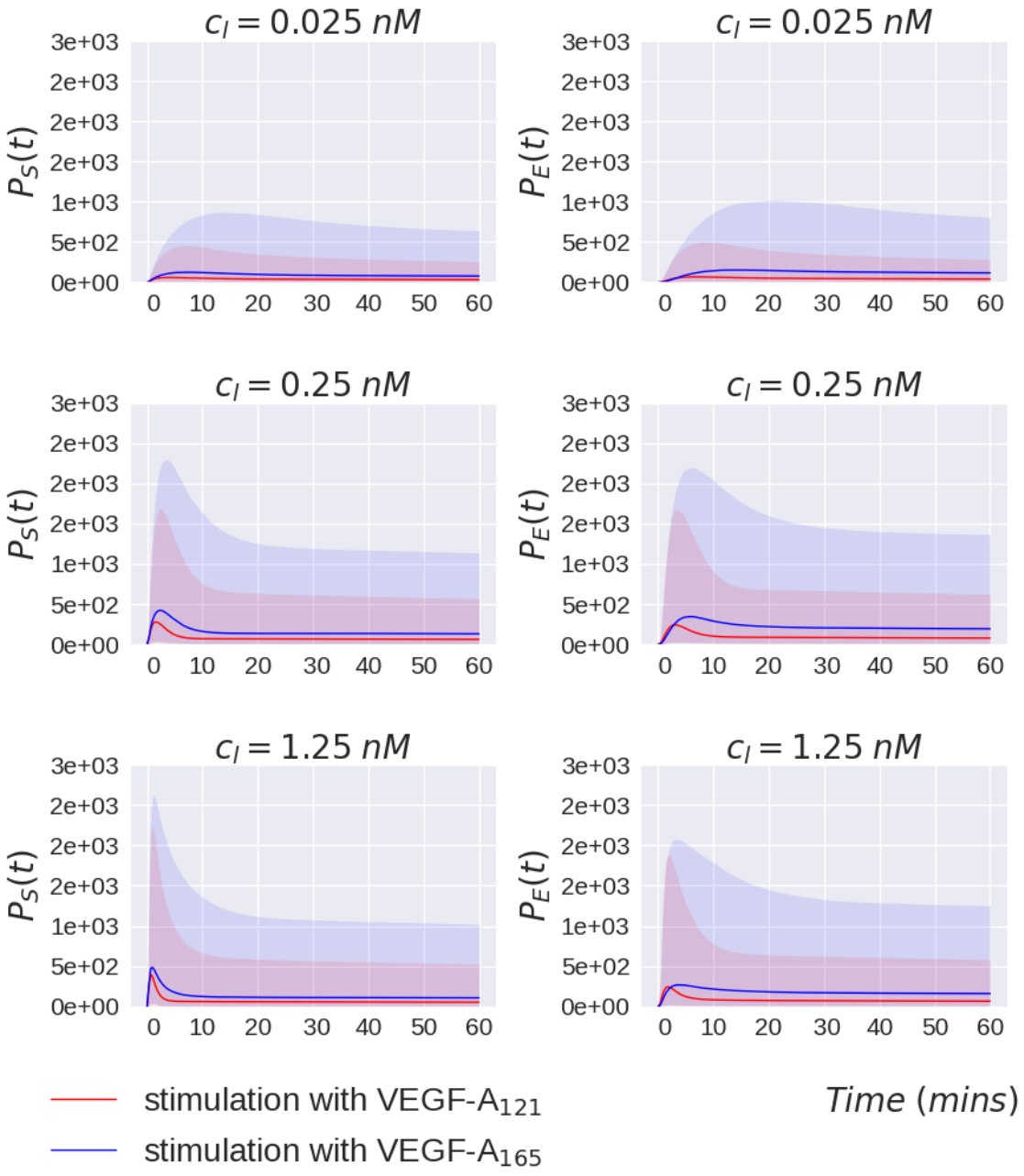

Figure 4.7: Numerical solution of Equation (4.5) using the parameters from *Posterior2*: phosphorylated dimers on the cell surface (*left* column) and in the endosome (*right* column) bound with VEGF-A_{121} and VEGF-A_{165}. The shaded area is found between the 5th and the 95th percentile at each time point over the simulations computed using all accepted $\hat{\boldsymbol{\theta}}$.

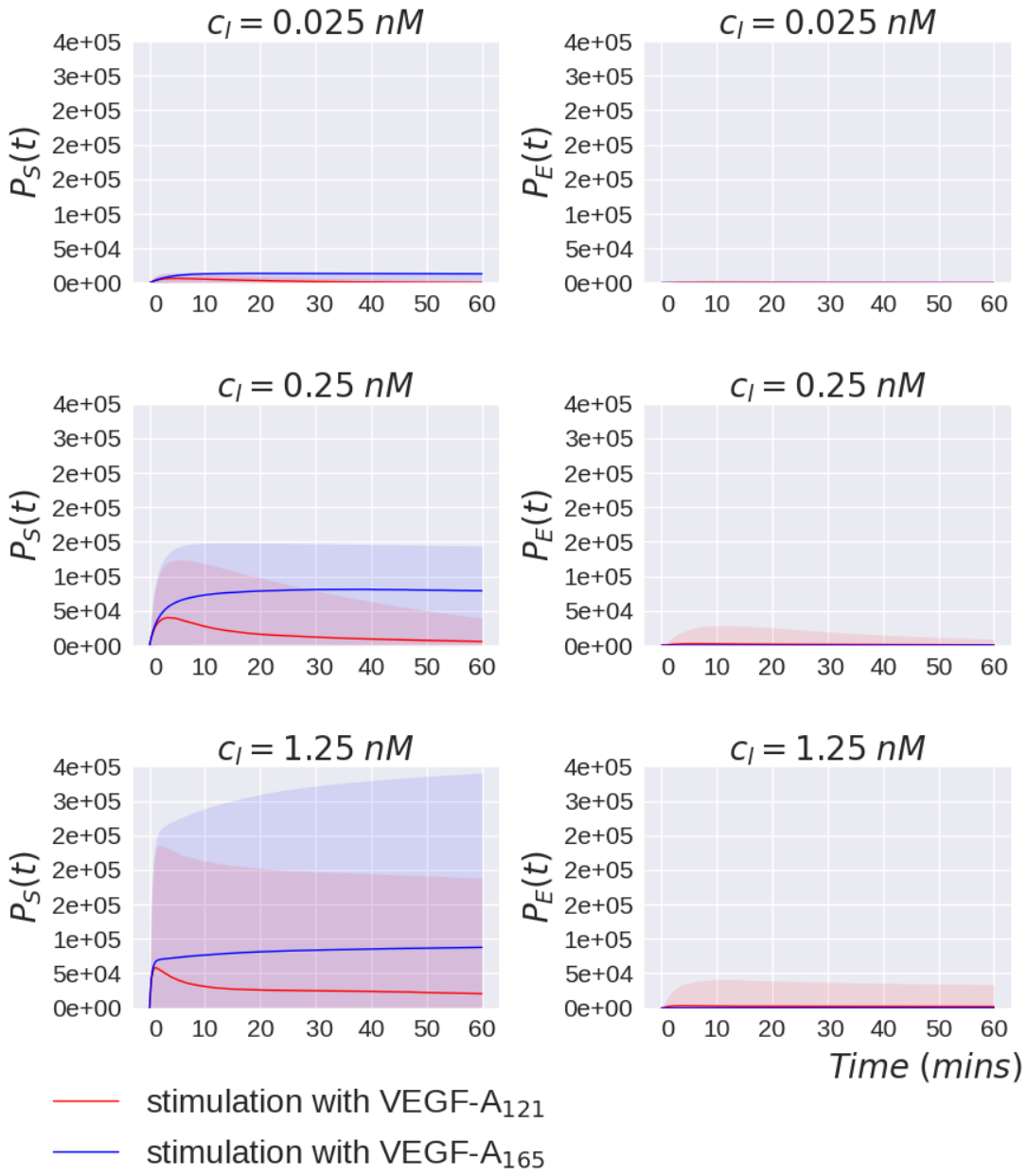

Figure 4.8: Numerical solution of Equation (4.5) using the parameters from *Posterior3*: phosphorylated dimers on the cell surface (*left* column) and in the endosome (*right* column) bound with VEGF-A$_{121}$ and VEGF-A$_{165}$. The shaded area is found between the 5th and the 95th percentile at each time point over the simulations computed using all accepted $\hat{\boldsymbol{\theta}}$.

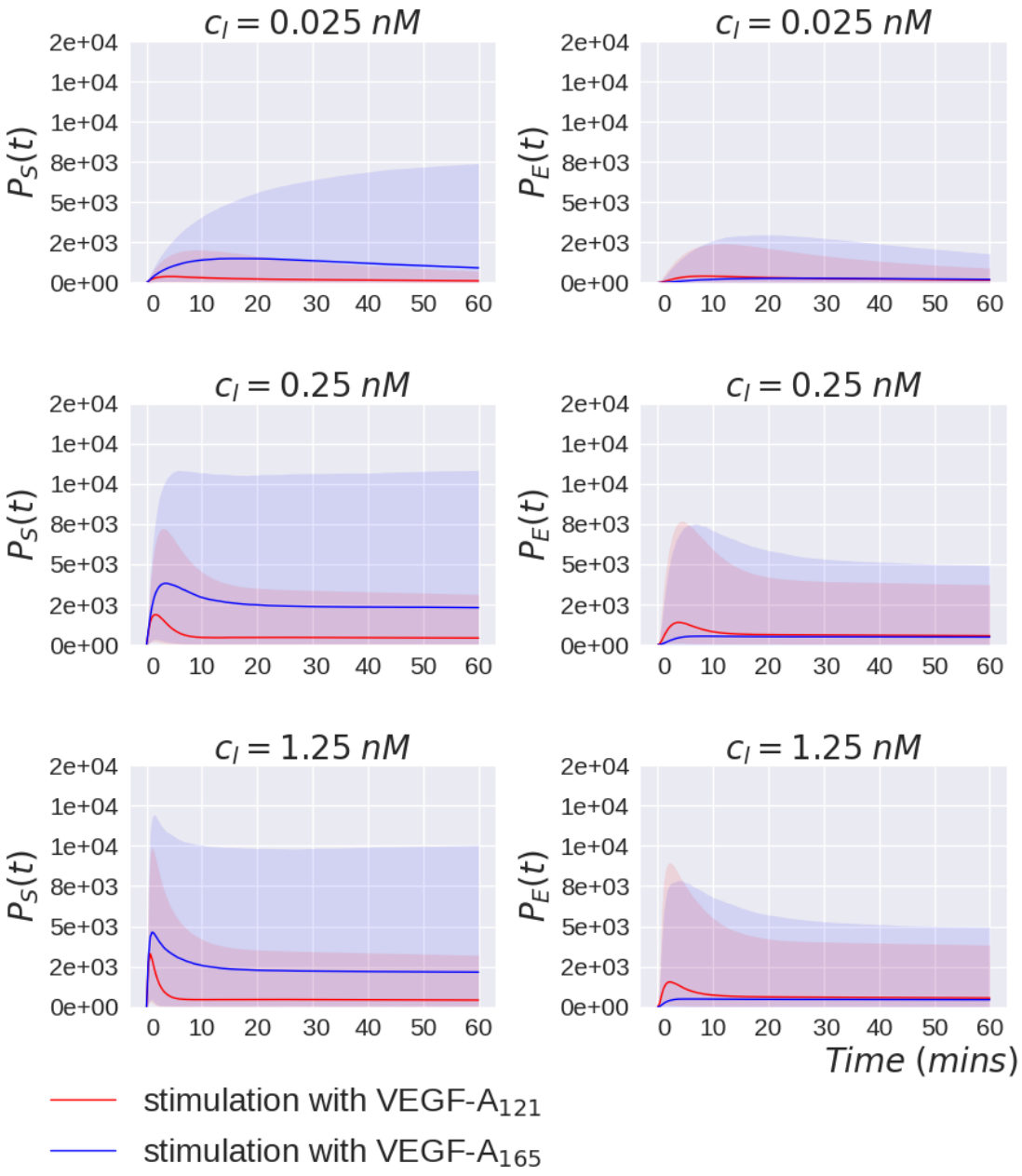

Figure 4.9: Numerical solution of Equation (4.5) using the parameters from *Posterior4*: phosphorylated dimers on the cell surface (*left* column) and in the endosome (*right* column) bound with VEGF-A_{121} and VEGF-A_{165}. The shaded area is found between the 5th and the 95th percentile at each time point over the simulations computed using all accepted $\hat{\boldsymbol{\theta}}$.

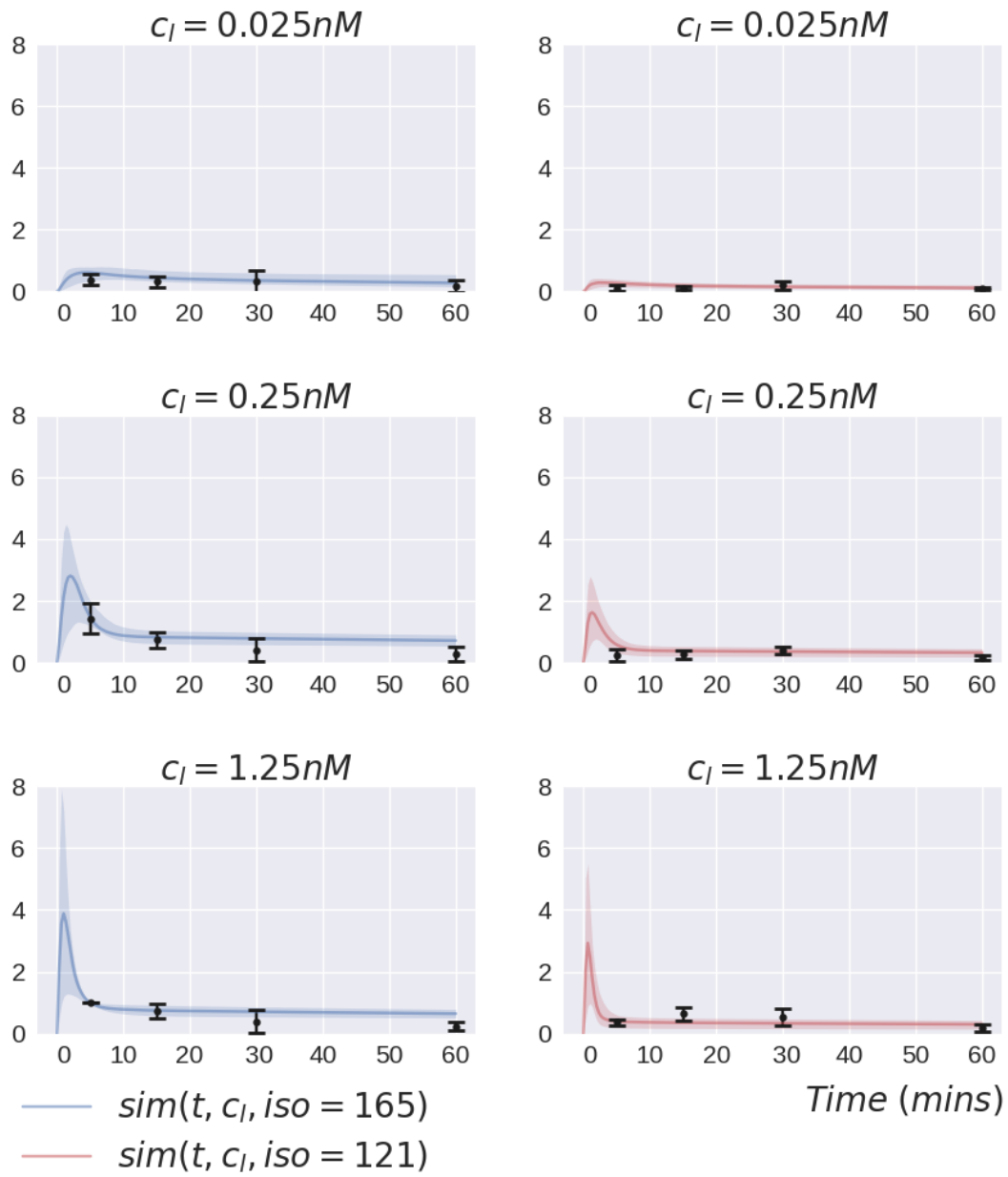

Figure 4.10: Quantified VEGFR2 phosphorylation from Table 4.1 plotted as black dots with bars representing 95% confidence interval of the data at each time point. The curves represent simulation of data given by Equation (4.5) using the parameters from *Posterior1*. The shaded area is found between the 5th and the 95th percentile at each time point over the simulations computed using all accepted $\hat{\boldsymbol{\theta}}$.

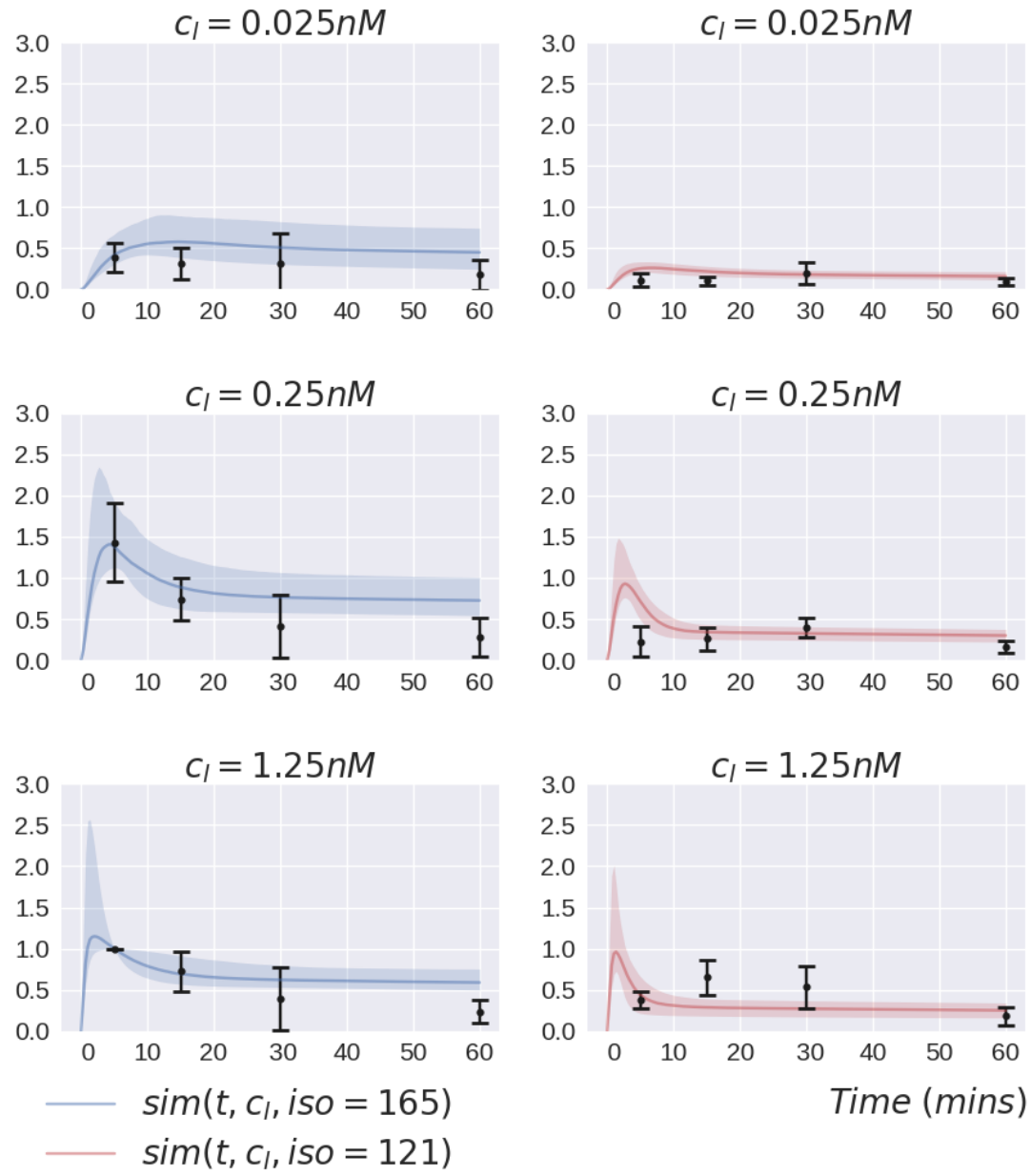

Figure 4.11: Quantified VEGFR2 phosphorylation from Table 4.1 plotted as black dots with bars representing 95% confidence interval of the data at each time point. The curves represent simulation of data given by Equation (4.5) using the parameters from *Posterior2*. The shaded area is found between the 5th and the 95th percentile at each time point over the simulations computed using all accepted $\hat{\boldsymbol{\theta}}$.

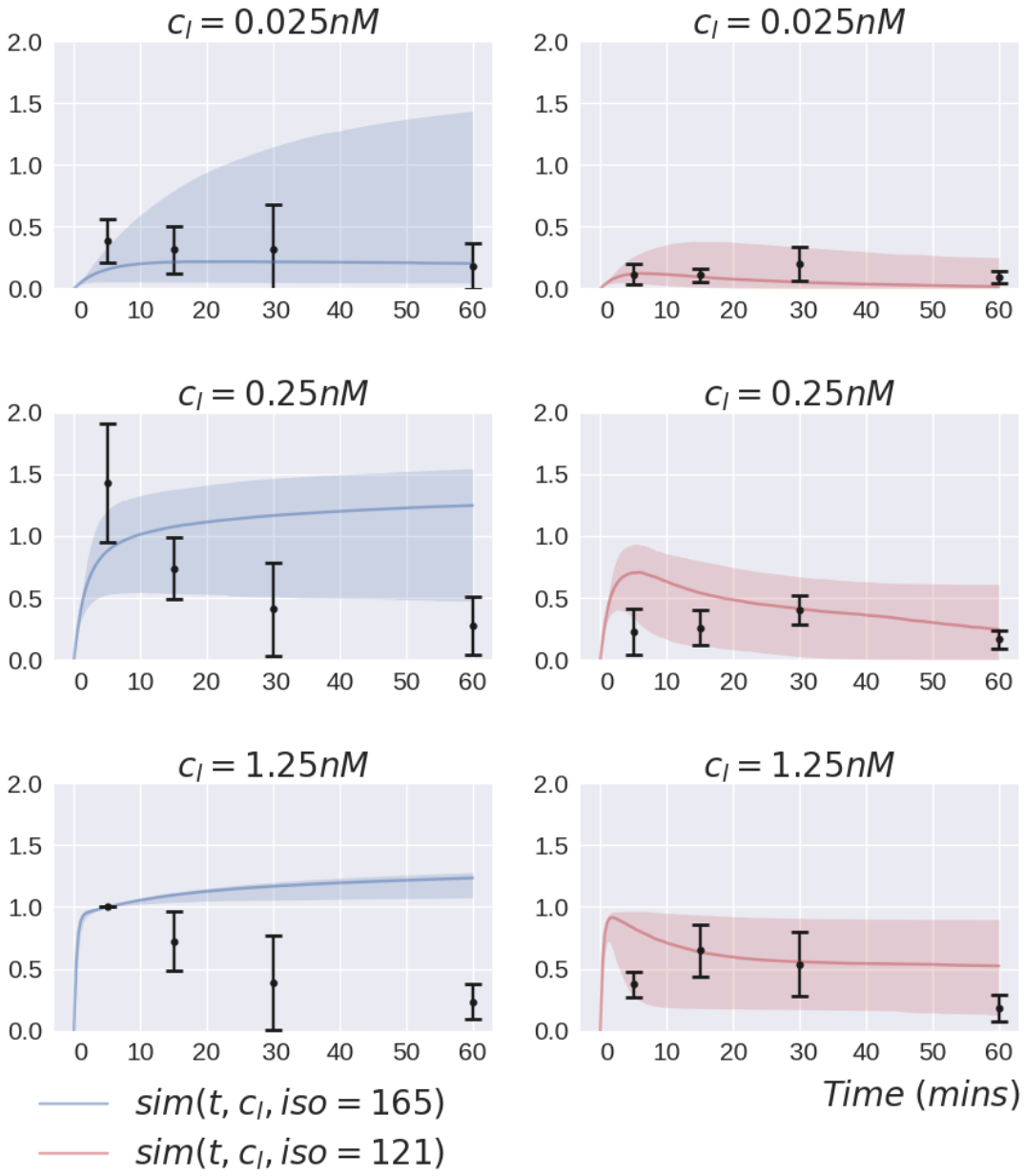

Figure 4.12: Quantified VEGFR2 phosphorylation from Table 4.1 plotted as black dots with bars representing 95% confidence interval of the data at each time point. The curves represent simulation of data given by Equation (4.5) using the parameters from *Posterior3*. The shaded area is found between the 5th and the 95th percentile at each time point over the simulations computed using all accepted $\hat{\boldsymbol{\theta}}$.

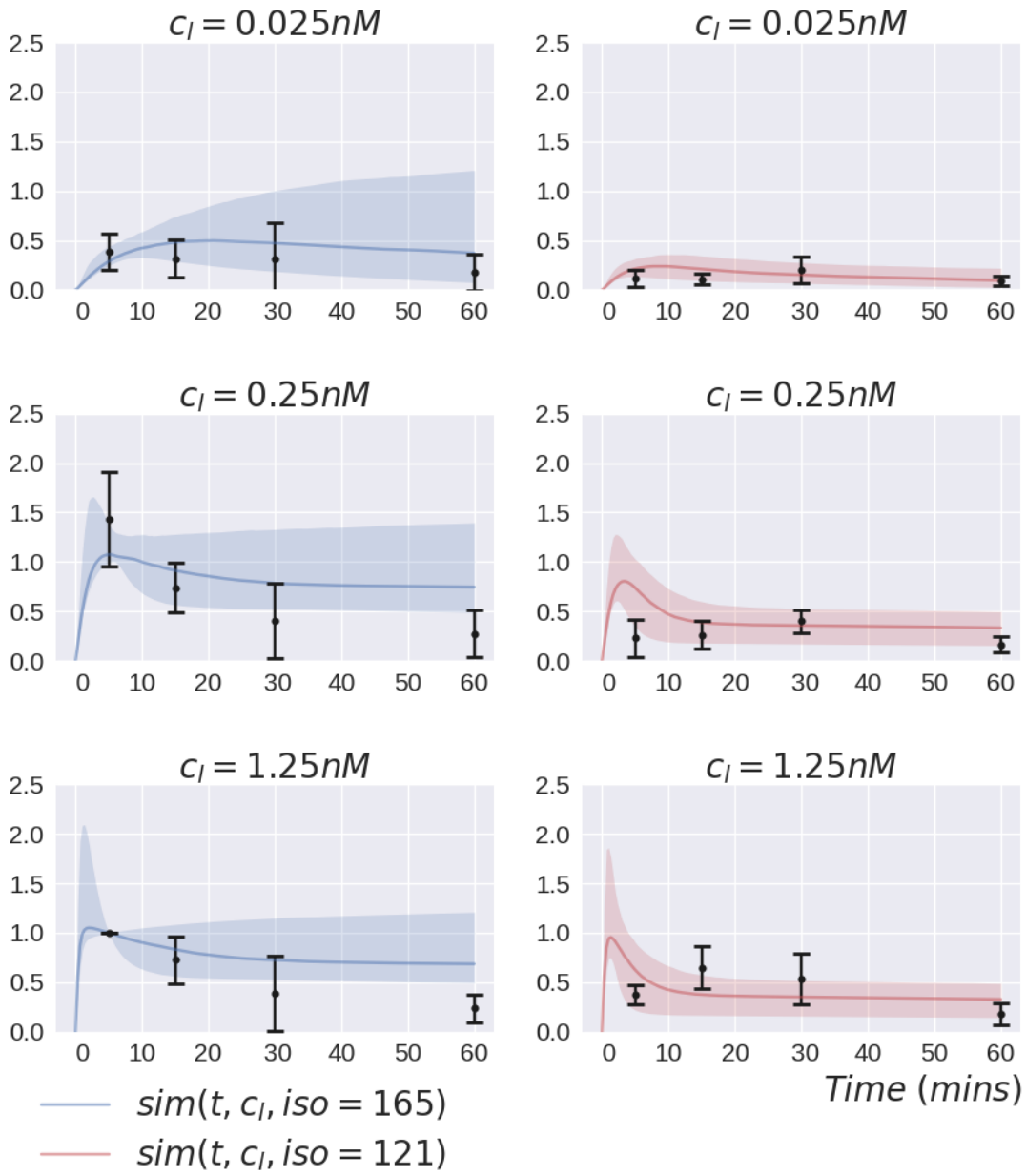

Figure 4.13: Quantified VEGFR2 phosphorylation from Table 4.1 plotted as black dots with bars representing 95% confidence interval of the data at each time point. The curves represent simulation of data given by Equation (4.5) using the parameters from *Posterior4*. The shaded area is found between the 5th and the 95th percentile at each time point over the simulations computed using all accepted $\hat{\boldsymbol{\theta}}$.

Figures 4.10, 4.11, 4.12 and 4.13 represent how the results from the ABC approach describe the data. The black dots are the mean of the data at each of the time points. The error bars show the 95% confidence interval. The solid line represents the numerical simulation of Equation 4.5 using the median of the ODE simulations for all accepted parameters obtained by the ABC algorithm with shaded area between the 5th and the 95th percentile of the ODE simulations found using the accepted parameters. The results for *Posterior3* do not describe well with the data. The simulation does not capture the data evolution behaviour.

For sufficiently complex models or large data sets, it is difficult, if not impossible, to find a model simulation that always describes the data within ϵ using the ABC algorithm (see Sadegh & Vrugt (2014)). This Bayesian methodology is very often computationally not very efficient, as it requires the simulation of millions of samples, a large majority of which, typically 99%, will be discarded for parameter estimation. More recently, Marjoram *et al.* (2003) proposed another likelihood-free approach where simulations are directly embedded within a Markov chain Monte Carlo (MCMC) framework. A problem linked with this approach is to define how close simulations need to be to data in order to accept them, which depends on (i) the acceptance rate and (ii) the mixing and the convergence of the chain, but also (iii) the burn-in period, since it may require a very large number of simulations to have the first accepted step if the starting point is in a region with low likelihood. Therefore MCMC method described in Subsection 2.4.3 is used on top of the ABC algorithm to improve the results. The other possibility is to run much more simulations for ABC algorithm which is time consuming.

Let $\boldsymbol{\theta} = \left(n_R^T,\ k_{int}^{P,165},\ k_{int}^{P,121},\ f^{165},\ f^{121}\right)$ be the vector of parameters, which follows its prior distribution π. I choose *Posterior1* and *Posterior2* as sampled prior distributions for my MCMC algorithm, that is $\pi \sim Posterior1$ or $\pi \sim Posterior2$, since these are arguably the ones that better explain the data. The distribution π is also used to adjust the transition kernel in MCMC algorithm (see step 3 in Algorithm 3) as follows,

$$\boldsymbol{\theta'} \sim N(\boldsymbol{\theta}, \varphi \cdot \boldsymbol{Cov}),$$

where $\boldsymbol{Cov}$ is the covariance matrix of the sampled prior distribution π and the coefficient φ expresses the units of variance in the propagation mechanism. The probability of the data for a particular isoform, $iso \in I$, denoted here as $data(p = \text{VEGFR2}, iso)$ given the parameter $\boldsymbol{\theta}$ is defined as,

$$Prob(data(p = \text{VEGFR2}, iso)|\boldsymbol{\theta}) = \prod_{c_l \in C_L} \prod_{t \in T} Prob(\mu_{data}(t, c_l, iso)|\boldsymbol{\theta}),$$

where $\mu_{data}(\cdot, \cdot, \cdot)$ is defined by Equation (4.7). It is assumed that

$$\mu_{data}(t, c_l, iso)|\boldsymbol{\theta} \sim N(sim(t, c_l, iso|\boldsymbol{\theta}), \sigma_{data}(t, c_l, iso)),$$

for $t \in T, c_l \in C_L$, $iso \in I$ where $sim(\cdot, \cdot, \cdot|\boldsymbol{\theta})$ is found from Equation (4.5) and the variance $\sigma_{data}(\cdot, \cdot, \cdot)$ is defined by Equation (4.7).

The chains obtained by MCMC algorithm were 3×10^6 long (for $\pi \sim Posterior1$ and $\pi \sim Posterior2$). Setting $\pi \sim Posterior1$ results with satisfactorily acceptance rate $r = 38.62\%$. The chain is mixed well enough (see the *left* column on Figure 4.14) however the autocorrelation plots, not reported here, did not decay with the time and this was adjusted by thinning the chain. The first 10^4 elements of the chain were chopped, which is called burning period, and then the chain was thinned by taking every 200th element of the burnt chain. This procedure allows to obtain a well mixed chain of 1.5×10^4 elements with quickly decaying autocorrelation (see Figure 4.15). Table 4.12 consists of the summary statistics of that chain.

MCMC algorithm allows learning more about the parameters. The *right* column on Figure 4.14 shows the distribution of the results obtained by MCMC algorithm (blue) versus the distribution obtained by the ABC algorithm (red), which accounts to *Posterior1*. The mean and the variance of the total number of receptors (n_R^T) becomes smaller. The internalisation rate and the dissociation constant for complexes built with VEGF-A_{165} have similar posterior distributions to its prior. The medians of these two rates become smaller. The results of the ABC algorithm did not bring any new information about the distribution of $k_{int}^{P,121}$ and f^{121} whereas MCMC approach results in obtaining informative posterior distributions for these rates (see Figure 4.14).

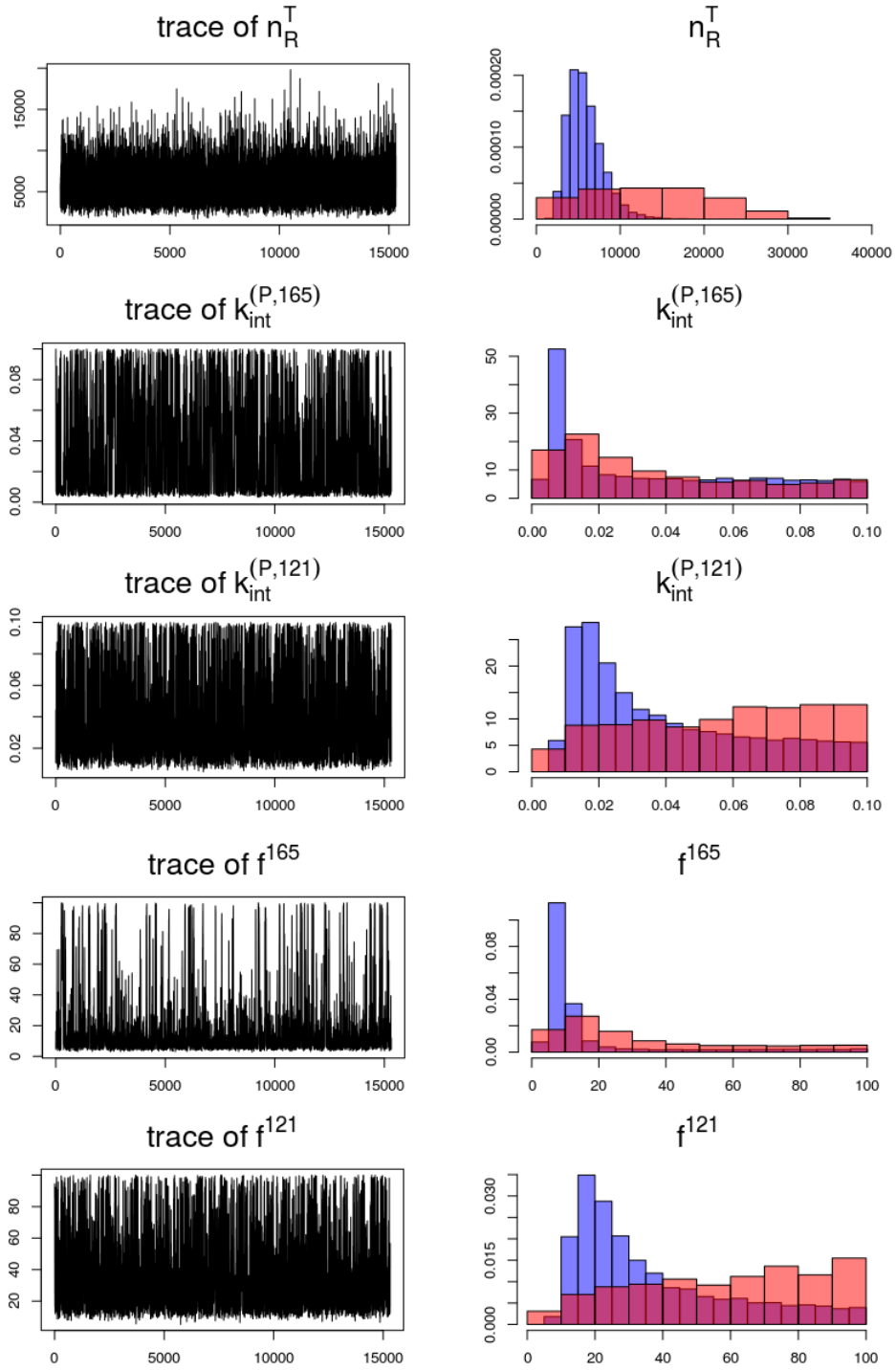

Figure 4.14: *Left* column: the trace; *right* column: histograms of *Posterior1* (red) versus histograms of the posterior distribution obtained by MCMC algorithm (blue).

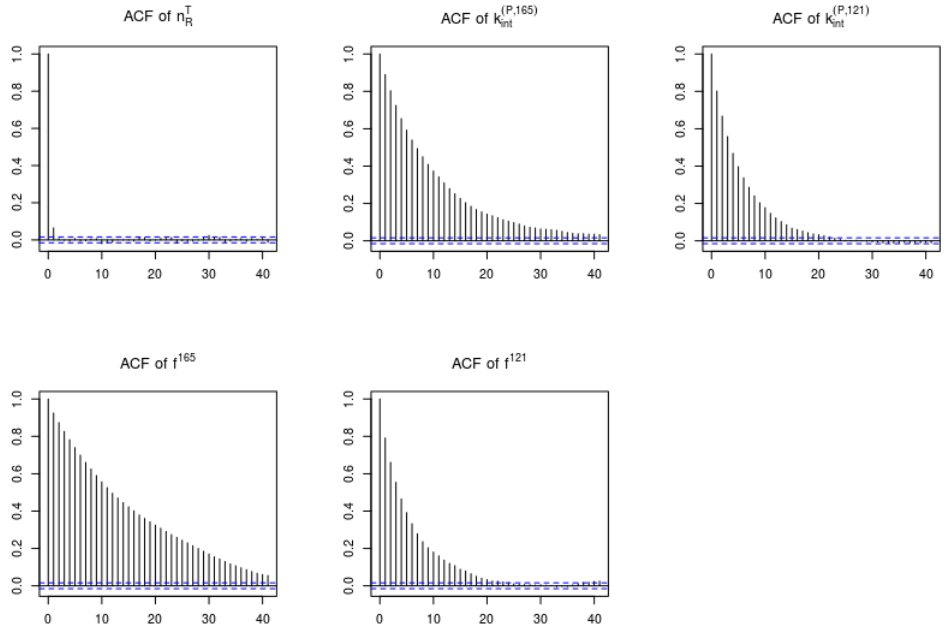

Figure 4.15: The autocorrelation functions (ACF) after thinning of the results obtained by MCMC algorithm for $\pi \sim$ *Posterior1*.

As it was noted before the internalisation rate for the dimers created with VEGF-A_{121} tends to be higher than for the dimers created with VEGF-A_{165}. The dissociation constant in the endosome is also greater for the molecules containing VEGF-A_{121}.

	n_R^T $[rec.\ per\ cell]$	$k_{int}^{P,165}$ $[s^{-1}]$	$k_{int}^{P,121}$ $[s^{-1}]$	f^{165}	f^{121}
Min.	1.69×10^3	2.53×10^{-3}	5.01×10^{-3}	2.74×10^0	5.18×10^0
1st Qu.	4.33×10^3	8.71×10^{-3}	1.79×10^{-2}	7.02×10^0	1.90×10^1
Median	5.49×10^3	2.52×10^{-2}	3.11×10^{-2}	8.93×10^0	2.82×10^1
Mean	5.84×10^3	3.62×10^{-2}	3.98×10^{-2}	1.72×10^1	3.70×10^1
3rd Qu.	6.98×10^3	6.18×10^{-2}	5.87×10^{-2}	1.30×10^1	4.97×10^1
Max.	1.98×10^4	1.00×10^{-1}	1.00×10^{-1}	1.00×10^2	1.00×10^2

Table 4.12: Summary statistics for the posterior distribution found by MCMC algorithm with $\pi \sim$ *Posterior1*.

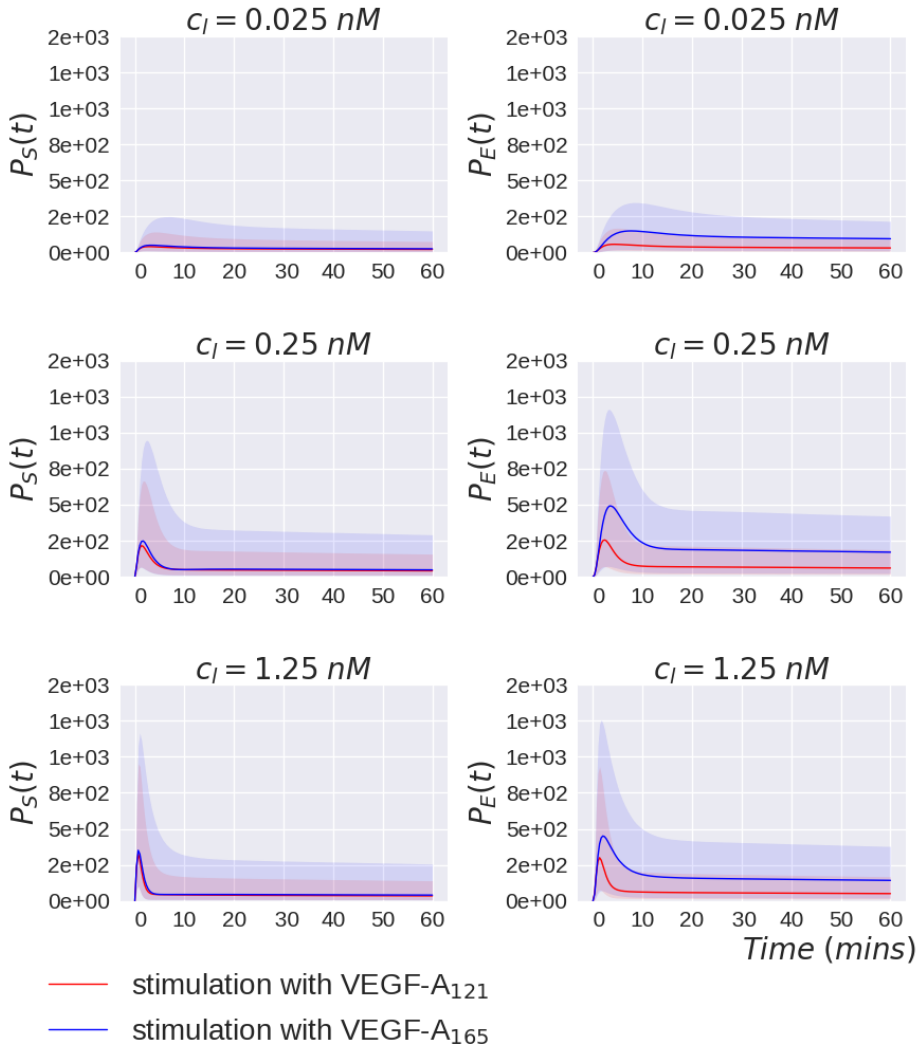

Figure 4.16: Numerical solution of Equation (4.5) using the parameters obtained by MCMC algorithm with $\pi \sim$ *Posterior1*: phosphorylated dimers on the cell surface (*left* column) and in the endosome (*right* column) bound with VEGF-A_{121} and VEGF-A_{165}. The shaded area is found between the 5th and the 95th percentile at each time point over the simulations computed using all accepted $\hat{\boldsymbol{\theta}}$.

Figure 4.16 shows the deterministic solution of Model 1 defined by Equation (4.5). As before, the curves shows the median at each time point over the simulations computed using all accepted parameters. The shaded area is between the 5th and the 95th percentile computed in the same way. The maximum phosphorylation

peak appears for initial concentration $c_l = 0.25nM$ before $t = 5\ min$. There is more VEGF-A_{165}-bound dimers in the endosome than on the cell surface whereas the number of bound VEGF-A_{121} dimers is similar in those two compartments over time. The simulations describe the data well (see Figure 4.17) revealing the fact that peak phosphorylation could actually be occurring within the first 5 minutes.

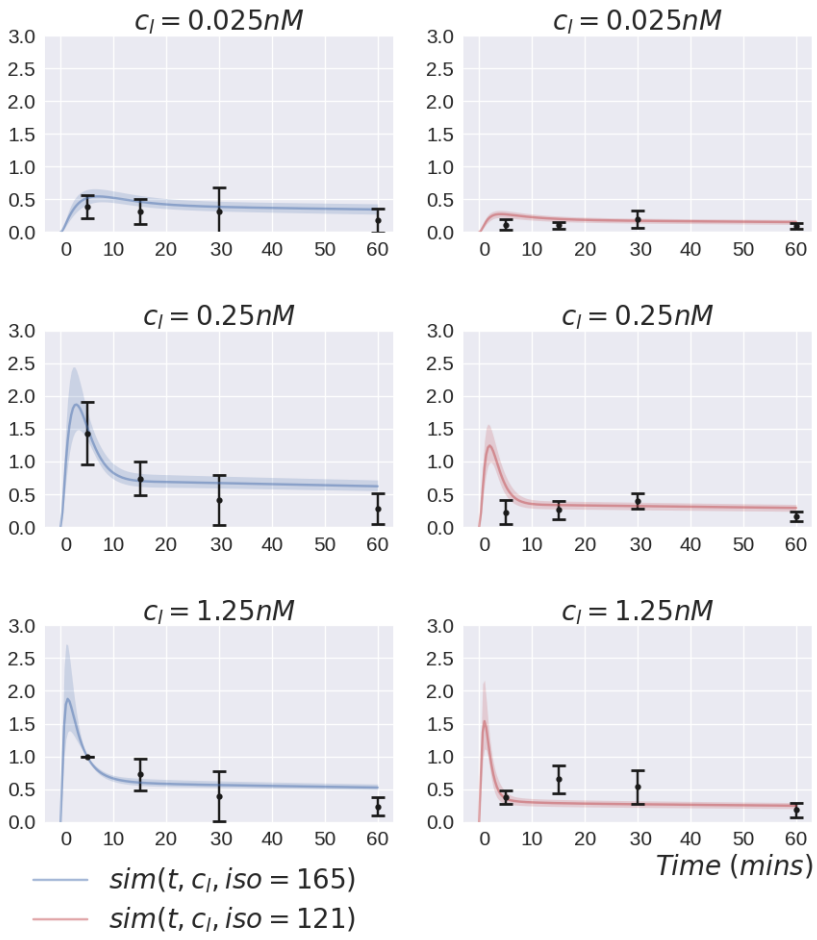

Figure 4.17: Quantified VEGFR2 phosphorylation from Table 4.1 plotted as black dots with bars representing 95% confidence interval of the data at each time point. The curves represent simulation of data given by Equation (4.5) using the results of MCMC algorithm with $\pi \sim Posterior1$. The shaded area is found between the 5th and the 95th percentile at each time point over the simulations computed using all accepted $\hat{\boldsymbol{\theta}}$.

The second MCMC algorithm was run with $\pi \sim$ *Posterior2* and gave the acceptance rate 31.51%. The chain is mixed well as shown on Figure 4.18.

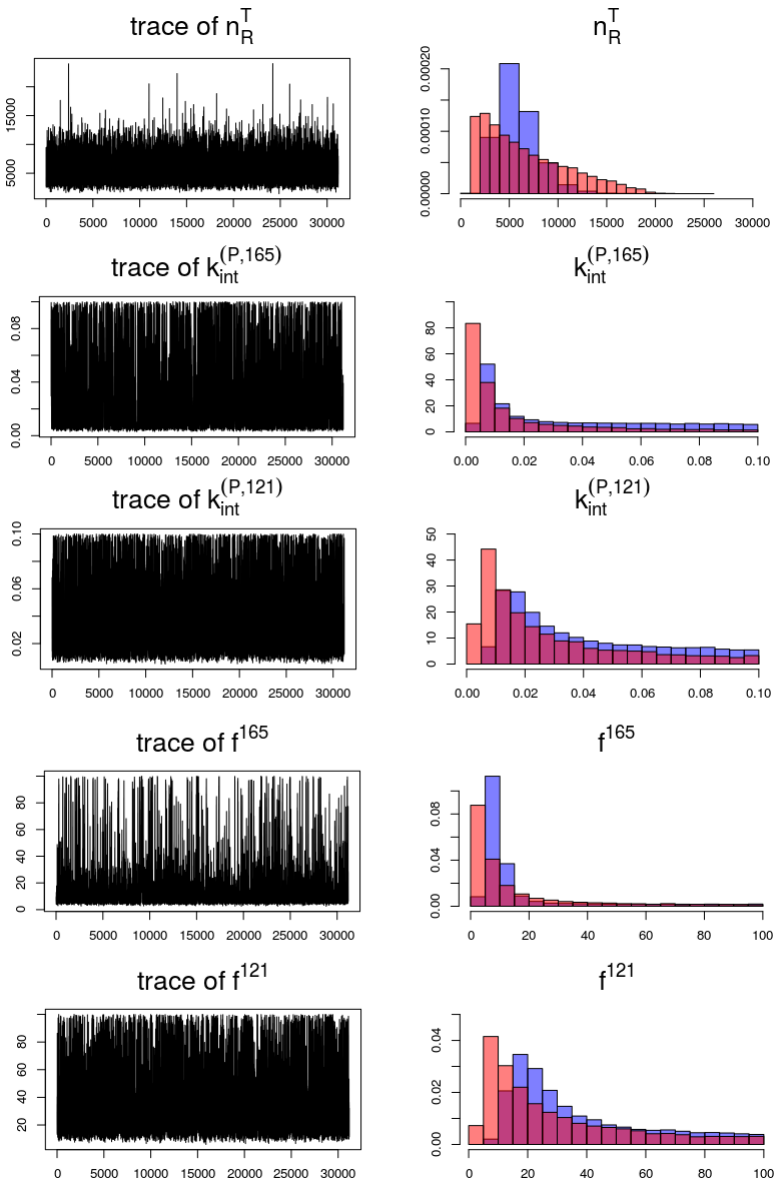

Figure 4.18: *Left* column: the trace; *right* column: histograms of *Posterior2* (red) versus histograms of the posterior distribution obtained in MCMC algorithm (blue).

After burning the first 10^4 chain and thinning the chain by taking every 100th element the autocorrelation plots decay in time (see Figure 4.19). The remaining chain is 3×10^4 long.

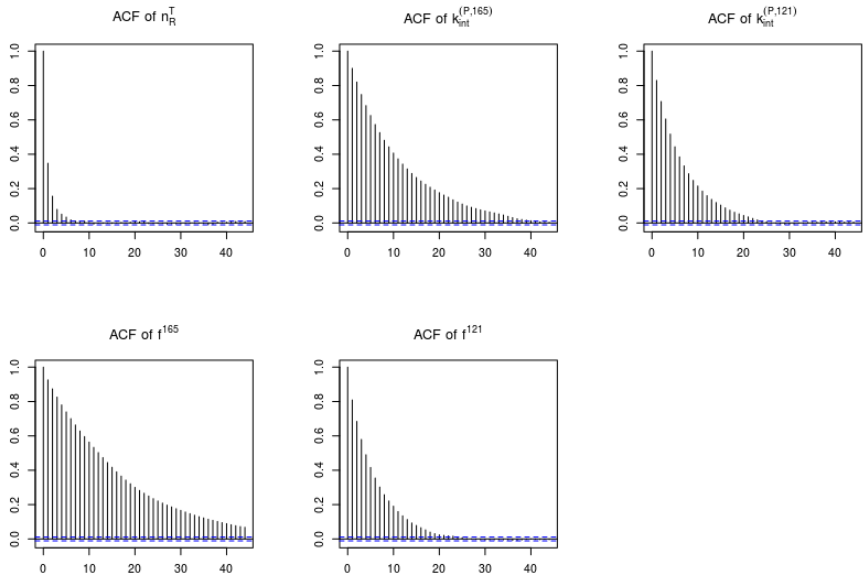

Figure 4.19: The autocorrelation functions (ACF) after thinning of the results obtained by MCMC with $\pi \sim$ *Posterior2*.

	n_R^T $[rec.\ per\ cell]$	$k_{int}^{P,165}$ $[s^{-1}]$	$k_{int}^{P,121}$ $[s^{-1}]$	f^{165}	f^{121}
Min.	1.46×10^3	2.83×10^{-3}	5.03×10^{-3}	2.50×10^0	5.91×10^0
1st Qu.	4.34×10^3	8.81×10^{-3}	1.75×10^{-2}	7.03×10^0	1.90×10^1
Median	5.51×10^3	2.41×10^{-2}	3.11×10^{-2}	8.92×10^0	2.81×10^1
Mean	5.83×10^3	3.55×10^{-2}	3.98×10^{-2}	1.65×10^1	3.70×10^1
3rd Qu.	6.96×10^3	5.98×10^{-2}	5.93×10^{-2}	1.29×10^1	5.01×10^1
Max.	2.40×10^4	1.00×10^{-1}	1.00×10^{-1}	1.00×10^2	1.00×10^2

Table 4.13: Summary statistics for the posterior distribution found by MCMC algorithm with $\pi \sim$ *Posterior2*.

Table 4.13 consists the summary statistic of the chain. Using $\pi \sim$ *Posterior2* reveals some new information about the parameters in comparison to the ABC

algorithm (see Figure 4.18). All parameter values tend to move towards larger values.

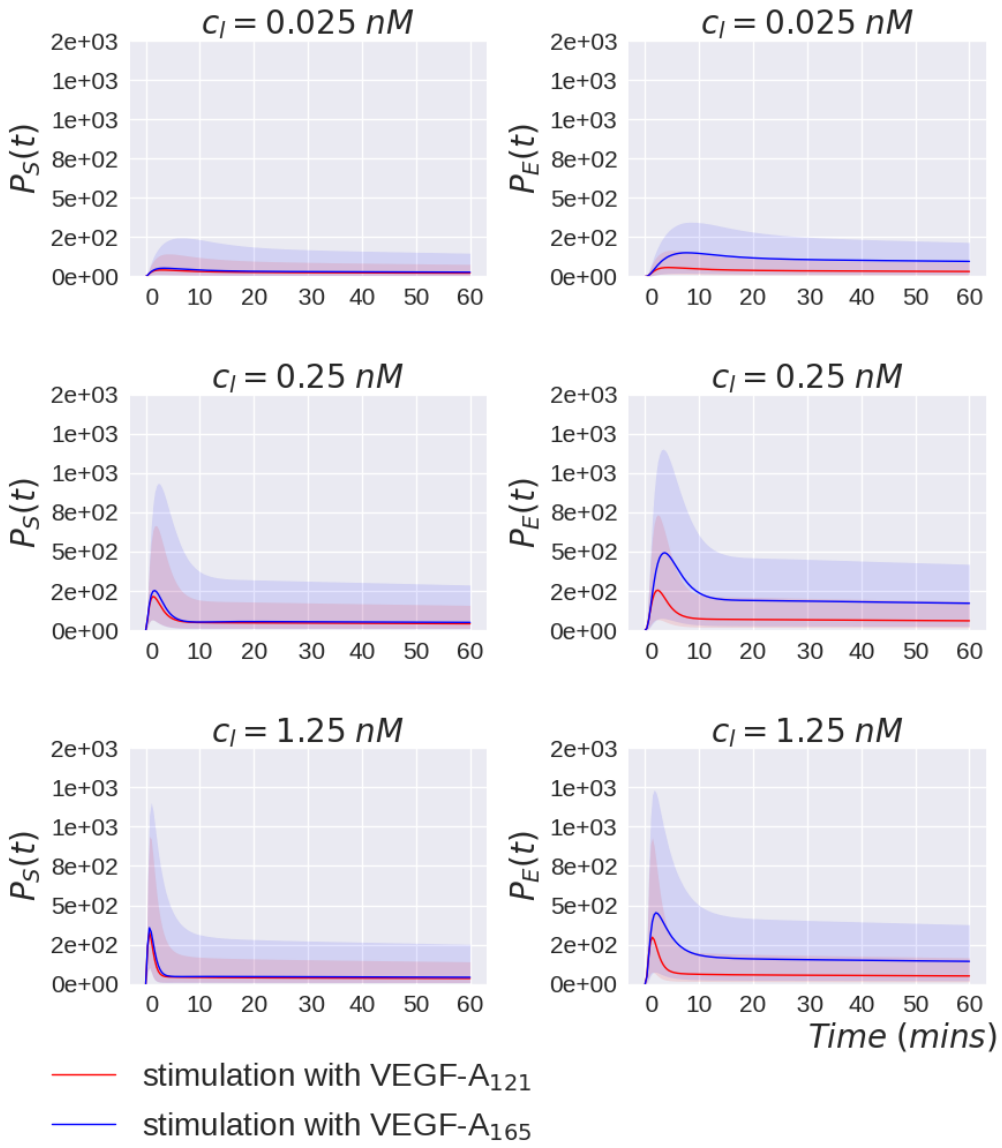

Figure 4.20: Numerical solution of Equation (4.5) using the parameters obtained by MCMC algorithm with $\pi \sim$ *Posterior2*: phosphorylated dimers on the cell surface (*left* column) and in the endosome (*right* column) with VEGF-A_{121} and VEGF-A_{165}. The shaded area is found between the 5th and the 95th percentile at each time point over the simulations computed using all accepted $\hat{\boldsymbol{\theta}}$.

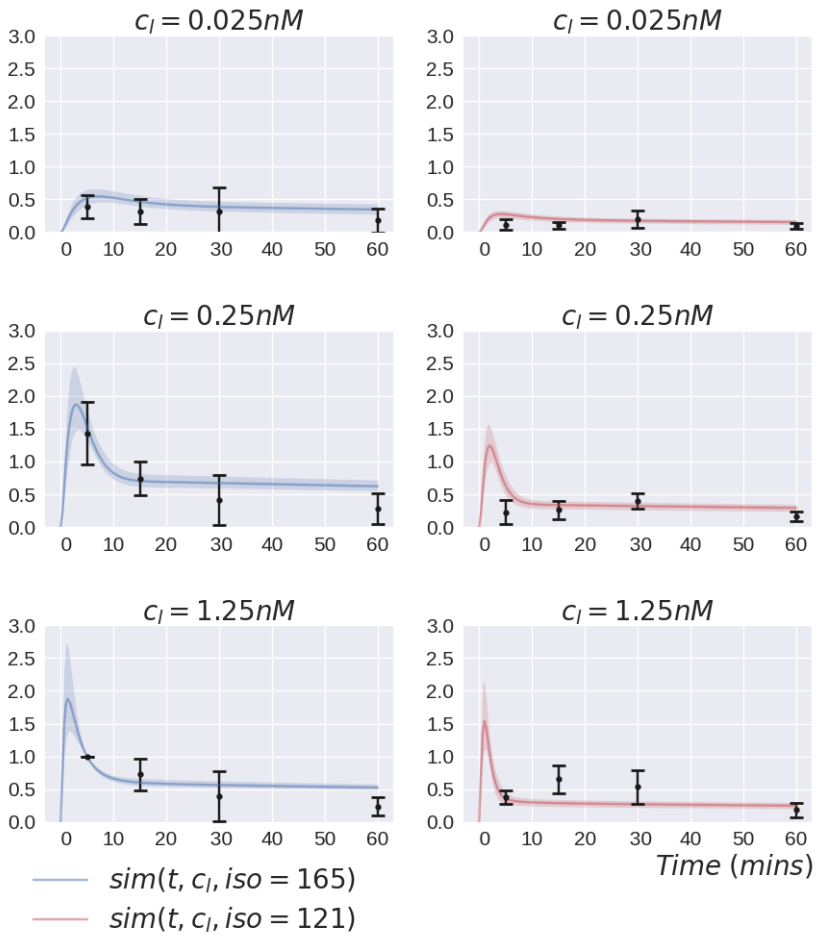

Figure 4.21: Quantified VEGFR2 phosphorylation from Table 4.1 plotted as black dots with bars representing 95% confidence interval of the data at each time point. The curves represent simulation of data given by Equation (4.5) using the results of MCMC algorithm with $\pi \sim$ *Posterior2*. The shaded area is found between the 5th and the 95th percentile at each time point over the simulations computed using all accepted $\hat{\boldsymbol{\theta}}$.

Figure 4.20 shows the deterministic solution of Model 1 given by Equation (4.5). The curves and the shaded areas are obtained as before. The maximum peak is reached before time point $t = 5$ *min* for the initial ligand concentration $c_l = 0.25nM$ for the phosphorylated dimers bound with VEGF-A_{165} in the endosome. The simulation describe the data reasonably well (see Figure 4.21) revealing again the fact that the peak phosphorylation could have happened earlier then at time

5 minutes after ligand stimulation.

The results from both MCMC approaches (with $\pi \sim Posterior1$ and $\pi \sim Posterior2$) are similar (see Tables 4.12 and 4.13). It is reassuring taking into consideration that the initial ABC prior distributions were different. The behaviour of the deterministic simulations are almost identical and describe well the data. It is interesting to see the posterior distribution of the synthesis rate which is found by Equation (4.4). Both approaches led to similar posterior distribution of the synthesis rate (see Figure 4.22 and the summary statistics in Table 4.14).

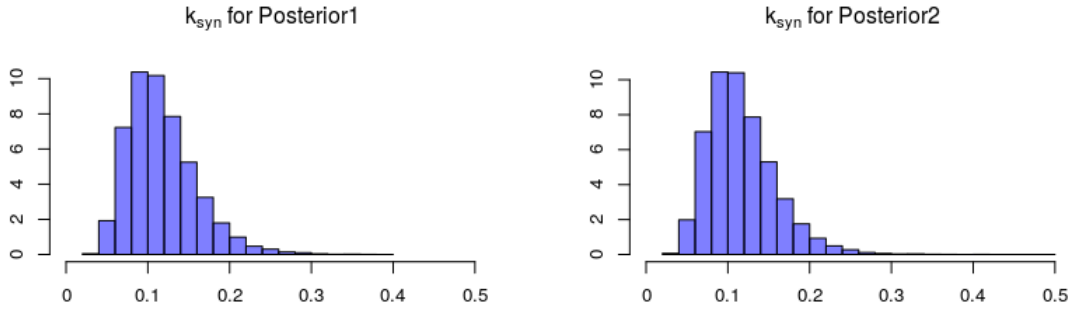

Figure 4.22: Posterior distributions of the synthesis rate k_{syn} obtained by MCMC algorithm and from Equation (4.4), for $\pi \sim Posterior1$ and $\pi \sim Posterior2$.

	$k_{syn}[s^{-1}]$ for *Posterior1*	$k_{syn}[s^{-1}]$ for *Posterior2*
Min.	3.38×10^{-2}	2.92×10^{-2}
1st Qu.	8.67×10^{-2}	8.69×10^{-2}
Median	1.10×10^{-1}	1.10×10^{-1}
Mean	1.17×10^{-1}	1.17×10^{-1}
Mean 3rd Qu.	1.40×10^{-1}	1.39×10^{-1}
Max.	3.96×10^{-1}	4.80×10^{-1}

Table 4.14: Summary statistics of the synthesis rate k_{syn}.

Quantification of the receptor degradation rate

Using the results from MCMC algorithm one may find that degradation of receptors in the endosome can happen two times more rapidly for stimulated cells. In

order to do that one more equation must be added to Equation (4.2),

$$\frac{dR_L(t)}{dt} = k_{deg} R_E(t), \tag{4.8}$$

where $R_L(t)$ is a strictly increasing variable accounting for the number of degraded receptors moved to the lysosome, up to time $t \leq 0$, with the initial condition $R_L(0) = 0$.

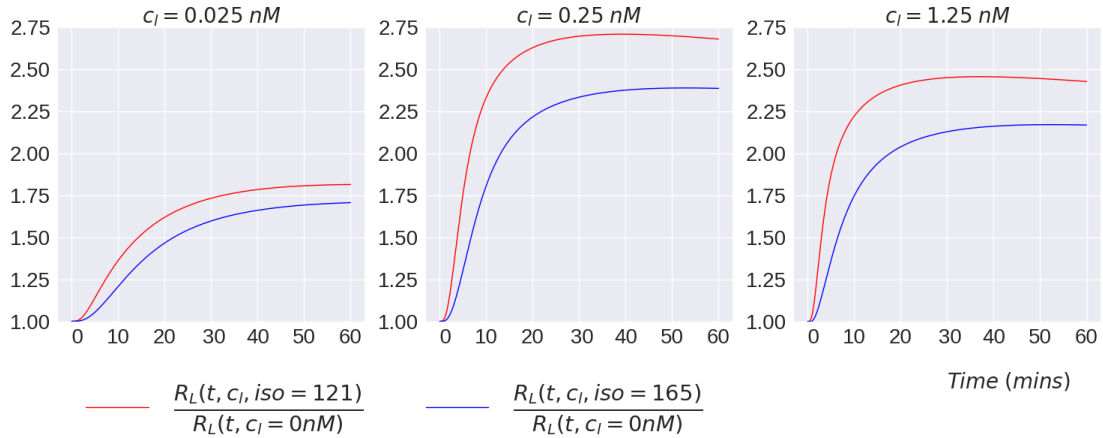

Figure 4.23: The ratio of degradation of the receptors in the endosome between stimulated (using VEGF-A_{121} and VEGF-A_{165}) and non-stimulated cells.

Figure 4.23 shows the time evolution of the ratio of degraded receptors from the endosome between stimulated and non-stimulated cells. Parameters used in Figure 4.23 are the median values reported in Table 4.12 for $\pi \sim Posterior1$. There are more degraded receptors if the cell is stimulated by VEGF-A_{121} than by VEGF-A_{165} which agrees with previous observation about faster turnover of receptors bound with VEGF-A_{121}. Additionally on average there is twice as many degraded receptors once the cell is stimulated with VEGF-A comparing to non-stimulated cell.

4.1.3 Model 2: ERK phosphorylation

Phosphorylation of vascular endothelial growth factor receptors is important at many stages of the signalling pathway. When a growth factor ligand binds to the

receptor, the receptor pairs up and acts as kinases, attaching phosphate groups to one another's intracellular tails. The activated receptors trigger a series of events (see Lodish *et al.* (1995)). These events activate the kinase Raf. Active Raf phosphorylates and activates MEK, which phosphorylates and activates the ERKs. The ERKs phosphorylate and activate a variety of target molecules which include the transcription factors, like ATF-2, as well as the cytoplasmic targets. The activated targets promote cell growth and division. Together, Raf, MEK, and the ERKs make up a three-tiered kinase signalling pathway called a mitogen-activated protein kinase (MAPK) cascade (a mitogen is a signal that causes cells to undergo mitosis, or divide).

A simple signalling model, referred to as Model 2, is introduced here in order to examine which types of the phosphorylated bound dimers are more likely to be responsible for ERK phosphorylation (see Figure 4.24). The MAPK cascade is modelled here by one equation which describes a signal response to the phosphorylated dimers. Assume that the ERK signal can decay at a constant rate μ and grows at a constant rate λ with the signal capacity κ. There are the following two hypotheses to be checked:

H_1) signal is generated from bound dimers on the cell surface with a delay τ

$$\frac{dS(t)}{dt} = -\mu S(t) + \lambda \frac{P_S(t-\tau)}{P_S(t-\tau)+\kappa}, \tag{4.9}$$

H_2) signal is generated from bound dimers in the endosome with a delay τ

$$\frac{dS(t)}{dt} = -\mu S(t) + \lambda \frac{P_E(t-\tau)}{P_E(t-\tau)+\kappa}, \tag{4.10}$$

where $S(t) = 0$ for $t < \tau$. Here I assume that rates μ, λ, τ are isoform-independent. However, ERK phosphorylation is still implicitly isoform-dependent, since the amounts of bound dimers $P_S(t)$ and $P_E(t)$ at any given time $t \geq 0$ do depend on the particular isoform used for stimulation.

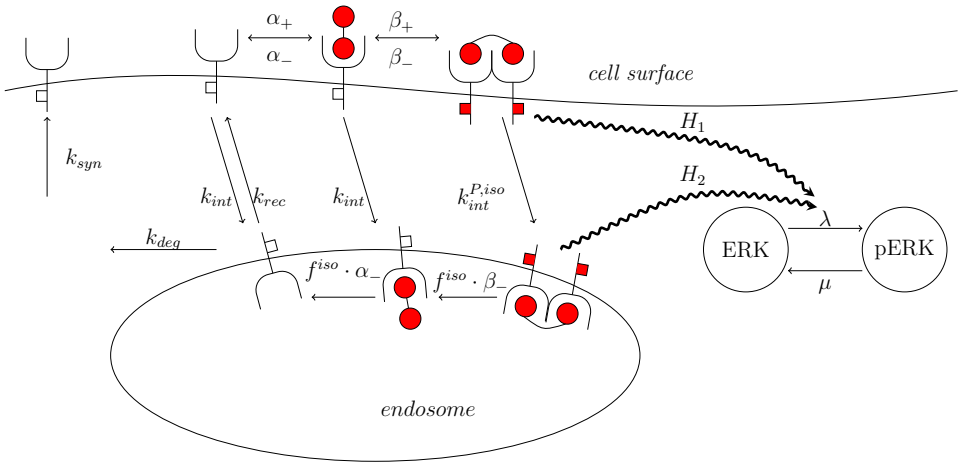

Figure 4.24: Events involved in Model 2 for binding and trafficking of the VEGFR2 receptor. H_1 and H_2 with the waved arrows indicates the hypothesis under consideration triggering ERK signalling (phosphorylation in this case).

Global sensitivity analysis of Model 2

The Sobol algorithm was run for the Model 2 for both hypotheses where the parameters μ, λ, κ and τ were varied (see Table 4.15).

$\mu[s^{-1}]$	$\lambda[molecules\ s^{-1}]$	$\kappa[molecules]$	$\tau[s]$
$(0, 10)$	$(0, 10)$	$(1, 10^4)$	$(0, 300)$

Table 4.15: Ranges considered for μ, λ, κ and τ for Model 2, when applying Sobol algorithm.

Similarly to $sim(t, c_l, iso)$ from Equation (4.5), to compare the simulation of Model 2 with the data from Table 4.2 the following expression must be computed

$$\overline{sim}(t, c_l, iso) = \frac{S(t, c_l, iso)}{S(t = 5\ min, c_l = 1.25nM, iso = 165)}, \tag{4.11}$$

where $t \in T$, $c_l \in C_L$ and $iso \in I$. Thus the parameter τ is constrained by the data normalisation to be less than 5 min, because if $\tau > 5\ min$ then $S(t = 5\ min, c_l = 1.25nM, iso = 165) = 0$ (due to the initial condition for Equations (4.9) and (4.10)) and $\overline{sim}(t, c_l, iso)$ is undefined. The analyses revealed that the

parameter τ is the most sensitive parameter to the model output (see Tables 4.16 and 4.17).

	S_1 mean	S_1 st deviation	S_1 range	S_T mean	S_T st deviation	S_T range
μ	$< 10^{-5}$	$< 10^{-5}$	-	0.02	0.01	(0.00,0.03)
λ	$< 10^{-5}$	$< 10^{-5}$	-	$< 10^{-5}$	$< 10^{-5}$	-
κ	0.00	0.01	(0.00, 0.02)	0.00	0.01	(0.00, 0.03)
τ	1.00	0.01	(0.97,1)	1.00	0.01	(0.98,1)

Table 4.16: The results for Sobol algorithm for Model 2 with the hypothesis H_1. The mean and the standard deviation were taken over all time points t and all initial ligand concentrations c_l.

	S_1 mean	S_1 st deviation	S_1 range	S_T mean	S_T st deviation	S_T range
μ	$< 10^{-5}$	$< 10^{-5}$	-	0.01	0.00	(0.00,0.01)
λ	$< 10^{-5}$	$< 10^{-5}$	-	$< 10^{-5}$	$< 10^{-5}$	-
κ	0.04	0.11	(0.00, 0.43)	0.04	0.12	(0.00, 0.48)
τ	0.96	0.12	(0.51,1)	0.96	0.11	(0.58,1)

Table 4.17: The results for Sobol algorithm for Model 2 with the hypothesis H_2. The mean and the standard deviation were taken over all time points t and all initial ligand concentrations c_l.

The main effect index S_1 and the total effect index S_T approximately equal to 1 for both hypotheses, whereas the rest of the parameter's indexes where approximately equal to 0 for the time points 15, 30 and 60 minutes, regardless of the initial concentration and the isoforms considered. The parameter κ matters more only for hypothesis H_2 for the outputs at the time point 5 minutes with the initial concentration 0.025nM or 0.25nM, where κ's main effect index $S_1 \approx 0.29$.

Parameter inference: Model 2

The ABC algorithm, described in Chapter 2 in Subsection 2.4.2 is used in order to find the distributions for the parameters μ, λ, κ and τ of Model 2. The prior distributions for these parameters are uniform distributions on ranges defined in

Table 4.15. The rest of parameters in Model 2 are taken from the median of the results of MCMC inference for $\pi \sim Posterior1$.

	$\mu[s^{-1}]$	$\lambda[molecules\ s^{-1}]$	$\kappa[molecules]$	$\tau[s]$
Min.	0.0015	0.02	148	7
1st Qu.	0.5477	2.26	3935	290
Median	3.3922	4.82	5975	292
Mean	3.8218	4.95	5859	273
3rd Qu.	6.6883	7.60	7984	292
Max.	9.9999	9.99	9993	292

Table 4.18: Summary statistics of the posterior distribution for hypothesis H_1.

	$\mu\ [s^{-1}]$	$\lambda\ [molecules\ s^{-1}]$	$\kappa[molecules]$	$\tau\ [s]$
Min.	0.0019	0.01	220	1
1st Qu.	0.0153	2.63	1671	217
Median	0.2774	4.88	2741	259
Mean	2.1217	4.99	3796	225
3rd Qu.	3.8907	7.39	5754	262
Max.	9.9999	9.99	9984	262

Table 4.19: Summary statistics of the posterior distribution for hypothesis H_2.

The ABC algorithm was run to get 10^6 samples for each hypotheses. The acceptance ratio was set to 0.1% which allows to obtain 1000 accepted samples. Table 4.18 contains the summary statistics for the computed posterior under hypothesis H_1 (signal is generated from the cell surface) whereas Table 4.19 contains the summary statistics for the computed posterior under the hypothesis H_2 (signal is generated from the endosome). The constant μ is much greater for the hypothesis H_2 indicating that the signal decay would be faster in that case. The capacity κ is greater for the model with signalling from the cell surface and the delay is similar for both hypotheses.

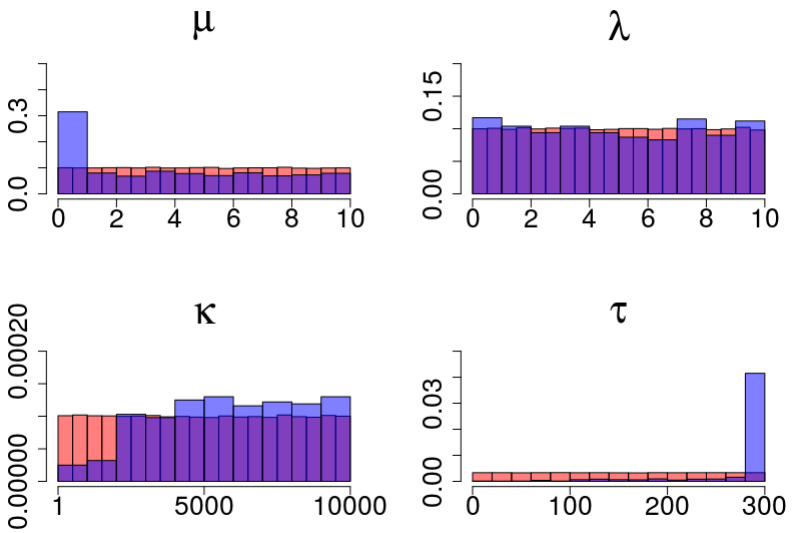

Figure 4.25: The probability histograms of the posterior distribution (in blue) versus the prior distribution (in red) assuming the hypothesis H_1.

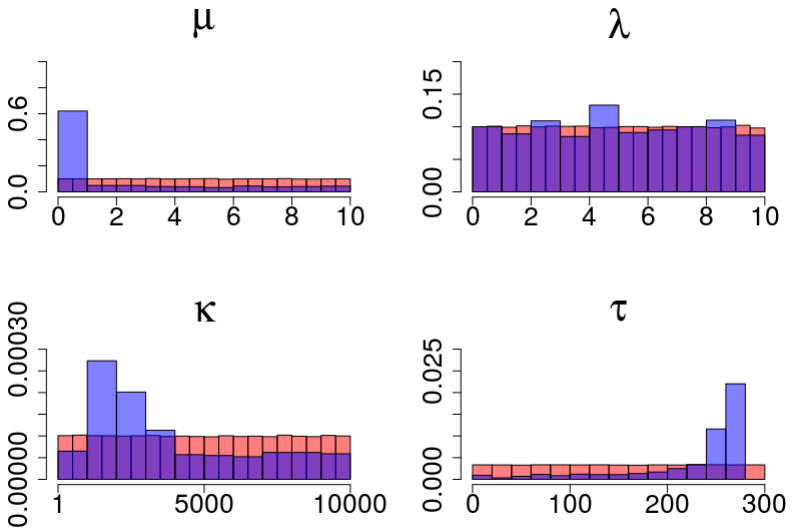

Figure 4.26: The probability histograms of the posterior distribution (in blue) versus the prior distribution (in red) assuming the hypothesis H_2.

The probability histograms of the posterior distributions obtained by the ABC algorithm are similar for the parameter τ for both hypotheses (see Figure 4.25 and

4.26). However, it seems that τ could be pushed even further than 300 seconds for the hypothesis H_1 whereas for the hypothesis H_2 the maximum is $\tau = 262$ seconds. Significant learning for parameter μ occurs under both hypotheses (see Figure 4.26). According to findings by Schoeberl *et al.* (2002) the de-phosphorylation rate of ERK is equal to $0.27s^{-1}$ for the first phosphorylation site and $0.30s^{-1}$ for the second phosphorylation site. The rate responsible for the de-phosphorylation or the signal decay in Model 2 is the rate μ. This rate is found to be close to the ones reported by Schoeberl *et al.* (2002) for the hypothesis H_2. The value of μ for the hypothesis H_1 is much too high. The distribution for κ is more spread out but the mass is concentrated around $\kappa = 2000$ for the hypothesis H_2 results. The distribution of λ in both hypotheses is similar to its prior distribution.

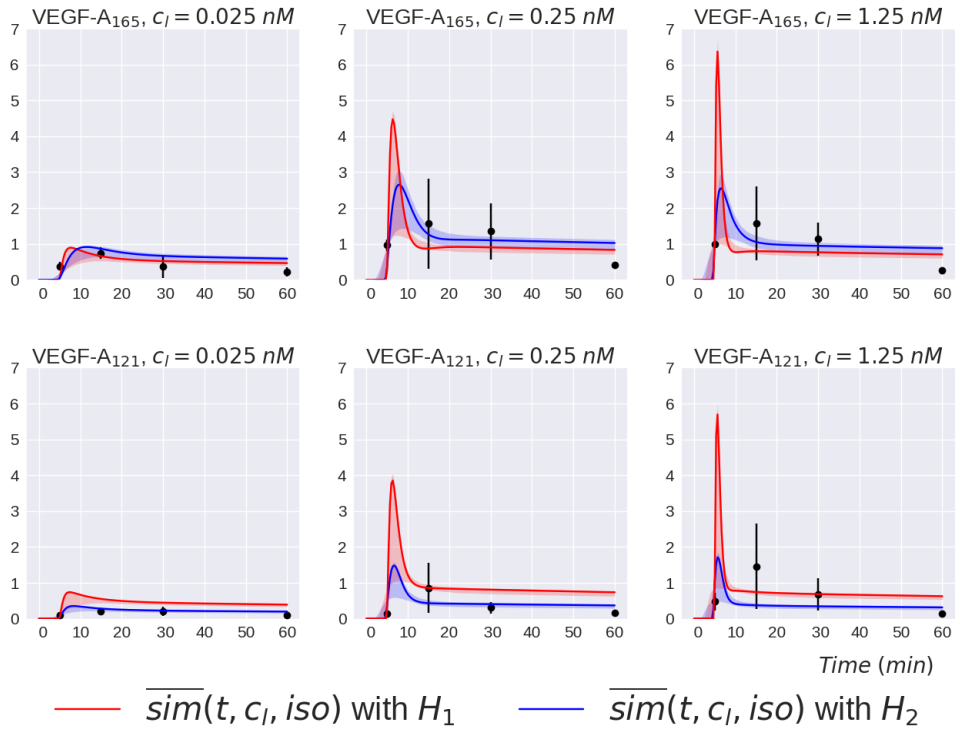

Figure 4.27: Quantified ERK phosphorylation from Table 4.2 plotted as black dots with bars representing 95% confidence interval of the data at each time point. The curves represent simulation defined by Equation (4.11) for the hypothesis H_1 and hypothesis H_2. The shaded area is found between the 5th and the 95th percentile at each time point over the simulations computed using all accepted $\hat{\boldsymbol{\theta}}$.

The curves on Figure 4.27 are obtained by finding the median taken over the numerical solution of Equation (4.5) together with Equation (4.9) or (4.10) (depending on the hypothesis) for all accepted parameters for the hypothesis H_1 (in red) and the hypothesis H_2 (in blue). The shaded area is between the 5th and the 95th percentile of these simulations. According to the experiment the peak of ERK phosphorylation is around 15-20 minutes. The peak is reached for the smallest concentration for the isoform VEGF-A_{165} (see Figures 4.27) for the hypothesis H_2. For the concentration 0.25nM and 1.25nM the peak is closer to 10 minutes for the hypothesis H_2 but the peak for the hypothesis H_1 is highly overestimated.

Model selection

The hypotheses can be compared by finding their relative probabilities, which have their grounds on Bayes theorem (see Theorem 2.4), defined as follows,

$$p(H_i|\delta = \delta^*) = \frac{f(H_i|\delta = \delta^*)}{f(H_1|\delta = \delta^*) + f(H_2|\delta = \delta^*)}, \tag{4.12}$$

where $f(H_i)$ is the number of accepted parameters given that in the ABC algorithm one accepts only the results with the distance equal or less than δ^*. Figure 4.28 shows how the relative probability changes for each hypothesis versus δ^*. Once threshold δ^* grows enough the relative probability of both hypotheses converges to $\frac{1}{2}$, meaning that all of the proposed parameters are being accepted under both hypotheses. The most plausible is the hypothesis H_2 with higher relative probability for small enough distance. Similarly the number of accepted parameters grows faster for the hypothesis H_2 compared to the hypothesis H_1.

The analysis of Model 2 indicates that the signal for ERK phosphorylation more likely comes from the endosome compartment. In the following section, I investigate how incorporating VEGFR1 into the model, which leads to the presence of heterodimers, can affect signalling. In particular, I test different hypotheses on how receptor transport from the Golgi to the cell surface can be triggered by signal generated at different cell locations.

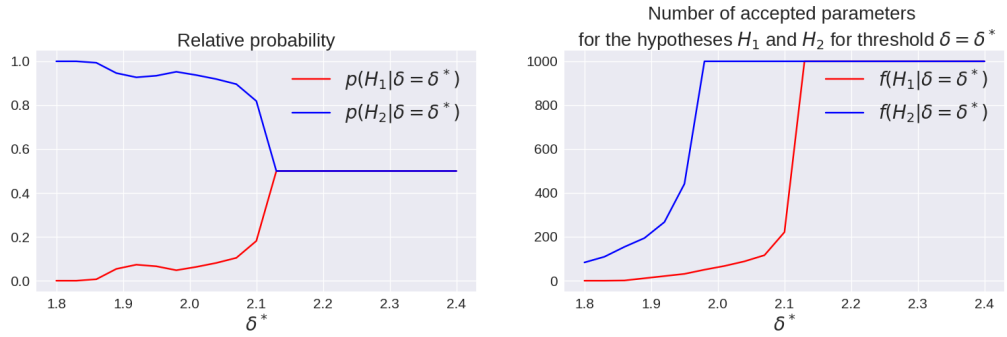

Figure 4.28: The relative probability for two tested hypotheses depending on the distance threshold δ^* and the frequency of two tested hypotheses.

4.2 Modelling calcium-regulated VEGFR2 signalling

Calcium ions play multiple regulatory roles in cell function and physiology (see Clapham (2007)). In mammals, calcium levels are tightly regulated to maintain millimolar ($10^{-3}mol/L$) concentrations in extracellular fluids, such as blood, but less than micromolar ($10^{-6}mol/L$) concentrations within the cytosol. Such a calcium gradient allows rapid fluxes of calcium ion levels in different intracellular compartments in response to external stimuli, with subsequent effects on cell and animal physiology (see Bao *et al.* (2012)). Changes in intracellular calcium-ion levels can modulate different aspects of endothelial physiology and vascular function, such as wound repair and blood pressure. Disruption of calcium homoeostasis in vascular endothelial cells is therefore associated with cellular dysfunction. Here, I investigate how VEGFR2 phosphorylation upon VEGF-A stimulation can regulate VEGFR synthesis through calcium ions release. I hypothesise that transportation of VEGFR1 or/and VEGFR2 from the Golgi to the cell surface is perturbed (either enhanced or inhibited) by signalling from phosphorylated VEGFR2 homodimers. This enhancement, or even a potential inhibition, is represented by parameters $\omega_t^{(j)} \in (-1, 1)$, for $j \in \{1, 2\}$, where the specific values will be estimated using the Bayesian inference.

4.2.1 Experimental data

The data presented in this section were provided by the group of Dr. Sreenivasan Ponnambalam from the School of Molecular and Cellular Biology at the University of Leeds. As in the previous section, the quantitative data were obtained via western blots analysis. In particular, human umbilical vein endothelial cells were stimulated with 0.25 of VEGF-A_{165} and protein level measurements were obtained at different time points within the first hour after stimulation:

- the intensity of VEGFR2 phosphorylation at the residue Y1175 at the cell surface,
- the intensity of VEGFR1 receptors at the cell surface,
- the intensity of VEGFR2 receptors at the cell surface,

where all these intensities were given normalised by the intensity of the *transferrin receptor* (TfR), and where all the experiments were repeated three times. The intensity data are given in Table 4.20.

The aim here is to use these data to estimate some of the parameters in the binding and trafficking model described later in Subsection 4.2.3. As the deterministic model describes how the numbers of each molecule change with time, it is not possible to make use of the intensity data directly. In Section 4.1 the data were given normalised by the intensity of phosphorylated VEGFR2 receptors at time 5 min. In this case one can choose the way of normalisation. Here the data are normalised by the sum of the intensities of VEGFR1 and VEGFR2 at the time 0 min (without any ligand stimulation). Let $ei(p,t,i)$ be the value for the experimental intensity of the protein p, at time point t, for the experiment from the set i, where $p \in M = \{\text{pVEGFR2}, \text{VEGFR1}, \text{VEGFR2}\}$, $t \in T = \{0\ min, 5\ min, 15\ min, 30\ min, 60\ min\}$, and $i \in I = \{1,2,3\}$ from Table 4.20. Hence the quantified data for the phosphorylated VEGFR2 at time t for the experimental set i, denoted as $q(\text{pVEGFR2}, t, i)$, is found from the following equation,

$$q(\text{pVEGFR2}, t, i) = \frac{ei(\text{pVEGFR2}, t, i)}{ei(\text{VEGFR1}, t = 0min, i) + ei(\text{VEGFR2}, t = 0min, i)},$$

for $t \in T$ and $i \in I$. The results of this quantification are given in Table 4.22.

Intensity of the phosphorylated VEGFR2 on the cell surface

time $[min]$	set 1	set 2	set 3	mean	sample SD
5	1.19	1.80	1.11	1.37	0.38
15	1.78	0.81	1.43	1.34	0.49
30	0.87	0.22	0.10	0.39	0.41
60	0.69	0.48	0.59	0.58	0.11

Intensity of VEGFR1 on the cell surface

time $[min]$	set 1	set 2	set 3	mean	sample SD
0	0.89	0.81	0.66	0.79	0.12
5	0.34	0.76	0.75	0.62	0.24
15	1.73	0.92	1.45	1.37	0.41
30	1.78	1.60	1.60	1.66	0.10
60	2.44	2.07	1.20	1.90	0.64

Intensity of VEGFR2 on the cell surface

time $[min]$	set 1	set 2	set 3	mean	sample SD
0	2.25	2.83	0.95	2.01	0.96
5	1.50	1.98	0.42	1.30	0.80
15	1.83	1.45	1.57	1.61	0.19
30	1.11	0.70	0.92	0.91	0.21
60	1.56	0.38	0.49	0.81	0.65

Table 4.20: The intensities of the phosphorylated VEGFR2, the total VEGFR1 and the total VEGFR2 on the cell surface upon $0.25nM$ of VEGF-A_{165} stimulation normalised by the level of the intensity of TfR.

As for the number of the membrane bound receptors one can translate the intensities from Table 4.20 into the actual numbers of receptors. In Section 4.1 it was assumed that the cell can be split into three different spatial compartments (*cell surface*, *endosome* and *the Golgi apparatus*). In the absence of ligand stimulation the relative fractions of receptors in these three compartments have been estimated as follows (see Table 4.21).

receptor	cell surface	endosome	Golgi
VEGFR1	20%	2%	78%
VEGFR2	60%	20%	20%

Table 4.21: The fractions of the receptors VEGFR1 and VEGFR2 located in different cell compartments according to observations made by Jopling *et al.* (2011).

This information together with the assumption about the mean number of receptors in the unstimulated cell is used to quantify the intensity data into numbers of receptors. According to private communication with Dr. Ponnambalam, the cells used in the experiments have on average 10^4 VEGFR1 and 2×10^5 VEGFR2 per cell, which agrees with observations reported by Napione *et al.* (2012). This indicates that there are 2×10^3 VEGFR1 and 1.2×10^5 VEGFR2 on the cell surface on average. The mean intensity of VEGFR1 at time point 0 *min* is equal to 0.79, which should correspond to 2×10^3 receptors. Therefore each intensity of VEGFR1 from Table 4.20 can be translated into numbers of receptors, using the following equation

$$q(VEGFR1, t, i) = \frac{ei(VEGFR1, t, i) \cdot 2000}{0.79}.$$

Similarly the intensities of VEGFR2 at the cell surface are translated into numbers of VEGFR2 using the following equation,

$$q(VEGFR2, t, i) = \frac{ei(VEGFR2, t, i) \cdot 120000}{2.01},$$

where 2.01 is the mean intensity of VEGFR2 at time point 0 *min*. This quantification for both receptors is reported in Table 4.22.

Quantified phosphorylated VEGFR2 data

time $[min]$	set 1	set 2	set 3	mean	sample SD
5	0.38	0.49	0.69	0.52	0.16
15	0.57	0.22	0.89	0.56	0.33
30	0.28	0.06	0.06	0.13	0.12
60	0.22	0.13	0.36	0.24	0.12

Quantified number of VEGFR1 per cell upon ligand stimulation

time $[min]$	set 1	set 2	set 3	mean	sample SD
0	2264	2060	1676	2000	299
5	863	1937	1902	1567	610
15	4398	2335	3680	3471	1048
30	4514	4066	4050	4210	263
60	6192	5261	3035	4829	1622

Quantified number of VEGFR1 per cell upon ligand stimulation

time $[min]$	set 1	set 2	set 3	mean	sample SD
0	134159	168899	56942	120000	57306
5	89188	117955	24902	77348	47643
15	109014	86287	93542	96281	11608
30	66251	41654	54982	54296	12313
60	92837	22629	29062	48176	38812

Table 4.22: Quantification of the data given in Table 4.20. The description of the quantification is in the text.

4.2.2 Basal mathematical model (no ligand)

Consider the human umbilical vein endothelial cells that express VEGFR1 and VEGFR2, which can be found in three different spatial compartments of the cell: the Golgi apparatus, the endosome and the cell surface. Schematic models for VEGFR1 and VEGFR2 basal trafficking are presented in Figures 4.29 and 4.30 where the following reactions are considered:

- $k_s^{(j)}$ - synthesis of receptors in the Golgi,

- $k_t^{(j)}$ - trafficking of receptors from the Golgi to the cell surface,
- $k_i^{(j)}$ - internalisation of receptors from the surface to the endosome,
- $k_r^{(j)}$ - recycling of receptors from the endosome to the surface,
- $k_d^{(j)}$ - degradation of receptors in the endosome,
- $k_e^{(j)}$ - trafficking of receptors from the endosome to the Golgi.

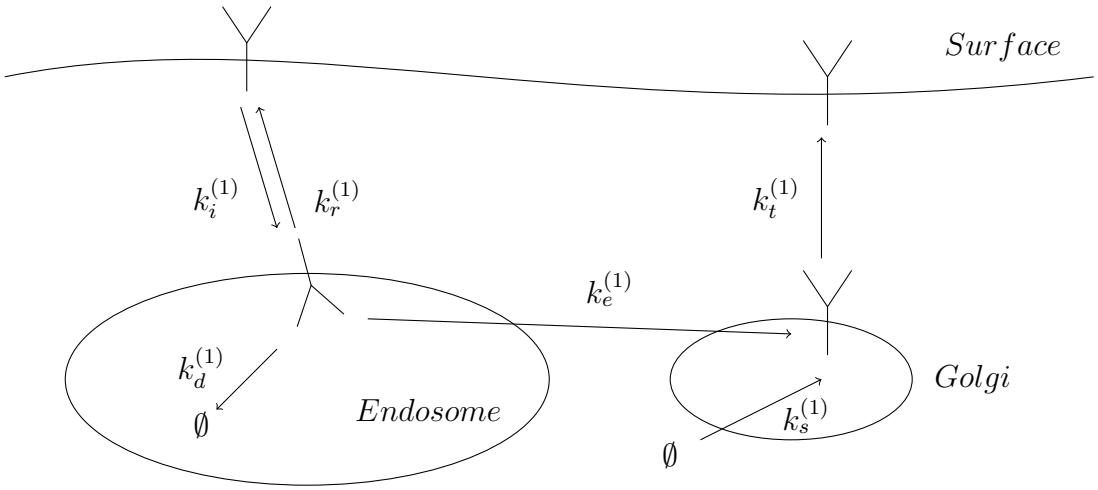

Figure 4.29: The schematic model for basal VEGFR1 receptor trafficking.

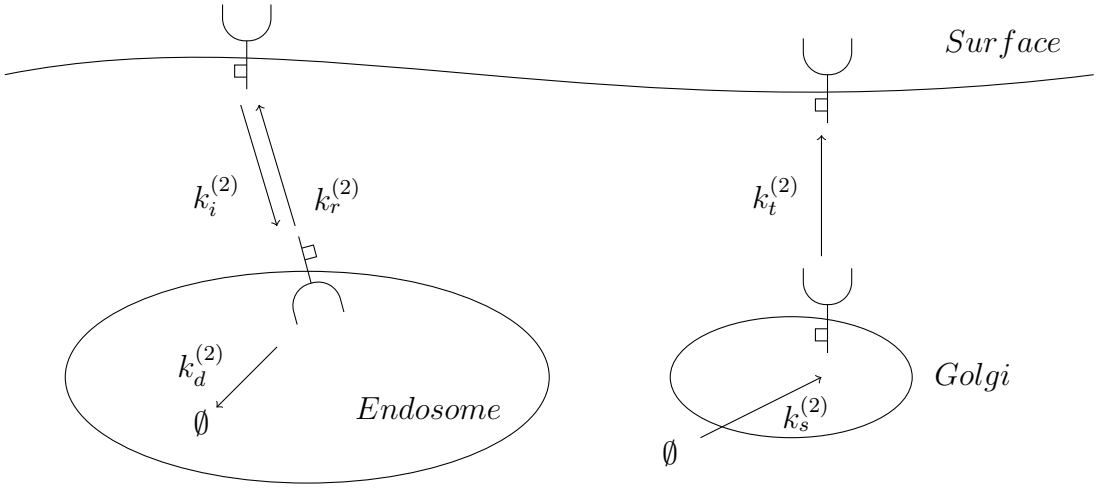

Figure 4.30: The schematic model for basal VEGFR2 receptor trafficking.

For rates above the index $j \in \{1, 2\}$ refers to VEGFR1 and VEGFR2, respectively. I assume that $k_e^{(2)} = 0$ since receptor VEGFR2 does not traffic from the endosome to the Golgi (see Simons (2012), Smith *et al.* (2015), Smith *et al.* (2016)). The fact that this rate vanishes implies that the trafficking dynamics of VEGFR1 and VEGFR2 are different. Note that VEGFR1 and VEGFR2 have independent trafficking dynamics in the absence of ligand, and thus, in the following sections, they will be analysed separately.

VEGFR1 basal dynamics

Dynamics of VEGFR1 without any ligand stimulation is different from the dynamics of VEGFR2. This is not only due to the different kinetic rates, but also due to the fact that VEGFR1 is known to traffic from the endosome to the Golgi. The variables of VEGFR1 the basal model can be defined as follows,

$$\begin{aligned} R_1^G(t) &= \text{“}\textit{number of free VEGFR1 in the Golgi apparatus at time } t\text{”}, \\ R_1^E(t) &= \text{“}\textit{number of free VEGFR1 in the endosome at time } t\text{”}, \\ R_1^S(t) &= \text{“}\textit{number of free VEGFR1 in the cell surface at time } t\text{”}, \end{aligned}$$

for $t \geq 0$. The dynamics of VEGFR1 described by Figure 4.29 can be expressed in terms of the following equations:

$$\begin{aligned} \frac{dR_1^G(t)}{dt} &= k_s^{(1)} + k_e^{(1)} R_1^E(t) - k_t^{(1)} R_1^G(t), \\ \frac{dR_1^E(t)}{dt} &= k_i^{(1)} R_1^S(t) - k_d^{(1)} R_1^E(t) - k_e^{(1)} R_1^E(t) - k_r^{(1)} R_1^E(t), \\ \frac{dR_1^S(t)}{dt} &= -k_i^{(1)} R_1^S(t) + k_r^{(1)} R_1^E(t) + k_t^{(1)} R_1^G(t), \end{aligned} \tag{4.13}$$

with initial conditions $R_1^G(0) = 7.8 \times 10^3, R_1^E(0) = 2 \times 10^2, R_1^S(0) = 2 \times 10^3$ given by proportions from Table 4.21, together with the total number of receptors per cell found from experiments (see Subsection 4.2.1 for details). The steady state

$\boldsymbol{R_1^*} = (R_1^{G,*}, R_1^{E,*}, R_1^{S,*})$ of Equation (4.13) is given as

$$\begin{aligned} R_1^{G,*} &= \frac{k_s^{(1)}(k_e^{(1)} + k_d^{(1)})}{k_t^{(1)} k_d^{(1)}}, \\ R_1^{E,*} &= \frac{k_s^{(1)}}{k_d^{(1)}}, \\ R_1^{S,*} &= \frac{k_s^{(1)}(k_d^{(1)} + k_r^{(1)} + k_e^{(1)})}{k_d^{(1)} k_i^{(1)}}. \end{aligned} \tag{4.14}$$

Hence, the total number of VEGFR1 per cell in steady state ($R_1^{T,*} = R_1^{G,*} + R_1^{E,*} + R_1^{S,*}$) can be found from the following equation

$$R_1^{T,*} = \frac{k_s^{(1)}\left(k_i^{(1)}(k_e^{(1)} + k_d^{(1)} + k_t^{(1)}) + k_t^{(1)}(k_r^{(1)} + k_e^{(1)} + k_d^{(1)})\right)}{k_i^{(1)} k_d^{(1)} k_t^{(1)}}. \tag{4.15}$$

In order to analyse the stability of this steady state defined by Equation (4.14), the Jacobian matrix $\boldsymbol{J_1}$ is computed

$$\boldsymbol{J_1} = \begin{pmatrix} -k_t^{(1)} & k_e^{(1)} & 0 \\ 0 & -(k_d^{(1)} + k_e^{(1)} + k_r^{(1)}) & k_i^{(1)} \\ k_t^{(1)} & k_r^{(1)} & -k_i^{(1)} \end{pmatrix}.$$

The eigenvalues of matrix $\boldsymbol{J_1}$ are obtained from the following characteristic polynomial

$$\begin{aligned} &\sigma^3 + \sigma^2\left(k_i^{(1)} + k_t^{(1)} + k_d^{(1)} + k_e^{(1)} + k_r^{(1)}\right) + \sigma\left(k_i^{(1)}k_d^{(1)} + k_t^{(1)}k_e^{(1)} + k_t^{(1)}k_r^{(1)}\right. \\ &\left. + k_i^{(1)}k_e^{(1)} + k_d^{(1)}k_i^{(1)} + k_t^{(1)}k_i^{(1)}\right) + k_d^{(1)}k_i^{(1)}k_t^{(1)} = 0. \end{aligned}$$

Routh-Hurwitz criteria (see Section 4.5 by Linda (2007) for details) can be used to show that steady state defined by Equation (4.14) is stable, by checking that the real parts of these eigenvalues are negative. In particular, for the characteristic polynomial of order three above, the Routh-Hurwitz criteria states that all its roots have negative real part if and only if

$$k_i^{(1)} + k_t^{(1)} + k_d^{(1)} + k_e^{(1)} + k_r^{(1)} > 0, \quad k_d^{(1)}k_i^{(1)}k_t^{(1)} > 0,$$

$$\left(k_i^{(1)} + k_t^{(1)} + k_d^{(1)} + k_e^{(1)} + k_r^{(1)}\right)\left(k_i^{(1)}(2k_d^{(1)} + k_e^{(1)}) + k_t^{(1)}(k_e^{(1)} + k_r^{(1)} + k_i^{(1)})\right)$$

$$> k_d^{(1)}k_i^{(1)}k_t^{(1)}.$$

These conditions are clearly verified for any positive values of the kinetic rates, so that the steady state is stable. From Equations (4.14) and (4.15), one can obtain the fractions of receptors in each compartment at steady state $\boldsymbol{f_1^*} = (f_1^{G,*}, f_1^{E,*}, f_1^{S,*})$, which are

$$\begin{aligned} f_1^{G,*} &= \frac{R_1^{G,*}}{R_1^{T,*}} = \frac{k_i^{(1)}(k_d^{(1)} + k_e^{(1)})}{k_i^{(1)}(k_e^{(1)} + k_d^{(1)} + k_t^{(1)}) + k_t^{(1)}(k_d^{(1)} + k_r^{(1)} + k_e^{(1)})}, \\ f_1^{E,*} &= \frac{R_1^{E,*}}{R_1^{T,*}} = \frac{k_t^{(1)} k_i^{(1)}}{k_i^{(1)}(k_d^{(1)} + k_t^{(1)} + k_e^{(1)}) + k_t^{(1)}(k_e^{(1)} + k_d^{(1)} + k_r^{(1)})}, \\ f_1^{S,*} &= \frac{R_1^{S,*}}{R_1^{T,*}} = \frac{k_t^{(1)}(k_e^{(1)} + k_d^{(1)} + k_r^{(1)})}{k_i^{(1)}(k_e^{(1)} + k_d^{(1)} + k_t^{(1)}) + k_t^{(1)}(k_e^{(1)} + k_d^{(1)} + k_r^{(1)})}, \end{aligned} \tag{4.16}$$

so that clearly $f_1^{G,*} + f_1^{E,*} + f_1^{S,*} = 1$.

VEGFR2 basal dynamics

As noted before VEGFR2 is not transported from the endosome to the Golgi (see Figure 4.30). The variables of the VEGFR basal model can be defined, for $t \geq 0$, as follows,

$$\begin{aligned} R_2^G(t) &= \text{“}\textit{number of free VEGFR2 in the Golgi apparatus at time } t\text{”}, \\ R_2^E(t) &= \text{“}\textit{number of free VEGFR2 in the endosome at time } t\text{”}, \\ R_2^S(t) &= \text{“}\textit{number of free VEGFR2 in the cell surface at time } t\text{”}. \end{aligned}$$

The dynamics for VEGFR2 can be expressed in terms of the following equations:

$$\begin{aligned} \frac{dR_2^G(t)}{dt} &= k_s^{(2)} - k_t^{(2)} R_2^G(t), \\ \frac{dR_2^E(t)}{dt} &= k_i^{(2)} R_2^S(t) - k_d^{(2)} R_2^E(t) - k_r^{(2)} R_2^E(t), \\ \frac{dR_2^S(t)}{dt} &= -k_i^{(2)} R_2^S(t) + k_r^{(2)} R_2^E(t) + k_t^{(2)} R_2^G(t), \end{aligned} \tag{4.17}$$

for $t \geq 0$, and initial conditions $R_2^G(0) = 4 \times 10^4$, $R_2^E(0) = 4 \times 10^4$, $R_2^S(0) = 1.2 \times 10^5$ taken from the experimental results (see Table 4.21 and comments

regarding the total number of receptors per cell in Subsection 4.2.1). The steady state $\boldsymbol{R_2^*} = (R_2^{G,*}, R_2^{E,*}, R_2^{S,*})$ of Equation (4.18) is given as

$$\begin{aligned} R_2^{G,*} &= \frac{k_s^{(2)}}{k_t^{(2)}}, \\ R_2^{E,*} &= \frac{k_s^{(2)}}{k_d^{(2)}}, \\ R_2^{S,*} &= \frac{k_s^{(2)}(k_d^{(2)} + k_r^{(2)})}{k_d^{(2)} k_i^{(2)}}. \end{aligned} \tag{4.18}$$

Hence, the total number of VEGFR2 per cell ($R_2^{T,*} = R_2^{G,*} + R_2^{E,*} + R_2^{S,*}$) at the steady state can be found from the following equation,

$$R_2^{T,*} = \frac{k_s^{(2)}\left(k_t^{(2)}(k_d^{(2)} + k_r^{(2)}) + k_i^{(2)}(k_t^{(2)} + k_d^{(2)})\right)}{k_i^{(2)} k_d^{(2)} k_t^{(2)}}. \tag{4.19}$$

In order to analyse the stability of this steady state, the Jacobian matrix $\boldsymbol{J_2}$ is computed,

$$\boldsymbol{J_2} = \begin{pmatrix} -k_t^{(2)} & 0 & 0 \\ 0 & -(k_d^{(2)} + k_r^{(2)}) & k_i^{(2)} \\ k_t^{(2)} & k_r^{(2)} & -k_i^{(2)} \end{pmatrix}.$$

The eigenvalues of the matrix $\boldsymbol{J_2}$ are

$$\begin{aligned} \sigma_1^{(2)} &= -k_t^{(2)}, \\ \sigma_2^{(2)} &= -\frac{1}{2}\left((k_d^{(2)} + k_i^{(2)} + k_r^{(2)}) + \sqrt{(k_i^{(2)} + k_d^{(2)} + k_r^{(2)})^2 - 4k_i^{(2)}k_d^{(2)}}\right), \\ \sigma_3^{(2)} &= -\frac{1}{2}\left((k_d^{(2)} + k_i^{(2)} + k_r^{(2)}) - \sqrt{(k_i^{(2)} + k_d^{(2)} + k_r^{(2)})^2 - 4k_i^{(2)}k_d^{(2)}}\right). \end{aligned}$$

$\sigma_1^{(2)}, \sigma_2^{(2)}$ and $\sigma_3^{(2)}$ are real and negative for any positive values of the kinetic rates. Thus, the steady state defined by Equation (4.18) is stable. The fractions of receptors in each compartment, $\boldsymbol{f_2^*} = (f_2^{G,*}, f_2^{E,*}, f_2^{S,*})$, at steady state can be

obtained from Equations (4.18) and (4.19), which are

$$\begin{aligned} f_2^{G,*} &= \frac{R_2^{G,*}}{R_2^{T,*}} = \frac{k_d^{(2)} k_i^{(2)}}{k_i^{(2)}(k_d^{(2)} + k_t^{(2)}) + k_t^{(2)}(k_d^{(2)} + k_r^{(2)})}, \\ f_2^{E,*} &= \frac{R_2^{E,*}}{R_2^{T,*}} = \frac{k_t^{(2)} k_i^{(2)}}{k_i^{(2)}(k_d^{(2)} + k_t^{(2)}) + k_t^{(2)}(k_d^{(2)} + k_r^{(2)})}, \\ f_2^{S,*} &= \frac{R_2^{S,*}}{R_2^{T,*}} = \frac{k_t^{(2)}(k_d^{(2)} + k_r^{(2)})}{k_i^{(2)}(k_d^{(2)} + k_t^{(2)}) + k_t^{(2)}(k_d^{(2)} + k_r^{(2)})}, \end{aligned} \tag{4.20}$$

so that clearly $f_2^{G,*} + f_2^{E,*} + f_2^{S,*} = 1$.

4.2.3 Model 3: mathematical model of ligand stimulation

In this section I introduce the model, called Model 3, with two different type of receptors, VEGFR1 and VEGFR2 and one type of ligand, VEGF-A_{165}. The variables at time t in Model 3 are defined as follows,

$L(t)$ = *"number of free ligands L"*,

$R_j^S(t)$ = *"number of free receptors R_j^S on the cell surface"*,

$M_j^S(t)$ = *"number of monomers M_j^S on the cell surface"*,

$P_j^S(t)$ = *"number of phosphorylated homodimers P_j^S on the cell surface "*,

$P_{12}^S(t)$ = *" number of phosphorylated heterodimers P_{12}^S on the cell surface"*,

$R_j^E(t)$ = *"number of free receptors R_j^E in the endosome"*,

$M_j^E(t)$ = *" number of monomers M_j^E in the endosome"*,

$P_j^E(t)$ = *"number of phosphorylated homodimers P_j^E in the endosome"*,

$P_{12}^E(t)$ = *" number of phosphorylated heterodimers P_{12}^E in the endosome"*,

$R_j^E(t)$ = *"number of free receptors R_j^G in the Golgi"*,

where $j \in \{1, 2\}$ denotes the receptor type involved in the corresponding complex ($j = 1$ for VEGFR1 and $j = 2$ for VEGFR2). The complexes which occur in Model 3 are described in Table 4.23.

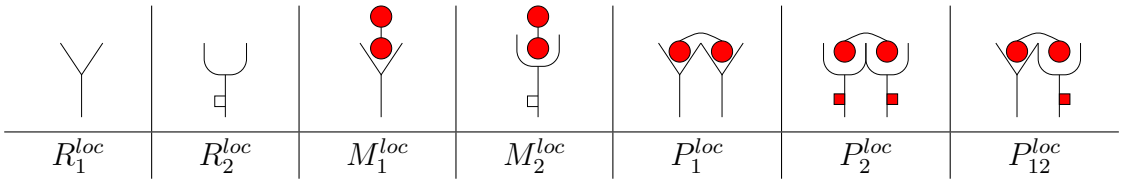

Table 4.23: Molecules occurring in Model 3. The index *loc* denotes the localisation of each molecule, that is $loc \in \{G, E, S\}$, where G, E, and S stands for a molecule in the Golgi apparatus, in the endosome and on the cell surface, respectively.

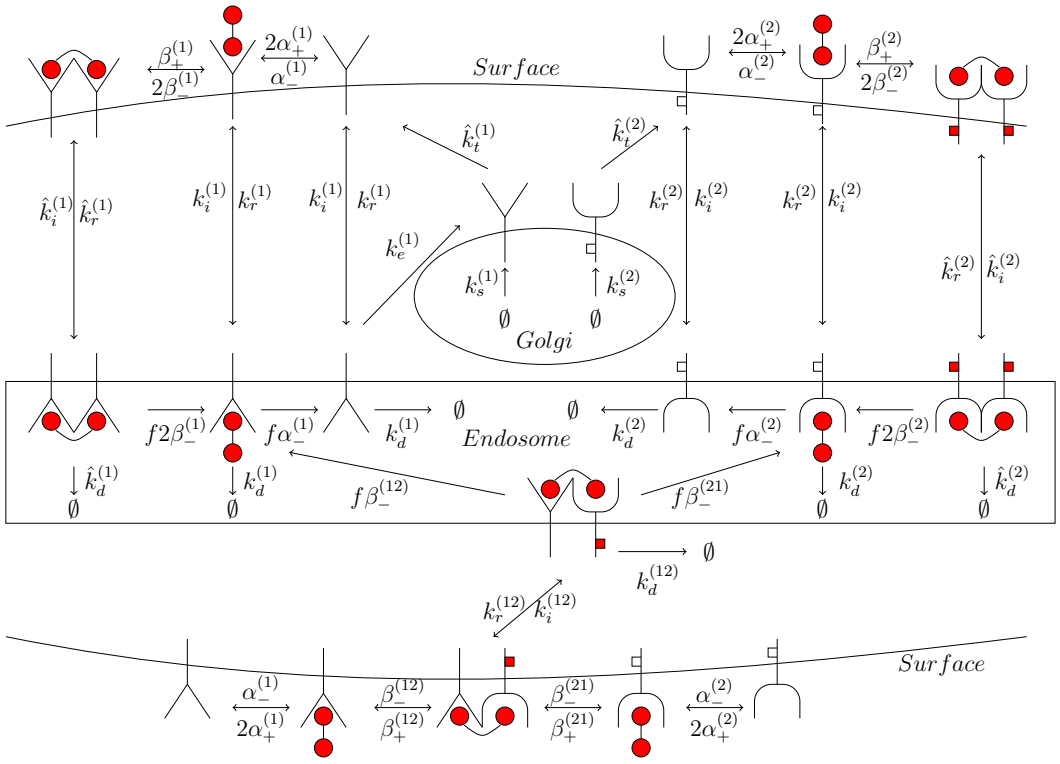

Figure 4.31: Events involved in the model for binding and trafficking of two receptor types (VEGFR1 and VEGFR2). The parameters of the model are described in the text.

The following reactions, from Figure 4.31, are considered in Model 3,

- binding (with rate $\alpha_+^{(j)}$) of free receptors VEGFRj (R_j^S) with free ligands on the cell surface, forming monomers M_j^S, and dissociation (with rate $\alpha_-^{(j)}$), where $j \in \{1, 2\}$;

- binding (with rate β_+^j) of monomers M_j^S with free receptors VEGFRj (R_j^S) forming phosphorylated homodimers P_j^S, and dissociation (with rate β_-^j), where $j \in \{1, 2\}$;

- binding (with rate β_+^{ij}) of monomers M_i^S with free receptors VEGFRj (R_j^S) forming phosphorylated heterodimers P_{ij}^S, and dissociation (with rate β_-^{ij}), where $i, j \in \{1, 2\}$ and $i \neq j$;

- internalisation from the cell surface to the endosome of free receptors VEGFRj (R_j^S) (with rate $k_i^{(j)}$), monomers M_j^S (with rate $k_i^{(j)}$), phosphorylated homodimers P_j^S (with rate $\hat{k}_i^{(j)}$), phosphorylated heterodimers P_{12}^S (with rate $k_i^{(12)}$), where $j \in \{1, 2\}$;

- recycling from the endosome to the cell surface of free receptors VEGFRj (R_j^S) (with rate $k_r^{(j)}$), monomers M_j^S (with rate $k_r^{(j)}$), phosphorylated homodimers P_j^S (with rate $\hat{k}_r^{(j)}$), phosphorylated heterodimers P_{12}^S (with rate $k_r^{(12)}$), where $j \in \{1, 2\}$;

- degradation of free receptors R_i^E (with rate $k_d^{(i)}$), monomers M_i^E (with rate $k_d^{(i)}$), phosphorylated homodimers P_i^E (with rate $\hat{k}_d^{(i)}$), phosphorylated heterodimers P_{12}^E (with rate $k_d^{(12)}$) in the endosome, where $i \in \{1, 2\}$;

- dissociation of phosphorylated dimers and monomers in the endosome, occurring with the same rates as on the cell surface, but multiplied by a factor $f > 1$ (as the more acidic environment in the endosome enhance the rate of dissociation in this compartment);

- synthesis of free receptors R_i^S into the Golgi (with rate $k_s^{(i)}$), where $i \in \{1, 2\}$;

- transport of free receptors R_i^S from the Golgi into the cell surface (with rate $\hat{k}_t^{(i)}$), where $i \in \{1, 2\}$;

- trafficking of receptors R_1^S from the endosome to the Golgi (with rate $k_e^{(1)}$).

As it was explained in Section 4.1 for Model 1, the internalisation rates are the same for free receptors and monomers as the conformational change of the receptor, which can affect its internalisation rate, is assumed to take place after dimerisation. There are number of rates with the symbol $\hat{}$, representing the effect receptor-ligand phosphorylation has on them. In particular, the following mechanism is studied in this section,

$$\hat{k}_t^{(j)}(s) \;=\; k_t^{(j)}\left(1+\omega_j\frac{x_s^{(j)}}{x_s^{(j)}+\kappa_j}\right), \quad j\in\{1,2\}, \tag{4.21}$$

for $s \geq 0$, where $x_s^{(j)}$ is the signal causing the enhancement (for $\omega_j > 0$) or the inhibition (for $\omega_j < 0$) of the transport of free VEGFRj from the Golgi to the cell surface, and κ_j is the carrying capacity of the signal. Two hypotheses are examined in this section assuming that the transport rate is changed by

H_1) the number of phosphorylated homodimers on the cell surface

$$x_s^{(j)} = P_S^{(2)}(s),$$

H_2) the number of phosphorylated homodimers in the endosome

$$x_s^{(j)} = P_E^{(2)}(s).$$

The signal can hypothetically cause the enhancement or the inhibition of the transport rate $\hat{k}_t^{(j)}(\cdot)$, which is also studied later in this section by proposing different prior distributions for ω_j during Bayesian parameterisation.

Initial conditions for Model 3 are set by combining the information about the total number of receptors per cell (see Subsection 4.2.1) together with the percentages from Table 4.21, yielding to $(L(0),\ R_1^S(0),\ R_2^S(0),\ M_1^S(0),\ M_2^S(0),\ P_1^S(0),\ P_2^S(0),\ P_{12}^S(0),\ R_1^E(0),\ R_2^E(0),\ M_1^E(0),\ M_2^E(0),\ P_1^E(0),\ P_2^E(0),\ P_{12}^E(0),\ R_1^G(0),\ R_2^G(0)\big) = (n_L,\ 2\times10^3,\ 1.2\times10^5,\ 0,\ 0,\ 0,\ 0,\ 0,\ 2\times10^2,\ 4\times10^4,\ 0,\ 0,\ 0,\ 0,\ 0,\ 7.8\times10^3,\ 4\times10^4)$, where $n_L = 1.5\times10^5$ which is equivalent to $0.25nM$ per cell.

Thus for $t \geq 0$ Model 3 is determined by the following system of ODEs

$$\begin{aligned}
\frac{dL(t)}{dt} &= \alpha_-^{(2)} M_2^S(t) + \alpha_-^{(1)} M_1^S(t) - 2\alpha_+^{(2)} R_2^S(t)L(t) - 2\alpha_+^{(1)} R_1^S(t)L(t), \\
\frac{dR_1^S(t)}{dt} &= \hat{k}_t^{(1)} R_1^G(t) + k_r^{(1)} R_1^E(t) + \alpha_-^{(1)} M_1^S(t) + 2\beta_-^{(1)} P_1^S(t) + \beta_-^{(21)} P_{12}^S(t) \\
&\quad -2\alpha_+^{(1)} R_1^S(t)L(t) - k_i^{(1)} R_1^S(t) - \beta_+^{(1)} M_1^S(t) R_1^S(t) - \beta_+^{(21)} M_2^S(t) R_1^S(t), \\
\frac{dR_2^S(t)}{dt} &= \hat{k}_t^{(2)} R_2^G(t) + k_r^{(2)} R_2^E(t) + \alpha_-^{(2)} M_2^S(t) + 2\beta_-^{(2)} P_2^S(t) + \beta_-^{(12)} P_{12}^S(t) \\
&\quad -2\alpha_+^{(2)} R_2^S(t)L(t) - k_i^{(2)} R_2^S(t) - \beta_+^{(2)} M_2^S(t) R_2^S(t) - \beta_+^{(12)} M_1^S(t) R_2^S(t), \\
\frac{dM_1^S(t)}{dt} &= 2\alpha_+^{(1)} R_1^S(t)L(t) + k_r^{(1)} M_1^E(t) + 2\beta_-^{(1)} P_1^S(t) + \beta_-^{(12)} P_{12}^S(t) \\
&\quad -\beta_+^{(1)} M_1^S(t) R_1^S(t) - \beta_+^{(12)} M_1^S(t) R_2^S(t) - \alpha_-^{(1)} M_1^S(t) - k_i^{(1)} M_1^S(t), \\
\frac{dM_2^S(t)}{dt} &= 2\alpha_+^{(2)} R_2^S(t)L(t) + k_r^{(2)} M_2^E(t) + 2\beta_-^{(2)} P_2^S(t) + \beta_-^{(21)} P_{12}^S(t) \\
&\quad -\beta_+^{(2)} M_2^S(t) R_2^S(t) - \beta_+^{(21)} M_2^S(t) R_1^S(t) - \alpha_-^{(2)} M_2^S(t) - k_i^{(2)} M_2^S(t), \\
\frac{dP_1^S(t)}{dt} &= \beta_+^{(1)} M_1^S(t) R_1^S(t) + \hat{k}_r^{(1)} P_1^E(t) - 2\beta_-^{(1)} P_1^S(t) - \hat{k}_i^{(1)} P_1^S(t), \\
\frac{dP_2^S(t)}{dt} &= \beta_+^{(2)} M_2^S(t) R_2^S(t) + \hat{k}_r^{(2)} P_2^E(t) - 2\beta_-^{(2)} P_2^S(t) - \hat{k}_i^{(2)} P_2^S(t), \\
\frac{dP_{12}^S(t)}{dt} &= \beta_+^{(21)} M_2^S(t) R_1^S(t) + \beta_+^{(12)} M_1^S(t) R_2^S(t) + k_r^{(12)} P_{12}^E(t) - \beta_-^{(21)} P_{12}^S(t) \\
&\quad -\beta_-^{(12)} P_{12}^S(t) - k_i^{(12)} P_{12}^S(t), \\
\frac{dR_1^E(t)}{dt} &= k_i^{(1)} R_1^S(t) + f\alpha_-^{(1)} M_1^E(t) + f\beta_-^{(21)} P_{12}^E(t) + 2f\beta_-^{(1)} P_1^E(t) - k_e^{(1)} R_1^E(t) \\
&\quad -k_d^{(1)} R_1^E(t) - k_r^{(1)} R_1^E(t), \\
\frac{dR_2^E(t)}{dt} &= k_i^{(2)} R_2^S(t) + f\alpha_-^{(2)} M_2^E(t) + 2f\beta_-^{(2)} P_2^E(t) + f\beta_-^{(12)} P_{12}^E(t) - k_d^{(2)} R_2^E(t) \\
&\quad -k_r^{(2)} R_2^E(t), \\
\frac{dM_1^E(t)}{dt} &= k_i^{(1)} M_1^S(t) + 2f\beta_-^{(1)} P_1^E(t) + f\beta_-^{(12)} P_{12}^E(t) - f\alpha_-^{(1)} M_1^E(t) - k_d^{(1)} M_1^E(t) \\
&\quad -k_r^{(1)} M_1^E(t),
\end{aligned}$$

$$\begin{aligned}
\frac{dM_2^E(t)}{dt} &= k_i^{(2)} M_2^S(t) + 2f\beta_-^{(2)} P_2^E(t) + f\beta_-^{(21)} P_{12}^E(t) - f\alpha_-^{(2)} M_2^E(t) - k_d^{(2)} M_2^E(t) \\
&\quad -k_r^{(2)} M_2^E(t), \\
\frac{dP_1^E(t)}{dt} &= \hat{k}_i^{(1)} P_1^S(t) - 2f\beta_-^{(1)} P_1^E(t) - \hat{k}_d^{(1)} P_1^E(t) - \hat{k}_r^{(1)} P_1^E(t), \\
\frac{dP_2^E(t)}{dt} &= \hat{k}_i^{(2)} P_2^S(t) - 2f\beta_-^{(2)} P_2^E(t) - \hat{k}_d^{(2)} P_2^E(t) - \hat{k}_r^{(2)} P_2^E(t), \\
\frac{dP_{12}^E(t)}{dt} &= k_i^{(12)} P_{12}^S(t) - f\beta_-^{(21)} P_{12}^E(t) - f\beta_-^{(12)} P_{12}^E(t) - k_r^{(12)} P_{12}^E(t) - k_d^{(12)} P_{12}^E(t), \\
\frac{dR_1^G(t)}{dt} &= k_s^{(1)} + k_e^{(1)} R_1^E(t) - \hat{k}_t^{(1)} R_1^G(t), \\
\frac{dR_2^G(t)}{dt} &= k_s^{(2)} - \hat{k}_t^{(2)} R_2^G(t).
\end{aligned} \tag{4.22}$$

4.2.4 Parameters' constraints

As for Model 1 in Section 4.1, the dimensionality of the parameter space can be reduced in a few ways. Firstly, note that the binding and the dissociation rates $\alpha_+^{(1)}, \alpha_+^{(2)}, \alpha_-^{(1)}, \alpha_-^{(2)}, \beta_+^{(1)}, \beta_+^{(2)}, \beta_+^{(12)}, \beta_+^{(21)}, \beta_-^{(1)}, \beta_-^{(2)}, \beta_-^{(12)}$ and $\beta_-^{(21)}$ are computed following the arguments described in Section 3.2.1 and 3.2.2. Additionally using Equations (4.16) and (4.20), for the fractions of the receptors in each compartment, together with Equations (4.15) and (4.19), for the total number of receptors per cell, the information about the fractions of receptors in each compartment from Table 4.21 and the assumption about the total number of receptors per cell ($R_1^{T,*} = 10^4, R_2^{T,*} = 2 \times 10^5$), one can find the equations for the following rates

$$\begin{aligned}
&k_t^{(1)} = \tfrac{1}{39}(k_e^{(1)} + k_d^{(1)}), \quad k_s^{(1)} = 2 \times 10^2 k_d^{(1)}, \quad k_i^{(1)} = \tfrac{1}{10}(k_d^{(1)} + k_r^{(1)} + k_e^{(1)}), \\
&\qquad k_t^{(2)} = k_d^{(2)}, \qquad k_s^{(2)} = 4 \times 10^4 k_d^{(2)}, \qquad k_i^{(2)} = \tfrac{1}{3}(k_d^{(2)} + k_r^{(2)}).
\end{aligned} \tag{4.23}$$

4.2.5 Global sensitivity analysis

Denote by $\boldsymbol{\theta}$ the vector of 19 parameters left in the model to be estimated,

$$\boldsymbol{\theta} = \Big(k_d^{(1)}, k_d^{(2)}, \hat{k}_d^{(1)}, \hat{k}_d^{(2)}, k_d^{(12)}, k_r^{(1)}, k_r^{(2)}, \hat{k}_r^{(1)}, \hat{k}_r^{(2)}, k_r^{(12)}, \hat{k}_i^{(1)}, \hat{k}_i^{(2)}, k_i^{(12)}, k_e^{(1)}, f, \kappa_1, \kappa_2, \omega_1, \omega_2\Big). \tag{4.24}$$

By using the Sobol method described in Section 2.3, one can learn about the impact of these parameters on the output of Model 3.

	S_1 mean	S_1 st. deviation	S_1 range	S_T mean	S_T st. deviation	S_T range
$k_d^{(1)}$	0.09	0.20	(0.00, 0.65)	0.09	0.20	(0.00, 0.67)
$k_d^{(2)}$	0.18	0.28	(0.00, 0.82)	0.19	0.30	(0.00, 0.88)
$\hat{k}_d^{(1)}$	$< 10^{-2}$	$< 10^{-2}$	-	$< 10^{-2}$	$< 10^{-2}$	-
$\hat{k}_d^{(2)}$	0.03	0.03	(0.00, 0.09)	0.11	0.11	(0.00, 0.36)
$k_d^{(12)}$	0.04	0.07	(0.00, 0.18)	0.06	0.09	(0.00, 0.22)
$k_r^{(1)}$	$< 10^{-2}$	$< 10^{-2}$	-	$< 10^{-2}$	$< 10^{-2}$	-
$k_r^{(2)}$	$< 10^{-2}$	$< 10^{-2}$	-	$< 10^{-2}$	$< 10^{-2}$	(0.00, 0.01)
$\hat{k}_r^{(1)}$	$< 10^{-2}$	$< 10^{-2}$	-	$< 10^{-2}$	$< 10^{-2}$	-
$\hat{k}_r^{(2)}$	0.01	0.02	(0.00, 0.04)	0.12	0.17	(0.00, 0.57)
$k_r^{(12)}$	0.01	0.02	(0.00, 0.07)	0.02	0.03	(0.00, 0.08)
$\hat{k}_i^{(1)}$	$< 10^{-2}$	$< 10^{-2}$	-	$< 10^{-2}$	$< 10^{-2}$	-
$\hat{k}_i^{(2)}$	0.39	0.36	(0.00, 0.83)	0.51	0.47	(0.00, 0.99)
$k_i^{(12)}$	0.14	0.26	(0.00, 0.74)	0.17	0.29	(0.00, 0.79)
$k_e^{(1)}$	$< 10^{-2}$	$< 10^{-2}$	-	$< 10^{-2}$	$< 10^{-2}$	-
f	$< 10^{-2}$	$< 10^{-2}$	-	0.02	0.01	(0.00, 0.06)
κ_1	$< 10^{-2}$	$< 10^{-2}$	(0.00, 0.01)	$< 10^{-2}$	$< 10^{-2}$	(0.00, 0.01)
κ_2	$< 10^{-2}$	$< 10^{-2}$	-	$< 10^{-2}$	$< 10^{-2}$	-
ω_1	$< 10^{-2}$	$< 10^{-2}$	(0.00, 0.01)	$< 10^{-2}$	0.01	(0.00, 0.02)
ω_2	$< 10^{-2}$	$< 10^{-2}$	-	$< 10^{-2}$	$< 10^{-2}$	-

Table 4.24: The results for the Sobol algorithm for the hypothesis H_1, where S_1 denotes the main effect index and S_T denotes the total effect index.

	S_1 mean	S_1 st. deviation	S_1 range	S_T mean	S_T st. deviation	S_T range
$k_d^{(1)}$	0.09	0.20	(0.00, 0.66)	0.09	0.20	(0.00, 0.67)
$k_d^{(2)}$	0.18	0.28	(0.00, 0.82)	0.19	0.30	(0.00, 0.87)
$\hat{k}_d^{(1)}$	$< 10^{-2}$	$< 10^{-2}$	-	$< 10^{-2}$	$< 10^{-2}$	-
$\hat{k}_d^{(2)}$	0.03	0.03	(0.00, 0.09)	0.11	0.11	(0.00, 0.35)
$k_d^{(12)}$	0.04	0.07	(0.00, 0.17)	0.06	0.09	(0.00, 0.22)
$k_r^{(1)}$	$< 10^{-2}$	$< 10^{-2}$	-	$< 10^{-2}$	$< 10^{-2}$	-
$k_r^{(2)}$	$< 10^{-2}$	$< 10^{-2}$	-	$< 10^{-2}$	$< 10^{-2}$	(0.00, 0.01)
$\hat{k}_r^{(1)}$	$< 10^{-2}$	$< 10^{-2}$	-	$< 10^{-2}$	$< 10^{-2}$	-
$\hat{k}_r^{(2)}$	0.01	0.01	(0.00, 0.04)	0.12	0.16	(0.00, 0.57)
$k_r^{(12)}$	0.01	0.02	(0.00, 0.07)	0.02	0.03	(0.00, 0.08)
$\hat{k}_i^{(1)}$	$< 10^{-2}$	$< 10^{-2}$	-	$< 10^{-2}$	$< 10^{-2}$	-
$\hat{k}_i^{(2)}$	0.39	0.36	(0.00, 0.84)	0.51	0.48	(0.00, 0.99)
$k_i^{(12)}$	0.14	0.26	(0.00, 0.74)	0.17	0.29	(0.00, 0.79)
$k_e^{(1)}$	$< 10^{-2}$	$< 10^{-2}$	-	$< 10^{-2}$	$< 10^{-2}$	-
f	$< 10^{-2}$	$< 10^{-2}$	-	0.02	0.01	(0.00, 0.06)
κ_1	$< 10^{-2}$	$< 10^{-2}$	-	$< 10^{-2}$	$< 10^{-2}$	(0.00, 0.01)
κ_2	$< 10^{-2}$	$< 10^{-2}$	-	$< 10^{-2}$	$< 10^{-2}$	-
ω_1	$< 10^{-2}$	$< 10^{-2}$	(0.00, 0.01)	$< 10^{-2}$	0.01	(0.00, 0.02)
ω_2	$< 10^{-2}$	$< 10^{-2}$	-	$< 10^{-2}$	$< 10^{-2}$	-

Table 4.25: The results for Sobol algorithm for the hypothesis H_1 where S_1 denotes the main effect index and S_T denotes the total effect index.

The input of the Sobol algorithm is a vector $\boldsymbol{\theta}$ defined by Equation (4.24), where parameters are studied in the following ranges, defined by taking into consideration similar values published by Mac Gabhann & Popel (2004), Vempati *et al.* (2010), Tan *et al.* (2013b), Anderson *et al.* (2011), Starbuck & Lauffenburger (1992), Tzafriri & Edelman (2007), that is $k_r^{(j)}, \hat{k}_d^{(j)}, \hat{k}_r^{(j)}, \hat{k}_i^{(j)}, k_d^{(12)}, k_r^{(12)}, k_i^{(12)}$ in interval $(10^{-3}, 10^{-1})$, $k_d^{(j)}$ in interval $(10^{-5}, 10^{-1})$, $k_e^{(1)}$ in interval $(10^{-5}, 10^{0})$, f in interval $(10^{0}, 10^{2})$, κ_j in interval $(10^{0}, 10^{5})$ and ω_j in interval $(-1, 100)$, where $j \in \{1, 2\}$. To define the output of the Sobol algorithm one can first find the solution of Equation (4.22) and then compute the following outputs,

$$out_1(i,t) = R_i^S(t) + M_i^S(t) + 2P_i^S(t) + P_{12}^S(t), \tag{4.25}$$

and the ratio

$$out_2(t) = \frac{2P_2^S(t) + P_{12}^S(t)}{out_1(1,0) + out_1(2,0)} \tag{4.26}$$

for $i \in \{1,2\}$, at the time point $t \in T$. The outputs $out_1(1,t), out_1(2,t)$ and $out_2(t)$ are analysed at each time point $t \in \{5\ min, 15\ min, 30\ min, 60\ min\}$. The mean, the sample standard deviation and the range are computed over twelve results for each parameter (four time points for the three types of outputs). These results are given in Tables 4.24 and 4.25 for hypotheses H_1 and H_2, respectively. Results from the Sobol algorithm give very similar results for hypotheses H_1 and H_2. The parameter with the strongest influence on the model outputs is $\hat{k}_i^{(2)}$, the internalisation rate of homodimers P_2^S. The degradation rate $k_d^{(2)}$ of free VEGFR2 receptors and the monomers M_2^S together with the internalisation rate $k_i^{(12)}$ of the heterodimers P_{12}^S are parameters with intermediate impact on the model outputs. Lastly, rates $k_d^{(1)}$ (degradation of free VEGFR1 and monomers M_1^S) and $k_d^{(12)}$ (degradation of heterodimers $P_{(12)}^E$) have an intermediate effect on the model outputs.

4.2.6 Bayesian inference and parameter estimation

Taking into consideration the results for the Sobol algorithm from the previous section on global sensitivity analysis I fix the parameters $\hat{k}_d^{(j)}, k_r^{(j)}, \hat{k}_r^{(j)}, k_r^{(12)}, \hat{k}_i^{(1)}, f$, and κ_j, where $j \in \{1,2\}$. Degradation rate $\hat{k}_d^{(2)}$ for homodimers is chosen to be two orders of magnitude higher than the degradation rate for free receptors and monomers, as observed by Tan *et al.* (2013c) and Tan *et al.* (2013b) after analysing four published data sets. Therefore $\hat{k}_d^{(2)} = 10^2 k_d^{(2)}$. Given that there are no experimental measurements of trafficking rates for VEGFR1, I have assumed the same recycling rate as VEGFR2 (free or bound). Values for the recycling rates $k_r^{(j)}, \hat{k}_r^{(j)}, k_r^{(12)}$ are given in Table 4.26. Moreover, I follow the assumption stated by Mac Gabhann & Popel (2004) that the internalisation rate for the homodimers is the same regardless of the receptor type. Therefore $\hat{k}_i^{(1)} = \hat{k}_i^{(2)}$ where $\hat{k}_i^{(2)}$ is going to be estimated by the ABC algorithm later in this section. The value of the dissociation coefficient f was estimated in Section 4.1 and it is chosen to be the median from Table 4.12. As a results of testing many simulations the carrying capacity κ_j are chosen arbitrary to be equal to 10^4 molecules for $j \in \{1,2\}$. This

choice allows one to study the difference between the hypotheses H_1 and H_2 as the number of the phosphorylated dimers differ between $10^4 - 10^5$ molecules on the cell surface and in the endosome. If the value for the capacity is chosen to be low, *e.g.* $\kappa_j = 10^3$ molecules, then the impact of the phosphorylation from the cell surface or from the endosome is almost the same as $P_2^S(t), P_2^E(t) >> 10^3$.

name	value	reference
$k_r^{(j)}$	$7.81 \times 10^{-2}\ s^{-1}$	Tan *et al.* (2013c)
$\hat{k}_r^{(j)}$	$5.07 \times 10^{-2} s^{-1}$	Tan *et al.* (2013c)
$k_r^{(12)}$	$5.07 \times 10^{-2} s^{-1}$	Tan *et al.* (2013c)
f	23.10	the result obtained in Subsection 4.1.2

Table 4.26: Values of some fixed parameters in Model 3, where $j \in \{1, 2\}$.

Parameters $k_e^{(1)}, \omega_1$ and ω_2 have very small impact on the model outputs but the aim here is to learn about these parameters in the view of the hypotheses H_1 and H_2 being tested. There are 8 remaining parameters to be estimated by the ABC algorithm,

$$\hat{\boldsymbol{\theta}} = \left(k_d^{(1)}, k_d^{(2)}, k_d^{(12)}, \hat{k}_i^{(2)}, k_i^{(12)}, k_e^{(1)}, \omega_1, \omega_2\right). \tag{4.27}$$

The prior distributions for $\hat{\boldsymbol{\theta}}$ are the uniform distributions taken on the ranges defined for the global sensitivity analysis in the previous subsection, except for $k_d^{(1)}, k_d^{(2)}$, ω_1 and ω_2. The prior distributions for the degradation rates $k_d^{(j)}$ are the uniform distributions on the range $(10^{-5}, 10^{-3})s^{-1}$ so that $\hat{k}_d^{(j)} \leq 10^{-1}s^{-1}$ for $j \in \{1, 2\}$. It is important to make sure that the prior distributions of all parameters are defined in the intervals tested by the Sobol algorithm. The aim here is to test not only hypotheses H_1 and H_2 but also to test if ligand stimulation causes the inhibition or the enhancement of the transport rate $\hat{k}_t^{(j)}$, where $j \in \{1, 2\}$. In order to do this, the parameters ω_1 and ω_2 are sampled for each hypothesis from the prior distributions in Table 4.27.

The ABC algorithm described in Subsection 2.4.2 of Chapter 2 was performed using the prior distributions for $\hat{\boldsymbol{\theta}}$ described above. Simulated values were generated from Equations (4.25) and (4.26) at the time point $t \in \{5\ min,\ 15\ min,$

30 min, 60 $min\}$ and compared with the data given in Table 4.22 using the Pearson distance, that is

$$\delta^2 = \sum_{i=1}^{2} \frac{(\boldsymbol{out_1}(i) - \boldsymbol{\mu_i})^2}{\boldsymbol{\sigma_i}} + \frac{(\boldsymbol{out_2} - \boldsymbol{\mu_p})^2}{\boldsymbol{\sigma_p}},$$

where $\boldsymbol{out_1}(i) = (out_1(i, 0\ min),\ out_1(i, 5\ min), out_1(i, 15\ min), out_1(i, 30\ min), out_1(i, 60\ min))$, $\boldsymbol{out_2} = (out_2(5\ min), out_2(15\ min), out_2(30\ min), out_2(60\ min))$, $\boldsymbol{\mu_i}$ is the vector of mean and $\boldsymbol{\sigma_i}$ is the vector of sampled standard deviation, of quantified number of VEGFRi per cell upon ligand stimulation, $\boldsymbol{\mu_p}$ is the vector of mean and $\boldsymbol{\sigma_p}$ is the vector of sampled standard deviation, of quantified phosphorylated VEGFR2 data. The algorithm was run 10^7 times for each hypothesis and each case. The acceptance ratio was set to 10^{-4} to obtain 10^3 results.

	ω_1	ω_2
case A	$U(-1, 0)$	$U(-1, 0)$
case B	$U(-1, 0)$	$U(0, 100)$
case C	$U(0, 100)$	$U(-1, 0)$
case D	$U(0, 100)$	$U(0, 100)$

Table 4.27: The prior distributions for ω_1 and ω_2. case A) the inhibition of VEGF receptors; case B) the inhibition of VEGFR1 and the enhancement of VEGFR2; case C) the enhancement of VEGFR1 and the inhibition of VEGFR2; case D) the enhancement of VEGF receptors upon VEGF-A_{165} stimulation.

Model selection

There were in fact eight cases tested, four for each hypothesis H_1 and H_2 depending on the prior distribution for ω_j, where $j \in \{1, 2\}$. Therefore first I compute the relative probabilities to test which case or cases give the highest probability of being accepted. Later I describe the results from the ABC algorithm for those cases. As it was done in Subsection 4.1.3, I denote the relative probability for Model 3 as follows,

$$p(H_j, \text{case } k|\delta = \delta^*) = \frac{f(H_j, \text{case } k|\delta = \delta^*)}{\sum\limits_{\substack{j=1,2 \\ k=A,B,C,D}} f(H_j, \text{case } k|\delta = \delta^*)}, \tag{4.28}$$

where $f(H_j, \text{case } k|\delta = \delta^*)$, called frequency, is the number of accepted parameters for hypothesis H_j with the prior distribution for ω_1 and ω_2 denoted as case k (see Table 4.27) and given that the distance between the simulation output and the data was equal or less than δ^* (arbitrary chosen value). These relative probabilities and frequencies are plotted in Figure 4.32.

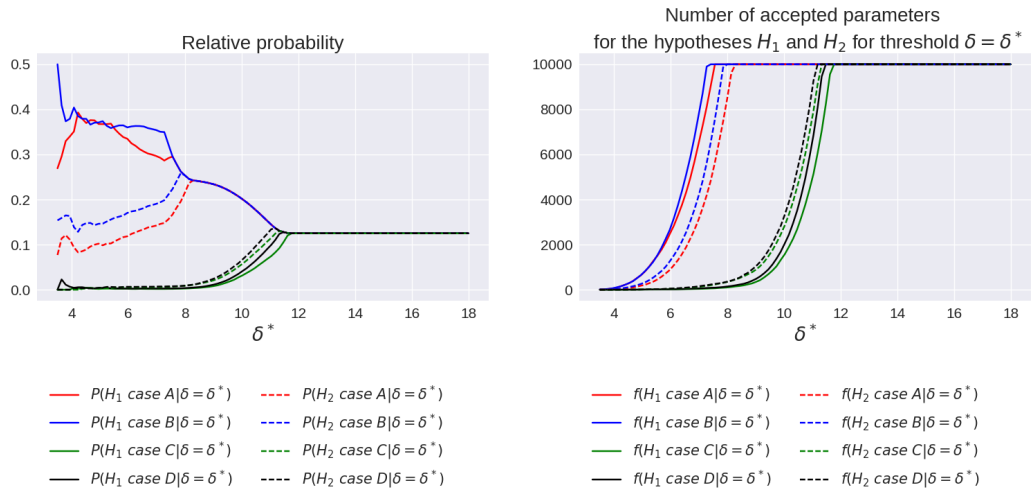

Figure 4.32: The relative probabilities defined by Equation (4.28) and the frequencies for hypotheses H_1 and H_2 assuming the prior distribution for ω_1 and ω_2 described by the cases A, B, C and D.

Largest relative probability is obtained for hypothesis H_1, assuming case B (inhibition of the transport rate of free receptors VEGFR1 from the Golgi to the cell surface upon ligand stimulation). If one assumes that this transport rate for free VEGFR1 receptors can only be only enhanced by ligand stimulation (cases C and D) then hypothesis H_2 gives the highest relative probability. According to the obtained results it is not important (when comparing model simulation with the experimental data) if the transport rate for receptors VEGFR2 from the Golgi to the cell surface is inhibited or enhanced (comparing the case A and B or C and D from Figure 4.32). Having that in mind I analyse in Subsection 4.2.6 the results for cases A and D only.

Results of the ABC algorithm for cases A and D.

Results for parameters from the vector $\hat{\boldsymbol{\theta}}$ defined by Equation (4.27), for both hypotheses assuming cases A and D, are given in Tables 4.29, 4.30, 4.31, 4.32. The summary statistics are also given in these tables for the parameters obtained by Equation (4.23) and for $\hat{k}_d^{(j)} = 10^2 k_d^{(j)}, \hat{k}_i^{(1)} = \hat{k}_i^{(2)}$ for $j \in \{1, 2\}$. The probability histograms for the prior and the posterior distributions are plotted only for parameters in vector $\hat{\boldsymbol{\theta}}$ (see Figures 4.33, 4.34, 4.35, 4.36).

Bayesian parameterisation did not revealed any new information for $k_d^{(1)}$ and ω_2, but some new information about the distribution of ω_1 is obtained for both hypotheses (see Figures 4.33, 4.34, 4.35, 4.36). The heterodimer trafficking rate has not been experimentally determined. One of the outcomes of the parameterisation is that the median of the degradation rate of phosphorylated heterodimers P_{12}^E is of the order of $10^{-3}s^{-1}$ regardless of the hypotheses tested. Similarly one can learn that the median of the internalisation rate for the phosphorylated heterodimers P_{12}^S is within the range $10^{-2} - 10^{-3}s^{-1}$. Values for $k_d^{(2)}, \hat{k}_d^{(2)}$ and $\hat{k}_i^{(2)}$ were previously computed from the data set of the experiments performed by Bruns *et al.* (2010) and published by Tan *et al.* (2013c)

$$\overline{k_d^{(2)}} = 3.86 \times 10^{-4}s^{-1}, \quad \overline{\hat{k}_d^{(2)}} = 5.51 \times 10^{-2}s^{-1}, \quad \overline{\hat{k}_i^{(2)}} = 7.80 \times 10^{-2}s^{-1}.$$

One can notice that the results for the hypothesis H_1 assuming case A (Table 4.29) and the results for the hypothesis H_2 assuming case D (Table 4.32) are very close to these published values, see Table 4.28.

		median	mean
H_1 with case A	$k_d^{(2)}$	$1.8 \times 10^{-4}s^{-1}$	$3.1 \times 10^{-4}s^{-1}$
	$\hat{k}_d^{(2)}$	$1.8 \times 10^{-2}s^{-1}$	$3.1 \times 10^{-2}s^{-1}$
	$\hat{k}_i^{(2)}$	$4.1 \times 10^{-3}s^{-1}$	$1.2 \times 10^{-2}s^{-1}$
H_2 with case D	$k_d^{(2)}$	$3.5 \times 10^{-4}s^{-1}$	$4.1 \times 10^{-4}s^{-1}$
	$\hat{k}_d^{(2)}$	$3.5 \times 10^{-2}s^{-1}$	$4.1 \times 10^{-2}s^{-1}$
	$\hat{k}_i^{(2)}$	$4.9 \times 10^{-3}s^{-1}$	$1.4 \times 10^{-2}s^{-1}$

Table 4.28: Comparison of some specific parameter values between the hypotheses which were previously published by Tan *et al.* (2013c).

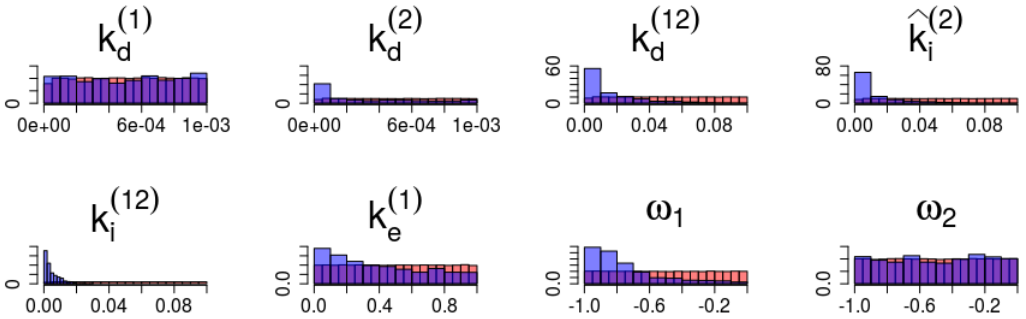

Figure 4.33: The probability histograms of the sample prior (in red) and posterior (in blue) distributions for the results for H_1 assuming the case A.

	Min.	1st Qu.	Median	Mean	3rd Qu.	Max.
$k_d^{(1)}$	1.1×10^{-5}	2.4×10^{-4}	5.2×10^{-4}	5.1×10^{-4}	7.7×10^{-4}	1.0×10^{-3}
$k_d^{(2)}$	1.0×10^{-5}	3.6×10^{-5}	1.8×10^{-4}	3.1×10^{-4}	5.6×10^{-4}	1.0×10^{-3}
$k_d^{(12)}$	1.0×10^{-3}	2.6×10^{-3}	7.5×10^{-3}	1.5×10^{-2}	2.2×10^{-2}	9.7×10^{-2}
$\hat{k}_i^{(2)}$	1.2×10^{-3}	2.5×10^{-3}	4.1×10^{-3}	1.2×10^{-2}	1.5×10^{-2}	9.3×10^{-2}
$k_i^{(12)}$	1.0×10^{-3}	1.5×10^{-3}	2.9×10^{-3}	5.0×10^{-3}	7.2×10^{-3}	2.8×10^{-2}
$k_e^{(1)}$	1.3×10^{-2}	1.3×10^{-1}	3.4×10^{-1}	3.9×10^{-1}	6.2×10^{-1}	1.0×10^{0}
ω_1	-1.00	-0.91	-0.82	-0.76	-0.68	-4.1×10^{-3}
ω_2	-1.00	-0.74	-0.49	-0.49	-0.24	-6.7×10^{-4}
$k_t^{(1)}$	3.4×10^{-4}	3.4×10^{-3}	8.8×10^{-3}	1.0×10^{-2}	1.6×10^{-2}	2.6×10^{-2}
$k_s^{(1)}$	2.1×10^{-3}	4.8×10^{-2}	1.0×10^{-1}	1.0×10^{-1}	1.5×10^{-1}	2.0×10^{-1}
$k_i^{(1)}$	9.2×10^{-3}	2.1×10^{-2}	4.2×10^{-2}	4.7×10^{-2}	7.0×10^{-2}	1.1×10^{-1}
$k_t^{(2)}$	1.0×10^{-5}	3.6×10^{-5}	1.8×10^{-4}	3.1×10^{-4}	5.6×10^{-4}	1.0×10^{-3}
$k_s^{(2)}$	4.0×10^{-1}	1.4×10^{0}	7.3×10^{0}	1.3×10^{1}	2.3×10^{1}	4.0×10^{1}
$k_i^{(2)}$	2.6×10^{-2}	2.6×10^{-2}	2.6×10^{-2}	2.6×10^{-2}	2.6×10^{-2}	2.6×10^{-2}
$\hat{k}_d^{(1)}$	1.1×10^{-3}	2.4×10^{-2}	5.2×10^{-2}	5.1×10^{-2}	7.7×10^{-2}	1.0×10^{-1}
$\hat{k}_d^{(2)}$	1.0×10^{-3}	3.6×10^{-3}	1.8×10^{-2}	3.1×10^{-2}	5.6×10^{-2}	1.0×10^{-1}

Table 4.29: Summary statistics for results under hypothesis H_1, assuming case A. ω_1, ω_2 are dimensionless (no units), κ_1, κ_2 are in $[molecules]$ and all other rates are in s^{-1}.

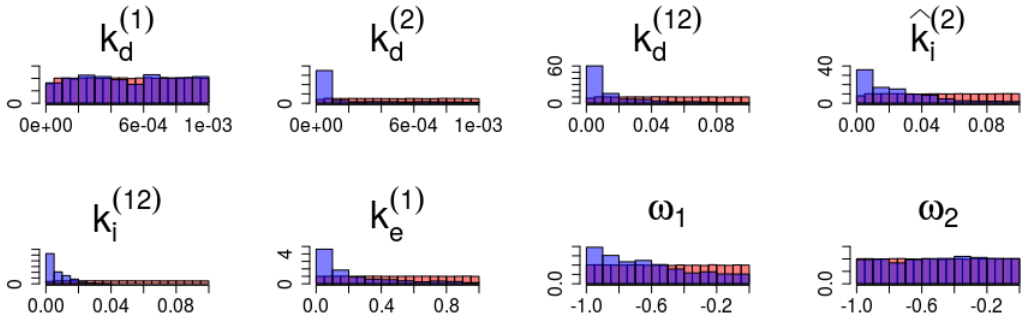

Figure 4.34: The probability histograms of the sample prior (in red) and posterior (in blue) distributions for the results for H_2 assuming the case A.

	Min.	1st Qu.	Median	Mean	3rd Qu.	Max.
$k_d^{(1)}$	1.0×10^{-5}	2.6×10^{-4}	5.0×10^{-4}	5.1×10^{-4}	7.7×10^{-4}	1.0×10^{-3}
$k_d^{(2)}$	1.0×10^{-5}	1.7×10^{-5}	3.4×10^{-5}	1.7×10^{-4}	1.6×10^{-4}	9.9×10^{-4}
$k_d^{(12)}$	1.0×10^{-3}	2.1×10^{-3}	6.0×10^{-3}	1.5×10^{-2}	1.9×10^{-2}	9.7×10^{-2}
$\hat{k}_i^{(2)}$	1.4×10^{-3}	4.8×10^{-3}	1.8×10^{-2}	2.5×10^{-2}	3.6×10^{-2}	9.9×10^{-2}
$k_i^{(12)}$	1.0×10^{-3}	1.8×10^{-3}	4.4×10^{-3}	7.0×10^{-3}	1.1×10^{-2}	3.7×10^{-2}
$k_e^{(1)}$	6.1×10^{-3}	5.6×10^{-2}	1.1×10^{-1}	2.2×10^{-1}	3.2×10^{-1}	1.0×10^{0}
ω_1	-1.00	-0.86	-0.68	-0.63	-0.43	-6.5×10^{-3}
ω_2	-1.00	-0.73	-0.48	-0.49	-0.24	-5.1×10^{-4}
$k_t^{(1)}$	1.8×10^{-4}	1.4×10^{-3}	2.9×10^{-3}	5.7×10^{-3}	8.1×10^{-3}	2.6×10^{-2}
$k_s^{(1)}$	2.1×10^{-3}	5.3×10^{-2}	1.0×10^{-1}	1.0×10^{-1}	1.5×10^{-1}	2.0×10^{-1}
$k_i^{(1)}$	8.5×10^{-3}	1.3×10^{-2}	1.9×10^{-2}	3.0×10^{-2}	3.9×10^{-2}	1.1×10^{-1}
$k_t^{(2)}$	1.0×10^{-5}	1.7×10^{-5}	3.4×10^{-5}	1.7×10^{-4}	1.6×10^{-4}	9.9×10^{-4}
$k_s^{(2)}$	4.0×10^{-1}	6.9×10^{-1}	1.3×10^{0}	6.6×10^{0}	6.6×10^{0}	4.0×10^{1}
$k_i^{(2)}$	2.6×10^{-2}	2.6×10^{-2}	2.6×10^{-2}	2.6×10^{-2}	2.6×10^{-2}	2.6×10^{-2}
$\hat{k}_d^{(1)}$	1.0×10^{-3}	2.6×10^{-2}	5.0×10^{-2}	5.1×10^{-2}	7.7×10^{-2}	1.0×10^{-1}
$\hat{k}_d^{(2)}$	1.0×10^{-3}	1.7×10^{-3}	3.4×10^{-3}	1.7×10^{-2}	1.6×10^{-2}	9.9×10^{-2}

Table 4.30: Summary statistics for results under hypothesis H_2, assuming case A. ω_1, ω_2 are dimensionless (no units), κ_1, κ_2 are in $[molecules]$ and all other rates are in s^{-1}.

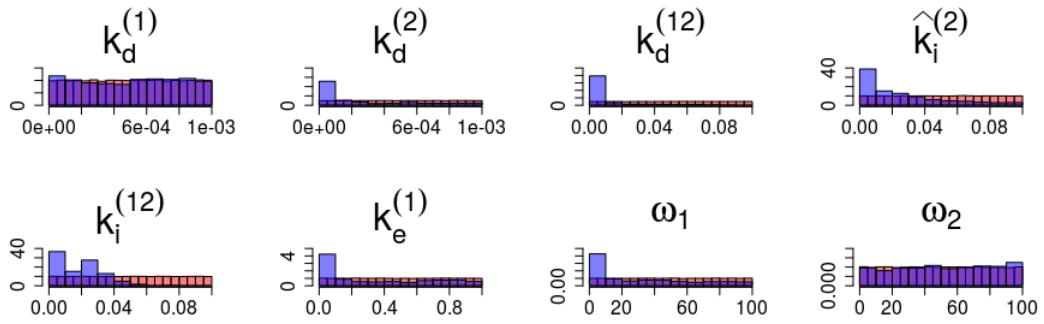

Figure 4.35: The probability histograms of the sample prior (in red) and posterior (in blue) distributions for the results for H_1 assuming the case D.

	Min.	1st Qu.	Median	Mean	3rd Qu.	Max.
$k_d^{(1)}$	1.0×10^{-5}	2.2×10^{-4}	5.2×10^{-4}	5.0×10^{-4}	7.5×10^{-4}	1.0×10^{-3}
$k_d^{(2)}$	1.0×10^{-5}	3.0×10^{-5}	8.8×10^{-5}	2.6×10^{-4}	4.8×10^{-4}	1.0×10^{-3}
$k_d^{(12)}$	1.0×10^{-3}	1.2×10^{-3}	1.5×10^{-3}	9.7×10^{-3}	7.7×10^{-3}	9.6×10^{-2}
$\hat{k}_i^{(2)}$	$1.2e \times 10^{-3}$	5.1×10^{-3}	1.7×10^{-2}	2.6×10^{-2}	3.8×10^{-2}	9.8×10^{-2}
$k_i^{(12)}$	1.0×10^{-3}	4.2×10^{-3}	1.9×10^{-2}	1.9×10^{-2}	2.8×10^{-2}	9.9×10^{-2}
$k_e^{(1)}$	2.3×10^{-5}	2.0×10^{-2}	1.8×10^{-1}	3.3×10^{-1}	6.5×10^{-1}	1.0×10^{0}
ω_1	2.1×10^{-4}	2	18	30	53	100
ω_2	2.9×10^{-2}	28	52	52	79	100
$k_t^{(1)}$	8.6×10^{-6}	5.2×10^{-4}	4.6×10^{-3}	8.4×10^{-3}	1.7×10^{-2}	2.6×10^{-2}
$k_s^{(1)}$	2.0×10^{-3}	4.5×10^{-2}	1.0×10^{-1}	1.0×10^{-1}	1.5×10^{-1}	2.0×10^{-1}
$k_i^{(1)}$	7.8×10^{-3}	9.8×10^{-3}	2.6×10^{-2}	4.1×10^{-2}	7.3×10^{-2}	1.1×10^{-1}
$k_t^{(2)}$	1.0×10^{-5}	3.0×10^{-5}	8.8×10^{-5}	2.6×10^{-4}	4.8×10^{-4}	1.0×10^{-3}
$k_s^{(2)}$	4.0×10^{-1}	1.2×10^{0}	3.5×10^{0}	1.0×10^{1}	1.9×10^{1}	4.0×10^{1}
$k_i^{(2)}$	2.6×10^{-2}	2.6×10^{-2}	2.6×10^{-2}	2.6×10^{-2}	2.6×10^{-2}	2.6×10^{-2}
$\hat{k}_d^{(1)}$	1.0×10^{-3}	2.2×10^{-2}	5.2×10^{-2}	5.0×10^{-2}	7.5×10^{-2}	1.0×10^{-1}
$\hat{k}_d^{(2)}$	1.0×10^{-3}	3.0×10^{-3}	8.8×10^{-3}	2.6×10^{-2}	4.8×10^{-2}	1.0×10^{-1}

Table 4.31: Summary statistics for results under hypothesis H_1, assuming case D. ω_1, ω_2 are dimensionless (no units), κ_1, κ_2 are in $[molecules]$ and all other rates are in s^{-1}.

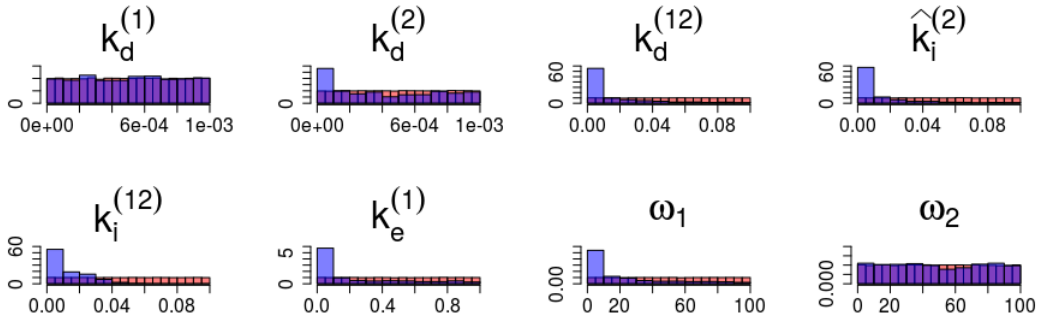

Figure 4.36: The probability histograms of the sample prior (in red) and posterior (in blue) distributions for the results for H_2 assuming the case D.

	Min.	1st Qu.	Median	Mean	3rd Qu.	Max.
$k_d^{(1)}$	1.1×10^{-5}	2.5×10^{-4}	5.1×10^{-4}	5.0×10^{-4}	7.5×10^{-4}	1.0×10^{-3}
$k_d^{(2)}$	1.0×10^{-5}	7.6×10^{-5}	3.5×10^{-4}	4.1×10^{-4}	7.1×10^{-4}	1.0×10^{-3}
$k_d^{(12)}$	1.0×10^{-3}	1.5×10^{-3}	4.0×10^{-3}	1.5×10^{-2}	2.0×10^{-2}	9.9×10^{-2}
$\hat{k}_i^{(2)}$	1.1×10^{-3}	2.7×10^{-3}	4.9×10^{-3}	1.4×10^{-2}	1.5×10^{-2}	1.0×10^{-1}
$k_i^{(12)}$	1.0×10^{-3}	2.3×10^{-3}	7.7×10^{-3}	1.2×10^{-2}	2.0×10^{-2}	9.2×10^{-2}
$k_e^{(1)}$	5.3×10^{-5}	1.6×10^{-2}	6.8×10^{-2}	2.2×10^{-1}	3.6×10^{-1}	1.0×10^{0}
ω_1	9.8×10^{-3}	2	8	21	30	100
ω_2	1.3×10^{-3}	24	47	49	76	100
$k_t^{(1)}$	6.2×10^{-6}	4.3×10^{-4}	1.8×10^{-3}	5.6×10^{-3}	9.2×10^{-3}	2.6×10^{-2}
$k_s^{(1)}$	2.2×10^{-3}	5.1×10^{-2}	1.0×10^{-1}	1.0×10^{-1}	1.5×10^{-1}	2.0×10^{-1}
$k_i^{(1)}$	7.8×10^{-3}	9.5×10^{-3}	1.5×10^{-2}	3.0×10^{-2}	4.4×10^{-2}	1.1×10^{-1}
$k_t^{(2)}$	1.0×10^{-5}	7.6×10^{-5}	3.5×10^{-4}	4.1×10^{-4}	7.1×10^{-4}	1.0×10^{-3}
$k_s^{(2)}$	4.1×10^{-1}	3.0×10^{0}	1.4×10^{1}	1.6×10^{1}	2.9×10^{1}	4.0×10^{1}
$k_i^{(2)}$	2.6×10^{-2}	2.6×10^{-2}	2.6×10^{-2}	2.6×10^{-2}	2.6×10^{-2}	2.6×10^{-2}
$\hat{k}_d^{(1)}$	1.1×10^{-3}	2.5×10^{-2}	5.1×10^{-2}	5.0×10^{-2}	7.5×10^{-2}	1.0×10^{-1}
$\hat{k}_d^{(2)}$	1.0×10^{-3}	7.6×10^{-3}	3.5×10^{-2}	4.1×10^{-2}	7.1×10^{-2}	1.0×10^{-1}

Table 4.32: Summary statistics for results under hypothesis H_2, assuming case D. ω_1, ω_2 are dimensionless (no units), κ_1, κ_2 are in $[molecules]$ and all other rates are in s^{-1}.

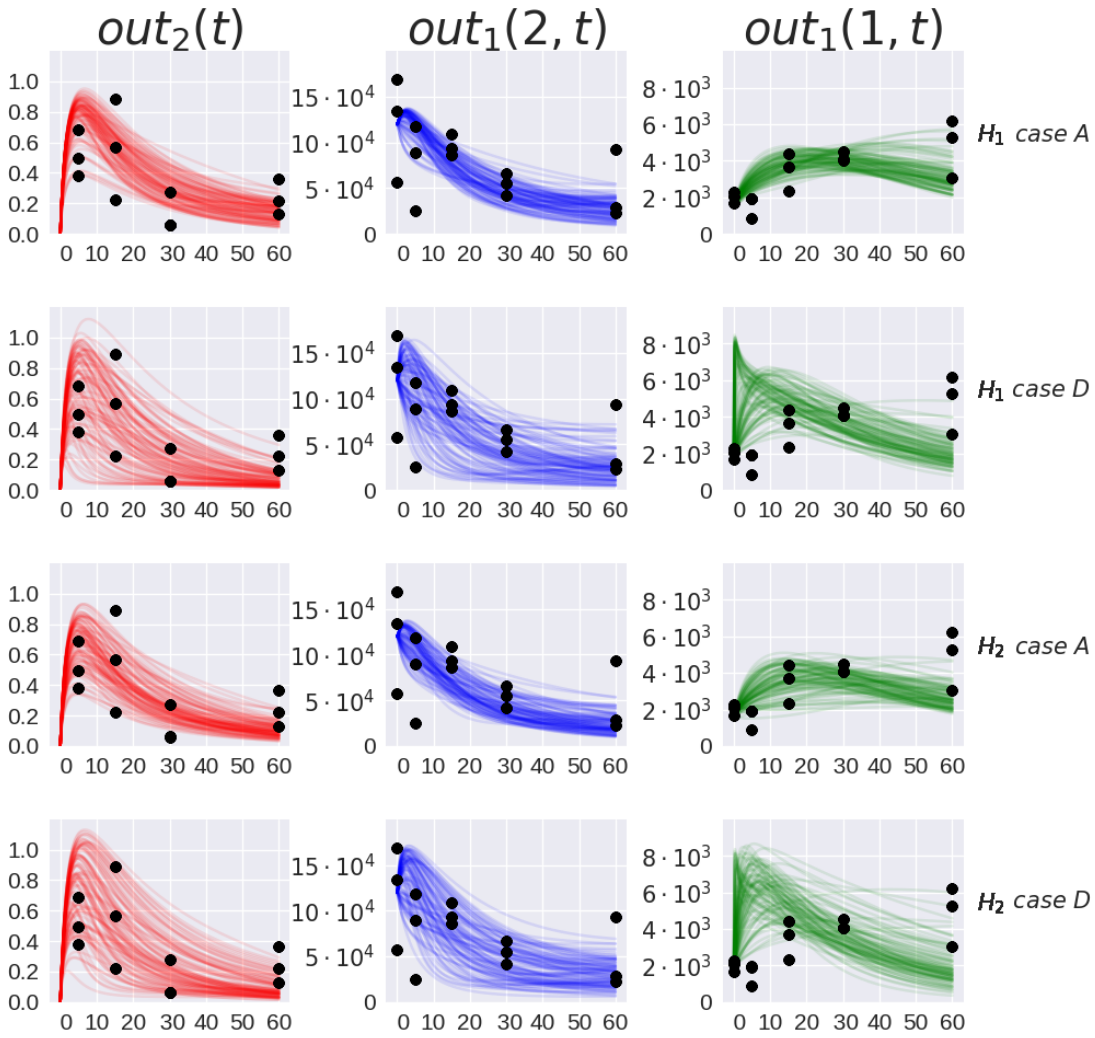

Figure 4.37: Numerical simulations versus experimental data. Simulations are generated using Equations (4.25) and (4.26) for 100 randomly sampled $\hat{\boldsymbol{\theta}}$ copies from the posterior distributions obtained assuming the hypothesis H_1 or H_2 with the case A or D. Black dots represent the quantified data from Table 4.22.

One can see on Figure 4.37 that the parameters estimation for all four cases analysed in this subsection result in capturing by the numerical simulation the pattern represented by the experimental data. Simulated results under hypotheses H_1 and H_2 with case A are closest to the mean of the data. The peak for number of VEGFR1 receptors ($out_1(1,t)$) is on average greater within first 5 minutes of simulation in the case D, in comparison to case A, for both hypotheses,

which is to be expected as the case D describes the enhancement of the receptors' synthesis.

The numerical results for both hypotheses and both cases are compared in Figure 4.38 for receptors in the Golgi apparatus and on the cell surface, and in Figure 4.39 for the phosphorylated dimers on the cell surface and in the endosome. The dynamics of VEGFR1 receptors in the Golgi changes between case A and case D but the dynamics is very similar between the hypotheses. The difference between the hypotheses is noticeable for VEGFR2 receptors in the Golgi. The number of $R_2^G(t)$ is higher for the hypothesis H_1 for $t \geq 0$, especially for the case D, that is, the assumption that synthesis is perturbed by the phosphorylated dimers on the cell surface leads to higher number of VEGFR2 receptors in the Golgi. This has an effect on the number of phosphorylated dimers, which is symmetric between case A and case D (see Figure 4.39). There is more phosphorylated dimers on the cell surface under hypothesis H_1 than under hypothesis H_2 if one assume that the receptor transport from the Golgi to the cell surface is inhibited upon ligand stimulation (case A). However the number of phosphorylated dimers in the endosome is higher under hypothesis H_2 in case A. Results for case D show opposite behaviour, that is there are more phosphorylated dimers on the cell surface under hypothesis H_2 and there are more phosphorylated dimers in the endosome under hypothesis H_1.

Model 3, together with the data, does not give a definite answer to which of the hypotheses and which case is more probable. However, Model 3 together with the data support better the inhibition of the receptors' synthesis under hypothesis H_1. However if one assumes that only the enhancement is possible, then the analysis above indicates that the signalling is more likely triggered by the phosphorylated dimers in the endosome (the hypothesis H_2). This would lead to higher number of phosphorylated heterodimers (P_{12}^S and P_{12}^E) in comparison with the case A. Also in the case A the dynamics of VEGFR2 seems to be not affected whereas in the case D one can clearly see that the number of $R_2^G(t)$ drops down quickly for $t \geq 0$.

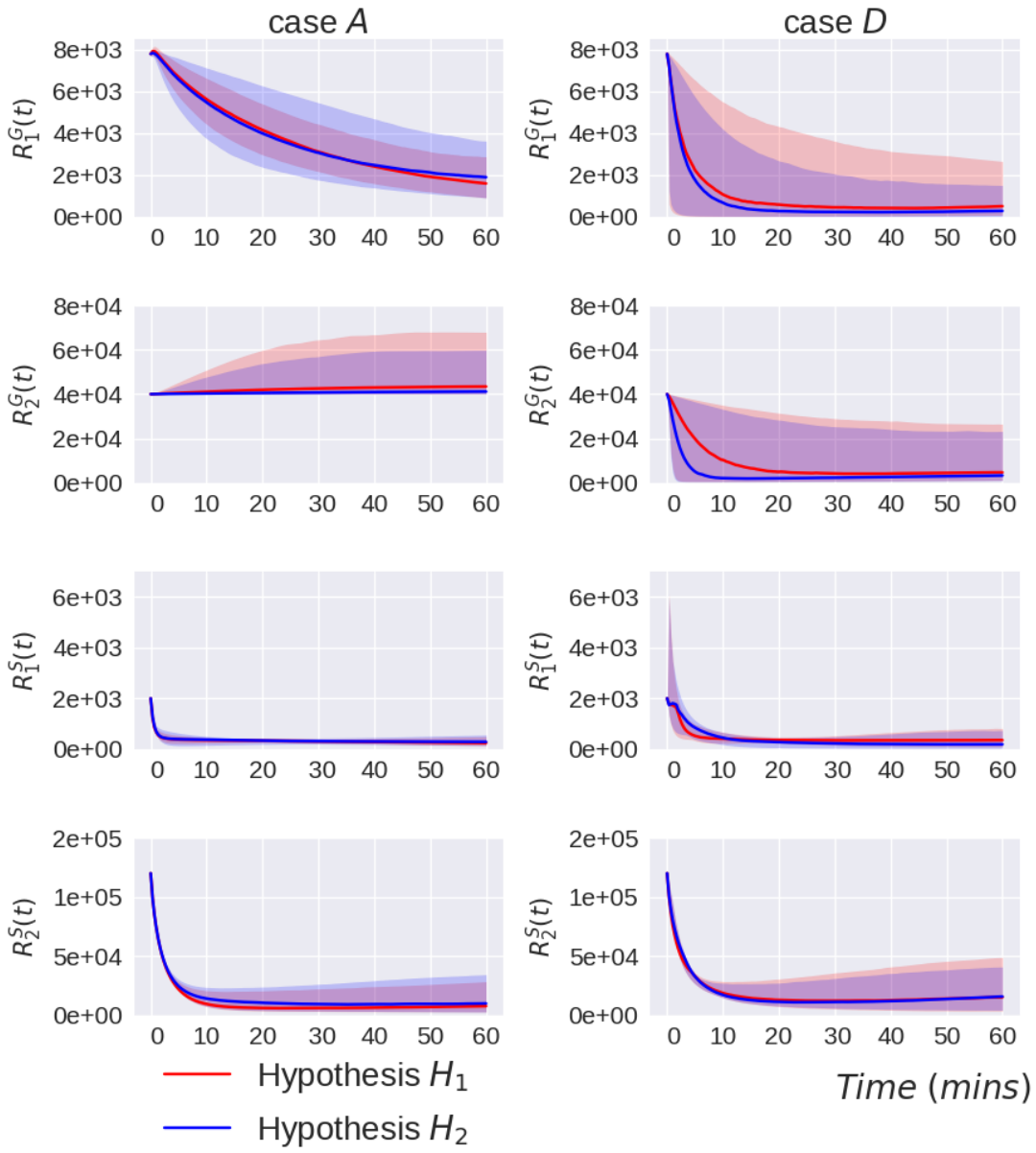

Figure 4.38: Numerical solutions for receptors in the Golgi and on the cell surface. Curves are plotted for the median whereas shaded areas are plotted between the 5th and the 95th percentile, taken over numerical solutions found for all accepted parameters $\hat{\boldsymbol{\theta}}$.

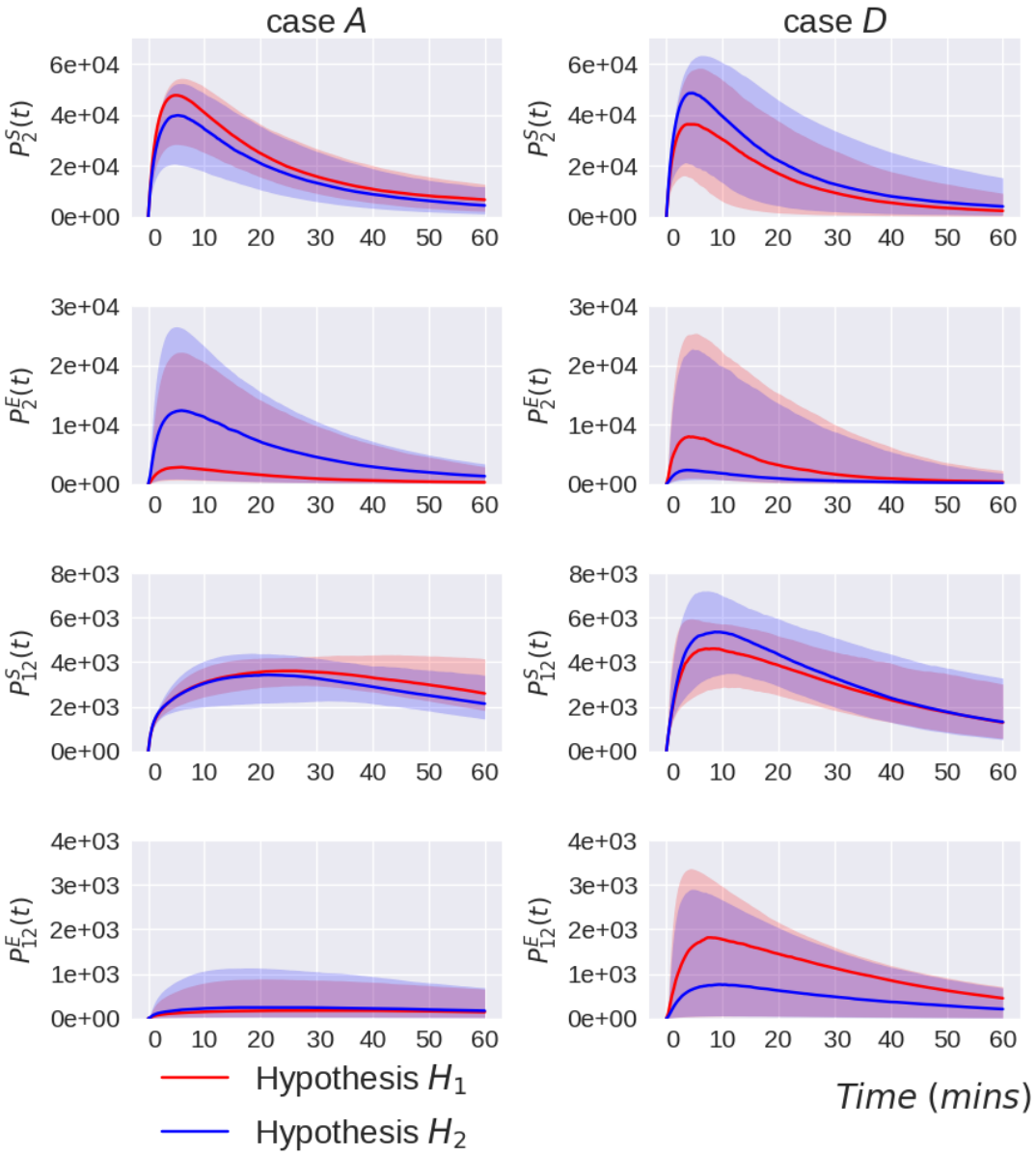

Figure 4.39: Numerical solutions for the phosphorylated dimers on the cell surface and in the endosome. Curves are plotted for the median whereas shaded areas are plotted between the 5th and the 95th percentile, taken over numerical solutions found for all accepted parameters $\hat{\boldsymbol{\theta}}$.

4.3 Discussion

In Chapter 4 binding and trafficking models have been studied. The parameters in these models have been calibrated with help of Bayesian methods and the experimental data. As it was shown here, it is often difficult to efficiently use the experimental data because they cannot be directly translated to the model molecules, signals, etc. In Subsection 4.1.3, it was demonstrated for Model 2 how the normalisation of the data can introduce an additional constraints for the parameters (here τ must be less then 5 min). The data used for parameterisation in Model 3 are easier to handle, as one can choose the way of normalisation in order to find a suitable way to compare the data with the model. It is important to emphasise how Bayesian methods, as the ABC or MCMC algorithms, can be helpful in inferring the parameters of such complex models.

The modelling in this chapter has allowed one to answer some questions relating to cell signalling upon ligand stimulation mediated by VEGFR2 phosphorylation and trafficking. The results of the hypotheses tested in Model 2 suggest that it is more likely that the phosphorylation from the endosomal compartments triggers ERK phosphorylation. This important discovery could not have been done without the help of mathematical models, as current experimental techniques do not allow to determine intracellular kinetic rates.

The other important result is that Model 3 with the data presented in Table 4.22 support best the hypotheses that the inhibition of the receptor synthesis upon ligands stimulation is caused by phosphorylated dimers from the cell surface. It has not been tested in any experiments if the receptors' synthesis is inhibited or enhanced upon ligand stimulation. The mathematical models presented in Section 4.2 provide new understanding about the mechanisms of this synthesis.

Binding rates in models studied in this chapter are computed by following the argument proposed by Lauffenburger & Linderman (1996) and explained in detail in Section 3.2 of Chapter 3. One could argue that the binding rates could have been estimated with help of the Bayesian inference instead. It would also be beneficial to include binding rates in the Sobol algorithm as it is possible that some of these rates (most probably α_+ for Model 1 and Model 2 and $\alpha_+^{(1)}$ or $\alpha_+^{(2)}$ for Model 3) have strong impact onto studied model output. In future the estimation

of rates for Model 1 and Model 2 could be done by simultaneously using both, VEGFR2 and ERK phosphorylation data. It would also be helpful to obtain new experimental results without its normalisation at time 5 min which imposed the constraint for τ in Model 2. The calibration of parameters in Model 3 could be more plausible if some experimental data could be provided for the number of receptors in the endosome and the Golgi during ligand stimulation. Furthermore, one could also consider introducing delay τ in $x^{(j)}_{s-\tau}$ in the expression for $\hat{k}^{(i)}_t(\cdot)$ given by Equation (4.21) (similarly to Model 2) which is possible taking into consideration that a signalling cascade triggered by VEGFR2 phosphorylation leads to $\hat{k}^{(i)}_t(\cdot)$ perturbation, not phosphorylated VEGFR2 itself.

Chapter 5

Mathematical models of T cell development in the thymus

In this chapter I present a mathematical model of T cell development in the thymus, which is an extensions of two mathematical models, which I developed as part of my MSc project (see Sawicka *et al.* (2014)). I incorporate here Bayesian inference methods learnt through my PhD studies, such as the ABC algorithm, into the modelling using the full data set provided by the group of Kristin Hogquist (see Stritesky *et al.* (2013)).

5.1 Introduction

T cells are a major component of the adaptive immune system that play a crucial role in protection against a wide variety of pathogens. T cells express T cell receptors on their surface. The T cell receptor is generated by somatic recombination and has a vast potential to recognise foreign organisms. However, T cells do not recognise pathogens directly, but rather through binding pathogen fragments displayed by major histocompatibility complex (MHC) proteins on the surface of antigen presenting cells. Since MHC molecules are highly polymorphic, useful T cells must be selected for in each individual of the species. These T cells must have lineage specific effector functions that include the production of cytokines and the ability to regulate immune reactions. Furthermore, some T cells have the potential to drive dangerous autoimmune responses (see Anderson *et al.*

(2007)). For all of these reasons, the development of a T cell repertoire is a highly specialised and tightly regulated process (see Stritesky *et al.* (2012) and Palmer (2003)). It takes place in a dedicated organ, the thymus, where unique properties in the micro-environment ensure the production of functional yet self-tolerant T cells (see Jameson *et al.* (1995), Werlen *et al.* (2003), Petrie & Zúñiga-Pflücker (2007)).

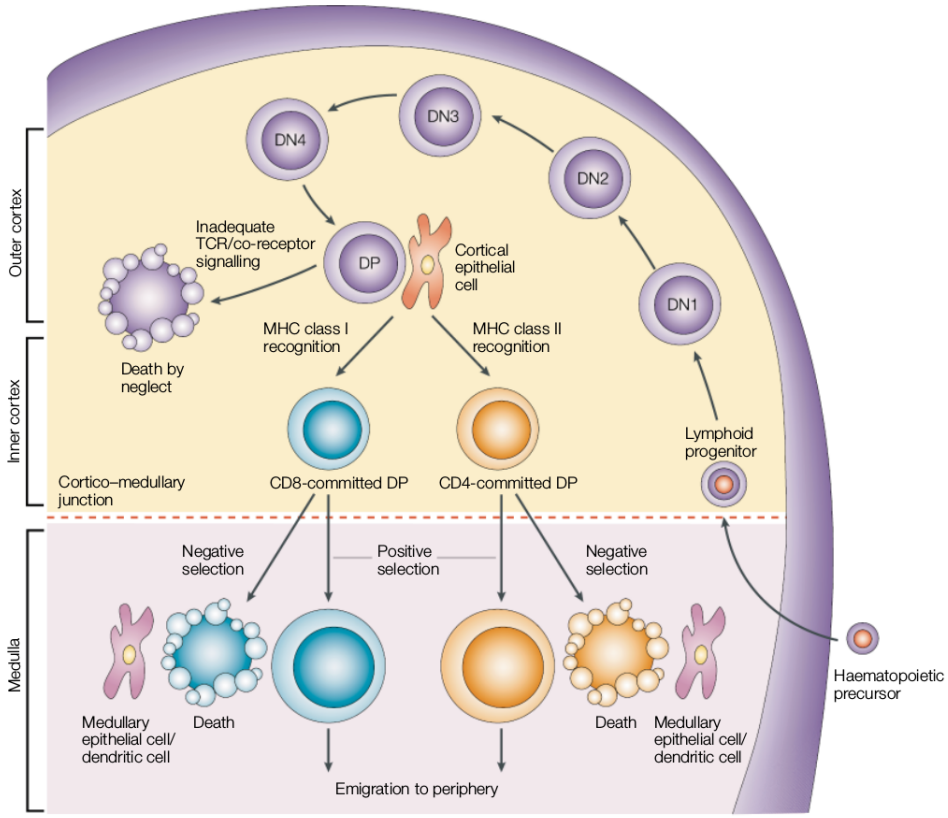

Figure 5.1: Scheme of T cell development in the thymus by Germain (2002).

Multipotent stem cells travel from the bone marrow to the thymus through the blood (see Di Nicola *et al.* (2002)). When they enter the thymus, these precursors commit to the T cell lineage and eventually transition from the double negative (DN) stage, where they do not express the co-receptors CD4 and CD8, to the double positive (DP) stage, where they express both co-receptors. At this stage a majority of cells have made productive T cell receptor (TCR) gene re-

arrangements and express a fully formed TCR on the cell surface. DP cells are located in the cortex region of the thymus, where they use their TCR to survey self-peptides presented by major histocompatibility complexes (MHC) on cortical thymic epithelial cells. DPs that recognise self-peptide MHC complexes with low affinity undergo positive selection whereas those with high affinity are deleted (negative selection). Those DPs that fail to recognise self-peptide MHC will undergo apoptosis in a process referred to as death by neglect. The DP cells that are positively selected will then transition to the single positive (SP) stage where they express either CD4 or CD8 co-receptor, depending upon their MHC class specificity. MHC class specificity also dictates gene expression changes that will ultimately determine the effector functions of that T cell, generally cytotoxicity for CD8 T cells, and cytokine production for CD4 T cells. All positively selected cells, whether MHC Class I or Class II specific, up-regulate the chemokine receptor CCR7, which facilitates their migration to the medulla, where they undergo further selection events. The medulla contains medullary epithelial cells that express tissue-restricted antigens regulated by the nuclear factor Aire (see Anderson *et al.* (2007)). Exposure to tissue-restricted antigens allows for further deletion of T cells specific for self-antigens they may encounter in the periphery. Finally, those cells that have been positively selected yet have avoided negative selection will mature and migrate to the periphery.

Previous studies have tried to determine the number of cells going through positive and negative selection in the thymus. However, reports estimating the relative number of cells undergoing negative selection compared to positive selection have been widely variable. Groups such as Surh & Sprent (1994), Laufer *et al.* (1996), van Meerwijk *et al.* (1997) and Merkenschlager *et al.* (1997) have reported that even two times more cells can undergo negative selection than positive selection. Two mathematical models of T cell development in the thymus were presented by Sawicka *et al.* (2014). The parameters of those models were calibrated using the data published in a report by Stritesky *et al.* (2012), where a novel approach was used to calculate the number of cells undergoing positive and negative selection. The parameters were calculated exactly from the steady state equations. Additionally the information about the residency time in the cortex and the medulla for different population were used together with recently

reported death rates for single positive thymocytes. In this chapter I show how a posterior probability distribution for the parameters can be estimated using an adaptation of the ABC algorithm described in Subsection 2.4.2. Model 1 and Model 2 described in Section 5.2 were presented by Sawicka *et al.* (2014) whereas Model 3 has been developed as part of my PhD project and it adds the novelty of considering regulatory T cells, which are generated during the SP CD4 stage (see Figure 5.4). Model 1 and Model 2 are parametrised using the ABC approach in this thesis which allows incorporating the uncertainty in the data in a way that the previous calibration of parameters by Sawicka *et al.* (2014) did not meet. Model 3 has been developed in order to make use of additional data that includes different subsets of thymocytes and the strength of their TCR signal. To this end, in Model 3, the possibility of rescuing from apoptosis those cells that have had a strong TCR signal has been allowed (see arrows with rates β_i where $i \in \{2, 4, 8\}$ in Figure 5.4).

5.2 Mathematical models

In this section I introduce three deterministic models of thymocyte development after the DN stage in the thymus (see Figure 5.1). The first model is required to calibrate the parameter values of the second model and subsequently the second model is required to calibrate the parameter values of the third model, which is done in Section 5.4 using Bayesian estimation methods. Overall, the models describe the population in two spatial compartments, the cortex and the medulla. In the cortex one can find the pre-selection DP (pre-DP) and post-selection DP (post-DP) thymocytes. The assumption here is that DN thymocytes differentiate to become pre-DP thymocytes with rate ϕ (cells/day). The SP thymocytes are found in the medulla and its fate is determined by the TCR signal, which a given thymocyte has received. Sinclair *et al.* (2013) and Stritesky *et al.* (2012) found no evidence of proliferation at pre-DP and post-DP stage, therefore, a proliferation term is only included in the SP thymocyte populations. All parameter values in the studied models are assumed to be positive unless otherwise stated.

5.2.1 Model 1

Model 1 describes three populations, pre-DP (n_1), post-DP (n_2) and SP (n_3) thymocytes. These three populations are involved in the following selection events in the cortex and the medulla (see Figure 5.2):

- $\emptyset \xrightarrow{\phi} n_1$ - flux of DN thymocytes into the pre-DP compartment (n_1),
- $n_1 \xrightarrow{\varphi_1} n_2$ - differentiation from pre-DP (n_1) to post-DP (n_2) thymocytes induced by TCR signal,
- $n_1 \xrightarrow{\mu_1} \emptyset$ - death by neglect of pre-DP thymocytes due to lack of (or weak) TCR signal,
- $n_2 \xrightarrow{\mu_2} \emptyset$ - apoptosis of post-DP (n_2) thymocytes due to strong TCR signal,
- $n_2 \xrightarrow{\varphi_2} n_3$ - differentiation from post-DP (n_2) to SP (n_3) thymocytes sustained by an intermediate TCR signal,
- $n_3 \xrightarrow{\varphi_3}$ periphery - exit of SP thymocytes (n_3) to the periphery (thymic maturation),
- $n_3 \xrightarrow{\lambda_3} n_3$ - proliferation of SP thymocytes (n_3) in the medulla,
- $n_3 \xrightarrow{\mu_3} \emptyset$ - apoptosis of SP (n_3) thymocytes due to strong TCR signal.

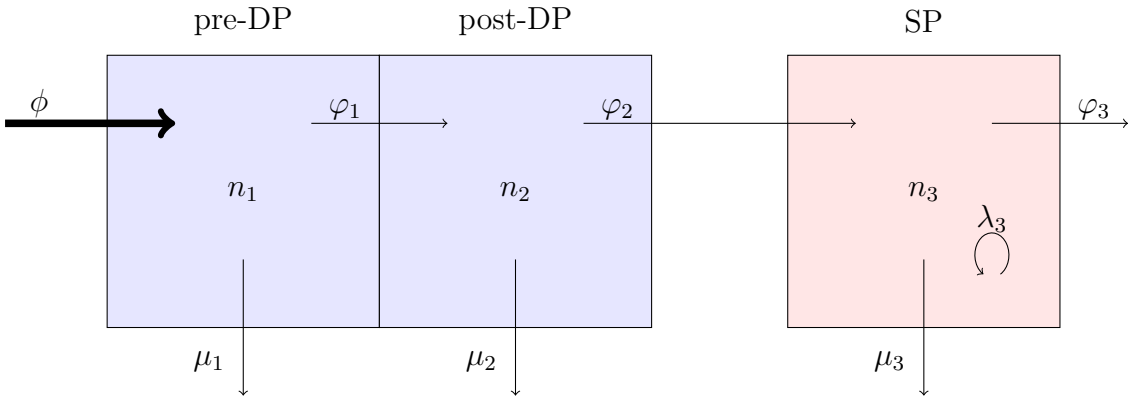

Figure 5.2: Thymic development as hypothesised in Model 1. The first two compartments (in blue) pre-DP and post-DP are part of the cortex of the thymus, whereas the third compartment (in red) SP is part of the medulla in the thymus.

The variables of Model 1 are defined as follows,

$$n_1(t) = \text{“number of pre-DP thymocytes } (n_1) \text{ at time } t,\text{”}$$

$$n_2(t) = \text{“number of post-DP thymocytes } (n_2) \text{ at time } t,\text{”}$$

$$n_3(t) = \text{“number of mature SP thymocytes } (n_3) \text{ at time } t,\text{”}$$

where $t \geq 0$. The time evolution of the three populations can be described by the following set of ODEs, which are based on the selection events described above:

$$\begin{aligned} \frac{dn_1(t)}{dt} &= \phi - (\varphi_1 + \mu_1)n_1(t), \\ \frac{dn_2(t)}{dt} &= \varphi_1 n_1(t) - (\varphi_2 + \mu_2)n_2(t), \\ \frac{dn_3(t)}{dt} &= \varphi_2 n_2(t) - (\varphi_3 + \mu_3 - \lambda_3)n_3(t), \end{aligned} \tag{5.1}$$

for $t \geq 0$. The experimental data, as explained further in Section 5.3, correspond to the population cell numbers of the steady state in the thymus, therefore the main interest here is in studying the steady state of these populations. The steady state of the ODE system (Equation (5.1)), called $\boldsymbol{n^*_{M1}} = (n_1^*, n_2^*, n_3^*)$, is given by

$$n_1^* = \frac{\phi}{\varphi_1 + \mu_1}, \quad n_2^* = \frac{n_1^* \varphi_1}{\varphi_2 + \mu_2}, \quad n_3^* = \frac{n_2^* \varphi_2}{\varphi_3 + \mu_3 - \lambda_3}, \tag{5.2}$$

and it exists and it is unique if and only if $\varphi_3 + \mu_3 - \lambda_3 > 0$, so that $n_3^* > 0$. In order to study the linear stability of the steady state the Jacobian matrix of Equation (5.1) is calculated,

$$\boldsymbol{J_1} = \begin{pmatrix} -(\varphi_1 + \mu_1) & 0 & 0 \\ \varphi_1 & -(\varphi_2 + \mu_2) & 0 \\ 0 & \varphi_2 & -(\varphi_3 + \mu_3 - \lambda_3) \end{pmatrix}.$$

$\boldsymbol{J_1}$ is also the Jacobian matrix at the steady state $\boldsymbol{n^*_{M1}}$ as the system of ODEs given by Equation (5.1) is linear. There are three eigenvalues of the matrix $\boldsymbol{J_1}$,

$$\delta_1 = -(\varphi_1 + \mu_1), \quad \delta_2 = -(\varphi_2 + \mu_2) \quad \delta_3 = -(\varphi_3 + \mu_3 - \lambda_3). \tag{5.3}$$

Therefore the steady state $\boldsymbol{n^*_{M1}}$ is stable if and only if $\varphi_3 + \mu_3 - \lambda_3 > 0$, which is also the condition for its existence.

5.2.2 Model 2

In the second model the SP population is subdivided in two classes: $CD4^+$ SP and $CD8^+$ SP thymocytes. This is an extension of Model 1 and is motivated by the fact that experimentally, SP thymocytes express either the CD4 or the CD8 co-receptor. Hence, for $t \geq 0$, there are four different thymocyte populations to be considered, $n_1(t)$, $n_2(t)$ (as in Model 1) and $n_4(t)$, $n_8(t)$ defined as,

$n_4(t)$ = *"the number of mature CD4$^+$ SP thymocytes (n_4) at time t,"*

$n_8(t)$ = *"the number of mature CD8$^+$ SP thymocytes (n_8) at time t."*

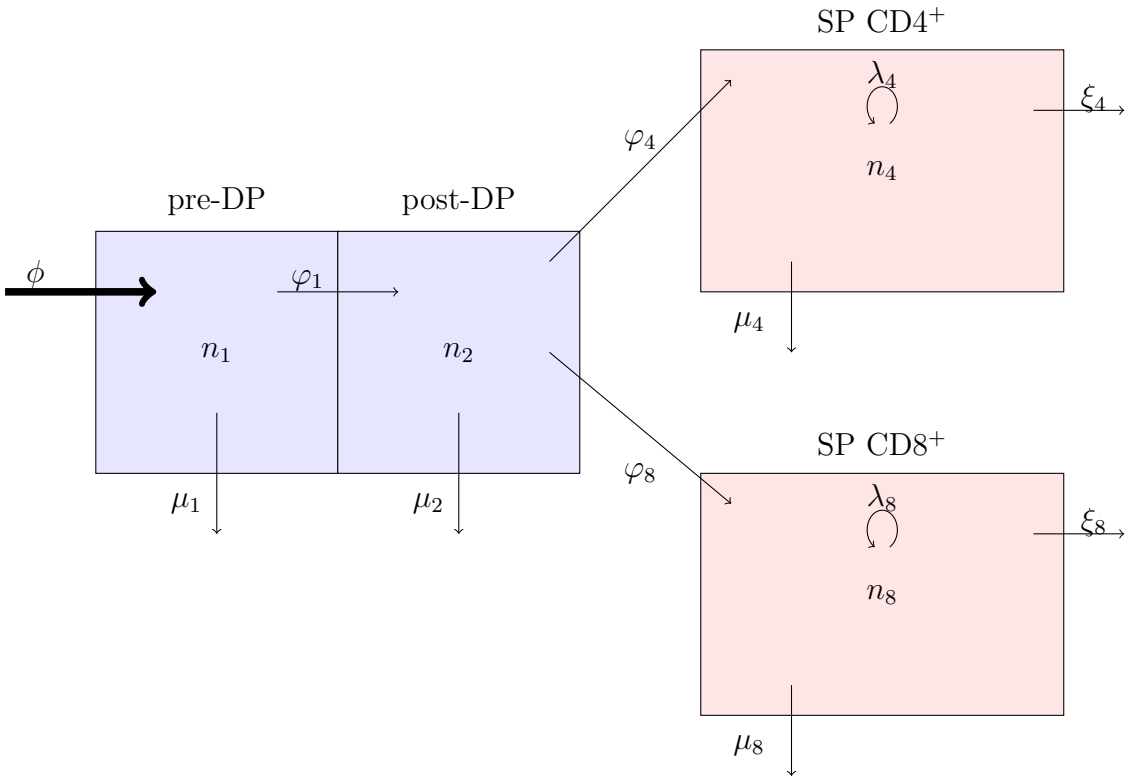

Figure 5.3: Thymic development as hypothesised in Model 2. The first two compartments (in blue) pre-DP and post-DP are part of the cortex of the thymus, whereas the remaining two compartments (in red) SP $CD4^+$ and SP $CD8^+$ are part of the medulla in the thymus.

The first four selection events, involving the parameters ϕ, μ_1, φ_1 and μ_2 are the same for Model 1 and Model 2. Additionally there are eight new selection

events in Model 2 due to division of the medulla into two compartments (see Figure 5.3),

- $n_2 \xrightarrow{\varphi_4} n_4$ - differentiation from post-DP (n_2) to CD4$^+$ SP (n_4) sustained by an intermediate TCR signal,
- $n_2 \xrightarrow{\varphi_8} n_8$ - differentiation from post-DP (n_2) to CD8$^+$ SP (n_8) sustained by an intermediate TCR signal,
- $n_4 \xrightarrow{\xi_4}$ periphery - exit of CD4$^+$ SP thymocytes (n_4) to the periphery (thymic maturation),
- $n_8 \xrightarrow{\xi_8}$ periphery - exit of CD8$^+$ SP thymocytes (n_8) to the periphery (thymic maturation),
- $n_4 \xrightarrow{\lambda_4} 2n_4$ - proliferation of CD4$^+$ SP thymocytes (n_4) in the medulla,
- $n_8 \xrightarrow{\lambda_8} 2n_8$ - proliferation of CD8$^+$ SP thymocytes (n_8) in the medulla,
- $n_4 \xrightarrow{\mu_4} \emptyset$ - apoptosis of CD4$^+$ SP thymocytes (n_4) due to strong TCR signal,
- $n_8 \xrightarrow{\mu 8} \emptyset$ - apoptosis of CD8$^+$ SP thymocytes (n_8) due to strong TCR signal.

The time evolution of $n_1(t), n_2(t), n_4(t)$ and $n_8(t)$ is described by the following set of ODEs,

$$\begin{aligned}
\frac{dn_1(t)}{dt} &= \phi - (\varphi_1 + \mu_1)n_1(t), \\
\frac{dn_2(t)}{dt} &= \varphi_1 n_1(t) - (\varphi_4 + \varphi_8 + \mu_2)n_2(t), \\
\frac{dn_4(t)}{dt} &= \varphi_4 n_2(t) - (\xi_4 + \mu_4 - \lambda_4)n_4(t), \\
\frac{dn_8(t)}{dt} &= \varphi_8 n_2(t) - (\xi_8 + \mu_8 - \lambda_8)n_8(t),
\end{aligned} \tag{5.4}$$

for $t \geq 0$.The steady state $\boldsymbol{n^*_{M2}} = (n_1^*, n_2^*, n_4^*, n_8^*)$ of Equation (5.4) is what one needs to compare to the experimental data,, where n_1^*, n_2^* are defined by Equation (5.2) and

$$n_4^* = \frac{n_2^* \varphi_4}{\xi_4 + \mu_4 - \lambda_4}, \quad n_8^* = \frac{n_2^* \varphi_8}{\xi_8 + \mu_8 - \lambda_8}. \tag{5.5}$$

The previous steady state exists and is unique if and only if $\xi_4 + \mu_4 - \lambda_4 > 0$ and $\xi_8 + \mu_8 - \lambda_8 > 0$, so that $n_4^* > 0$ and $n_8^* > 0$. The Jacobian matrix $\boldsymbol{J_2}$ is calculated to study the linear stability of the steady state of Equation (5.4),

$$\boldsymbol{J_2} = \begin{pmatrix} -(\varphi_1 + \mu_1) & 0 & 0 & 0 \\ \varphi_1 & -(\varphi_4 + \varphi_8 + \mu_2) & 0 & 0 \\ 0 & \varphi_4 & -(\xi_4 + \mu_4 - \lambda_4) & 0 \\ 0 & \varphi_8 & 0 & -(\xi_8 + \mu_8 - \lambda_8) \end{pmatrix}.$$

$\boldsymbol{J_2}$ is also the Jacobian at steady state $\boldsymbol{n^*_{M2}}$ as the ODE system defined in Equation (5.4) is linear. There are four eigenvalues of the matrix $\boldsymbol{J_2}$,

$$\begin{aligned} \delta_1 = -(\varphi_1 + \mu_1), \qquad \delta_2 = -(\varphi_4 + \varphi_8 + \mu_2), \\ \delta_3 = -(\xi_4 + \mu_4 - \lambda_4), \quad \delta_4 = -(\xi_8 + \mu_8 - \lambda_8). \end{aligned} \tag{5.6}$$

Hence the steady state $\boldsymbol{n^*_{M2}}$ is stable if and only if $\xi_4 + \mu_4 - \lambda_4 > 0$ and $\xi_8 + \mu_8 - \lambda_8 > 0$, which is also the condition for its existence.

5.2.3 Model 3

The first two models were described and studied, using different parameterisation techniques from those used in this thesis (see Sawicka *et al.* (2014)). The third model takes into account the level of activation of thymocytes in the post-DP and the SP compartments. Therefore post-DP, SP CD4$^+$ and SP CD8$^+$ stages are all subdivided into two compartments for high and low signal response of thymocytes. Additionally there is another set of the data taken into account, describing the regulatory T cell population. Treg cells can be found in the medulla at the SP CD4$^+$ stage. Hence there are in fact three compartments at the SP CD4$^+$ stage (see Figure 5.4). There are eight populations of thymocytes to be considered, where $t \geq 0$,

$n_1(t)$ = *"the number of pre-DP thymocytes* (n_1) *at time* t*,"*

$n_{2L}(t)$ = *"the number of post-DP thymocytes that have received a low TCR signal* (n_{2L}) *at time* t*,"*

$n_{2H}(t)$ = *"the number of post-DP thymocytes that have received a high TCR signal* (n_{2H}) *at time* t*,"*

$n_{4L}(t)$ = *"the number of mature CD4$^+$ SP thymocytes that have received a low TCR signal (n_{4L}) at time t,"*

$n_{4H}(t)$ = *"the number of mature CD4$^+$ SP thymocytes that have received a high TCR signal (n_{4H}) at time t,"*

$n_R(t)$ = *"the number of regulatory T cells (n_R) at time t,"*

$n_{8L}(t)$ = *"the number of mature CD8$^+$ SP thymocytes that have received a low TCR signal (n_{8L}) at time t,"*

$n_{8H}(t)$ = *"the number of mature CD8$^+$ SP thymocytes that have received a high TCR signal (n_{8H}) at time t."*

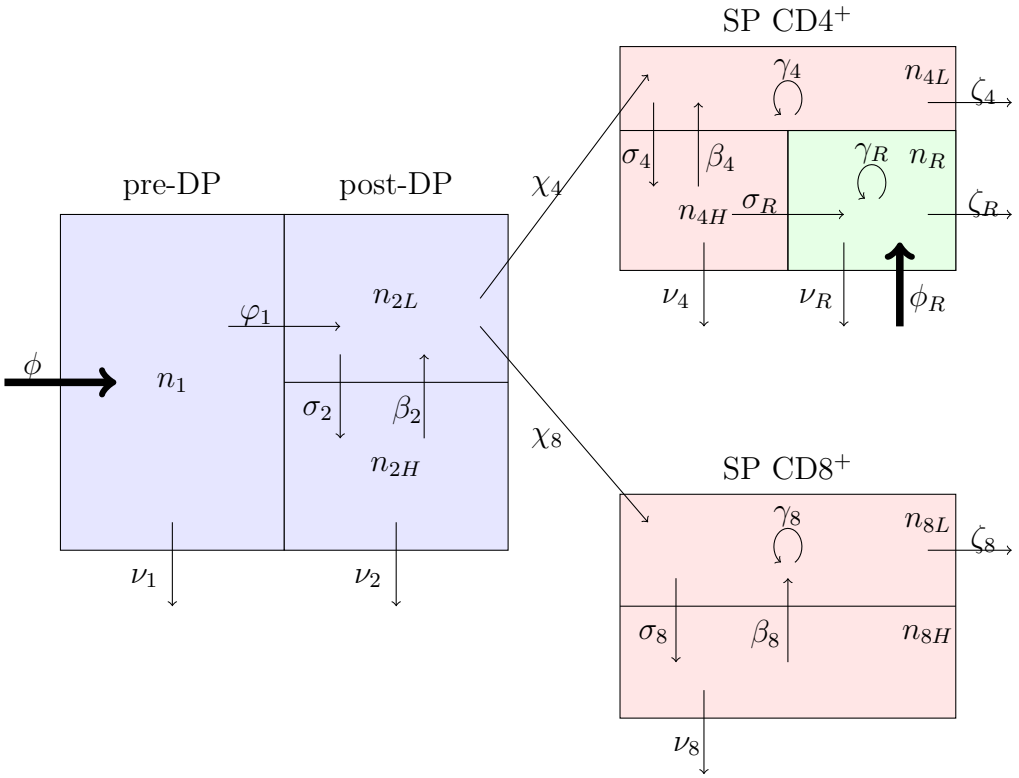

Figure 5.4: Thymic development as hypothesised in Model 3. The first two compartments (in blue) pre-DP and post-DP are part of the cortex of the thymus, whereas the remaining compartments (in red and in green) SP CD4$^+$ and SP CD8$^+$ are part of the medulla in the thymus. The compartment in green represents the Treg population within SP CD4$^+$ thymocytes.

These eight populations are involved in the following selection events in the cortex and the medulla (see Figure 5.4),

- $\emptyset \xrightarrow{\phi} n_1$ - flux of DN thymocytes into the pre-DP compartment,
- $n_1 \xrightarrow{\varphi_1} n_{2L}$ - differentiation from pre-DP (n_1) to post-DP (n_{2L}) thymocytes induced by TCR signal,
- $n_1 \xrightarrow{\nu_1} \emptyset$ - death by neglect of pre-DP thymocytes due to lack of (or weak) TCR signal,
- $n_{2L} \xrightarrow{\sigma_2} n_{2H}$ - negative selection of post-DP thymocytes n_{2L} into n_{2H} due to strong TCR signal,
- $n_{2H} \xrightarrow{\beta_2} n_{2L}$ - rescue of thymocytes that have received a strong TCR signal,
- $n_{2H} \xrightarrow{\nu_2} \emptyset$ - apoptosis of post-DP (n_{2H}) thymocytes due to strong TCR signal,
- $n_{2L} \xrightarrow{\chi_4} n_{4L}$ - differentiation from post-DP (n_{2L}) to CD4$^+$ SP (n_{4L}) sustained by an intermediate TCR signal,
- $n_{2L} \xrightarrow{\varphi_8} n_{8L}$ - differentiation from post-DP (n_{2L}) to CD8$^+$ SP (n_{8L}) sustained by an intermediate TCR signal,
- $n_{4L} \xrightarrow{\zeta_4}$ periphery - exit of CD4$^+$ SP thymocytes (n_{4L}) to the periphery (thymic maturation),
- $n_{4L} \xrightarrow{\gamma_4} 2n_{4L}$ - proliferation of CD4$^+$ SP thymocytes (n_{4L}) in the medulla,
- $n_{4L} \xrightarrow{\sigma_4} n_{4H}$ - negative selection of SP CD4$^+$ thymocytes n_{4L} into n_{4H} due to strong TCR signal,
- $n_{4H} \xrightarrow{\beta_4} n_{4L}$ - rescue of thymocytes that have received a strong TCR signal,
- $n_{4H} \xrightarrow{\nu_4} \emptyset$ - apoptosis of CD4$^+$ SP thymocytes (n_{4H}) due to strong TCR signal,
- $n_{4H} \xrightarrow{\sigma_R} n_R$ - positive selection of n_{4H} thymocytes into Treg cells (n_R),

- $n_R \xrightarrow{\gamma_R} 2n_R$ - proliferation of Treg cells (n_R) in the medulla,
- $n_R \xrightarrow{\zeta_R}$ periphery - exit of Treg thymocytes (n_R) to the periphery (thymic maturation),
- $n_R \xrightarrow{\nu_R} \emptyset$ - apoptosis of Treg cells (n_R),
- $\emptyset \xrightarrow{\phi_R} n_R$ - flux of Treg cells from the periphery,
- $n_{8L} \xrightarrow{\zeta_8}$ periphery - exit of CD8$^+$ SP thymocytes (n_{8L}) to the periphery (thymic maturation),
- $n_{8L} \xrightarrow{\gamma_8} 2n_{8L}$ - proliferation of CD8$^+$ SP thymocytes (n_{8L}) in the medulla,
- $n_{8L} \xrightarrow{\sigma_8} n_{8H}$ - negative selection of SP CD4$^+$ thymocytes n_{8L} into n_{8H} due to strong TCR signal,
- $n_{8H} \xrightarrow{\beta_8} n_{8L}$ - rescue of thymocytes that have received a strong TCR signal,
- $n_{8H} \xrightarrow{\nu 8} \emptyset$ - apoptosis of CD8$^+$ SP thymocytes (n_{8H}) due to strong TCR signal.

Model 3 can be described by the following ODEs,

$$\begin{aligned}
\frac{dn_1(t)}{dt} &= \phi - (\varphi_1 + \nu_1)n_1(t), \\
\frac{dn_{2L}(t)}{dt} &= \varphi_1 n_1(t) - (\chi_4 + \chi_8 + \sigma_2)n_{2L}(t) + \beta_2 n_{2H}(t), \\
\frac{dn_{2H}(t)}{dt} &= \sigma_2 n_{2L}(t) - (\beta_2 + \nu_2)n_{2H}(t), \\
\frac{dn_{4L}(t)}{dt} &= \chi_4 n_{2L}(t) - (\sigma_4 + \zeta_4 - \gamma_4)n_{4L}(t) + \beta_4 n_{4H}(t), \\
\frac{dn_{4H}(t)}{dt} &= \sigma_4 n_{4L}(t) - (\beta_4 + \sigma_R + \nu_4)n_{4H}(t), \\
\frac{dn_R(t)}{dt} &= \sigma_R n_{4H}(t) - (\nu_R + \zeta_R - \gamma_R)n_R(t) + \phi_R, \\
\frac{dn_{8L}(t)}{dt} &= \chi_8 n_{2L}(t) - (\sigma_8 + \zeta_8 - \gamma_8)n_{8L}(t) + \beta_8 n_{8H}(t), \\
\frac{dn_{8H}(t)}{dt} &= \sigma_8 n_{8L}(t) - (\beta_8 + \nu_8)n_{8H}(t),
\end{aligned} \tag{5.7}$$

for $t \geq 0$.$\boldsymbol{n^*_{M3}} = (n^*_1,\ n^*_{2L},\ n^*_{2H},\ n^*_{4L},\ n^*_{4H},\ n^*_R,\ n^*_{8L},\ n^*_{8H})$ is the steady state of Equation (5.7) where n^*_1 is defined in Equation (5.2) and

$$\begin{aligned}
n^*_{2L} &= n^*_1 \frac{\varphi_1(\beta_2+\nu_2)}{\sigma_2\nu_2 + (\chi_4+\chi_8)(\beta_2+\nu_2)},\\
n^*_{2H} &= n^*_{2L}\frac{\sigma_2}{\beta_2+\nu_2},\\
n^*_{4L} &= n^*_{2L}\frac{\chi_4(\beta_4+\sigma_R+\nu_4)}{(\zeta_4-\gamma_4)(\beta_4+\sigma_R+\nu_4)+\sigma_4(\sigma_R+\nu_4)},\\
n^*_{4H} &= n^*_{4L}\frac{\sigma_4}{\beta_4+\sigma_R+\nu_4},\\
n^*_R &= \frac{\phi_R+\sigma_R n^*_{4H}}{\nu_R+\zeta_R-\gamma_R},\\
n^*_{8L} &= n^*_{2L}\frac{\chi_8(\beta_8+\nu_8)}{\sigma_8\nu_8+(\zeta_8-\gamma_8)(\beta_8+\nu_8)},\\
n^*_{8H} &= n^*_{8L}\frac{\sigma_8}{\beta_8+\nu_8}.
\end{aligned} \tag{5.8}$$

The unique steady state $\boldsymbol{n^*_{M3}}$ exists if and only if $(\zeta_4-\gamma_4)(\beta_4+\sigma_R+\nu_4)+\sigma_4(\sigma_R+\nu_4) > 0$, $\nu_R+\zeta_R-\gamma_R > 0$ and $(\zeta_8-\gamma_8)(\beta_8+\nu_8)+\sigma_8\nu_8 > 0$, so that $n^{L*}_4 > 0, n^*_R > 0$ and $n^{L*}_8 > 0$. The Jacobian matrix $\boldsymbol{J_3}$ is calculated to study the linear stability of the steady state $\boldsymbol{n^*_{M3}}$. The matrix $\boldsymbol{J_3} = (j_{ij})_{i,j\in S}$, where $S = \{1,2,\ldots,8\}$, is 8×8 matrix with its elements equal to 0 except the following,

$$\begin{array}{lll}
j_{11} = -\varphi_1 - \nu_1, & j_{12} = \varphi_1, & j_{22} = -\sigma_2 - \chi_4 - \chi_8,\\
j_{23} = \sigma_2, & j_{24} = \chi_4, & j_{27} = \chi_8,\\
j_{32} = \beta_2, & j_{33} = -\beta_2 - \nu_2, & j_{44} = \gamma_4 - \sigma_4 - \zeta_4,\\
j_{45} = \sigma_4, & j_{54} = \beta_4, & j_{55} = -\beta_4 - \sigma_R - \nu_4,\\
j_{56} = \sigma_R, & j_{66} = \gamma_R - \nu_R - \zeta_R, & j_{77} = \gamma_8 - \sigma_8 - \zeta_8,\\
j_{78} = \sigma_8 & j_{87} = \beta_8, & j_{88} = -\beta_8 - \nu_8.
\end{array}$$

There are eight eigenvalues of the matrix $\boldsymbol{J_3}$,

$$\begin{aligned}
\delta_1 = &\ -\varphi_1 - \nu_1 \\
\delta_2 = &\ -\tfrac{1}{2}(\sigma_2 + \chi_4 + \chi_8 + \beta_2 + \nu_2) + \tfrac{1}{2}\{(\sigma_2 + \chi_4 + \chi_8 + \beta_2 + \nu_2)^2 \\
&\ -4(\sigma_2\nu_2 + (\chi_4 + \chi_8)(\beta_2 + \nu_2))\}^{\frac{1}{2}} \\
\delta_3 = &\ -\tfrac{1}{2}(\sigma_2 + \chi_4 + \chi_8 + \beta_2 + \nu_2) - \tfrac{1}{2}\{(\sigma_2 + \chi_4 + \chi_8 + \beta_2 + \nu_2)^2 \\
&\ -4(\sigma_2\nu_2 + (\chi_4 + \chi_8)(\beta_2 + \nu_2))\}^{\frac{1}{2}} \\
\delta_4 = &\ -\tfrac{1}{2}(\beta_4 + \sigma_R + \nu_4 + \sigma_4 + \zeta_4 - \gamma_4) + \tfrac{1}{2}\{(\beta_4 + \sigma_R + \nu_4 + \sigma_4 + \zeta_4 - \gamma_4)^2 \\
&\ -4((\zeta_4 - \gamma_4)(\beta_4 + \sigma_R + \nu_4) + \sigma_4(\sigma_R + \nu_4))\}^{\frac{1}{2}}, \\
\delta_5 = &\ -\tfrac{1}{2}(\beta_4 + \sigma_R + \nu_4 + \sigma_4 + \zeta_4 - \gamma_4) - \tfrac{1}{2}\{(\beta_4 + \sigma_R + \nu_4 + \sigma_4 + \zeta_4 - \gamma_4)^2 \\
&\ -4((\zeta_4 - \gamma_4)(\beta_4 + \sigma_R + \nu_4) + \sigma_4(\sigma_R + \nu_4))\}^{\frac{1}{2}}, \\
\delta_6 = &\ \gamma_R - \nu_R - \zeta_R \\
\delta_7 = &\ -\tfrac{1}{2}(\beta_8 + \nu_8 + \sigma_8 + \zeta_8 - \gamma_8) + \tfrac{1}{2}\{(\beta_8 + \nu_8 + \sigma_8 + \zeta_8 - \gamma_8)^2 \\
&\ +4(\sigma_8\gamma_8 + (\zeta_8 - \gamma_8)(\beta_8 + \nu_8))\}^{\frac{1}{2}} \\
\delta_8 = &\ -\tfrac{1}{2}(\beta_8 + \nu_8 + \sigma_8 + \zeta_8 - \gamma_8) - \tfrac{1}{2}\{(\beta_8 + \nu_8 + \sigma_8 + \zeta_8 - \gamma_8)^2 \\
&\ +4(\sigma_8\gamma_8 + (\zeta_8 - \gamma_8)(\beta_8 + \nu_8))\}^{\frac{1}{2}}
\end{aligned}$$

The steady state $\boldsymbol{n^*_{M3}}$ exists and it is stable if and only if the following constraints are satisfied,

$$\begin{aligned}
&1.\quad (\zeta_4 - \gamma_4)(\beta_4 + \sigma_R + \nu_4) + \sigma_4(\sigma_R + \nu_4) > 0, \\
&2.\quad \nu_R + \zeta_R - \gamma_R > 0, \\
&3.\quad (\zeta_8 - \gamma_8)(\beta_8 + \nu_8) + \sigma_8\nu_8 > 0, \\
&4.\quad \beta_4 + \sigma_R + \nu_4 + \sigma_4 + \zeta_4 > \gamma_4, \\
&5.\quad \beta_8 + \nu_8 + \sigma_8 + \zeta_8 > \gamma_8.
\end{aligned} \tag{5.9}$$

5.3 Experimental data

The original experimental data were previously published by Stritesky *et al.* (2013). The experiment was carried out on seven mice aged between 5.5 and

17 weeks. The data are the experimental thymocyte cell counts at the steady state of each mouse, in each of the eight compartments defined by Model 3 (see Subsection 5.2.3).

mouse	$\bar{n}_1^k$	$\bar{n}_{2L}^k$	$\bar{n}_{2H}^k$	$\bar{n}_{4L}^k$	$\bar{n}_{4H}^k$	$\bar{n}_R^k$	$\bar{n}_{8L}^k$	$\bar{n}_{8H}^k$
$k=1$	82.58	5.79	3.51	9.37	4.48	-	2.62	1.89
$k=2$	142.19	14.46	5.49	14.31	4.43	-	4.63	2.83
$k=3$	89.00	3.84	2.14	8.28	3.60	-	2.32	1.78
$k=4$	29.32	1.70	0.39	3.59	0.81	0.15	0.98	0.23
$k=5$	51.26	2.98	2.95	4.70	2.15	0.46	1.1	1.06
$k=6$	64.48	3.74	3.07	5.89	3.14	0.54	1.28	1.33
$k=7$	218.94	9.33	6.09	18.59	10.88	2.60	5.14	5.6

Table 5.1: Each column represents the thymocyte counts $\bar{n}_i^k$ (each row for kth mouse) for population n_i, described by Model 3 from Subsection 5.2.3, given in units $[10^6\ cells]$, where $i \in \{1, 2L, 2H, 4L, 4H, R, 8L, 8H\}$.

The data are used in the next Section 5.4 to estimate the parameters of all three models presented in Section 5.2. The data for Model 1 and Model 2 are found from the following equations,

$$\bar{n}_2^k = \bar{n}_{2L}^k + \bar{n}_{2H}^k, \quad \bar{n}_4^k = \bar{n}_{4L}^k + \bar{n}_{4H}^k, \quad \bar{n}_8^k = \bar{n}_{8L}^k + \bar{n}_{8H}^k, \quad \bar{n}_3^k = \bar{n}_4^k + \bar{n}_8^k. \tag{5.10}$$

Published data suggest that the mean time spent by a single cell in the pre-DP stage is $\tau_1 = 2.5$ days, whereas the mean time spent by a single cell in the post-DP stage is $\tau_2 = 16$ hours (see Egerton *et al.* (1990), Saini *et al.* (2010), McCaughtry *et al.* (2007)). It is also known, according to the experimental data presented by Stritesky *et al.* (2013), Thomas-Vaslin *et al.* (2008), and Scollay *et al.* (1980), that the flux from the medulla is about $1 - 4 \times 10^6$ cells per day. The death rates for SP CD4$^+$ and SP CD8$^+$ thymocytes were also estimated to be 0.04 day^{-1} and 0.11 day^{-1} respectively (see Sinclair *et al.* (2013)). This information is summarised in Table 5.2.

name	value
mean time spent by a single cell in the pre-DP stage	$\tau_1 = 2.5$ days
mean time spent by a single cell in the post-DP stage	$\tau_2 = 16$ hours
mean flux from the medulla	$\phi_{out} \in (10^6, 4 \times 10^6)$ cells/day
death rate at the SP CD4$^+$ stage	$\bar{\mu}_4 = 0.04$ day^{-1}
death rate at the SP CD8$^+$ stage	$\bar{\mu}_8 = 0.11$day^{-1}

Table 5.2: Additional published information regarding T cell development in the thymus.

5.4 Bayesian parameter estimation

An adapted version of the ABC algorithm described in Chapter 2 Subsection 2.4.2 is used to estimate the parameters in all three models of thymocyte development in the thymus. The data allow the use of the Mahalanobis distance to decide whether to accept or reject parameter samples for Model 1 and Model 2. The covariance matrix of the data for eight compartments of Model 3 is not positive definite therefore it is not possible to compute the inverse of this matrix thereby the Mahalanobis distance cannot be calculated. Hence, Pearson distance (also called normalised Euclidean distance) is used instead. In the following subsections I describe how the prior distributions for the parameters in each model are chosen.

5.4.1 Prior distributions in Model 1

The information about T cell development in the thymus from Table 5.2 is used to define the prior distribution for some of the parameters in Model 1.

Assume that the exit rate r_i from compartment i is a random variable and it follows an exponential distribution with parameter τ_i, for $i = 1, 2$. Therefore the expectation of r_i is equal to τ_i^{-1}. The cumulative distribution function for the exponential distribution is $F(r_i) = 1 - e^{(-\tau_i r_i)}$. The variable r_i satisfies the inequality $0.975 > F(r_i) > 0.025$ if $-\tau_i^{-1}\log(0.975) < r_i < -\tau_i^{-1}\log(0.025)$.

The exit rate in each compartment is defined as $r_i = \varphi_i + \mu_i$. Hence the proposal for $\varphi_i + \mu_i$ (and for φ_i, μ_i separately) is expected to be in the interval $\left(-\tau_i^{-1}\log(0.975), -\tau_i^{-1}\log(0.025)\right)$ for $i = 1, 2$.

The information about death rates in the SP populations is also provided. As the death rates for SP CD4$^+$ and SP CD8$^+$ are given separately one can compute the overall average death rate in the SP compartment of Model 1 as $\bar{\mu}_3 = \bar{\mu}_4 a_4 + \bar{\mu}_8 a_8$, where coefficients a_4 and a_8 are found from the data reported in Table 5.1 using linear regression (see Freedman (2009)), that is

$$a_4 = \sum_{k=1}^{7} (\bar{n}_4^k \bar{n}_3^k) \left(\sum_{k=1}^{7} (\bar{n}_3^k \bar{n}_3^k) \right)^{-1}, \quad a_8 = \sum_{k=1}^{7} (\bar{n}_8^k \bar{n}_3^k) \left(\sum_{k=1}^{7} (\bar{n}_3^k \bar{n}_3^k) \right)^{-1},$$

where $\bar{n}_3^k, \bar{n}_4^k, \bar{n}_8^k$ are defined by Equation (5.10). Assume now that the death rate μ_3 is a random variable and it follows an exponential distribution with parameter $\bar{\mu}_3$. Therefore, similarly to the approach with the exit rate, the proposal μ_3 is expected to be in the interval $(-\bar{\mu}_3 \log(0.975), -\bar{\mu}_3 \log(0.025))$.

ϕ and φ_3 are sampled from arbitrarily chosen uniform distributions to explore wide ranges of possible values for these rates. The prior distribution for λ_3 is constrained to be less or equal to $\varphi_3 + \mu_3$ to get the stability of the steady state $\boldsymbol{n}^*_{\boldsymbol{M1}}$ (see Equation (5.3) for the eigenvalues of Jacobian matrix $\boldsymbol{J_1}$).

The flux from the medulla in Model 1 can be computed as, $\phi_{out} = n_3^* \varphi_3$, where n_3^* is defined in Equation (5.2). The flux from the medulla is expected to be between 10^5 and 10^7 cells per day. In this way the algorithm is able to explore a wider prior distribution for parameters than aiming to match exactly the flux reported by the experimental data.

The mice considered in the experimental study are 5.5-17 weeks old and their thymus is in the steady state (see Egerton *et al.* (1990)). It is expected that the parameter values can only be accepted if the corresponding system of ODEs given by Equation (5.1) attains steady state by 3 weeks. Therefore the only accepted parameters for the prior distributions are ones that provide thymocyte counts at time $t = 21$ days within 5% of the values at steady state.

The prior distributions for the parameters in Model 1 can be sampled from Algorithm 11. The prior distribution is the combination of the distribution in step A1 and constraints in step A2 where a typical prior would be just the distribution from step A1.

A1. Let $\boldsymbol{\theta} = (\phi, \varphi_1, \varphi_2, \varphi_3, \mu_1, \mu_2, \mu_3, \lambda_3)$. *Sample each element of the vector* $\boldsymbol{\theta}$ *from the following distributions,*

$$\begin{aligned} \phi &\sim U(1, 10^9)\ cells \cdot day^{-1}, \\ \varphi_i, \mu_i &\sim U\left(-\tau_i^{-1}\log(0.975), -\tau_i^{-1}\log(0.025)\right)\ for\ i = 1, 2, \\ \varphi_3 &\sim U(0, 10) day^{-1}, \\ \mu_3 &\sim U(-\bar{\mu}_3\log(0.975), -\bar{\mu}_3\log(0.025)), \\ \lambda_3 &\sim U\left(0, \varphi_3 + \mu_3\right). \end{aligned}$$

A2. Check the following constraints,

1. $-\tau_1^{-1}\log(0.975) < \varphi_1 + \mu_1 < -\tau_1^{-1}\log(0.025)$.
2. $-\tau_2^{-1}\log(0.975) < \varphi_2 + \mu_2 < -\tau_2^{-1}\log(0.025)$.
3. *Compute the steady state* $\boldsymbol{n^*_{M1}} = (n_1^*, n_2^*, n_3^*)$ *using Equation (5.2) and parameters from* $\boldsymbol{\theta}$. *Check if*
$$10^5\ cells\ day^{-1} < n_3^*\varphi_3 < 10^7\ cells\ day^{-1}.$$
4. *Find a numerical solution of Equation (5.1) at time* $t = 21$ *days, using parameters from* $\boldsymbol{\theta}$, *and call it* $\boldsymbol{m} = (m_1, m_2, m_3)$. *Check if for* $i = 1, 2, 3$
$$|m_i - n_i^*| < 0.05 \cdot n_i^*.$$

Accept $\boldsymbol{\theta}$ *if all the constraints 1-4 in point A2 hold.*

Algorithm 11: to sample from the prior distributions in Model 1.

The Mahalanobis distance is used in the ABC algorithm and it is given by the following equation

$$\delta(\boldsymbol{n^*}, \bar{\boldsymbol{n}}) = (\boldsymbol{n^*} - \bar{\boldsymbol{n}})\boldsymbol{\Sigma}^{-1}(\boldsymbol{n^*} - \bar{\boldsymbol{n}})^T \tag{5.11}$$

where $\boldsymbol{n^*} = \boldsymbol{n^*_{M1}}$ is the steady state defined by Equation (5.2), $\bar{\boldsymbol{n}}_{\boldsymbol{M1}} = (\bar{n}^j_{M1})_{j\in\{1,2,3\}}$ is a vector of the mean thymocyte counts from Table 5.1 , that is,

$$\bar{\boldsymbol{n}}_{\boldsymbol{M1}} = \left(\frac{1}{7}\sum_{k=1}^{7}\bar{n}_j^k\right)_{j\in\{1,2,3\}} = (96.82\times10^6, 9.35\times10^6, 18.14\times10^6)\ cells,$$

where n_2^k, n_3^k are defined in Equation (5.10). The covariance matrix of the thymocyte counts $\mathbf{\Sigma} = \mathbf{\Sigma_{M1}} = \left(\frac{1}{6} \sum_{k=1}^{7} (n_i^k - \bar{n}_{M1}^i)(n_j^k - \bar{n}_{M1}^j) \right)_{i,j \in \{1,2,3\}}$, hence

$$\mathbf{\Sigma_{M1}} = \begin{pmatrix} 4.15 \times 10^{15} & 3.30 \times 10^{14} & 7.58 \times 10^{14} \\ 3.30 \times 10^{14} & 3.85 \times 10^{13} & 6.09 \times 10^{13} \\ 7.58 \times 10^{14} & 6.09 \times 10^{13} & 1.40 \times 10^{14} \end{pmatrix} cells^2.$$

5.4.2 Prior distributions in Model 2

Some of the results from the parameterisation of Model 1 are used as a prior for some of the parameters in Model 2. To be precise, the joint posterior distribution of $\phi, \varphi_1, \mu_1, \mu_2$ obtained in Model 1 is used as a prior distribution for these parameters in Model 2. This approach is valid under the assumption that the dynamics in the pre-DP compartment and the post-DP compartment is the same for those two models. The rest of parameters from Model 2 is sampled from prior distributions defined below based on information from Table 5.2.

The thymocytes' differentiation from the post-DP to the SP stage is encoded in two parameters φ_4 and φ_8 instead of one parameter φ_2. In Model 1, the parameter φ_2 was sampled from the uniform distribution $U(-\tau_2^{-1} \log(0.975), -\tau_2^{-1} \log(0.025))$. Therefore the parameters φ_4 and φ_8 are sampled from the same distribution and they are expected to be in the same distribution as a sum to make sure the overall flux from post-DP to SP thymocytes stays the same. Additionally, as it was shown for Model 1, the proposal for $\varphi_4 + \varphi_8 + \mu_2$ (and for φ_4, φ_8 separately) is expected to be in the interval $(-\tau_2^{-1} \log(0.975), -\tau_2^{-1} \log(0.025))$.

Similarly, the proposal for μ_i, is expected to be in the interval $(-\bar{\mu}_i \log(0.975), -\bar{\mu}_i \log(0.025))$ for $i = 4, 8$.

ξ_4 and ξ_8 are sampled from arbitrarily chosen uniform distributions to explore wide ranges of possible values for these rates. As before, the prior distributions for λ_4 and λ_8 are constrained by the requirements of the steady state $\boldsymbol{n^*_{M2}}$ stability (see Equation (5.6) for the eigenvalues of Jacobian matrix $\boldsymbol{J_2}$).

The assumption about the flux from the medulla is also used and this time, this flux can be written as

$$\phi_{out} = \xi_4 n_4^* + \xi_8 n_8^*,$$

where n_4^* and n_8^* are found from Equation (5.5).

Lastly the parameters of Model 2 must yield thymocyte counts at time $t = 21$ days within 5% of their observed value at the steady state.

A1. Let $\boldsymbol{\theta} = (\phi, \varphi_1, \varphi_4, \varphi_8, \mu_1, \mu_2, \mu_4, \mu_8, \lambda_4, \lambda_8, \xi_4, \xi_8)$. *Sample each element of* $\boldsymbol{\theta}$ *from the following distributions,*

$(\phi, \varphi_1, \mu_1, \mu_2) \sim \pi_1$, *where* π_1 *is the join posterior distribution of the parameters obtained by the ABC algorithm for Model 1,*

$$\begin{aligned}
\varphi_i &\sim U(-\tau_2^{-1}\log(0.975), -\tau_2^{-1}\log(0.025)) \text{ for } i = 4, 8,\\
\mu_i &\sim U(-\bar{\mu}_i\log(0.975), -\bar{\mu}_i\log(0.025)) \text{ for } i = 4, 8,\\
\xi_i &\sim U(0, 10) \ day^{-1} \text{ for } i = 4, 8,\\
\lambda_i &\sim U(0, \xi_i + \mu_i) \text{ for } i = 4, 8.
\end{aligned}$$

A2. Check the following constraints,

1. $-\tau_2^{-1}\log(0.975) < \varphi_4 + \varphi_8 < -\tau_2^{-1}\log(0.025)$.
2. $-\tau_2^{-1}\log(0.975) < \varphi_4 + \varphi_8 + \mu_2 < -\tau_2^{-1}\log(0.025)$.
3. *Compute the steady state* $\boldsymbol{n^*_{M2}} = (n_1^*, n_2^*, n_4^*, n_8^*)$ *from Equations (5.2) and (5.5) using parameters from* $\boldsymbol{\theta}$. *Check if*
$$10^5 \ cells \ day^{-1} < n_4^*\xi_4 + n_8^*\xi_8 < 10^7 \ cells \ day^{-1}.$$
4. *Find a numerical solution of Equation (5.4) at time* $t = 21$ *days, using parameters from* $\boldsymbol{\theta}$, *and call it* $\boldsymbol{m} = (m_1, m_2, m_4, m_8)$. *Check if for* $i = 1, 2, 4, 8$
$$|m_i - n_i^*| < 0.05 n_i^*.$$

Accept $\boldsymbol{\theta}$ *if all the constraints 1-4 in point A2 hold.*

Algorithm 12: to sample from the prior distributions in Model 2.

The prior distribution of the rates in Model 2 can be found using Algorithm 12. As noted before, the Mahalanobis distance defined in Equation (5.11) is used in the ABC algorithm where $\boldsymbol{n^*} = \boldsymbol{n^*_{M2}} = (n_1^*, n_2^*, n_3^*, n_4^*)$ is the steady state defined by Equations (5.2) and (5.5), $\bar{\boldsymbol{n}} = \bar{\boldsymbol{n}}_{\boldsymbol{M2}} = (96.82 \times 10^6, 9.35 \times 10^6, 13.46 \times 10^6, 4.68 \times$

10^6) *cells* is the vector of the mean thymocyte counts, and the covariance matrix of the thymocyte counts $\mathbf{\Sigma} = \mathbf{\Sigma_{M2}}$ (both the mean and the covariance matrix can be found in a similar way to that shown for Model 1), where

$$\mathbf{\Sigma_{M2}} = \begin{pmatrix} 4.15 \times 10^{15} & 3.30 \times 10^{14} & 5.43 \times 10^{14} & 2.15 \times 10^{14} \\ 3.30 \times 10^{14} & 3.85 \times 10^{13} & 4.30 \times 10^{13} & 1.79 \times 10^{13} \\ 5.43 \times 10^{14} & 4.30 \times 10^{13} & 7.20 \times 10^{13} & 2.83 \times 10^{13} \\ 2.15 \times 10^{14} & 1.79 \times 10^{13} & 2.83 \times 10^{13} & 1.13 \times 10^{13} \end{pmatrix} cells^2.$$

5.4.3 Prior distributions in Model 3

ϕ, φ_1 and μ_1 are the parameters with join posterior distribution taken from the ABC algorithm applied in Model 2. This distribution is used as prior distribution in the Bayesian parameterisation of Model 3.

The mean time spent by a single cell in the post-DP stage is found to be 16 hours (see Table 5.2). However in Model 3 the post-DP stage is divided into two thymocyte types, those that have received a low TCR signal (n_{2L}) and those that have received a high TCR signal (n_{2H}) . It is assumed here that the mean time spent by a single cell at the n_{2H} stage is equal to $\tau_{2H} = \tau_2$ whereas the average time spent by cell at the n_{2L} stage is longer and equal to $\tau_{2L} = \tau_2 + 4$ hours, to allow more time for a cell to decide its fate.

The thymocytes' differentiation parameters, called now χ_4 and χ_8, are sampled from a uniform distribution on the range $(-\tau_{2L} \log(0.975), -\tau_{2L} \log(0.025))$ and their sum is expected to be in the same interval. As the mean time which a single cell spends at the n_{2L} stage is proportional to τ_{2L} the proposal for $\chi_4 + \chi_8 + \sigma_2$ (and for σ_2 separately) is expected to be found in the interval $(-\tau_{2L} \log(0.975), -\tau_{2L} \log(0.025))$. Similarly the proposal for β_2 and ν_2 are supposed to be found as a sum in the interval $(-\tau_{2H} \log(0.975), -\tau_{2H} \log(0.025))$.

The death rates of SP thymocytes, called ν_4 and ν_8, are sampled as μ_4 and μ_8 in Model 2.

As there is not much information provided about $\sigma_4, \sigma_8, \sigma_R, \nu_R, \zeta_4, \zeta_8, \zeta_R$, and ϕ_R, the prior distributions for them are set to a uniform distribution on wide intervals. The prior distributions for γ_4, γ_8 and γ_R are set as a uniform distributions on some intervals which ensure that the constraints 2, 4 and 5 from Equation (5.9) hold, which is necessary for the existence and the stability of the steady states.

There is no clear evidence suggesting that the rescue of thymocytes which have received a high TCR signal takes place in vivo. Therefore the prior distributions for the rates β_2, β_4 and β_8 must be set to take that uncertainty into account. Therefore I introduce the probability of rescue ω_i, where ω_i follows $U(0,1)$ for $i \in 2, 4, 8$. Then β_i is equal to 0 with probability $(1-\omega_i)$. The prior distribution of parameters in Model 3 can be found using Algorithm 13.

A1. Let $\boldsymbol{\theta} = (\phi, \varphi_1, \chi_4, \chi_8, \nu_1, \nu_2, \nu_4, \nu_R, \nu_8, \sigma_2, \sigma_4, \sigma_R, \sigma_8, \gamma_4, \gamma_R, \gamma_8, \zeta_4, \zeta_R, \zeta_8, \phi_R, \beta_2, \beta_4, \beta_8)$. *Sample each element of* $\boldsymbol{\theta}$ *from the following distributions,*

$(\phi, \varphi_1, \mu_1) \sim \pi_2$, *where* π_2 *is the join posterior distribution of the parameters obtained by the ABC algorithm for Model 2,*

$$
\begin{aligned}
\sigma_2 &\sim U(-\tau_{2L}^{-1}\log(0.975), -\tau_{2L}^{-1}\log(0.025)),\\
\nu_2 &\sim U(-\tau_{2H}^{-1}\log(0.975), -\tau_{2H}^{-1}\log(0.025)),\\
\chi_i &\sim U(-\tau_{2L}^{-1}\log(0.975), -\tau_{2L}^{-1}\log(0.025)) \text{ for } i = 4, 8,\\
\sigma_i &\sim U(0, 10) \ days^{-1} \text{ for } i = 4, 8, R,\\
\nu_i &\sim U(-\bar{\mu}_i\log(0.975), -\bar{\mu}_i\log(0.025)) \text{ for } i = 4, 8,\\
\nu_R &\sim U(0, 10) \ days^{-1},\\
\zeta_i &\sim U(0, 10) \ days^{-1} \text{ for } i = 4, 8, R,\\
\phi_R &\sim U(1, 10^8) \text{cells per day},\\
\gamma_i &\sim U(0, \zeta_i + \sigma_i) \text{ for } i = 4, 8,\\
\gamma_R &\sim U(0, \nu_R + \zeta_R),
\end{aligned}
$$

$$
\beta_2 \sim \begin{cases} U(-\tau_{2H}^{-1}\log(0.975), -\tau_{2H}^{-1}\log(0.025)) & \text{with probability } \omega_2\\ 0 \text{ per day} & \text{with probability } 1-\omega_2, \end{cases}
$$

$$
\beta_i \sim \begin{cases} U(0, 10) \ days^{-1} & \text{with probability } \omega_i \text{ for } i = 4, 8,\\ 0 \text{ per day} & \text{with probability } 1-\omega_i, \end{cases}
$$

where $\omega_i \sim U(0,1)$ *for* $i \in \{2, 4, 8\}$.

A2. Check the following constraints,

1. $(\zeta_4 - \gamma_4)(\beta_4 + \sigma_R + \nu_4) + \sigma_4(\sigma_R + \nu_4) > 0,$
2. $(\zeta_8 - \gamma_8)(\beta_8 + \nu_8) + \sigma_8\nu_8 > 0,$

3. $-\tau_{2L}^{-1}\log(0.975) < \chi_4 + \chi_8 < -\tau_{2L}^{-1}\log(0.025)$,

4. $-\tau_{2L}^{-1}\log(0.975) < \chi_4 + \chi_8 + \sigma_2 < -\tau_{2L}^{-1}\log(0.025)$,

5. $-\tau_{2H}^{-1}\log(0.975) < \nu_2 + \beta_2 < -\tau_{2H}^{-1}\log(0.025)$,

6. *Compute the steady state* $\boldsymbol{n^*_{M3}} = (n_1^*, n_{2L}^*, n_{2H}^*, n_{4L}^*, n_{4H}^*, n_R^*, n_{8L}^*, n_{8H}^*)$ *from Equations* (5.2) *and* (5.8) *using parameters from* $\boldsymbol{\theta}$. *Check if*

$$10^5 \text{ cells day}^{-1} < n_4^{L*}\zeta_4 + n_8^{L*}\zeta_8 + n_R^*\zeta_R < 10^7 \text{ cells day}^{-1}.$$

7. *Find a numerical solution of Equation* (5.7) *at time* $t = 21$ *days using the parameters from* $\boldsymbol{\theta}$ *and call it* $\boldsymbol{m} = (m_1, m_{2L}, m_{2H}, m_{4L}, m_{4H}, m_R, m_{8L}, m_{8H})$. *Check if for* $i \in I = \{1, 2L, 2H, 4L, 4H, R, 8L, 8H\}$

$$|m_i - n_i^*| < 0.05\ n_i^*.$$

Accept $\boldsymbol{\theta}$ *if all the constraints 1-7 in point A2 hold.*

Algorithm 13: to sample from the prior distributions in Model 3.

As the inverse of the covariance matrix of the full data set is unstable, the Pearson (normalised Euclidean) distance is used instead in the ABC algorithm,

$$\delta(\boldsymbol{n^*}, \bar{\boldsymbol{n}}) = \sqrt{\sum_{i,j\in I} \frac{(n_i^* - \bar{n}_j)^2}{\rho_j^2}},$$

where $\boldsymbol{n^*} = \boldsymbol{n^*_{M3}} = (n_1^*, n_{2L}^*, n_{2H}^*, n_{4L}^*, n_{4H}^*, n_R^*, n_{8L}^*, n_{8H}^*)$ is the steady state found from Equations (5.2) and (5.8), $\bar{\boldsymbol{n}} = \bar{\boldsymbol{n}}_{\boldsymbol{M3}} = (96.82 \times 10^6, 5.98 \times 10^6, 3.38 \times 10^6, 9.25 \times 10^6, 4.21 \times 10^6, 0.94 \times 10^6, 2.58 \times 10^6, 2.10 \times 10^6)$ *cells* is the vector of mean thymocyte counts, and $\boldsymbol{\rho} = \boldsymbol{\rho_{M3}} = (\rho_i)_{i\in I}$ is the vector of sample variances of thymocyte counts, $\boldsymbol{\rho_{M3}} = (4.15\times10^{15}, 2.00\times10^{13}, 3.76\times10^{12}, 2.96\times10^{13}, 1.03\times10^{13}, 1.26 \times 10^{12}, 2.88 \times 10^{12}, 3.02 \times 10^{12})$ *cells*.

5.5 Results

In this section I present the results of the ABC algorithm described in Subsection 2.4.2 (Algorithm 2) where the prior distributions π for the parameters is described by Algorithm 11, 12 and 13 for Model 1, Model 2 and Model 3, respectively.

5.5.1 Results of the parameter estimation in Model 1

The ABC algorithm was performed 10^8 times. The acceptance ratio was set to 0.01% to accept 10^4 samples. This gave the distance threshold $\delta^* \simeq 0.76$.

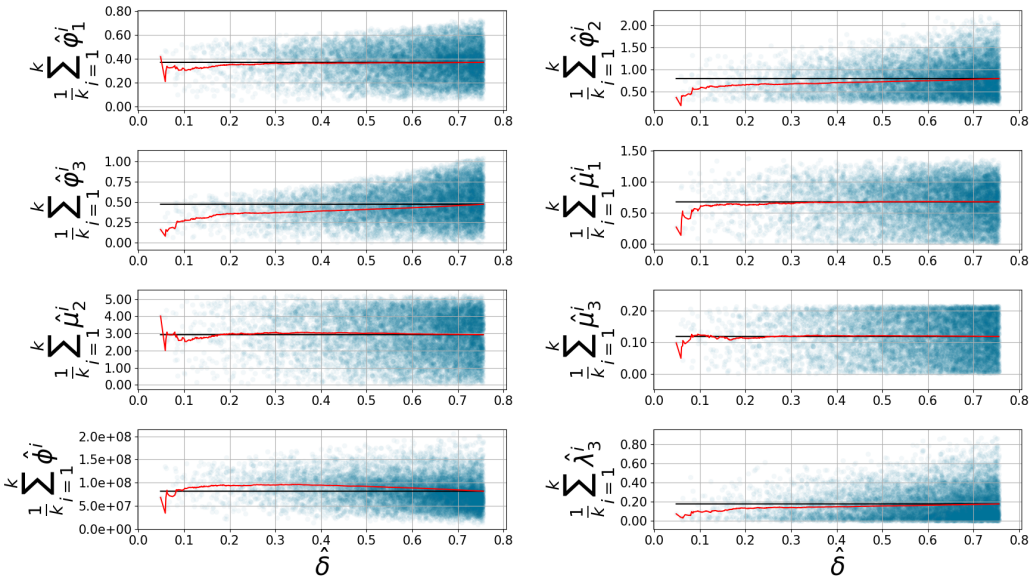

Figure 5.5: The blue dots show the accepted parameter as a function of the distance δ. The black line shows the mean of the accepted value for the given parameter. Denote a vector of the obtained ordered distances $\hat{\boldsymbol{\delta}} = (\delta_1, \delta_2, \ldots, \delta_n)$ $\delta_1 < \delta_2 < \ldots < \delta_n$ where $n = 10^4$. For each δ_k the red line shows the mean of the accepted parameter value $(\hat{\phi}^k, \hat{\varphi}_1^k, \hat{\varphi}_2^k, \hat{\varphi}_3^k, \hat{\mu}_1^k, \hat{\mu}_2^k, \hat{\mu}_3^k, \hat{\lambda}_3^k)$ which gave the distance $\leq \delta_k$.

Denote a vector of increasingly ordered accepted distances $\hat{\boldsymbol{\delta}} = (\delta_1, \delta_2, \ldots, \delta_n)$, where $n = 10^4$. Each element of $\hat{\boldsymbol{\delta}}$ is computed using the relative set of the accepted parameters. One can study how the mean of each parameter value

changes as the distance grows. Figure 5.5 shows how the choice of the distance may affect each parameter. The parameter values vary (red line) for small values of $\hat{\boldsymbol{\delta}}$ where there is only a few parameters accepted. As the distance threshold increases the values of the parameters are close to its mean. Note that the death rates are fairly sensitive to the choice of distance threshold.

Figure 5.6 represents the solution of the system of ODEs given by Equation (5.1) for 100 randomly chosen sets of accepted parameters. As one can observe the solutions converge to the mean of the data within a 95% confidence interval.

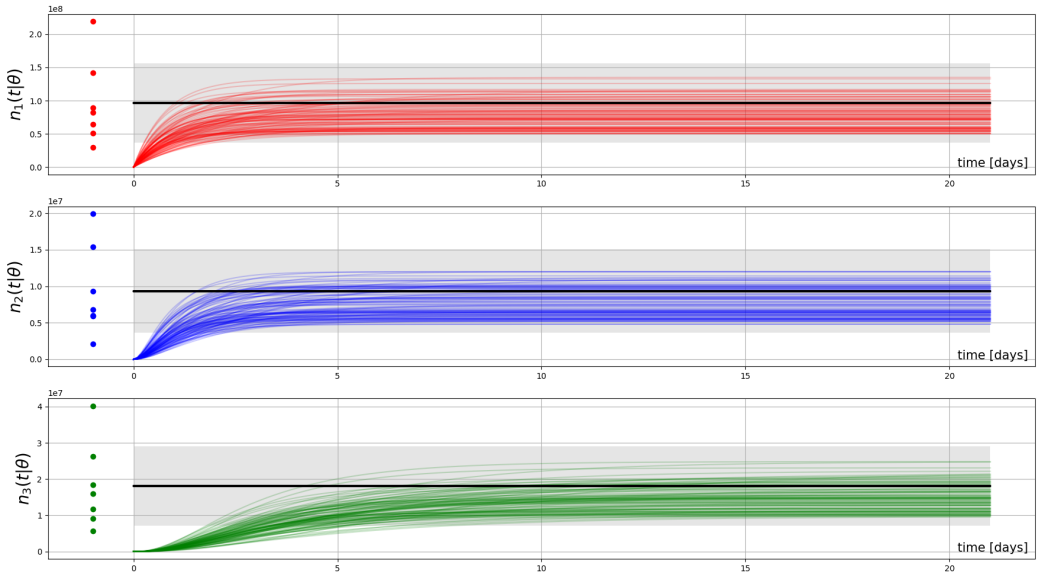

Figure 5.6: The solution of the ODE system given by Equation (5.1) for 100 randomly chosen sets of parameters obtained from the posterior distribution. The black line is the mean of the data. The grey area is the 95% confidence interval of the data. The dots on the left hand side of the plots represent the data points.

The statistics of the results obtained by the ABC algorithm for Model 1 are given in Table 5.3.

	Mean	Median	95% CI	Minimum-maximum interval range
ϕ	8.16×10^7	7.86×10^7	$(2.68 \times 10^7, 1.46 \times 10^8)$	$(9.63 \times 10^6, 2.06 \times 10^8)$
φ_1	0.371	0.375	$(0.112, 0.614)$	$(0.044, 0.731)$
φ_2	0.799	0.742	$(0.262, 1.485)$	$(0.225 , 2.200)$
φ_3	0.475	0.468	$(0.099, 0.864)$	$(0.008, 1.050)$
μ_1	0.673	0.703	$(0.054, 1.185)$	$(0.010, 1.400)$
μ_2	2.930	3.091	$(0.450, 4.877)$	$(0.042, 5.250)$
μ_3	0.119	0.124	$(0.016, 0.216)$	$(0.002, 0.216)$
λ_3	0.177	0.138	$(6.68 \times 10^{-5}, 0.477)$	$(6.68 \times 10^{-5}, 0.872)$

Table 5.3: Means, medians, 95% credible intervals and minimum-maximum intervals of the parameters in Model 1. ϕ is in units *cells per day* whereas the rest of the parameters in the table are in units day^{-1}.

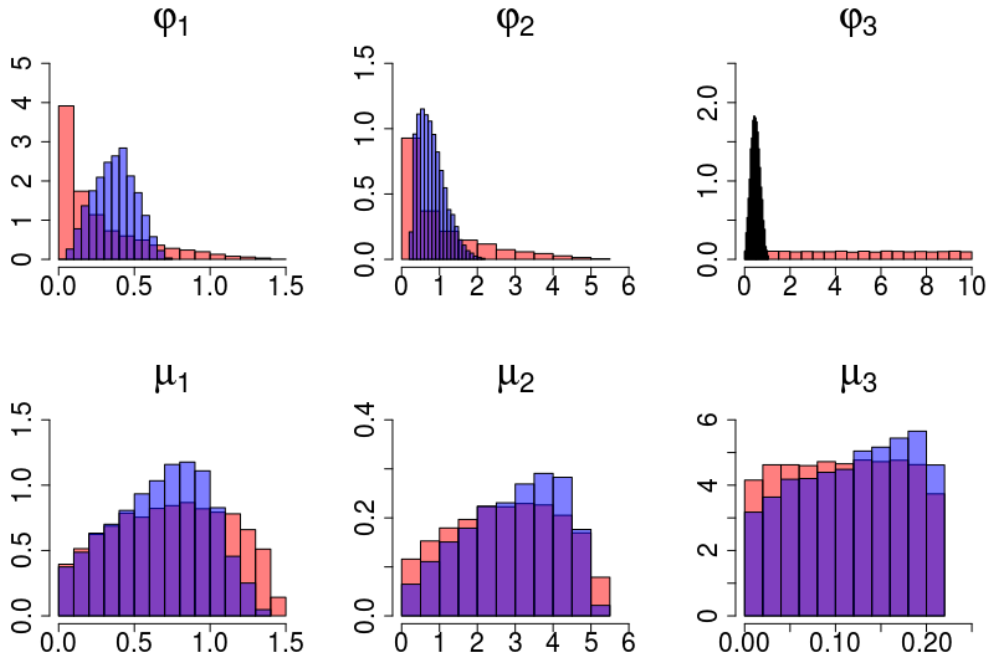

Figure 5.7: The prior distributions (in red) versus the posterior distributions (in blue) generated by the ABC algorithm for Model 1 for the parameters $\varphi_1, \varphi_2, \varphi_3, \mu_1, \mu_2$ and μ_3.

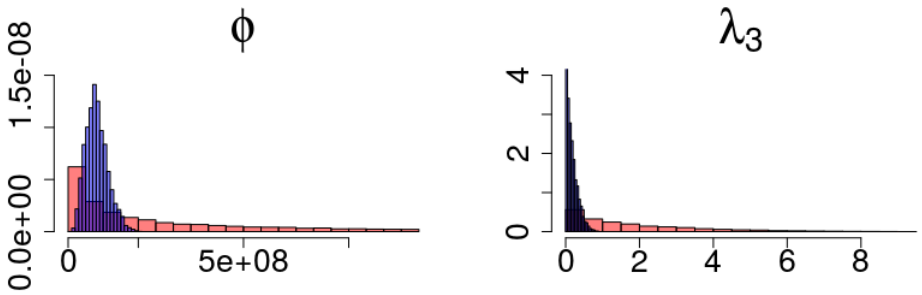

Figure 5.8: The prior distributions (in red) versus the posterior distributions (in blue) generated by the ABC algorithm for Model 1 for the parameters ϕ and λ_3.

The prior distributions described by Algorithm 11 are shown as the red histograms in Figures 5.7 and 5.8 including the effects of the deterministic and the stochastic constraints embedded in this algorithm, whereas the posterior distributions are shown as the blue histograms. The data helped to learn mostly about parameters $\phi, \varphi_1, \varphi_2, \varphi_3$ and λ_3. The posterior distributions for the death rates μ_1, μ_2 and μ_3 are very similar to their prior distributions.

One can investigate how each parameter can affect the steady state value by plotting the steady state against the accepted parameter value. Looking at Figure 5.9 one can examine how each of the parameters $\phi, \varphi_2, \varphi_3, \lambda_3$ separately contributes to the steady state value. As the flux to the thymus ϕ increases the minimum of the steady state value, which can be obtained for this ϕ, grows with it. One interpretation can be that the higher flux of new cells into the cortex leads to more cells at the steady state in each compartment, which is obvious as there is linear relation between ϕ and n_1^*, n_2^*, and n_3^* (see Equation (5.2)). The parameters φ_2, φ_3 and λ_3 have the opposite effect: the higher value of each of those parameters is causing a decrease in the maximum number of cells in the steady state in each compartment. This relationship can be explained for the differentiation rates φ_2 and φ_3 as follows, the higher value of φ_2 or φ_3 is forcing cells to leave each compartment resulting in fever number of cells left. As for the proliferation rate λ_3 it is unclear why the increase of cells in the medulla would cause the decrease of cells in this compartment at the steady state. It is possible that with the higher proliferation rate more cells are leaving the medulla which leads to a lower number of cells left to proliferate.

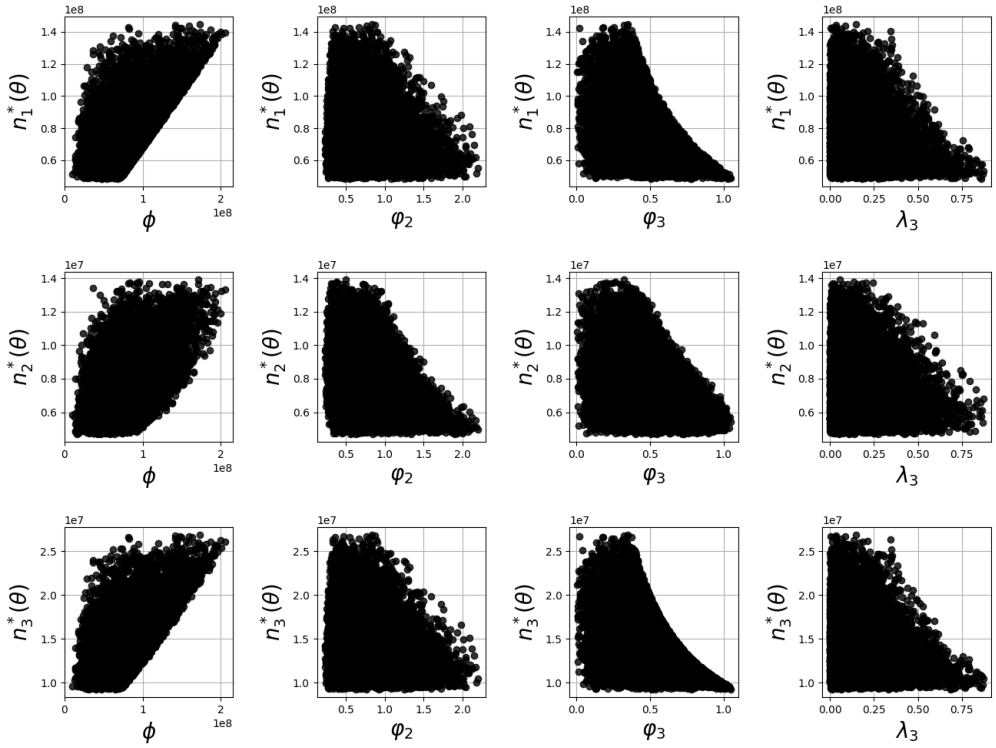

Figure 5.9: The relationship plots between the accepted parameters and the steady state value in each compartment. The plots for the death rates μ_i where $i \in \{1, 2, 3\}$ and the differentiation rate φ_1 are not included as there is no clear relation between them and the steady state values.

To examine the relationship between the parameters, scatter plots have been displayed in Figure 5.10. The black dots represent the values from the prior distribution whereas the yellow overlapping dots represent the accepted values from the posterior distribution. Some of the constraints built in Algorithm 11 are clearly visible in Figure 5.10; the third subplot in the second row (φ_1 versus μ_1 — constraint 1), the second subplot in the third row (φ_2 versus μ_2 — constraint 2). The first subplot in the fourth row (φ_3 versus λ_3) is the result of sampling the proliferation rate λ_3 from a uniform distribution on the interval $(0, \varphi_3 + \mu_3)$. It can be noticed that as a results of the ABC algorithm most of the correlations between the parameters stay the same but on the truncated intervals. However there is a clear positive correlation between φ_1 and μ_2 which can be explained as more pre-DP thymocytes differentiate to the post-DP stage and thus, more

post-DP thymocytes die by apoptosis. Similarly there is a positive correlation between ϕ and μ_1, if more thymocytes become pre-DP cells, then more will die due to negative selection at this stage. There is no clear correlation between φ_2 and μ_3 probably due to the proliferation term at the SP stage.

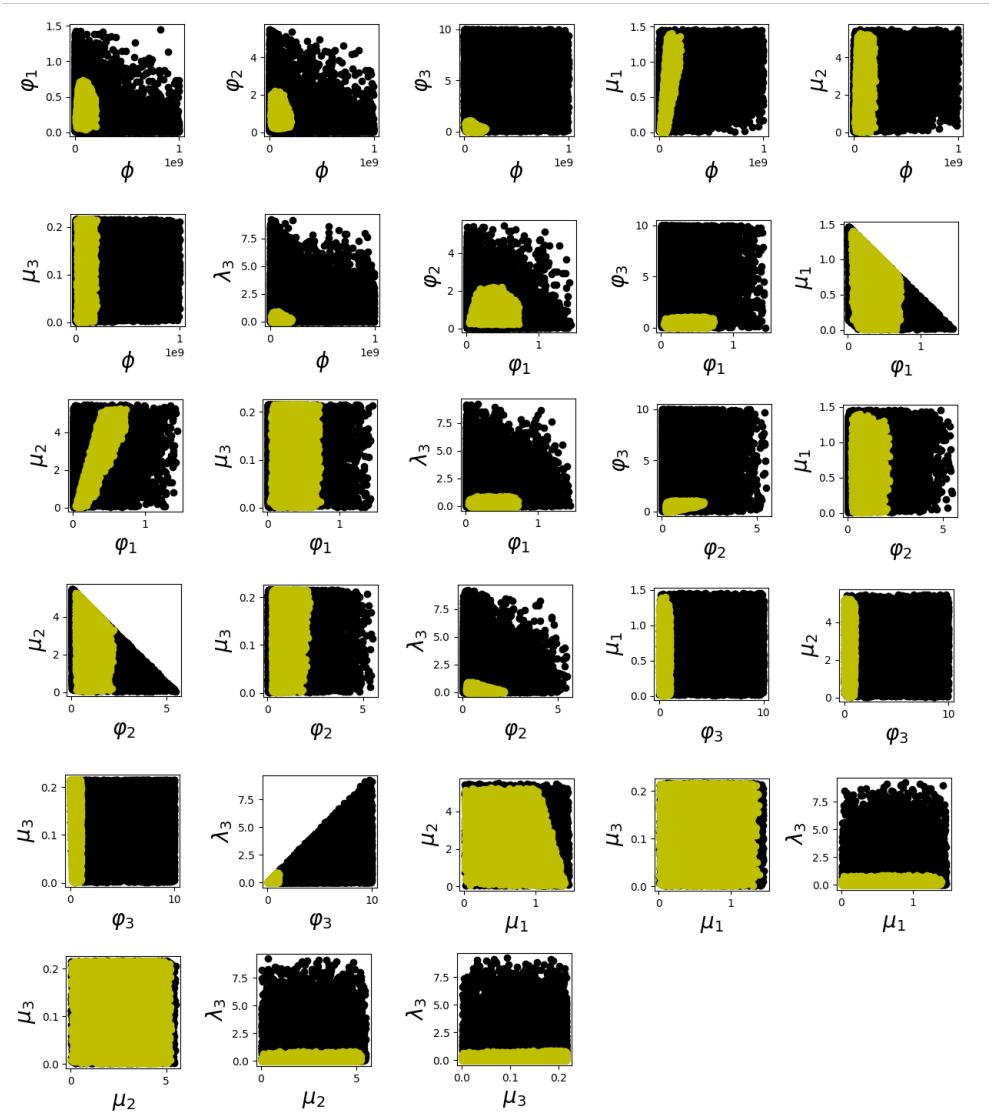

Figure 5.10: The scatter plots of the parameters obtained by the ABC algorithm for Model 1. The black dots represent the values from the prior distribution whereas the overlapping yellow dots represent the values from the posterior distribution.

5.5.2 Results of the parameter estimation in Model 2

The ABC algorithm for Model 2 was performed 10^8 times and 0.01% of the results were accepted which gave the distance threshold $\delta^* \simeq 1.23$. As it was done for Model 1 one can investigate how the choice of the threshold δ^* affects the results by plotting Figure 5.11. The change of the acceptance threshold does not have great effect on the proliferation rates λ_4, λ_8 and the death rates μ_1, μ_4, μ_8.

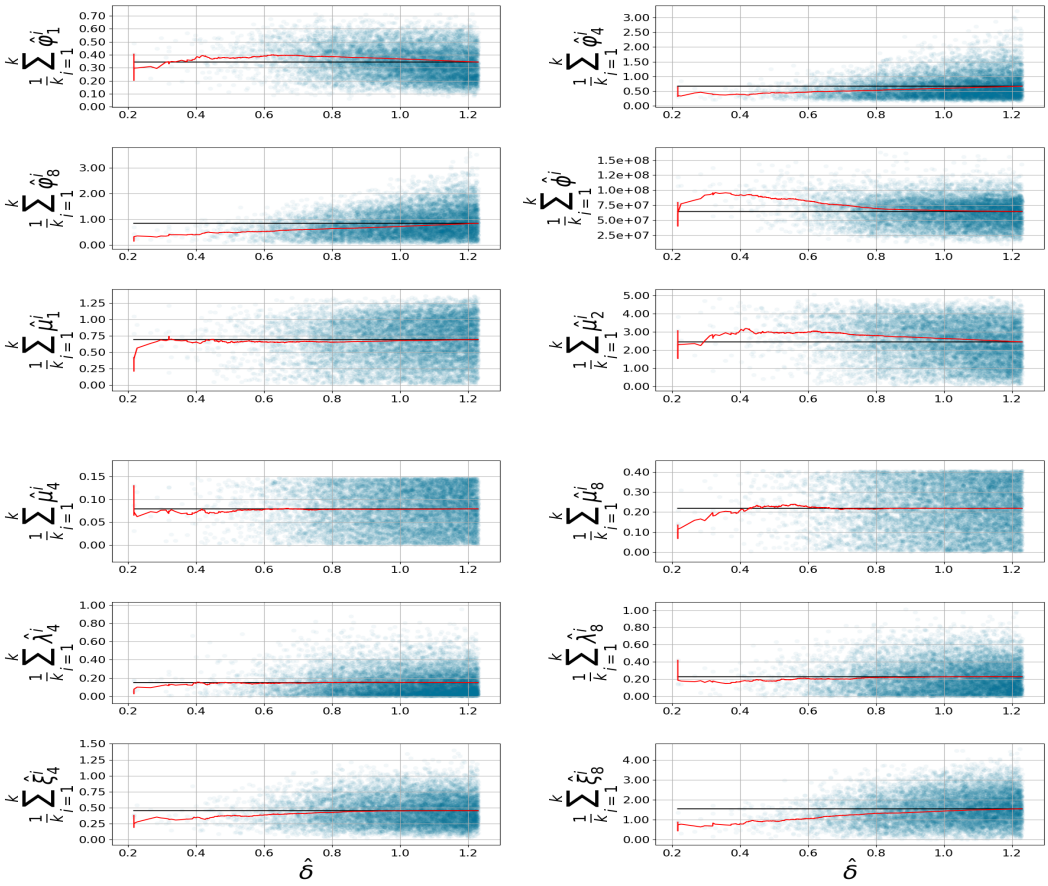

Figure 5.11: The blue dots show the accepted parameter as a function of the distance δ. The black line shows the mean of the accepted value for the given parameter. Denote a vector of the obtained ordered distances $\hat{\boldsymbol{\delta}} = (\delta_1, \delta_2, \ldots, \delta_n)$ $\delta_1 < \delta_2 < \ldots < \delta_n$ where $n = 10^4$. For each δ_k the red line shows the mean of the accepted parameter value $(\hat{\phi}^k, \hat{\varphi}_1^k, \hat{\varphi}_4^k, \hat{\varphi}_8^k, \hat{\mu}_1^k, \hat{\mu}_2^k, \hat{\mu}_4^k, \hat{\mu}_8^k, \hat{\xi}_4^k, \hat{\xi}_8^k, \hat{\lambda}_4^k, \hat{\lambda}_8^k)$ which gave the distance less or equal to δ_k.

Figure 5.12 presents the solution of the system of ODEs given by Equation (5.4) for 100 randomly chosen sets of the accepted parameters. Closer inspection of Figure 5.12 indicates that 97% of curves are below the mean of the data. This implies that Model 2, predicts on average lower cell counts than the experimental results.

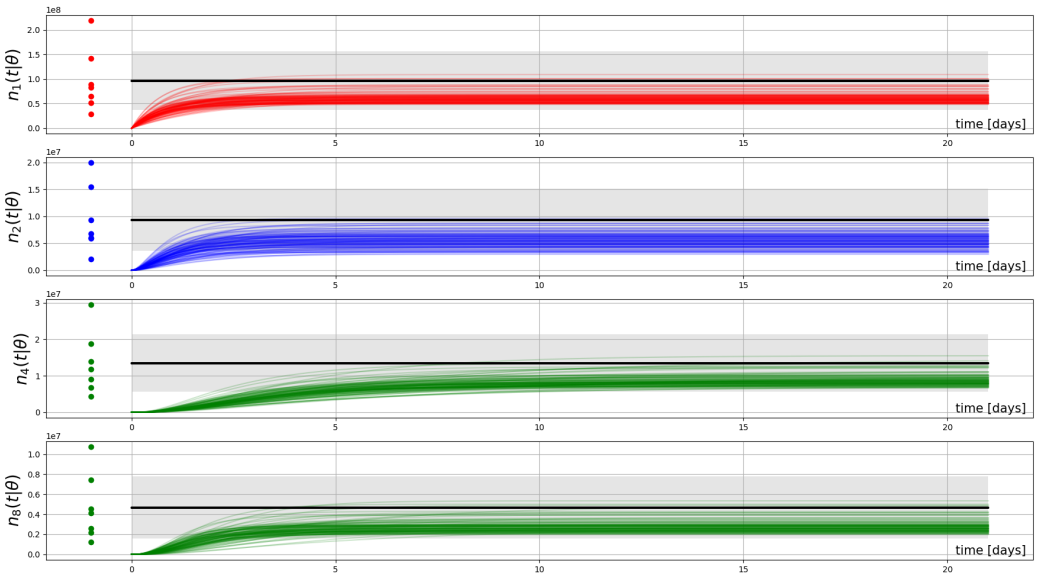

Figure 5.12: The solution of the ODE system given by Equation (5.4) for 100 randomly chosen sets of the accepted parameters. The black line is the mean of the data. The grey area is the 95% confidence interval of the data. The dots on the left hand side of the plots represent the data points.

The statistics of the results obtained by the ABC algorithm performed on Model 2 are reported in Table 5.4. One can notice that on average there are more cells coming to the SP CD8$^+$ compartment than SP CD4$^+$ compartment as $\varphi_8 > \varphi_4$. However the data suggest that there are more SP CD4$^+$ thymocytes. On the other hand the death rate μ_8 and the differentiation rate ξ_8 are significantly higher for SP CD8$^+$ thymocytes, which agrees with the lower cell count at the SP CD8$^+$ stage, when compared to the CD4$^+$ stage.

	Mean	Median	95% CI	Minimum-maximum interval range
ϕ	6.42×10^7	6.49×10^7	$(2.32 \times 10^7, 1.05 \times 10^8)$	$(9.63 \times 10^6, 1.63 \times 10^8)$
φ_1	0.344	0.336	$(0.137, 0.571)$	$(0.061, 0.715)$
φ_4	0.672	0.577	$(0.179, 1.450)$	$(0.150, 3.220)$
φ_8	0.846	0.755	$(0.076, 1.812)$	$(0.058, 3.590)$
μ_1	0.691	0.723	$(0.054, 1.180)$	$(0.010, 1.360)$
μ_2	2.450	2.490	$(0.422, 4.304)$	$(0.046, 5.060)$
μ_4	0.079	0.082	$(0.011, 0.148)$	$(0.001, 0.148)$
μ_8	0.219	0.225	$(0.026, 0.406)$	$(0.003, 0.406)$
ξ_4	0.445	0.429	$(0.086, 0.872)$	$(0.020, 1.400)$
ξ_8	1.550	1.484	$(0.190, 2.992)$	$(0.007, 4.570)$
λ_4	0.148	0.113	$(6.00 \times 10^{-6}, 0.412)$	$(6.00 \times 10^{-5}, 0.954)$
λ_8	0.227	0.194	$(2.80 \times 10^{-5}, 0.558)$	$(2.80 \times 10^{-5}, 1.010)$

Table 5.4: Means, medians, 95% credible intervals and minimum-maximum intervals of the parameters in Model 2. ϕ is in units *cells per day* whereas the rest of the parameters in the table are in units day^{-1}.

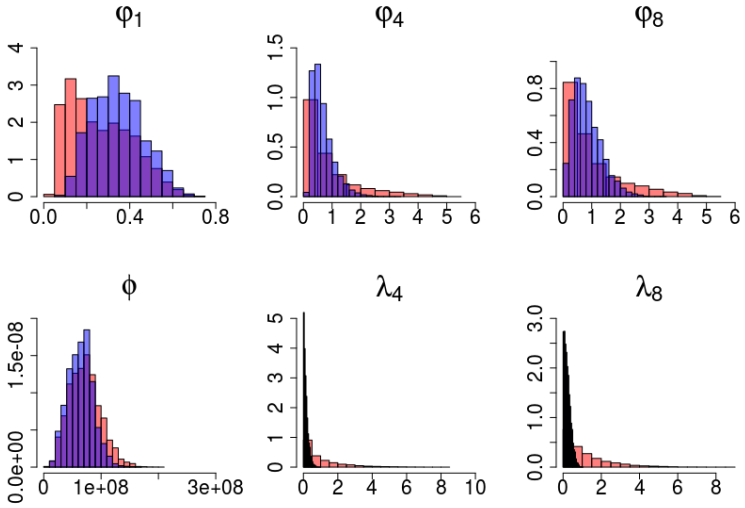

Figure 5.13: The results of the ABC algorithm for the parameters $\varphi_1, \varphi_4, \varphi_8, \phi, \lambda_4, \lambda_8$ for Model 2. The red histograms correspond to the prior distributions whereas the blue histograms correspond to the posterior distributions.

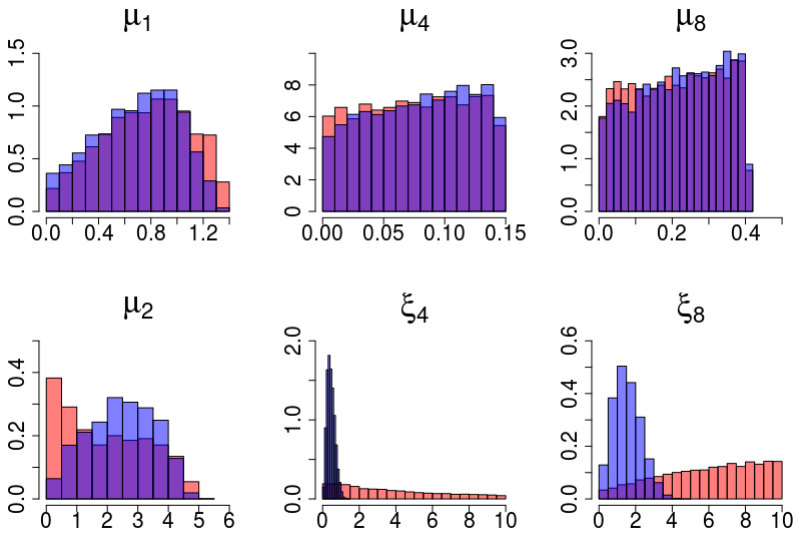

Figure 5.14: The results of the ABC algorithm for the parameters $\mu_1, \mu_2, \mu_4, \mu_8, \xi_4, \xi_8$ for Model 2. The red histograms correspond to the prior distributions whereas the blue histograms correspond to the posterior distributions.

Figures 5.13 and 5.14 show the probability histograms of the prior distributions (in red) versus the probability histograms of the posterior distributions (in blue) of the parameters. Significant learning is achieved for the parameters $\lambda_4, \lambda_8, \xi_4$ and ξ_8. The posterior distributions of $\varphi_1, \varphi_2, \varphi_4$ are shifted to the right whereas the distribution of φ_8 is shifted to the left compared to its prior distributions. There is no additional learning for the death rates μ_1, μ_4 and μ_8.

The corresponding rates between Model 1 and Model 2 which were split into two compartments in the medulla, $\varphi_2 \to \varphi_4$ and φ_8, $\mu_3 \to \mu_4$ and μ_8, $\varphi_3 \to \xi_4$ and ξ_8, and $\lambda_3 \to \lambda_4$ and λ_8 can be compared. The probability histograms of those rates are shown in Figure 5.15. The overall shapes of the distributions remain similar. The distributions of the parameters describing the SP $CD4^+$ compartment are more like those obtained from Model 1 in the SP compartment. The distributions for the parameters describing the SP $CD8^+$ compartment are more spread out.

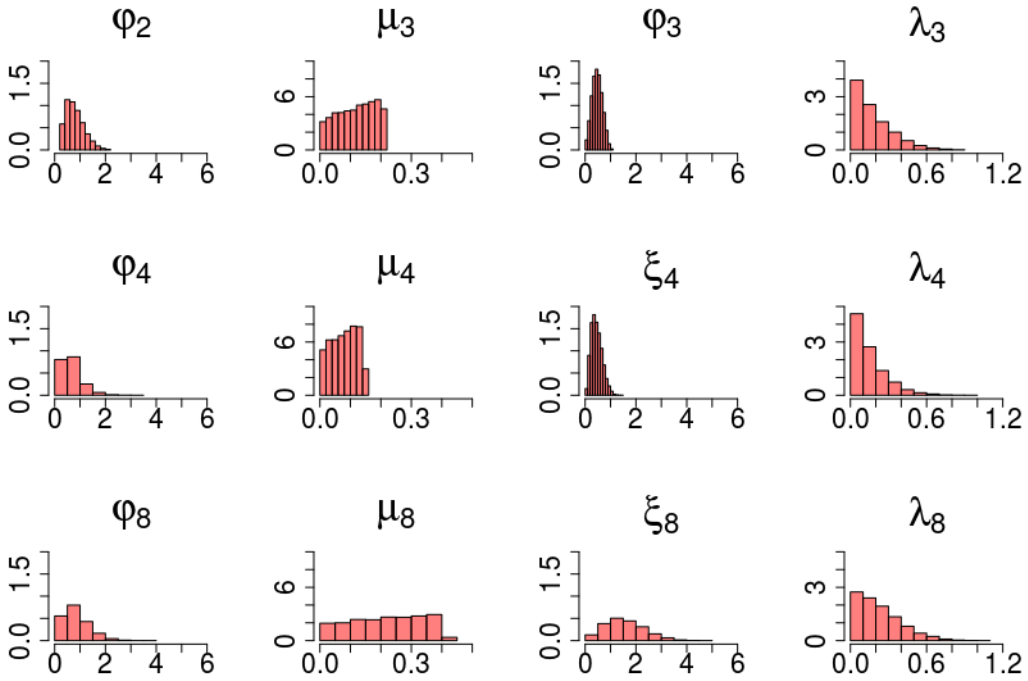

Figure 5.15: The probability histograms of the parameters in the medulla for Model 1 versus Model 2. In the first row the parameters refer to the results of the ABC algorithm for Model 1. The second and the third row refer to the results of the ABC algorithm for Model 2.

Figure 5.16 shows the difference between some quantities related to the SP compartment for Model 1 (in red) and Model 2 (in blue). The first plot in the first row shows the estimated probability density of the number of post-DP thymocytes becoming SP cells for Model 1 (in red) versus Model 2 (in blue) per day. On average Model 2 predicts that the number of thymocytes differentiating to the single positive cells is higher than that predicted by Model 1. The second plot in the first row of Figure 5.16 shows the density of the number of thymocytes dying due to strong signal in the medulla per day. This number is higher on average for Model 1 (in red) compared to Model 2 (in blue). There are more proliferating cells in the medulla per day for Model 2 than Model 1 (the first plot in the second row of Figure 5.16). Also on average there are more thymocytes leaving the thymus per day according to Model 2 than Model 1 (the second plot in the second

row of Figure 5.16). Overall Model 2 predicts that there is more thymocyte differentiation from post-DP to SP cells, therefore there is more proliferation, death and differentiation in the medulla compartment.

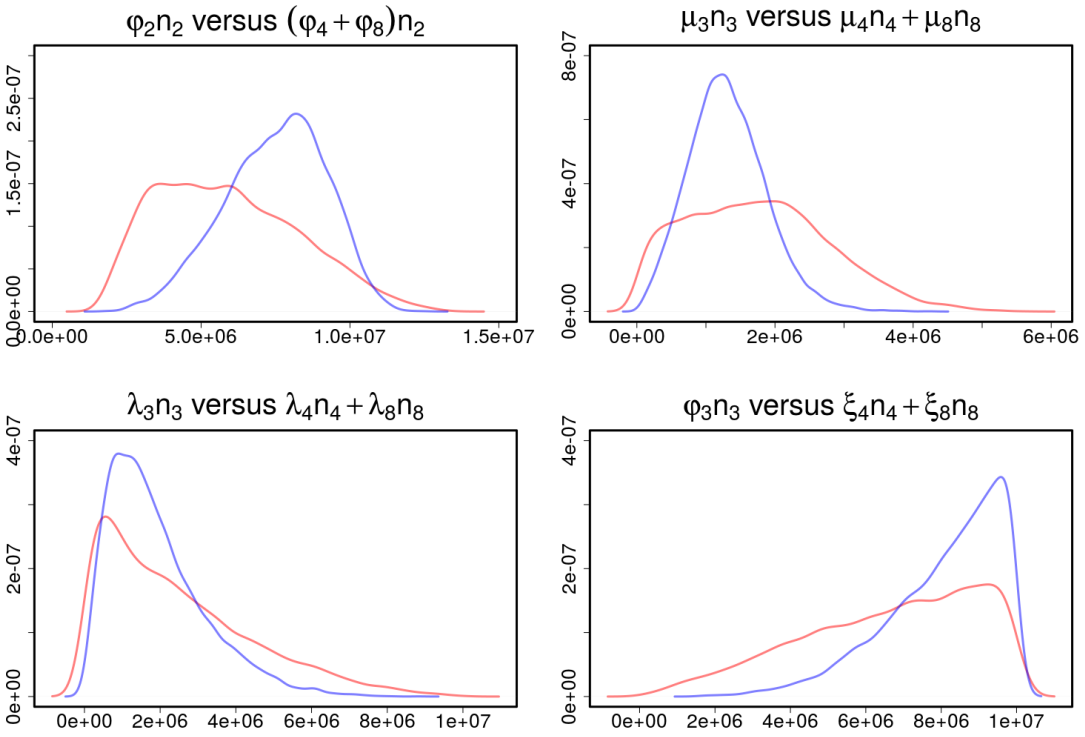

Figure 5.16: The comparison of the estimated probability density of cell counts per day differentiating into SP thymocytes (top left plot); dying due to strong TCR signal at the SP stage (bottom left plot); proliferating in the SP compartment (top right plot); exiting the medulla to the periphery (bottom right plot). The density of those quantities are plotted for Model 1 (in red) and Model 2 (in blue).

As it was shown for Model 1, the relationship between each parameter and the steady state value can be plotted. Figure 5.17 shows plots where the relationship was clear. As the number of thymocytes coming into the pre-DP stage per day grows, the minimum of the number of cells at the steady state in each compartment is higher. As the differentiation rates $\varphi_4, \varphi_8, \xi_4, \xi_8$ or the proliferation rates λ_4, λ_8 grow, the maximum number of cells in each compartment at the steady

state decreases.

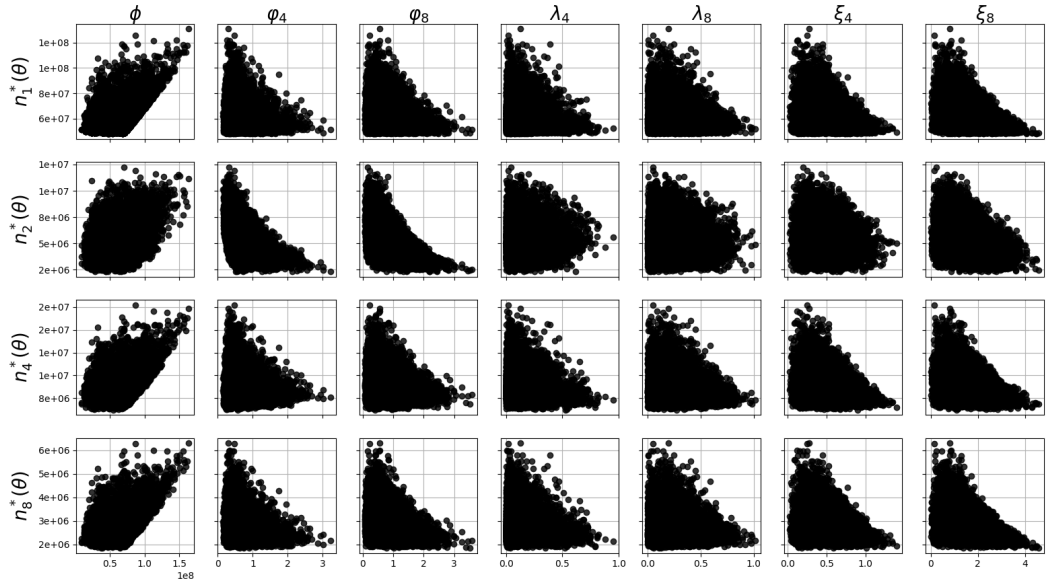

Figure 5.17: The relationship plots between the accepted parameters and the steady state value in each compartment. The plots for the death rates μ_i where $i \in \{1, 2, 4, 8\}$ and the differentiation rates φ_1, φ_2 are not included as there is no clear relation between them and the steady states.

To examine the relationship between the parameters the scatter plots are given in Figure 5.18. The black dots represent the values taken from the prior distribution whereas the overlapping yellow dots represent the values taken from the posterior distribution. Most of the correlation plots look the same for the prior and the posterior distribution or the correlations are the truncated version of the prior correlations. The positive correlations between ξ_i and φ_i for $i \in \{4, 8\}$ appear after performing the ABC algorithm on Model 2 (see Figure 5.18). It means that if more thymocytes differentiate from the pre-DP to the SP stage, then more cells leave the medulla to the periphery.

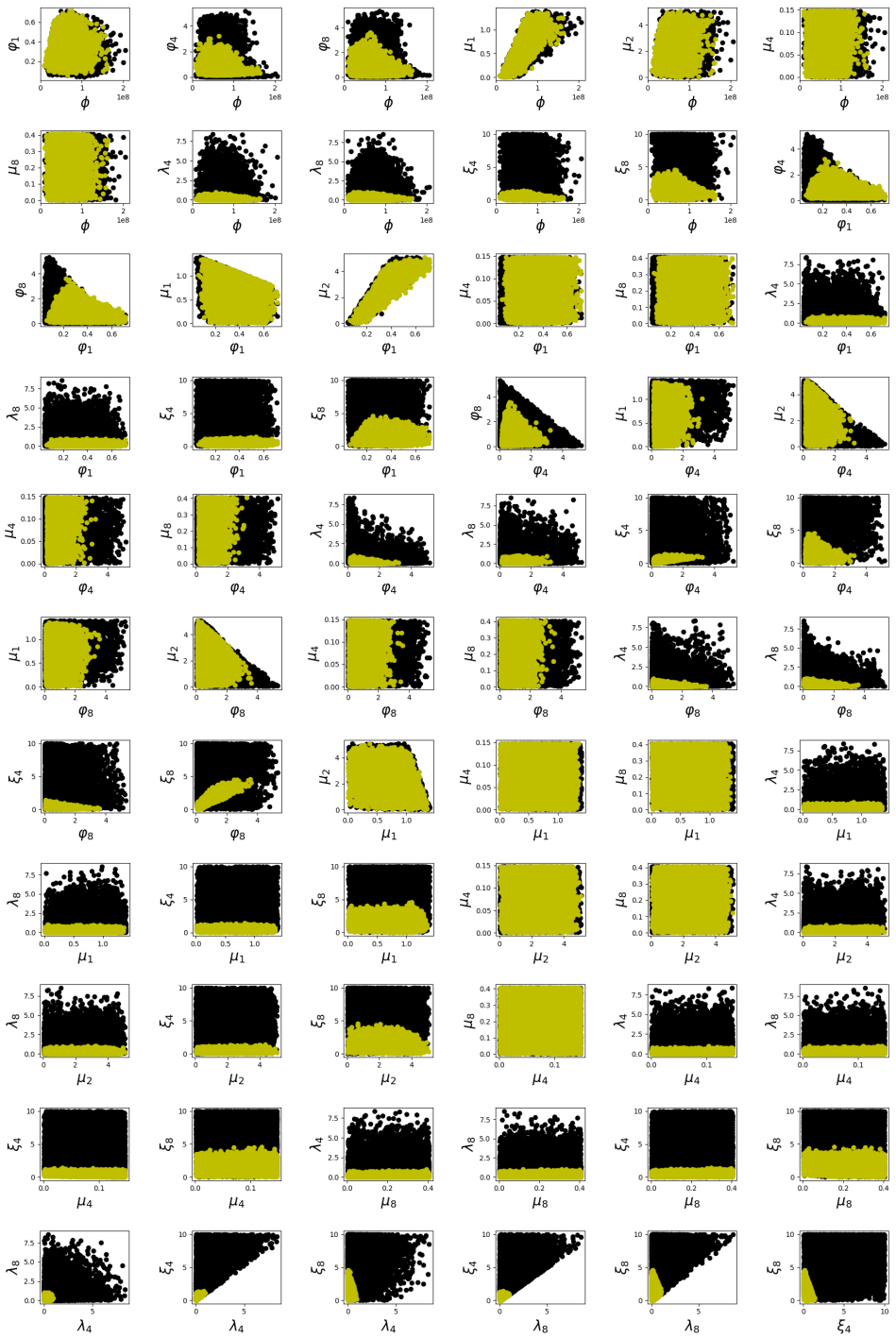

Figure 5.18: The scatter plots of the parameters obtained by the ABC algorithm for Model 2. The black dots represent the values from the prior distribution whereas the overlapping yellow dots represent the values from the posterior distribution.

5.5.3 Results of the parameter estimation in Model 3

The ABC algorithm was performed 10^7 times for Model 3. The acceptance ratio was set to 0.1% to accept 10^4 samples. This gave the threshold $\delta^* \simeq 2.20$. Figure 5.19 shows how the choice of the threshold would affect the parameter values. As one can observe most of the parameters are on average close to its mean regardless the choice of distance. The most variable parameters are $\sigma_4, \sigma_R, \zeta_4, \zeta_8, \gamma_4$ and γ_8.

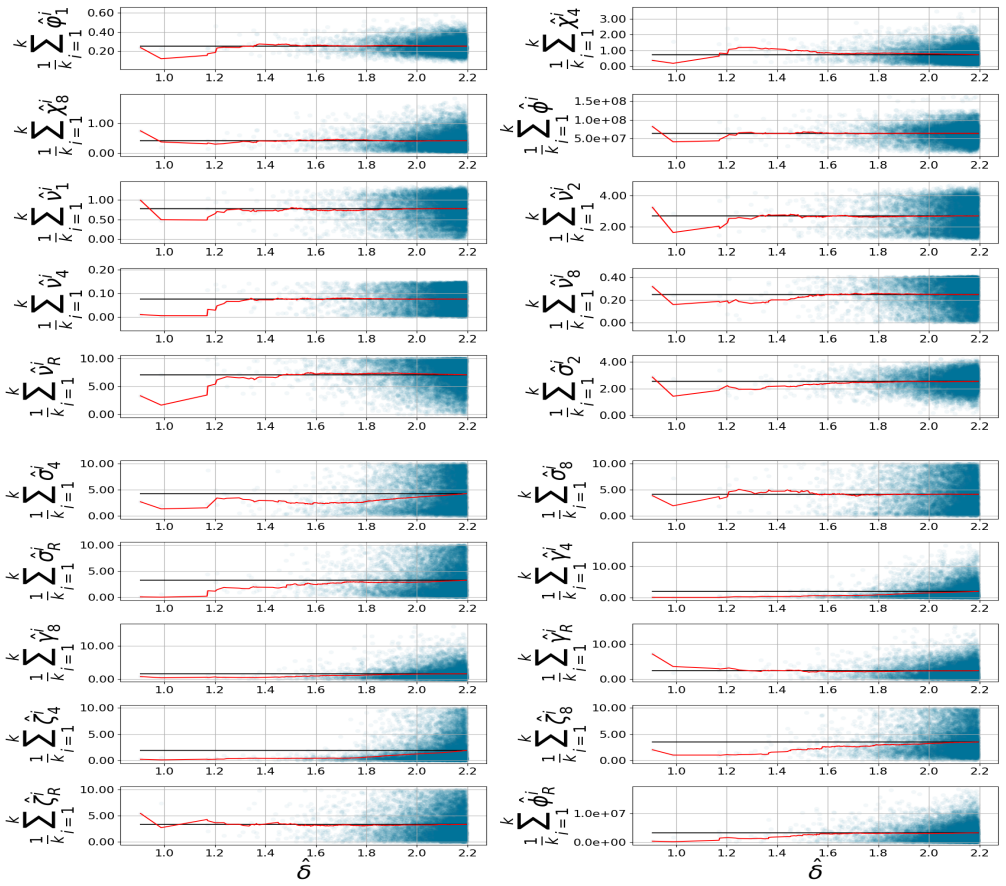

Figure 5.19: The blue dots show the accepted parameter as a function of the distance δ. The black line shows the mean of the accepted value for the given parameter. Denote a vector of the obtained ordered distances $\hat{\boldsymbol{\delta}} = (\delta_1, \delta_2, \ldots, \delta_n)$ $\delta_1 < \delta_2 < \ldots < \delta_n$ where $n = 10^4$. For each δ_k the red line shows the mean of the accepted parameter value $\left(\hat{\phi}^k, \hat{\varphi}_1^k, \hat{\chi}_4^k, \hat{\chi}_8^k, \hat{\nu}_1^k, \hat{\nu}_2^k, \hat{\nu}_R^k, \hat{\nu}_4^k, \hat{\nu}_8^k, \hat{\sigma}_2^k, \hat{\sigma}_R^k, \hat{\sigma}_4^k, \hat{\sigma}_8^k, \hat{\zeta}_4^k, \hat{\zeta}_8^k, \hat{\zeta}_R^k, \hat{\gamma}_4^k, \hat{\gamma}_R^k, \hat{\gamma}_8^k, \hat{\phi}_R^k, \hat{\beta}_2^k, \hat{\beta}_4^k, \hat{\beta}_8^k\right)$ which gave the distance less or equal to δ_k.

Figure 5.20 represents the solution of Equation (5.7) for 100 randomly chosen sets of the parameters from the posterior distribution obtained by the ABC algorithm. As it was noted in Model 2, Model 3 predicts that the average cell count in each compartment is lower than the average experimental value.

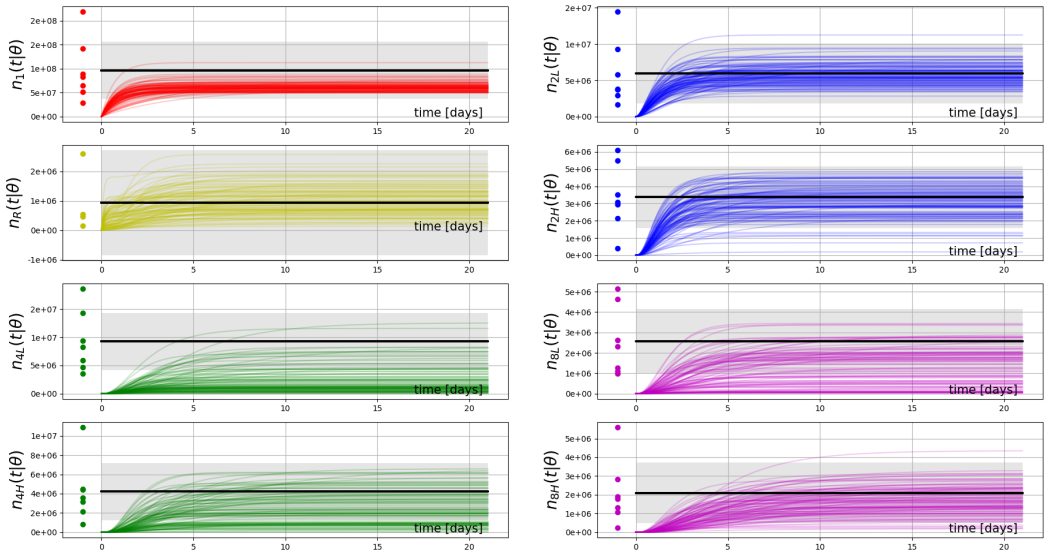

Figure 5.20: The solution of the ODE system given by Equation (5.7) for 100 randomly chosen sets of the parameters obtained by the ABC algorithm. The black line is the mean of the data. The grey area shows the 95% confidence interval of the data. The dots on the left hand side of the plots represent the data points.

The results of the ABC algorithm performed on Model 3 are reported in Table 5.5 except for the rates β_2, β_4 and β_8 which are shown in Table 5.6. Adding the regulatory T cell compartment to Model 3 changes the overall cell behaviour compared to Model 2. Model 3 parameterisation reveals that there are more cells coming into the SP CD4$^+$ compartment then into the SP CD8$^+$ from the post-DP population ($\chi_4 > \chi_8$). As there is an additional flux into the Treg compartment proportional to ϕ_R, there is more Treg cells at the SP CD4$^+$ stage. However most of the posterior distributions obtained from the ABC algorithm are similar to the prior distributions (see Figures 5.21-5.24).

	Mean	Median	95% CI	Minimum-maximum interval range
ϕ	6.35×10^7	6.50×10^7	$(1.87 \times 10^7, 1.03 \times 10^8)$	$(9.63 \times 10^6, 1.61 \times 10^8)$
φ_1	0.250	0.239	$(0.127, 0.394)$	$(0.083, 0.584)$
χ_4	0.726	0.627	$(0.056, 1.625)$	$(0.033, 3.500)$
χ_8	0.414	0.348	$(0.032, 0.970)$	$(0.032, 1.830)$
ν_1	0.777	0.821	$(0.181, 1.301)$	$(0.010, 1.360)$
ν_2	2.690	2.680	$(1.285, 4.078)$	$(1.150, 4.700)$
ν_4	0.076	0.076	$(0.007, 0.146)$	$(0.001, 0.148)$
ν_R	7.060	7.580	$(2.615, 9.999)$	$(0.006, 10.00)$
ν_8	0.246	0.264	$(0.042, 0.406)$	$(0.003, 0.406)$
σ_2	2.550	2.580	$(1.262, 3.743)$	$(0.102, 4.240)$
σ_4	4.240	3.740	$(0.019, 9.323)$	$(3.04 \times 10^{-4}, 10.00)$
σ_R	3.290	2.480	$(0.039, 8.836)$	$(0.001, 10.00)$
σ_8	4.120	3.740	$(0.068, 9.272)$	$(0.002, 10.00)$
γ_4	1.970	1.080	$(5.67 \times 10^{-4}, 6.924)$	$(5.66 \times 10^{-4}, 16.80)$
γ_R	2.390	1.860	$(1.77 \times 10^{-4}, 6.500)$	$(1.77 \times 10^{-4}, 15.10)$
γ_8	1.580	0.928	$(1.09 \times 10^{-5}, 5.450)$	$(1.09 \times 10^{-5}, 16.00)$
ζ_4	1.900	0.960	$(2.45 \times 10^{-4}, 7.217)$	$(2.45 \times 10^{-4}, 9.990)$
ζ_R	3.340	2.760	$(2.86 \times 10^{-4}, 8.430)$	$(2.85 \times 10^{-4}, 10.00)$
ζ_8	3.520	2.780	$(0.204, 8.881)$	$(4.62 \times 10^{-4}, 10.00)$
ϕ_R	3.26×10^6	2.5×10^6	$(3.85 \times 10^2, 8.91 \times 10^6)$	$(385, 1.85 \times 10^7)$

Table 5.5: Means, medians, 95% credible intervals and minimum-maximum intervals of the parameters in Model 3. ϕ and ϕ_R are in units *cells per day* whereas the rest of the parameters in the table are in units day^{-1}.

There is some learning about the flux rate into Treg compartment ϕ_R, and the differentiation rates from post-DP to SP stage (χ_4 and χ_8) are shifted to the right (see Figure 5.21). Bayesian parameter estimation has not revealed anything new compared to the prior beliefs for the death rates (see Figure 5.22). The distribution of the negative selection rate for SP thymocytes, σ_4 and σ_8 is shifted to the left compared with theirs priors (see Figure 5.23). This can be compared with the positive selection rates for SP cells, ζ_4 and ζ_8 (see Figure 5.24). It seems

like on average more cells are going through the negative selection at the SP stage than through positive selection. Nevertheless, a death due to high TCR signal, is more likely than a positive selection event or exit to the periphery for the Treg population (on average $\zeta_R < \nu_R$).

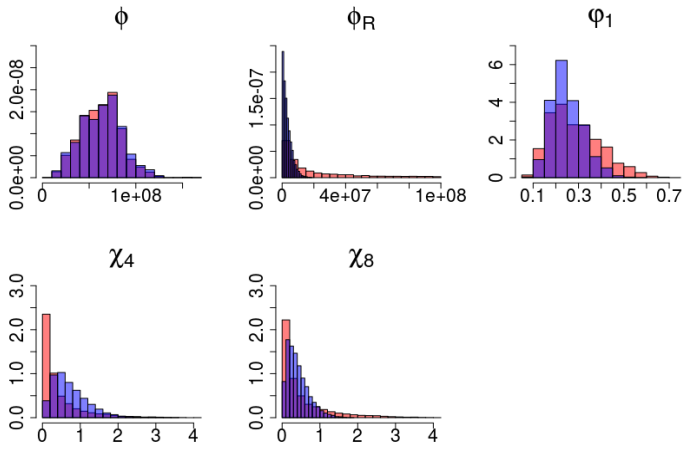

Figure 5.21: The prior distributions (in red) versus the posterior distributions (in blue) generated by the ABC algorithm for Model 3 for the parameters $\phi, \phi_R, \varphi_1\chi_4$, and χ_8.

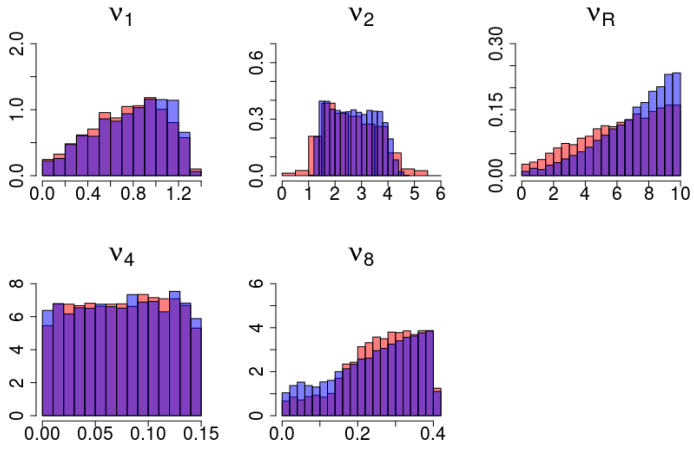

Figure 5.22: The prior distributions (in red) versus the posterior distributions (in blue) generated by the ABC algorithm for Model 3 for the parameters $\nu_1, \nu_2, \nu_R, \nu_4$ and ν_8.

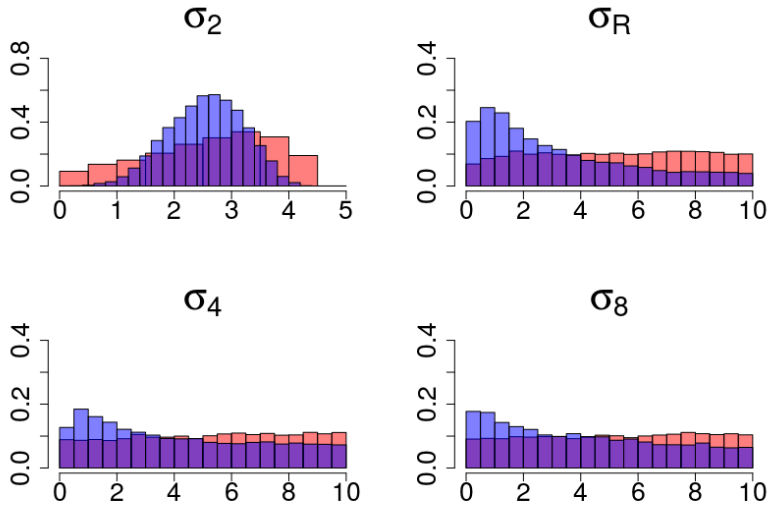

Figure 5.23: The prior distributions (in red) versus the posterior distributions (in blue) generated by the ABC algorithm for Model 3 for the parameters $\sigma_2, \sigma_R, \sigma_4$ and σ_8.

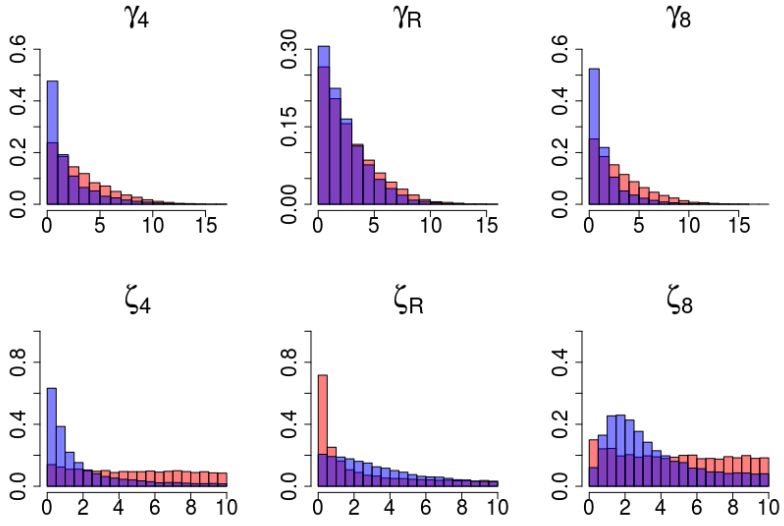

Figure 5.24: The prior distributions (in red) versus the posterior distributions (in blue) generated by the ABC algorithm for Model 3 for the parameters $\gamma_4, \gamma_R, \gamma_8, \zeta_4, \zeta_R$ and ζ_8.

The results for the recovery rates β_2, β_4 and β_8 need to be interpreted separately due to their prior distribution (see Algorithm 13). The prior and the posterior distributions of these rates are plotted in Figure 5.25. β_2, as can be seen in Figure 5.25, is not likely to be close to 0, indicating that at this post-DP stage, there is a non-zero probability of being rescued from the high TCR signal compartment to the low TCR signal compartment. As for the rescuing of thymocytes at the SP stage ($CD4^+$ and $CD8^+$) the answer is ambiguous. The probability that $\beta_4 = 0$ is equal to 0.62 whereas the probability that $\beta_8 = 0$ is equal to 0.32 based on the posterior sample (see Table 5.6). Hence, it is more likely that thymocytes are going to be rescued (from high TCR to low TCR) at the SP $CD8^+$ stage than the $CD4^+$ stage.

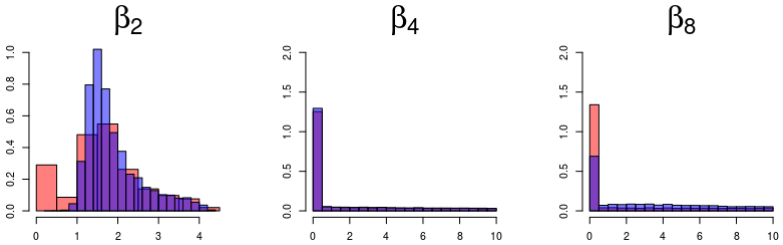

Figure 5.25: The prior distributions (in red) versus the posterior distributions (in blue) generated by the ABC algorithm for Model 3 for the parameters β_2, β_4 and β_8.

	$Prob(\beta_i = 0)$	mean of β_i for $\beta_i \neq 0$	median of β_i for $\beta_i \neq 0$	95% CI for $\beta_i \neq 0$
β_2	0.00	1.890	1.680	$(0.979, 3.516)$
β_4	0.62	4.489	4.215	$(6.52 \times 10^{-5}, 9.364)$
β_8	0.32	4.688	4.434	$(0.355, 9.622)$

Table 5.6: Means, medians and credible intervals for β_2, β_4 and β_8 obtained by the ABC algorithm performed on Model 3. β_i are in units day^{-1} for $i \in \{2, 4, 8\}$.

One can study the relationship between the parameters and the steady state values as it was done for Models 1 and 2. There are three relationships worth noticing, which are plotted in Figure 5.26.

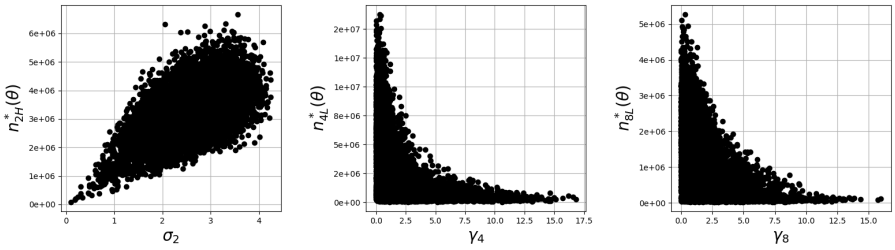

Figure 5.26: The relationship plots between the accepted parameters and the steady state values obtained from the ABC algorithm performed on Model 3.

The first plot from the left shows a positive relation between the negative selection rate σ_2 and the number of cells in the n_{2H} compartment. It is clear that higher σ_2 leads to a higher number of thymocytes receiving a strong TCR signal. The other two are not so obvious as they suggest that a higher proliferation rate at the SP stage for those thymocytes that have received a low TCR signal, results in a lower number of cells in the SP stage. To investigate this feature the scatter plots for γ_i were plotted against χ_i, σ_i and ζ_i for $i \in \{4, 8\}$ in Figure 5.27.

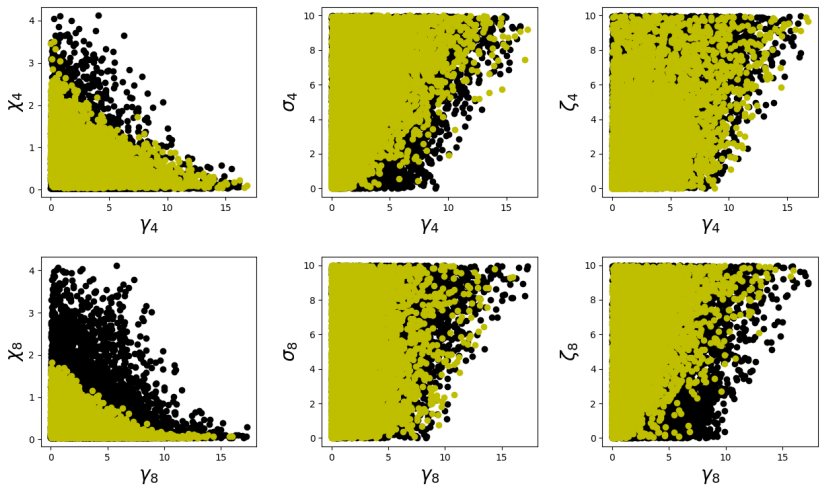

Figure 5.27: The relevant scatter plots obtained from the ABC algorithm performed on Model 3. The black dots represent the values from the prior distribution whereas the overlapping yellow dots represent the values from the posterior distribution.

The plots suggest that by increasing the proliferation in one of those two SP compartments the positive selection rate χ_i is decreasing, whereas the exit rates σ_i and ζ_i increase. It means that if more cells are proliferating at the SP stage, then more are leaving this stage and less are allowed to differentiate from the post-DP stage into the SP stage.

5.5.4 Comparison of the differentiation and the proliferation rates

The estimated posterior distributions are very similar to their prior distributions for the death rates regardless of the model used (see Figures 5.7, 5.14 and 5.22). It indicates that there is nothing new one can learn about the death rates from the data on top of the prior beliefs. However, Bayesian computation reveals some more information about the differentiation rates in all models, especially about φ_1 and φ_2 (see Figures 5.7 and 5.13). Hence the data may suggest how many cells go through the differentiation process in each compartment. These quantities are compared between the models in Table 5.7.

	pre-DP to post-DP	post-DP to SP	SP to the periphery
Model 1	$\varphi_1 n_1^*$	$\varphi_2 n_2^*$	$\varphi_3 n_3^*$
mean	28.61	5.91	6.60
95% CI	$(7.04, 51.96)$	$(1.93, 10.36)$	$(2.29, 10.00)$
Model 2	$\varphi_1 n_1^*$	$(\varphi_4 + \varphi_8) n_2^*$	$\xi_4 n_4^* + \xi_8 n_8^*$
mean	21.22	7.49	8.08
95% CI	$(7.30, 35.68)$	$(4.19, 10.61)$	$(5.13, 10.00)$
Model 3	$\varphi_1 n_1^*$	$(\chi_4 + \chi_8) n_{2L}^*$	$\zeta_4 n_{4L}^* + \zeta_8 n_{8L}^*$
mean	19.20	8.32	6.92
95% CI	$(2.50, 42.94)$	$(0.75, 20.74)$	$(0.25, 16.69)$

Table 5.7: Number of cells that go through differentiation for Model 1, Model 2 and Model 3, where $n_1^*, n_2^*, n_3^*, n_4^*, n_8^*, n_{2L}^*, n_{4L}^*$ and n_{8L}^* are found from Equations (5.2), (5.5) and (5.8) using the parameters obtained from the prior distributions found by the ABC algorithm. All values are given in units $10^6 cells\ per\ day$.

The estimated number of cells differentiate from the pre-DP to the post-DP stage goes down with each model, that is Model 3 predicts approximately one third less cells entering the post-DP stage in comparison to Model 1. This result is mainly due to fact that the flux into the thymus (with rate ϕ) is lowest and the death rate in the first compartment (ν_1) is the highest for Model 3. The differentiation from the post-DP to the SP stage have the opposite behaviour, that is Model 3 predicts the highest number of cells going into the SP stage (5.30×10^6 *cells per day* expressing CD4 and 3.02×10^6 *cells per day* expressing CD8). Model 2 estimates similar numbers but with more thymocytes expressing CD8 (4.14×10^6 *cells per day*) than CD4 (3.35×10^6 *cells per day*). However, published work by Sinclair *et al.* (2013) suggests that the number of thymocytes go into the SP stage is lower for those expressing CD8 when compare to CD4. This agrees with what has been found in Model 3. Model 2 predicts a higher number of cells leaving the thymus than Model 1, which means Model 1 has a more strict differentiation process as there are more cells going into the thymus for Model 1 than for Model 2. Model 3 reveals additionally that per day 5.64×10^6 SP CD4$^+$ thymocytes have received a high TCR signal (n_{4H} population) and have become Treg cells ($\sigma_R n^*_{4H}$, where n^*_{4H} defined by Equation (5.8)).

The Bayesian methods presented in this Chapter have helped to learn more about the proliferation rates, especially λ_3 in Model 1 and λ_4, λ_8 in Model 2 (see Figures 5.8 and 5.13). Model 3 with the data did not change much the prior beliefs about the proliferation rates (see Figure 5.24). Nevertheless the numbers of proliferating cells in the medulla are compared between the models. These results are given in Table 5.8. The results of the Bayesian inference for Model 2 indicate that there are 1.9×10^6 cells per day proliferating on average at the SP stage. This agrees with numbers of proliferating cells estimated by Thomas-Vaslin *et al.* (2008) (1.8×10^6 cells per day). The Bayesian inference did not introduced any new information about proliferation rates in Model 3, γ_4 and γ_8, on top of prior beliefs (see Figure 5.24), and therefore one can not truly learn anything new about number of proliferating cells per day at the SP stage.

	SP	SP CD4$^+$	SP CD8$^+$
Model 1	$\lambda_3 n_3^*$	-	-
mean	2.47	-	-
95% CI	$(0.00, 6.42)$	-	-
Model 2	$\lambda_4 n_4^* + \lambda_8 n_8^*$	$\lambda_4 n_4^*$	$\lambda_8 n_8^*$
mean	1.90	1.28	0.62
95% CI	$(0.08, 4.46)$	$(0.00, 3.56)$	$(0.00, 1.50)$
Model 3	$\gamma_4 n_{4L}^* + \gamma_8 n_{8L}^*$	$\gamma_4 n_{4L}^*$	$\gamma_8 n_{8L}^*$
mean	5.03	3.42	1.61
95% CI	$(0.03, 14.44)$	$(0.00, 11.45)$	$(0.00, 5.50)$

Table 5.8: Number of proliferating cells at the SP stage for Model 1, Model 2 and Model 3, where $n_3^*, n_4^*, n_8^*, n_{4L}^*$ and n_{8L}^* are given by Equations (5.2), (5.5) and (5.8) using the posterior parameters obtained making use of the ABC algorithm. All values are given in units $10^6 cells\ per\ day$.

Model 1 with the data provide the estimated posterior distribution for the number of cells coming into the thymus into the pre-DP stage (ϕ) which differs greatly from its prior. The distribution of ϕ does not change for Model 2 and Model 3 as it is calibrated well enough by Model 1. The exit rates from the thymus are calibrated well for each model (see Figures 5.7, 5.14 and 5.24). Model 3 with the data provide new information about the distribution of ϕ_R (the flux to the Treg compartment from the periphery) on top of prior beliefs (see Figure 5.21). Taking all of that into consideration one may compare the stringency of the thymic selection between the three models considered (see in Table 5.9). The three models indicate that about 85%-90% of thymocytes die through thymic selection. These results agree with previous estimations by Klein *et al.* (2014).

	Model 1	Model 2	Model 3
the stringency	$\frac{\varphi_3 n_3}{\phi}$	$\frac{\xi_4 n_4 + \xi_8 n_8}{\phi}$	$\frac{\zeta_4 n_{4L} + \zeta_8 n_{8L}}{\phi}$
mean	0.10	0.15	0.11
95% CI	$(0.01, 0.21)$	$(0.04, 0.30)$	$(0.01, 0.25)$

Table 5.9: Stringency of thymic selection

As the posterior distributions for the proliferation and the exit rates in Model 1 and Model 2 differ from their prior distributions one may say that the models with the data can provide information about the probability to proliferate and the probability to exit the thymus. The probability to proliferate (p_3) in the medulla and the probability to exit the thymus (q_4) for Model 1 are defined as follows,

$$p_3 = \frac{\lambda_3}{\lambda_3 + \mu_3 + \varphi_3}, \quad q_3 = \frac{\varphi_3}{\lambda_3 + \mu_3 + \varphi_3}. \tag{5.12}$$

Similarly one can find the probability to proliferate at the SP CD4$^+$ stage (p_4) or at the SP CD8$^+$ stage (p_8) and the probability to exit the thymus as a mature CD4 thymocyte (q_4) or as a mature CD8 thymocyte (q_8) in Model 2 from the following equations,

$$\begin{aligned} p_4 &= \frac{\lambda_4}{\lambda_4 + \mu_4 + \varphi_4}, \quad p_8 = \frac{\lambda_8}{\lambda_8 + \mu_8 + \varphi_8}, \\ q_4 &= \frac{\xi_4}{\lambda_4 + \mu_4 + \xi_4}, \quad q_8 = \frac{\xi_8}{\lambda_8 + \mu_8 + \xi_8}. \end{aligned} \tag{5.13}$$

The results of the Bayesian parameterisation performed on Model 3 reveal some information about the selection of thymocytes in the cortex and the medulla. Hence one can find the probability of negative selection at the post-DP stage (h_2) or the probability to rescue thymocytes which have received a strong TCR signal (r_2). It is also worth to study the probability of positive selection of thymocytes that have received a strong TCR signal into Treg cells (h_R) as the posterior distribution for σ_R brings some new information compared to its prior. Those two probabilities are defined by the following equations,

$$h_2 = \frac{\sigma_2}{\sigma_2 + \chi_4 + \chi_8}, \quad h_R = \frac{\sigma_R}{\sigma_R + \beta_4 + \nu_4}. \tag{5.14}$$

One of the main reasons to introduce Model 3 was to consider the possibility of rescuing thymocytes which have received a strong TCR signal. Therefore the probability to be rescued at the SP CD4$^+$ stage (r_4) and at the SP CD8$^+$ stage (r_8) have been studied. Those probabilities are defined as follows

$$r_2 = \frac{\beta_2}{\beta_2 + \nu_2}, \quad r_4 = \frac{\beta_4}{\beta_4 + \sigma_R + \nu_4}, \quad r_8 = \frac{\beta_8}{\beta_8 + \nu_8}. \tag{5.15}$$

The results for all probabilities defined in this section are given in Table 5.10.

	mean	95% CI
p_3	0.21	(0.00, 0.40)
p_4	0.19	(0.00, 0.38)
p_8	0.12	(0.00, 0.31)
q_3	0.62	(0.36, 0.93)
q_4	0.67	(0.44, 0.93)
q_8	0.75	(0.46, 0.98)
h_2	0.69	(0.46,0.91)
h_R for $\beta_4 > 0$	0.46	(0.03, 0.91)
h_R for $\beta_4 = 0$	0.94	(0.77 1.00)
r_2 for $\beta_2 > 0$	0.42	(0.21,0.72)
r_4 for $\beta_4 > 0$	0.53	(0.08, 0.96)
r_8 for $\beta_4 > 0$	0.92	(0.72, 1.00)

Table 5.10: Means with 95% credible intervals for the probabilities defined by Equations (5.12), (5.13), (5.14), (5.15). Note that the results for h_R are given in two cases, assuming that the transition from n_{4H} to n_{4L} is possible ($\beta_4 > 0$) or not ($\beta_4 = 0$). The probabilities r_2, r_4 and r_8 are equal to zero for $\beta_2 = 0, \beta_4 = 0, \beta_8 = 0$, respectively.

5.6 Discussion

There were three deterministic models introduced to study thymocyte development in the thymus. The first model, called Model 1, is the simplest version but the steady state given by Equation (5.2), for 100 randomly chosen sets of parameters obtained by the Bayesian inference, is reached within first 21 days and it is close to the average of the data (see Figure 5.6). Model 2 was studied to understand how the split between SP CD4$^+$ and SP CD8$^+$ thymocytes takes place. The last model, called Model 3, was analysed to check if it is plausible for cells which have received a high TCR signal to be rescued and for the ones to have received a low TCR signal to go through positive selection. The Bayesian inference has helped to learn only about some of the parameters of Model 3 in

comparison to Model 1 and Model 2. It is mainly caused by including the Treg population, which was not part of Model 1 or Model 2. Hence, Model 3 could be calibrated better if one has more information regarding the rates connected with the Treg compartment. Nevertheless Model 3 is worth studying to reveal some information regarding the rescue rates β_i for $i \in \{2, 4, 8\}$.

According to the analysis performed in Subsection 5.5.4 the probability to exit the medulla (for Model 1) is around three times higher than the probability to proliferate (see Table 5.10). A similar ratio can be observed for the thymocytes at the SP CD4$^+$ stage in Model 2. It is even more probable that the cell at the SP CD8$^+$ stage will exit rate than proliferate in Model 2. It would suggests that once a thymocyte commits to become an SP CD8 cell, it would leave the thymus to the periphery rather than stay and proliferate.

The possibility of thymocyte rescue from apoptotic death due a a strong TCR signal has been studied in Model 3. The probability of such rescue at the post-DP stage is 0.42, with a wide credible interval (see Table 5.10). On the other hand, the analysis reveals that on average there is 69% chance that a thymocyte, which receives low TCR signal at the post-DP stage, starts receiving high TCR signal.

The probability of being rescued from the high TCR signal compartment to the low TCR compartment is equal to 0.62 for the SP CD4$^+$ stage and 0.32 for the SP CD8$^+$ stage. Hence, it is more likely that thymocytes are going to be rescued (from high TCR to low TCR) at the SP CD8$^+$ stage than at the SP CD4$^+$ stage. Interestingly, assuming that this rescue is possible ($\beta_4 \neq 0$ and $\beta_8 \neq 0$), the probability to start receiving low TCR signal instead of high TCR signal at the SP CD8$^+$ stage is much higher (0.92) then at the SP CD4$^+$ stage (0.53).

The last value to be analysed is the probability of positive selection of thymocytes that have received a strong TCR signal into Treg cells (h_R). The result of the Bayesian inference of Model 3 indicate that thymocytes that have received a strong TCR signal can be positively selected into Treg cells with probability 0.94, assuming that $\beta_4 = 0$. It is not so clear for opposite case when $\beta_4 \neq 0$ as the credible interval for h_R covers almost whole unit interval.

Chapter 6

Concluding remarks

The binding and trafficking models for VEGFR/VEGF-A systems have been extensively studied previously by Mac Gabhann & Popel (2004), Mac Gabhann & Popel (2005), Mac Gabhann *et al.* (2005), Alarcón & Page (2007), Tan *et al.* (2013c), Tan *et al.* (2013b) and many others. Assumptions for the cell surface models presented in this thesis are similar to the published ones but have not been explored before in this configuration. The binding and trafficking models are studied here with use of some experimental data obtained thanks to Dr Sreenivasan Ponnambalam from School of Molecular and Cellular Biology at University of Leeds.

In Chapter 3 I focus on the cell surface only to analyse different ways of signalling through VEGFR2 phosphorylation. The IP R_2 model in Subsection 3.1.1 and the DP R_2 model in Subsection 3.1.2 consist of processes where ligand VEGF-A binds receptor VEGFR2 in order to form monomers and dimers, which can eventually dissociate. Dimers become instantaneously phosphorylated in the IP R_2 model, while in the DP R_2 model phosphorylation is considered as a new reaction in the process. The IP R_1/R_2 model, from Subsection 3.1.3, and the DP R_1/R_2 model, from Subsection 3.1.4, are extensions of the IP R_2 and the DP R_2 models respectively, where two types of receptor are considered, VEGFR1 and VEGFR2. These different stochastic models help to analyse how varying the initial number of ligand, n_L, or how the competition for ligand (in the IP R_1/R_2 and the DP R_1/R_2 models) by two receptors, can affect number of phosphorylated dimers, which is a key determinant in endothelial cell signalling.

6. CONCLUDING REMARKS

It is shown in Subsection 3.3.3 that high ligand stimulation can actually lead to lower number of phosphorylated dimers. To be precise, high ligand stimulation can cause that there are lots of receptors occupied by ligands, as bound monomers, and there are not enough free receptors to create bound dimers with these monomers. This important discovery lead to the conclusion that the binding process for VEGFR receptors should be analysed in two steps, formation of monomers and then dimers, to peak up this behaviour. Many previously published models were studied assuming dimer formation as one step process (see Mac Gabhann & Popel (2004), Mac Gabhann *et al.* (2005), Mac Gabhann & Popel (2007), Mac Gabhann & Popel (2005), Tan *et al.* (2013a), Tan *et al.* (2013b) Tan *et al.* (2013c)). This type of model can overestimate the number of phosphorylated dimers for higher ligand concentration (see Mac Gabhann & Popel (2007)) so it is important to consider two step dimerisation process.

As it should be expected the number of phosphorylated VEGFR2 dimers decrease by including two receptors in the model. However total number of phosphorylated dimers, homodimers and heterodimers, is higher for the IP R_1/R_2 and the DP R_1/R_2 models compared to the IP R_2 and the DP R_2 models respectively. Although, it is important to mention that phosphorylation of homodimers and heterodimers can lead to different signalling outcomes (see Cudmore *et al.* (2012) and Simons *et al.* (2016)).

The phosphorylation is also included as a separate reaction in the DP R_2 and the DP R_1/R_2 model to explore how does it change receptors phosphorylation. This extension shows quantitative change of the number phosphorylated dimers, that is approximately 20% decrease for the number of VEGFR2 homodimers in the DP R_2 model with respect to the IP R_2 model for small ligand concentrations $c_L \in \{1pM\,,\, 2.5pM,\, 5pM\}$ and approximately 16% for higher ligand concentrations. However, the dynamics of the processes is not qualitatively changed.

In the IP R_2 and the DP R_2 models, matrix-analytic techniques have been applied in order to study the time until reaching a threshold of phosphorylated VEGFR2 dimers on the cell membrane, and the steady-state distribution of the corresponding CTMPs. Moreover, the construction of the DP R_2 as an extension of the IP R_2 permits, not only to analyse the role played by the phosphorylation reaction, but also to show how different reactions may be incorporated while

adapting the matrix-analytic approach. The analysis of the results shows again that including phosphorylation as a separate reaction seems to quantitatively affect the timescale for signal formation, but does not qualitatively change the dynamics of the processes. The additional study demonstrates that ligands tend to form signal (here dimer phosphorylation) with probability near one, where the phosphorylation/de-phosphorylation reactions can only cause a delay on this occurring.

In Section 3.5 it is shown how to exploit the Markovian nature of the stochastic process under study in order to analyse a number of characteristics of interest in the process. I analyse in this section different hypotheses of signal creation, such as the number of bound dimers (**DS**), the accumulated number of bound dimers (**AS**) and the accumulated number of bound dimers with delay λ (**ASD-λ**). These three hypotheses are compared in Subsection 3.5.4 by analysing the time to reach a signalling threshold. The process under the **ASD-λ** hypothesis is an intermediate regime between the **DS** and the **AS** case, for moderate values of the rate λ. The results suggest that the initial concentration of ligand would play a more important role if cellular mechanisms led to low signal decay rates. For higher values of the decay signal λ, the signalling threshold S is reached slowly independent of the ligand concentration. Additional analysis of the impact of the different kinetic rates in the descriptor indicates that the monomer formation rate α_+ is the most important rate regardless of the hypothesis under consideration.

It is important to emphasise that any particular tyrosine residue has not been specified in the models described in Chapter 3. In future models different phosphorylation kinases could be studied which may or may not be phosphorylated symmetrically.

From a biological perspective, it should be noted that the total number of VEGFR2s per cell varies according to Ewan *et al.* (2006b) and Napione *et al.* (2012) and could be larger than the numbers used in this thesis (see Imoukhuede & Popel (2012)). A larger number of VEGFR2 receptors on the cell surface would, however, only quantitatively change the results, and in particular a higher optimum ligand concentration threshold would be reported. The sensitivity analysis carried out for the descriptors enables one to show how the monomeric formation rate, α_+, plays a crucial role in these models, with an effect which can be more

than twice the effect of any other rate for some of the descriptors considered in this thesis. Finally, the numerical results presented in Chapter 3 for the VEGF-A and VEGFR system have allowed quantifying the effect of different ligand concentrations on the timescales to signalling, the late time behaviour of the system and the time course dynamics of the individual molecular species. Increasing ligand concentration decreases the times to reach any signalling threshold and increases the maximum potential signalling thresholds to be reached. However, high ligand concentrations can result in saturated scenarios, where the phosphorylation of bound dimers is reduced and monomeric bound complexes are enhanced. The approach presented here could be, in principle, applied to other RTKs, most notably the epidermal growth factor receptor (EGFR), which is over-expressed in a variety of epithelial tumours. This receptor is of special relevance in clinical oncology, since a series of promising anti-EGFR small-molecule tyrosine kinase inhibitors have already been designed. Unfortunately, treatment resistance emerges over time and it is important to understand the molecular mechanisms that underlie the development of treatment resistance (see Wheeler *et al.* (2010)). Other RTKs of interest, for example, are those of the fibroblast growth factor receptor family, insulin receptor family and the leukocyte receptor tyrosine kinase family.

The main aim of Chapter 4 is to show how mathematical modelling can bring some more insights into the studies of vascular system by using data generated by experimental researchers. In Chapter 4 the models including binding and trafficking are studied. The parameters of the models in this chapter are calibrated by using the experimental data after performing careful global sensitivity analyses. There are two mechanisms studied in this chapter, in Section 4.1 I study how the signalling (here phosphorylation) of ERK is triggered and in Section 4.2 I study how the transport of receptors from Golgi to cell surface is perturbed upon ligand stimulation. In the both sections I hypothesise that the localisation of phosphorylated dimers can have impact on these mechanisms.

The model studied in Section 4.1, called Model 1, considers only one receptor type, VEGFR2, and two type of ligands, VEGF-A_{165} and VEGF-A_{121}. The analysis of Model 1 in Subsection 4.1.2, describing binding and trafficking of VEGFR2 upon ligand stimulation, stays with the agreement of the outcomes of the experiment published by Fearnley *et al.* (2014), that is VEGF-A_{165} is better

VEGFR phosphorylation prompter than VEGF-A_{121}. It is also shown in this subsection that turnover of VEGF-A_{121} bound monomers and dimers is faster than molecules bound with VEGF-A_{165}. There are also more degraded receptors if the cell is stimulated with VEGF-A_{121} then by VEGF-A_{165}. Additionally on average there is twice as many degraded receptors once the cell is stimulated with VEGF-A comparing to non-stimulated which stays in the agreement with results shown by Smith *et al.* (2017). Moreover the order of internalisation rates of bound dimers agrees with results published by Tan *et al.* (2013c) using the experimental data from Lamalice *et al.* (2007), Chabot *et al.* (2009), Bruns *et al.* (2010) and Zhang *et al.* (2010).

Analysis of Model 2, which is an extension of Model 1, includes description of ERK signalling. Results from Subsection 4.1.3 suggest that the ERK phosphorylation is most likely triggered by the phosphorylated dimers in the endosome, rather than on the cell surface. This important result could be potentially tested by blocking internalisation to measure and compare level of ERK phosphorylation. Additionally the result for ERK de-phosphorylation rate agrees with the value published by Schoeberl *et al.* (2002).

Model 2 describes the internal signalling cascade by the ordinary equation with delay, which take into account all events involved in that cascade. This simplification omits all internal molecules involved in triggering ERK phosphorylation. Therefore one can only learn about level of delay involved in that process. To study the whole cascade a new model such as that proposed by Tan *et al.* (2013c) should be used. On the other hand parametrisation of Model 2 is easier to handle because of simplification of internal signalling cascade.

It would be beneficial to test the current model with one more isoform (VEGF-A_{145}) as there are data available. Additionally in future one could develop a model which includes events involved in VCAM-1 gene regulation, which was extensively studied by Fearnley *et al.* (2014). VCAM-1 expression controls endothelial leukocyte-interactions and it is regulated by VEGF-A stimulation and through ERK activation. Different VEGF-A isoforms play different roles in regulation of many gene expression (see Ferrara *et al.* (2003)).

The model studied in Section 4.2, called Model 3, considers two receptor types, VEGFR1 and VEGFR2, and one type of ligand VEGF-A_{165}. Model 3 is built to

study how the transport rate of free receptors from the Golgi to the cell surface can be perturbed by ligand stimulation. This process has not been studied in detail yet and there are no experimental results suggesting a way of transport perturbation. The analyses performed in Subsection 4.2.6 indicates that the rate is inhibited by ligand stimulation (which is in contradiction with common belief, hence case D was chosen to be explored in detail together with case A regardless low relative probability being obtained). Moreover one cannot learn about the character of perturbation of VEGFR2, that is results for case A and B or case C and D are very similar. It is also shown that it is more likely that the transport from Golgi to the surface is triggered by the phosphorylated VEGFR2 homodimers on the cell surface. It is noted here that additional hypotheses, that the heterodimers can be involved in this process, was studied with the same outcome.

The binding rates in Model 2 and Model 3 are computed by following the argument proposed by Lauffenburger & Linderman (1996). The binding rates could have been estimated using Bayesian inference instead in future. New experiments measuring levels of receptors in internal compartments (endosome and Golgi) could bring more information about trafficking rates and perturbation rate ω_1 and ω_2. More data could also help in supporting or rejecting inhibition hypotheses. One could also design an experiment to validate Model 3 by following individual receptors in some part of the cell as shown by Pryor *et al.* (2013).

Future work for Model 3 could also use the MCMC algorithm for parameters inference instead of ABC algorithm. It was shown for Model 2 that the MCMC approach leads to more robust results as one does not have to rely on choosing appropriate distance measure.

To summarise models from Chapter 3 can be used as good description of short time binding and cell surface phosphorylation events as for longer time behaviour ($\geq$ 15 min) internalisation and recycling should be taken into consideration. Model 1 from Section 4.1.2 describes binding and trafficking events without using high level of complexity. The phosphorylated dimers peak is however to be found earlier then at 5 minutes (as suggested by the data). This observation could be tested by performing experiment which could measure the level of phosphorylation at time point earlier then 5 minutes. Both Model 1 and

Model 2 would also benefit by introducing second receptor VEGFR1 or other co-receptors as Neuropilin which play important role in regulation of VEGFR activity. Some models with co-receptors were proposed by Mac Gabhann & Popel (2004) or Mac Gabhann & Popel (2005). As Model 3 is already complex (with many parameters to be estimated) one should decide about introducing any co-receptors after performing some analyses on extended Model 1 or Model 2 with co-receptors.

Some of the work presented in Chapter 3 are under second revision and soon should be published. Results gained from the analyses of Model 1 and Model 2 are under preparation to be published. Model 3 explores some interesting hypotheses and will be carefully studied in future. New experiments will be designed to prove or reject the hypothesis stating that the transport rate is inhibited upon ligand stimulation.

Chapter 5 is an extension of my MSc project describing T cell development in the thymus. The modelling in this chapter bring some more insights into the mechanism of thymocytes selection, indicating that it is possible for thymocytes receiving high TCR signal at the post-DP compartment in the cortex of the thymus, to avoid death fate by starting receiving intermediate (or low) signal which allow that thymocyte to be positively selected into the medulla. The similar scenario is not so clear at the SP CD4 and at the SP CD8 compartments in the medulla as probability of possible rescue is 0.62 and 0.32, respectively. This additional chapter contains Bayesian estimation methods for parameters under studied models and should be read separately.

As the data describe the steady state only in each compartment one should expect to learn only about the ratio of the parameters. As there is high variability between mice for thymocytes counts one could also consider normalisation of all data by the thymocytes counts in first compartment that is pre-DP n_1 (see Table 5.1). In future parameters in all three models, Model 1, Model 2 and Model 3, will be estimated using MCMC algorithm for the reasons explained before in receptor-ligand case. It would also be beneficial to gain more prior beliefs about some of the rates or at least residency times in each compartment (especially for Model 3).

References

Abate, J. & Whitt, W. (1992). Numerical inversion of probability generating functions. *Operations Research Letters*, **12**, 245–251. 91

Aird, W. (2007). Phenotypic heterogeneity of the endothelium i. structure, function, and mechanisms. *Circulation Research*, **100**, 158–173. 72

Alarcón, T. & Page, K. (2006). Stochastic models of receptor oligomerization by bivalent ligand. *Journal of The Royal Society Interface*, **3**, 545–559. 6, 39, 72, 83, 111

Alarcón, T. & Page, K. (2007). Mathematical models of the VEGF receptor and its role in cancer therapy. *Journal of The Royal Society Interface*, **4**, 283–304. 5, 47, 77, 259

Allen, L.J. (2003). *An introduction to stochastic processes with applications to biology*. Pearson Education New Jersey. 7, 11, 20, 23

Almqvist, N., Bhatia, R., Primbs, G., Desai, N., Banerjee, S. & Lal, R. (2004). Elasticity and adhesion force mapping reveals real-time clustering of growth factor receptors and associated changes in local cellular rheological properties. *Biophysical Journal*, **86**, 1753–1762. 53

Anderson, G., Lane, P.J. & Jenkinson, E.J. (2007). Generating intrathymic microenvironments to establish t-cell tolerance. *Nature Reviews Immunology*, **7**, 954–963. 209, 211

Anderson, S.M., Shergill, B., Barry, Z.T., Manousiouthakis, E., Chen, T.T., Botvinick, E., Platt, M.O., Iruela-Arispe, M.L. &

Segura, T. (2011). Vegf internalization is not required for vegfr-2 phosphorylation in bioengineered surfaces with covalently linked vegf. *Integrative biology*, **3**, 887–896. 140, 192

Andrieu, C., De Freitas, N., Doucet, A. & Jordan, M.I. (2003). An introduction to mcmc for machine learning. *Machine learning*, **50**, 5–43. 36

Ballmer-Hofer, K., Andersson, A.E., Ratcliffe, L.E. & Berger, P. (2011). Neuropilin-1 promotes vegfr-2 trafficking through rab11 vesicles thereby specifying signal output. *Blood*, **118**, 816–826. 130

Bao, L., Odell, A.F., Stephen, S.L., Wheatcroft, S.B., Walker, J.H. & Ponnambalam, S. (2012). The s100a6 calcium-binding protein regulates endothelial cell-cycle progression and senescence. *The FEBS journal*, **279**, 4576–4588. 175

Beaumont, M.A., Zhang, W. & Balding, D.J. (2002). Approximate bayesian computation in population genetics. *Genetics*, **162**, 2025–2035. 34

Berezhkovskii, A.M. & Szabo, A. (2013). Effect of ligand diffusion on occupancy fluctuations of cell-surface receptors. *The Journal of chemical physics*, **139**, 09B610_1. 51

Berg, H.C. & Purcell, E.M. (1977). Physics of chemoreception. *Biophysical journal*, **20**, 193–219. 51

Boys, R.J., Wilkinson, D.J. & Kirkwood, T.B. (2008). Bayesian inference for a discretely observed stochastic kinetic model. *Statistics and Computing*, **18**, 125–135. 34

Bruns, A., Herbert, S., Odell, A., Jopling, H., Hooper, N., Zachary, I., Walker, J. & Ponnambalam, S. (2010). Ligand-stimulated vegfr2 signaling is regulated by co-ordinated trafficking and proteolysis. *Traffic*, **11**, 161–174. 197, 263

Campolongo, F. & Cariboni, J. (2007). Sensitivity analysis: how to detect important factors in large models. *Institute for the Protection and Security of the Citizen*. 31

Casaletto, J. & McClatchey, A. (2012). Spatial regulation of receptor tyrosine kinases in development and cancer. *Nature Reviews Cancer*, **12**, 387–400. 47, 73

Caswell, H. (2011). Perturbation analysis of continuous-time absorbing markov chains. *Numerical Linear Algebra with Applications*, **18**, 901–917. 82, 99, 118

Chabot, C., Spring, K., Gratton, J.P., Elchebly, M. & Royal, I. (2009). New role for the protein tyrosine phosphatase dep-1 in akt activation and endothelial cell survival. *Molecular and cellular biology*, **29**, 241–253. 263

Ciarlet, P., Miara, B. & Thomas, J. (1989). *Introduction to numerical linear algebra and optimisation*. Cambridge University Press. 116

Clapham, D.E. (2007). Calcium signaling. *Cell*, **131**, 1047–1058. 175

Cudmore, M.J., Hewett, P.W., Ahmad, S., Wang, K.Q., Cai, M., Al-Ani, B., Fujisawa, T., Ma, B., Sissaoui, S., Ramma, W. *et al.* (2012). The role of heterodimerization between vegfr-1 and vegfr-2 in the regulation of endothelial cell homeostasis. *Nature communications*, **3**, 972. 260

Currie, J., Castro, M., Lythe, G., Palmer, E. & Molina-París, C. (2012). A stochastic t cell response criterion. *Journal of The Royal Society Interface*, **9**, 2856–2870. 111

de Almodovar, C.R., Lambrechts, D., Mazzone, M. & Carmeliet, P. (2009). Role and therapeutic potential of vegf in the nervous system. *Physiological reviews*, **89**, 607–648. 1

Delcombel, R., Janssen, L., Vassy, R., Gammons, M., Haddad, O., Richard, B., Letourneur, D., Bates, D., Hendricks, C., Waltenberger, J. *et al.* (2013). New prospects in the roles of the c-terminal domains of vegf-a and their cooperation for ligand binding, cellular signaling and vessels formation. *Angiogenesis*, **16**, 353–371. 130, 135

DeLisi, C. (1980). The biophysics of ligand–receptor interactions. *Quarterly reviews of biophysics*, **13**, 201–230. 51

Di Nicola, M., Carlo-Stella, C., Magni, M., Milanesi, M., Longoni, P.D., Matteucci, P., Grisanti, S. & Gianni, A.M. (2002). Human bone marrow stromal cells suppress t-lymphocyte proliferation induced by cellular or nonspecific mitogenic stimuli. *Blood*, **99**, 3838–3843. 210

Egerton, M., Scollay, R. & Shortman, K. (1990). Kinetics of mature t-cell development in the thymus. *Proceedings of the National Academy of Sciences*, **87**, 2579–2582. 223, 225

Eigen, M. (1974). Diffusion control in biochemical reactions. In *Quantum statistical mechanics in the natural sciences*, 37–61, Springer. 51

Erickson, J., Goldstein, B., Holowka, D. & Baird, B. (1987). The effect of receptor density on the forward rate constant for binding of ligands to cell surface receptors. *Biophysical journal*, **52**, 657–662. 52

Ewan, L., Jopling, H., Jia, H., Mittar, S., Bagherzadeh, A., Howell, G., Walker, J., Zachary, I. & Ponnambalam, S. (2006a). Intrinsic tyrosine kinase activity is required for vascular endothelial growth factor receptor 2 ubiquitination, sorting and degradation in endothelial cells. *Traffic*, **7**, 1270–1282. 53, 77, 110

Ewan, L., Jopling, H., Jia, H., Mittar, S., Bagherzadeh, A., Howell, G., Walker, J., Zachary, I. & Ponnambalam, S. (2006b). Intrinsic tyrosine kinase activity is required for vascular endothelial growth factor receptor 2 ubiquitination, sorting and degradation in endothelial cells. *Traffic*, **7**, 1270–1282. 110, 261

Fearnley, G., Odell, A., Latham, A., Mughal, N., Bruns, A., Burgoyne, N., Homer-Vanniasinkam, S., Zachary, I., Hollstein, M., Wheatcroft, S. *et al.* (2014). Vegf-a isoforms differentially regulate atf-2–dependent vcam-1 gene expression and endothelial–leukocyte interactions. *Molecular biology of the cell*, **25**, 2509–2521. 130, 131, 147, 262, 263

Fearnley, G.W., Bruns, A.F., Wheatcroft, S.B. & Ponnambalam, S. (2015). Vegf-a isoform-specific regulation of calcium ion flux, transcriptional activation and endothelial cell migration. *Biology open*, **4**, 731–742. 130

Fearnley, G.W., Smith, G.A., Abdul-Zani, I., Yuldasheva, N., Mughal, N.A., Homer-Vanniasinkam, S., Kearney, M.T., Zachary, I.C., Tomlinson, D.C., Harrison, M.A. *et al.* (2016). Vegf-a isoforms program differential vegfr2 signal transduction, trafficking and proteolysis. *Biology open*, bio–017434. 130

Ferrara, N., Gerber, H.P. & LeCouter, J. (2003). The biology of vegf and its receptors. *Nature medicine*, **9**, 669–676. 263

Freedman, D.A. (2009). *Statistical models: theory and practice*. cambridge university press. 225

French, A.R., Tadaki, D.K., Niyogi, S.K. & Lauffenburger, D.A. (1995). Intracellular trafficking of epidermal growth factor family ligands is directly influenced by the ph sensitivity of the receptor/ligand interaction. *Journal of Biological Chemistry*, **270**, 4334–4340. 140

Germain, R.N. (2002). T-cell development and the cd4-cd8 lineage decision. *Nature reviews. Immunology*, **2**, 309. 19, 210

Gillespie, C. (2009a). Moment-closure approximations for mass-action models. *IET systems biology*, **3**, 52–58. 82

Gillespie, C.S. (2009b). Moment-closure approximations for mass-action models. *IET systems biology*, **3**, 52–58. 25

Gillespie, D. (1977). Exact stochastic simulation of coupled chemical reactions. *The Journal of Physical Chemistry*, **81**, 2340–2361. 7, 82

Gillespie, D.T. (1976). A general method for numerically simulating the stochastic time evolution of coupled chemical reactions. *Journal of computational physics*, **22**, 403–434. 30, 31, 40, 41

Gómez-Corral, A. & López García, M. (2012a). Extinction times and size of the surviving species in a two-species competition process. *Journal of Mathematical Biology*, **64**, 255–289. 40

Gómez-Corral, A. & López García, M. (2012b). On the number of births and deaths during an extinction cycle, and the survival of a certain individual in a competition process. *Computers & Mathematics with Applications*, **64**, 236–259. 40

Gourlaouen, M., Welti, J.C., Vasudev, N.S. & Reynolds, A.R. (2013). Essential role for endocytosis in the growth factor-stimulated activation of erk1/2 in endothelial cells. *Journal of Biological Chemistry*, **288**, 7467–7480. 8

Harper, S.J. & Bates, D.O. (2008). Vegf-a splicing: the key to anti-angiogenic therapeutics? *Nature reviews. Cancer*, **8**, 880. 2

He, Q. (2014). *Fundamentals of matrix-analytic methods*. Springer. 8, 20, 112

Hespanha, J. (2008a). Moment closure for biochemical networks. In *Communications, Control and Signal Processing, 2008. ISCCSP 2008. 3rd International Symposium on*, 142–147, IEEE. 7, 25, 26, 40, 41

Hespanha, J. (2008b). Moment closure for biochemical networks. In *Communications, Control and Signal Processing, 2008. ISCCSP 2008. 3rd International Symposium on*, 142–147, IEEE. 82

Homma, T. & Saltelli, A. (1996). Importance measures in global sensitivity analysis of nonlinear models. *Reliability Engineering & System Safety*, **52**, 1–17. 33

Imoukhuede, P. & Popel, A. (2011). Quantification and cell-to-cell variation of vascular endothelial growth factor receptors. *Experimental Cell Research*, **317**, 955–965. 47, 55

Imoukhuede, P. & Popel, A. (2012). Expression of VEGF receptors on endothelial cells in mouse skeletal muscle. *PloS ONE*, **7**, e44791. 47, 55, 72, 110, 261

Jameson, S.C., Hogquist, K.A. & Bevan, M.J. (1995). Positive selection of thymocytes. *Annual review of immunology*, **13**, 93–126. 210

Jopling, H., Odell, A., Hooper, N., Zachary, I., Walker, J. & Ponnambalam, S. (2009). Rab GTPase regulation of VEGFR2 trafficking and signaling in endothelial cells. *Arteriosclerosis, Thrombosis, and Vascular Biology*, **29**, 1119–1124. 8

Jopling, H., Howell, G., Gamper, N. & Ponnambalam, S. (2011). The vegfr2 receptor tyrosine kinase undergoes constitutive endosome-to-plasma membrane recycling. *Biochemical and biophysical research communications*, **410**, 170–176. 134, 178

Karihaloo, A., Karumanchi, S.A., Cantley, W.L., Venkatesha, S., Cantley, L.G. & Kale, S. (2005). Vascular endothelial growth factor induces branching morphogenesis/tubulogenesis in renal epithelial cells in a neuropilin-dependent fashion. *Molecular and Cellular Biology*, **25**, 7441–7448. 3

Keizer, J. (1985). Theory of rapid bimolecular reactions in solution and membranes. *Accounts of Chemical Research*, **18**, 235–241. 51

Keyt, B., Berleau, L., Nguyen, H., Chen, H., Heinsohn, H., Vandlen, R. & Ferrara, N. (1996). The carboxyl-terminal domain (111165) of vascular endothelial growth factor is critical for its mitogenic potency. *Journal of Biological Chemistry*, **271**, 7788–7795. 130

Klein, L., Kyewski, B., Allen, P.M. & Hogquist, K.A. (2014). Positive and negative selection of the t cell repertoire: what thymocytes see and don't see. *Nature reviews. Immunology*, **14**, 377. 255

Koch, S., van Meeteren, L., Morin, E., Testini, C., Weström, S., Björkelund, H., Le Jan, S., Adler, J., Berger, P. & Claesson-Welsh, L. (2014). NRP1 presented in trans to the endothelium arrests VEGFR2 endocytosis, preventing angiogenic signaling and tumor initiation. *Developmental Cell*, **28**, 633–646. 8

Kulkarni, V. (1996). *Modeling and analysis of stochastic systems*. Chapman & Hall Texts in Statistical Science Series, London. 7, 20, 41, 82, 112

Kut, C., Mac Gabhann, F. & Popel, A. (2007). Where is VEGF in the body? a meta-analysis of VEGF distribution in cancer. *British Journal of Cancer*, **97**, 978–985. 83

Lamalice, L., Le Boeuf, F. & Huot, J. (2007). Endothelial cell migration during angiogenesis. *Circulation research*, **100**, 782–794. 263

Lanahan, A., Hermans, K., Claes, F., Kerley-Hamilton, J., Zhuang, Z., Giordano, F., Carmeliet, P. & Simons, M. (2010). VEGF receptor 2 endocytic trafficking regulates arterial morphogenesis. *Developmental Cell*, **18**, 713–724. 8

Lanahan, A., Zhang, X., Fantin, A., Zhuang, Z., Rivera-Molina, F., Speichinger, K., Prahst, C., Zhang, J., Wang, Y., Davis, G. *et al.* (2013). The neuropilin 1 cytoplasmic domain is required for VEGF-A-dependent arteriogenesis. *Developmental Cell*, **25**, 156–168. 8

Lanahan, A., Lech, D., Dubrac, A., Zhang, J., Zhuang, Z., Eichmann, A. & Simons, M. (2014). PTP1b is a physiologic regulator of vascular endothelial growth factor signaling in endothelial cells. *Circulation*, **130**, 902–909. 8

Latouche, G. & Ramaswami, V. (1999). *Introduction to matrix analytic methods in stochastic modeling*. SIAM. 8, 20, 93

Laufer, T.M., DeKoning, J., Markowitz, J.S., Lo, D. & Glimcher, L.H. (1996). Unopposed positive selection and autoreactivity in mice expressing class ii mhc only on thymic cortex. *Nature*, **383**, 81. 211

Lauffenburger, D. & Linderman, J. (1993). *Receptors: models for binding, trafficking, and signaling*, vol. 365. Oxford University Press New York:. 7, 40, 52, 54, 72

Lauffenburger, D. & Linderman, J. (1996). *Receptors: models for binding, trafficking, and signaling*. Oxford University Press, USA. 51, 206, 264

Linda, J.A. (2007). An introduction to mathematical biology. 182

Linderman, J.J. & Lauffenburger, D.A. (2013). *Receptor/ligand sorting along the endocytic pathway*, vol. 78. Springer Science & Business Media. 72

Lodish, H., Baltimore, D., Berk, A., Zipursky, S.L., Matsudaira, P. & Darnell, J. (1995). *Molecular cell biology*, vol. 3. Scientific American Books New York. 168

Mac Gabhann, F. & Popel, A. (2007). Dimerization of VEGF receptors and implications for signal transduction: a computational study. *Biophysical chemistry*, **128**, 125–139. 5, 41, 47, 72, 260

Mac Gabhann, F. & Popel, A.S. (2004). Model of competitive binding of vascular endothelial growth factor and placental growth factor to vegf receptors on endothelial cells. *American Journal of Physiology-Heart and Circulatory Physiology*, **55**, H153. 46, 140, 192, 193, 259, 260, 265

Mac Gabhann, F. & Popel, A.S. (2005). Differential binding of vegf isoforms to vegf receptor 2 in the presence of neuropilin-1: a computational model. *American Journal of Physiology-Heart and Circulatory Physiology*, **288**, H2851–H2860. 137, 259, 260, 265

Mac Gabhann, F., Yang, M. & Popel, A. (2005). Monte carlo simulations of VEGF binding to cell surface receptors in vitro. *Biochimica et Biophysica Acta (BBA)-Molecular Cell Research*, **1746**, 95–107. 6, 72, 259, 260

Magnus, J. & Neudecker, H. (1985). Matrix differential calculus with applications to simple, hadamard, and kronecker products. *Journal of Mathematical Psychology*, **29**, 474–492. 99

Mahmood, T. & Yang, P.C. (2012). Western blot: technique, theory, and trouble shooting. *North American journal of medical sciences*, **4**, 429. 129

Manickam, V., Tiwari, A., Jung, J.J., Bhattacharya, R., Goel, A., Mukhopadhyay, D. & Choudhury, A. (2011). Regulation of vascular endothelial growth factor receptor 2 trafficking and angiogenesis by Golgi localized t-SNARE syntaxin 6. *Blood*, **117**, 1425–1435. 8

Marjoram, P., Molitor, J., Plagnol, V. & Tavaré, S. (2003). Markov chain monte carlo without likelihoods. *Proceedings of the National Academy of Sciences*, **100**, 15324–15328. 34, 156

McCaughtry, T.M., Wilken, M.S. & Hogquist, K.A. (2007). Thymic emigration revisited. *The Journal of experimental medicine*, **204**, 2513–2520. 223

Merkenschlager, M., Graf, D., Lovatt, M., Bommhardt, U., Zamoyska, R. & Fisher, A.G. (1997). How many thymocytes audition for selection? *Journal of Experimental Medicine*, **186**, 1149–1158. 211

Mittar, S., Ulyatt, C., Howell, G., Bruns, A., Zachary, I., Walker, J. & Ponnambalam, S. (2009). VEGFR1 receptor tyrosine kinase localization to the golgi apparatus is calcium-dependent. *Experimental Cell Research*, **315**, 877–889. 53

Moler, C. & Van Loan, C. (2003). Nineteen dubious ways to compute the exponential of a matrix, twenty-five years later. *SIAM review*, **45**, 3–49. 113

Nakayama, M., Nakayama, A., van Lessen, M., Yamamoto, H., Hoffmann, S., Drexler, H., Itoh, N., Hirose, T., Breier, G., Vestweber, D. *et al.* (2013). Spatial regulation of VEGF receptor endocytosis in angiogenesis. *Nature Cell Biology*, **15**, 249–260. 8

Napione, L., Pavan, S., Veglio, A., Picco, A., Boffetta, G., Celani, A., Seano, G., Primo, L., Gamba, A. & Bussolino, F. (2012). Unraveling the influence of endothelial cell density on VEGF-A signaling. *Blood*, **119**, 5599–5607. 110, 178, 261

Neudecker, H. & Magnus, J. (1988). Matrix differential calculus with applications in statistics and econometrics. 99

Neuts, M. (1994). *Matrix-geometric solutions in stochastic models: an algorithmic approach, second edition*. Courier Dover Publications. 8, 40

Olsson, A., Dimberg, A., Kreuger, J. & Claesson-Welsh, L. (2006). VEGF receptor signalling? in control of vascular function. *Nature Reviews Molecular Cell Biology*, **7**, 359–371. 11, 2, 5, 6

Palmer, E. (2003). Negative selectionclearing out the bad apples from the t-cell repertoire. *Nature Reviews Immunology*, **3**, 383–391. 210

Petrie, H.T. & Zúñiga-Pflücker, J.C. (2007). Zoned out: functional mapping of stromal signaling microenvironments in the thymus. *Annu. Rev. Immunol.*, **25**, 649–679. 210

Pryor, M.M., Low-Nam, S.T., Halász, Á.M., Lidke, D.S., Wilson, B.S. & Edwards, J.S. (2013). Dynamic transition states of erbb1 phosphorylation predicted by spatial stochastic modeling. *Biophysical journal*, **105**, 1533–1543. 264

Rennel, E., Varey, A., Churchill, A., Wheatley, E., Stewart, L., Mather, S., Bates, D. & Harper, S. (2009). Vegf121b, a new member of the vegfxxxb family of vegf-a splice isoforms, inhibits neovascularisation and tumour growth in vivo. *British journal of cancer*, **101**, 1183. 3

Ruch, C., Skiniotis, G., Steinmetz, M., Walz, T. & Ballmer-Hofer, K. (2007). Structure of a VEGF–VEGF receptor complex determined by electron microscopy. *Nature Structural & Molecular Biology*, **14**, 249–250. 41

Sadegh, M. & Vrugt, J.A. (2014). Approximate bayesian computation using markov chain monte carlo simulation: Dream (abc). *Water Resources Research*, **50**, 6767–6787. 156

Saini, M., Sinclair, C., Marshall, D., Tolaini, M., Sakaguchi, S. & Seddon, B. (2010). Regulation of zap70 expression during thymocyte development enables temporal separation of cd4 and cd8 repertoire selection at different signaling thresholds. *Science signaling*, **3**, ra23–ra23. 223

Saltelli, A., Tarantola, S., Campolongo, F. & Ratto, M. (2004). *Sensitivity analysis in practice: a guide to assessing scientific models*. John Wiley & Sons. 31

Sawicka, M., Stritesky, G.L., Reynolds, J., Abourashchi, N., Lythe, G., Molina-París, C. & Hogquist, K.A. (2014). From pre-dp, post-dp, sp4, and sp8 thymocyte cell counts to a dynamical model of cortical and medullary selection. *Frontiers in immunology*, **5**. 9, 209, 211, 212, 217

Schoeberl, B., Eichler-Jonsson, C., Gilles, E.D. & Müller, G. (2002). Computational modeling of the dynamics of the map kinase cascade activated by surface and internalized egf receptors. *Nature biotechnology*, **20**, 370–375. 173, 263

Scollay, R.G., Butcher, E.C. & Weissman, I.L. (1980). Thymus cell migration: quantitative aspects of cellular traffic from the thymus to the periphery in mice. *European journal of immunology*, **10**, 210–218. 223

Scott, A. & Mellor, H. (2009). Vegf receptor trafficking in angiogenesis. 11, 4

Shoup, D. & Szabo, A. (1982). Role of diffusion in ligand binding to macromolecules and cell-bound receptors. *Biophysical Journal*, **40**, 33–39. 51

Simons, M. (2012). An inside view: Vegf receptor trafficking and signaling. *Physiology*, **27**, 213–222. 3, 181

Simons, M., Gordon, E. & Claesson-Welsh, L. (2016). Mechanisms and regulation of endothelial vegf receptor signalling. *Nature Reviews Molecular Cell Biology*, **17**, 611–625. 3, 260

Sinclair, C., Bains, I., Yates, A.J. & Seddon, B. (2013). Asymmetric thymocyte death underlies the cd4: Cd8 t-cell ratio in the adaptive immune system. *Proceedings of the National Academy of Sciences*, **110**, E2905–E2914. 212, 223, 254

Smith, G.A., Fearnley, G.W., Tomlinson, D.C., Harrison, M.A. & Ponnambalam, S. (2015). The cellular response to vascular endothelial growth factors requires co-ordinated signal transduction, trafficking and proteolysis. *Bioscience reports*, **35**, e00253. 1, 181

Smith, G.A., Fearnley, G.W., Abdul-Zani, I., Wheatcroft, S.B., Tomlinson, D.C., Harrison, M.A. & Ponnambalam, S. (2016). Vegfr2 trafficking, signaling and proteolysis is regulated by the ubiquitin isopeptidase usp8. *Traffic*, **17**, 53–65. 181

Smith, G.A., Fearnley, G.W., Abdul-Zani, I., Wheatcroft, S.B., Tomlinson, D.C., Harrison, M.A. & Ponnambalam, S. (2017). Ubiquitination of basal vegfr2 regulates signal transduction and endothelial function. *Biology open*, **6**, 1404–1415. 263

Smoluchowski, M.v. (1917). Grundriß der koagulationskinetik kolloider lösungen. *Colloid & Polymer Science*, **21**, 98–104. 52

Sobol, I.M. (1993). Sensitivity estimates for nonlinear mathematical models. *Mathematical Modelling and Computational Experiments*, **1**, 407–414. 32, 33

Starbuck, C. & Lauffenburger, D.A. (1992). Mathematical model for the effects of epidermal growth factor receptor trafficking dynamics on fibroblast proliferation responses. *Biotechnology progress*, **8**, 132–143. 140, 192

Starbuck, C., Wiley, H. & Lauffenburger, D. (1990). Epidermal growth factor binding and trafficking dynamics in fibroblasts: relationship to cell proliferation. *Chemical Engineering Science*, **45**, 2367–2373. 6, 83, 111

Stritesky, G.L., Jameson, S.C. & Hogquist, K.A. (2012). Selection of self-reactive t cells in the thymus. *Annual review of immunology*, **30**, 95–114. 210, 211, 212

Stritesky, G.L., Xing, Y., Erickson, J.R., Kalekar, L.A., Wang, X., Mueller, D.L., Jameson, S.C. & Hogquist, K.A. (2013). Murine thymic selection quantified using a unique method to capture deleted t cells. *Proceedings of the National Academy of Sciences*, **110**, 4679–4684. 209, 222, 223

Surh, C.D. & Sprent, J. (1994). T-cell apoptosis detected in situ during positive and negative selection in the thymus. *Nature*, **372**, 100. 211

Tan, W., Popel, A. & Mac Gabhann, F. (2013a). Computational model of VEGFR2 pathway to erk activation and modulation through receptor trafficking. *Cellular signalling*, **25**, 2496–2510. 6, 77, 260

Tan, W.H., Popel, A.S. & Mac Gabhann, F. (2013b). Computational model of gab1/2-dependent vegfr2 pathway to akt activation. *PloS one*, **8**, e67438. 192, 193, 259, 260

Tan, W.H., Popel, A.S. & Mac Gabhann, F. (2013c). Computational model of vegfr2 pathway to erk activation and modulation through receptor trafficking. *Cellular signalling*, **25**, 2496–2510. 140, 193, 194, 197, 259, 260, 263

Taylor, H.M. & Karlin, S. (2014). *An introduction to stochastic modeling*. Academic press. 11

Teis, D. & Huber, L. (2003). The odd couple: signal transduction and endocytosis. *Cellular and Molecular Life Sciences CMLS*, **60**, 2020–2033. 4

Thomas-Vaslin, V., Altes, H.K., de Boer, R.J. & Klatzmann, D. (2008). Comprehensive assessment and mathematical modeling of t cell population dynamics and homeostasis. *The Journal of Immunology*, **180**, 2240–2250. 223, 254

Toni, T., Welch, D., Strelkowa, N., Ipsen, A. & Stumpf, M.P. (2009). Approximate bayesian computation scheme for parameter inference and model selection in dynamical systems. *Journal of the Royal Society Interface*, **6**, 187–202. 34

Tzafriri, A.R. & Edelman, E.R. (2007). Endosomal receptor kinetics determine the stability of intracellular growth factor signalling complexes. *Biochemical Journal*, **402**, 537–549. 140, 192

Van Kampen, N.G. (1992). *Stochastic processes in physics and chemistry*, vol. 1. North holland. 7, 26, 27, 61

van Meerwijk, J.P., Marguerat, S., Lees, R.K., Germain, R.N., Fowlkes, B. & MacDonald, H.R. (1997). Quantitative impact of thymic clonal deletion on the t cell repertoire. *Journal of Experimental Medicine*, **185**, 377–384. 211

Vempati, P., Mac Gabhann, F. & Popel, A.S. (2010). Quantifying the proteolytic release of extracellular matrix-sequestered vegf with a computational model. *PloS one*, **5**, e11860. 140, 192

Wegmann, D., Leuenberger, C. & Excoffier, L. (2009). Efficient approximate bayesian computation coupled with markov chain monte carlo without likelihood. *Genetics*, **182**, 1207–1218. 34, 37

Weiss, N.A. (2006). *A course in probability*. Addison-Wesley. 17

Werlen, G., Hausmann, B., Naeher, D. & Palmer, E. (2003). Signaling life and death in the thymus: timing is everything. *Science*, **299**, 1859–1863. 210

Wheeler, D.L., Dunn, E.F. & Harari, P.M. (2010). Understanding resistance to egfr inhibitorsimpact on future treatment strategies. *Nature reviews Clinical oncology*, **7**, 493–507. 262

Whitaker, G.B., Limberg, B.J. & Rosenbaum, J.S. (2001). Vascular endothelial growth factor receptor-2 and neuropilin-1 form a receptor complex that is responsible for the differential signaling potency of vegf165 and vegf121. *Journal of Biological Chemistry*, **276**, 25520–25531. 3

Wilkinson, D.J. (2011). *Stochastic modelling for systems biology*. CRC press. 34

Wu, J., Dhingra, R., Gambhir, M. & Remais, J.V. (2013). Sensitivity analysis of infectious disease models: methods, advances and their application. *Journal of The Royal Society Interface*, **10**, 20121018. 31

Yamada, K., Nakajima, Y., Geyer, M., Wary, K., Ushio-Fukai, M., Komarova, Y. & Malik, A. (2014). KIF13B regulates angiogenesis through Golgi to plasma membrane trafficking of VEGFR2. *Journal of Cell Science*, **127**, 4518–4530. 8

Zhang, X., Lanahan, A. & Simons, M. (2013). VEGFR2 trafficking: speed doesnt kill. *Cell Cycle*, **12**, 2163–2164. 8

Zhang, Z., Neiva, K., Lingen, M., Ellis, L. & Nör, J. (2010). Vegf-dependent tumor angiogenesis requires inverse and reciprocal regulation of vegfr1 and vegfr2. *Cell Death & Differentiation*, **17**, 499–512. 263